High-Energy Phenomena

# in Relativistic Outflows V

Proceedings

La Plata, Argentina

October 5-8, 2015

Asociación Argentina de Astronomía

High-Energy Phenomena in Relativistic Outflows V
Proceedings

La Plata, Argentina, October 5–8, 2015

Leonardo J. Pellizza & Gustavo E. Romero, eds.

Credits

Cover: Schlieren map of a 3D GRB jet once it has broken out of the progenitor (see López Cámara et al., pp. 61–66).

Asociación Argentina de Astronomía

Fundada en 1958

Personería Jurídica (Legajo 21.459 - Matr. 1.421), Pcia. de Buenos Aires

Comisión Directiva
(2014–2017)

Presidente:	Dr. Guillermo Bosch
Vicepresidente:	Dra. Andrea Costa
Secretario:	Dr. Roberto Venero
Tesorera:	Dra. Mónica Cardaci
Vocal 1ro:	Dr. Javier Ahumada
Vocal 2do:	Dr. Jorge Combi
Vocal Sup. 1ro:	Dr. Sergio Dasso
Vocal Sup. 2do:	Dr. Federico González

Comisión Revisora de Cuentas

Titulares:	Dra. Cristina Cappa
	Dra. Gabriela Castelleti
	Dr. Alejandro Córsico

Comité Nacional de Astronomía

Secretaria:	Dra. Estela Reynoso
Miembros:	Dra. Andrea Torres
	Dr. Christian Giuppone
	Dr. Rene Rohrmann
	Dr. Mariano Domínguez

Asociación Argentina de Astronomía

High-Energy Phenomena in Relativistic Outflows V
Proceedings

La Plata, Argentina, October 5–8, 2015

Scientific Organizing Committee

Chair: G.E. Romero (IAR - FCAG, Argentina)
Members: F.A. Aharonian (DIAS, Ireland - MPIK, Germany)
E. Amato (INAF - Osservatorio Astrofisico di Arcetri, Italy)
M. Begelman (University of Colorado, USA)
G.S. Bisnovatyi-Kogan (Space Research Institute, Russia)
V. Bosch-Ramon (Universitat de Barcelona, Spain)
K.S. Cheng (University of Hong-Kong, China)
P. Coppi (Yale University, USA)
D. Khangulyan (Japan Aerospace Exploration Agency, Japan)
S. Lizano (Centro de Radioastronomía y Astrofísica, UNAM, Mexico)
Y. Lyubarsky (Ben-Gurion University, Israel)
A. Marscher (Boston University, USA)
P. Mészáros (Pennsylvania State University, USA)
J. M. Paredes (Universitat de Barcelona, Spain)
Y. Uchiyama (Rikkyo University, Japan)

Local Organizing Committee

Chair: Gustavo E. Romero (IAR - FCAG)
Co-chair: Gabriela S. Vila (IAR)
Members: Ileana Andruchow (IALP - FCAG)
Ma. Victoria del Valle (IAR)
Carolina Pepe (IAR)
Cintia Peri (IAR)
Matías Tueros (IAR)
Florencia L. Vieyro (IAR)

Editorial Committee

Members: Leonardo J. Pellizza
Gustavo E. Romero
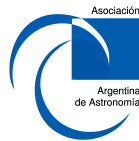
Sponsors

Foreword

The fifth meeting of the High-Energy Phenomena in Relativistic Outflows (HEPRO) series (`http://hepro5.iar.unlp.edu.ar/`) was successfully held in the city of La Plata, Argentina between 5 and 8 October 2015. It was organized by the Relativist Astrophysics Group And Radioastronomy (GARRA, `http://garra.iar.unlp.edu.ar/`) based at the Argentine Institute for Radioastronomy (IAR-CONICET-CIC). The previous meetings of the series took place in Dublin (2007), Buenos Aires (2009), Barcelona (2011) and Heidelberg (2013).

The meeting was attended by 79 participants from 16 countries in the Americas, Europe, Africa and Asia. There were 9 invited talks, 7 featured talks, 25 contributed talks, and 28 poster contributions. There were abundant and interesting discussions among the participants during the talks, which extended to the intervals of rest and social activities. The papers presented covered almost all fields of high-energy astrophysics: acceleration of particles, plasma and astrophysical flows (jets, winds, accretion discs), production of high-energy radiation, sources of non-thermal radiation (different types of binaries, active galactic nuclei, gamma ray bursts, pulsar nebulae, and more) and cosmic rays. The topics were approached from the point of view of the observations, theory and numerical simulations. This book contains a good sample of articles based on the lectures.

The HEPRO V organization was sponsored by the National Council for Scientific and Technical Research (CONICET), the National Agency for the Promotion of Science and technology (ANPCyT), the Committee for Scientific Research of the Province of Buenos Aires (CIC), the IAR, the Argentine Astronomical Society, the Faculty of Astronomy and Geophysics (FCAG-UNLP), the Argentine Physical Association (AFA), and the Abdus Salam Center for Theoretical Physics (ICTP). The event was declared of Legislative Interest by the Honorable Chamber of Senators of the Province of Buenos Aires, and of Municipal Interest by the Municipality of La Plata. We are grateful to all these organizations.

We thank the Scientific Organizing Committee for excellent advice that helped to shape the program, and the reviewers that read the papers offered in this volume. Special thanks go to the members of the LOC and those students who helped with the organization.

Gustavo E. Romero
Leonardo J. Pellizza

Conference picture.

Contents

Poster contributions

Invited contributions

Relativistic jets: an overview of recent progress

Elena Pian[1,2]

[1]*INAF IASF Bologna, Via P. Gobetti 101, 40129 Bologna, Italy*
[2]*Piazza dei Cavalieri 7, 56126 Pisa, Italy*

Abstract. Despite their different nature and physics, blazars and γ-ray bursts have in common very powerful relativistic jets, which make them the most luminous sources in the Universe. The energy extraction from the central compact object, the jet collimation, the role and geometry of the magnetic fields, the structure of the jet itself represent still big enough questions that a complete paradigm cannot yet be drawn. This article is concerned with the main observational facts about blazars and gamma-ray burst jets, based on multi-wavelength campaigns, and on the clues one can glean from these on jet formation, behavior and powering. The future generation of telescopes and instruments and the contributions from multi-messenger investigation (astroparticle diagnostics and gravitational waves) will warrant further significant progress.

1. Introduction

Jets are ubiquitous in astrophysics, both in the Galaxy from parsec (proto-stars) to kilo-parsec (X-ray binaries, a.k.a. micro-quasars) scales, and outside, in nearby radio-galaxies like Centaurus A (4 Mpc) and M87 (15 Mpc), and at cosmological distances, where they are responsible for the blazar and gamma-ray burst (GRB) phenomenon. Accordingly, their observed luminosities span a wide range and the kinematic regimes of the expanding plasma are very different, from Newtonian in protostellar objects, to ultra-relativistic in GRBs. In X-ray binaries, where the bolometric luminosities reach $\sim 10^{39}$ erg s^{-1} (Mirabel & Rodríguez 1999; Fender & Belloni 2004), Lorentz factors of a few can be directly estimated from observation of both jet and counter-jet. Blazars can reach luminosities of $\sim 10^{48}$ erg s^{-1} during outbursts, when generally the gamma-ray output dominates the total observed luminosity, and Lorentz factors of $\sim$10-20 are inferred from superluminal motions (Jorstad et al. 2013) and compactness arguments (McBreen 1979; Maraschi, Ghisellini, & Celotti 1992). Gamma-ray luminosities of $\sim 10^{51}$ erg s^{-1} and energy outputs of $\sim 10^{52}$ erg are observed in GRBs (e.g. Amati et al. 2008), that are the most extreme macroscopic relativistic sources in the Universe, with Lorentz factors in excess of 100 (Mészáros 2002; Piran 2004).

According to a now widely accepted unifying scenario (Urry & Padovani 1995), blazar jets are the analogues of the kilo-parsec elongated structures angularly resolved with the VLBI in radio-galaxies, only closely (less than 10 degrees) aligned to the line of sight. On the other hand, in GRBs, while there is evidence of plasma relativistic expansion from radio observations of the afterglows, that has made possible the derivation of a Lorentz factor at a few days after the explo-

sion (Frail et al. 1997; Mesler et al. 2012), no direct observation of jets has ever been reported. However, their presence is inferred from the model-independent argument that the huge observed energy outputs (on average 10^{52} erg and sometimes in excess of 10^{54} erg) coupled with the millisecond variability timescales imply that the binding energy of a stellar-size collapsing/exploding object is transformed into radiation with 100% efficiency. This leads almost naturally to the conclusion that the radiation, instead of being emitted isotropically, must be collimated in a narrow beam, whose aperture is estimated to be of a few degrees (e.g. Frail et al. 2001; Grupe et al. 2006). Typical signatures of jets are thought to be the achromatic temporal breaks seen in their afterglow light curves, and due to the fact that plasma deceleration and Lorentz factor drop make the jet edge causally connect with the observer (Rhoads 1999; Beuermann et al. 1999; Harrison et al. 1999; Israel et al. 1999; Stanek et al. 1999; Panaitescu & Kumar 2002).

Recently, Nemmen et al. (2012) have shown that jets produced by blazars and GRBs exhibit the same correlation between the kinetic power carried by accelerated particles and the gamma-ray luminosity, with blazars and GRBs lying at the low- and high-luminosity ends, respectively, of the correlation.This result implies that the efficiency of energy dissipation in jets is similar over 10 orders of magnitude in jet power, establishing a physical analogy between blazars and GRBs, despite the macroscopic differences, i.e. primarily the persistence of jets in blazars, as opposed to their rapidly transient nature in GRBs. This leads us to compare these two classes of sources, in an attempt to clarify how jet physics scales from compact central engines in GRBs (stellar black holes or highly magnetized rotating neutron stars) to supermassive black holes in active galactic nuclei.

2.   Blazars

Blazars are detected from radio to very high gamma-ray frequencies, they constitute the majority of extragalactic sources detected in MeV-GeV gamma-rays (Acero et al. 2015) and are the only known cosmological TeV emitters (Aharonian et al. 2013)[1]. Their spectral energy distributions (νf_ν representation) are dominated by non-thermal processes: synchrotron radiation at the lower frequencies from a population of leptons, with a spectral peak between the infrared and soft-X-ray domain, and a radiation component at high energies (hard-X- and gamma-rays) that can be due either to inverse Compton scattering of synchrotron photons or external photons off leptons or to proton-synchrotron emission, π_0 decay photons, synchrotron, and Compton emission from secondary decay products of charged pions, and the output from pair cascades initiated by these high-energy emissions intrinsically absorbed by photon-photon pair production (see Böttcher et al. 2013, and Falomo, Pian, & Treves 2014 for reviews).

Occasionally, the synchrotron peak can reach frequencies larger than 100 keV during outbursts, as often observed in the BL Lac Mkn 501 (Pian et al.

---

[1]Blazars are virtually the only extragalactic sources detected by Cherenkov telescopes, the exceptions being the very nearby starburst galaxies M82 and NGC253 (Itoh et al. 2002; VERITAS Collaboration 2009).

1998; Furniss et al. 2015), and, less conspicuously, in other blazars (Giommi, Padovani, & Perlman 2000; Costamante et al. 2001). During these hard X-ray outbursts, the source is usually also in a high TeV state, although the radiation at these energies is dramatically affected by the large Klein-Nishina cross-section, if due to synchrotron self-Compton scattering. Sources with this extreme behavior are the tracers of the most energetic radiating particles, so that their identification represents an effective investigation tool of the most powerful and efficient acceleration mechanisms in astrophysics. Optimal methods to select "extreme synchrotron" blazar candidates include TeV detection (for the nearest sources, that are less affected by extragalactic background suppression, Costamante 2013) and a characteristic multi-wavelength spectral shape (Bonnoli et al. 2015). Interestingly, not all extreme-synchrotron candidates actually display extremely high peak energies during outbursts, the most remarkable case being Mkn 421: a very close spectral analogue of Mkn 501, its synchrotron peak energy never exceeds 10-15 keV during the major historical X-ray outbursts (Pian et al. 2014, and references therein, see Figure 1), which suggests the action of an "inhibiting" parameter (perhaps an external photon field that is more significant than in Mkn 501).

A relationship links the total luminosity and the location of the characteristic spectral peaks in blazars, in the sense that blazars of higher luminosity tend to have these peaks at lower frequencies (with exceptions, Padovani, Giommi, & Rau 2012; Arsioli et al. 2015). This "blazar sequence" (Fossati et al. 1998) implies an anti-correlation between the radiation energy density and the particles break energy, that indicates a rough constant cooling rate for all sources near peak energy (Ghisellini et al. 1998; Ghisellini 1999). A viable interpretation consists in the different role played by the external photon fields in the cooling, more luminous sources having more prominent accretion disk components and more intense broad emission lines, that make cooling of accelerated particles via inverse Compton scattering more efficient. However, in individual sources the opposite behavior is observed during outbursts: the luminosity and the peak energy both rise and decrease simultaneously in a correlated way during the outburst, likely because the equilibrium configuration is temporarily lost (see e.g. Tavecchio et al. 2000).

3. Gamma-ray bursts

Nearly twenty years after the beginning of the "afterglow era", started with the rapid and accurate localizations of the *BeppoSAX* satellite (Costa et al. 1997), over 1000 GRBs have been localized at gamma- and X-rays by various space missions — the majority with the *Swift* satellite (Gehrels et al. 2004) — and have well observed multi-wavelength counterparts. These witness the presence and behavior of jets, whose geometry, structure, composition and dynamics are still matter of investigation. The biggest crucible related to GRBs however is the nature of their progenitors and the jet powering mechanism. While short GRBs[2] seem to be compatible with the merger of a coalescing binary compact

---

[2]The majority of observed GRBs have durations longer than $\sim$2 s (Kouveliotou et al. 1993) and are thus defined as long GRBs, as opposed to short or sub-second GRBs.
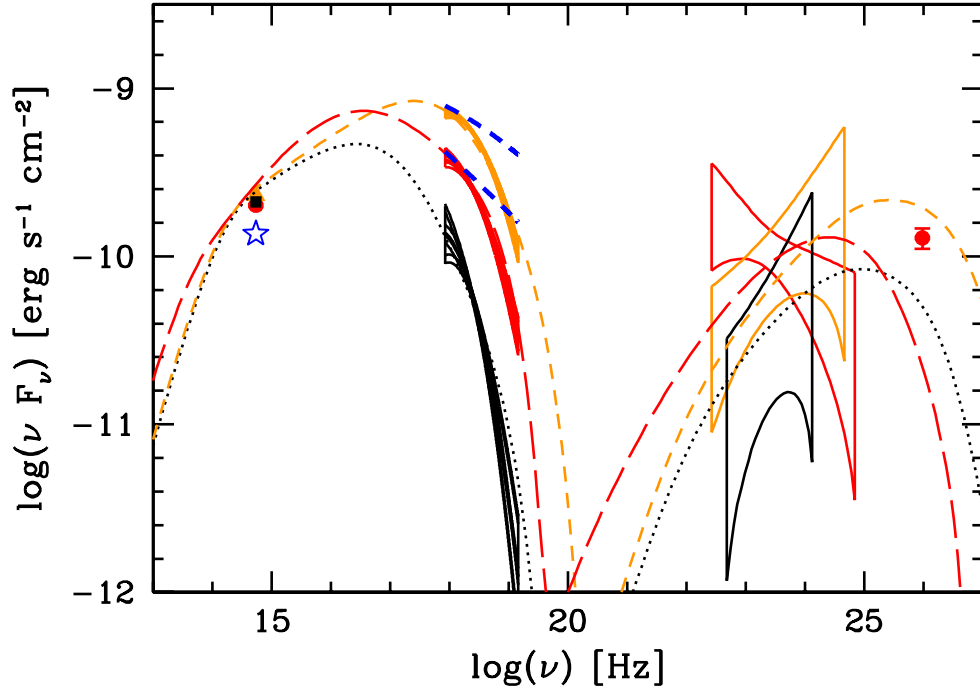
Figure 1.   Spectral energy distributions of Mkn 421 at the average UT epochs of 16.1–16.5 (red), 17.1–17.4 (orange), and 19.0–19.5 (black) April 2013 from simultaneous *INTEGRAL* IBIS/ISGRI, JEM-X and OMC, and *Fermi*-LAT data. The optical data were corrected for Galactic absorption and for the contamination by galaxies in the field. The 1-σ error contours of the joint JEM-X and IBIS/ISGRI spectra and LAT spectra are reported. The TeV point from VERITAS (red), taken on April 16.3, is also shown. The models (long dash: April 16, short dash: April 17, dot: April 19) include a synchrotron component at the lower energies, produced in a single emitting zone, and a synchrotron self-Compton scattering component at higher energies. For comparison, the JEM-X and IBIS/ISGRI quiescent and active state spectra of June 2006 are reported as thick dashed blue lines. The average optical flux at the same epoch is shown as a blue star. Credit: Pian et al., A&A, 570, A77, (2014), reproduced with permission ©ESO. See also Lichti et al. (2008).

star system, whose indirect evidence may be represented by a nucleo-synthetic near-infrared signal (Tanvir et al. 2013; Berger, Fong, & Chornock 2013), long GRBs are connected with supernovae: with two exceptions, that raised however considerable debate (Della Valle et al. 2006a; Fynbo et al. 2006; Gal-Yam et al. 2006; Gehrels et al. 2006; Ofek et al. 2007; McBreen et al. 2008; Jin et al. 2015), all GRBs at $z \lesssim 0.2$ are associated with supernovae that were classified as type Ic (i.e. core-collapse supernovae with stripped hydrogen and helium envelopes) based on the unambiguous identification of typical atomic species in their ejecta (e.g., Galama et al. 1998; Hjorth et al. 2003; Malesani et al. 2004; Modjaz et al. 2006; Pian et al. 2006; Bufano et al. 2012; D'Elia et al. 2015). At higher redshifts, the identification of spectroscopic features is made more arduous by the contamination of the host galaxy and afterglow, but a general spectral resemblance with GRB-supernovae at lower redshifts is found, or, lacking a reliable spectrum, the SN presence is signalled by the rebrightening of the light curve at around 10-15 rest-frame days after GRB explosion (Della Valle et al. 2003;2006b; Fynbo et al. 2004; Soderberg et al. 2005;2006; Bersier et al. 2006; Berger et al. 2011; Cano et al. 2014; Melandri 2012;2014). The bolometric light curves of the two nearest known GRB-SNe, SN1999bw and SN2006aj and of a regular (i.e. not accompanied by a high energy transient) Ic supernova, SN1994I, are shown in Figure 2.

The most remarkable aspect of GRB-supernovae is their kinetic energies, that are of the order of $\sim 10^{52}$ erg or higher i.e. a factor 10 or more larger than those of regular core-collapse supernovae (Mazzali et al. 2006a). When a correction for jet collimation is applied to the gamma-ray energy output of the GRB, this is a small fraction (less than 10%) of the supernova kinetic energy, indicating that the energetically dominant player in the phenomenon is the supernova, not the GRB (Woosley & Bloom 2006; Mazzali et al. 2014). This has led to the scenario in which a rapidly rotating newly formed neutron star with a large magnetic field, a magnetar, may be responsible for GRBs, by powering the supernova with its rotational energy (which is indeed of the order of $\sim 10^{52}$ erg for a millisecond proto-neutron star) and producing a relativistic outflow along its rotation axis, where energy is radiated away via magnetic dipole mechanism in a time compatible with a GRB duration if the field is of the order of $\sim 10^{14}$ Gauss, as typically seen in a magnetar (Usov 1992). This picture has gathered impulse (Mazzali et al. 2006b; Kasen & Bildsten 2010; Metzger et al. 2011;2015) as an alternative to the collapsar, that envisages GRBs originating from accretion disks promptly formed around black holes that result from massive stars core collapse (MacFadyen & Woosley 1999).

Among the findings of *Swift* is the detection of an observationally rare class of GRBs, whose duration of about 10000 seconds exceeds significantly the average duration of long GRBs. The afterglow of one of these "ultra-long" GRBs, GRB111209A, was thoroughly studied at X-ray and optical wavelengths (Gendre et al. 2013; Stratta et al. 2013; Levan et al. 2014), and the regular and intensive optical/near-infrared monitoring with the GROND instrument on the ESO 2.2m telescope revealed the presence of a supernova, dubbed SN2011kl (Greiner et al. 2015). SN2011kl does not resemble any of the GRB-supernovae previously detected, being more luminous and very poor in metals. Its luminosity places it at halfway between "classical" GRB-supernovae and the so called super-luminous supernovae (see Figure 2), a class of supernovae recently discovered, very massive
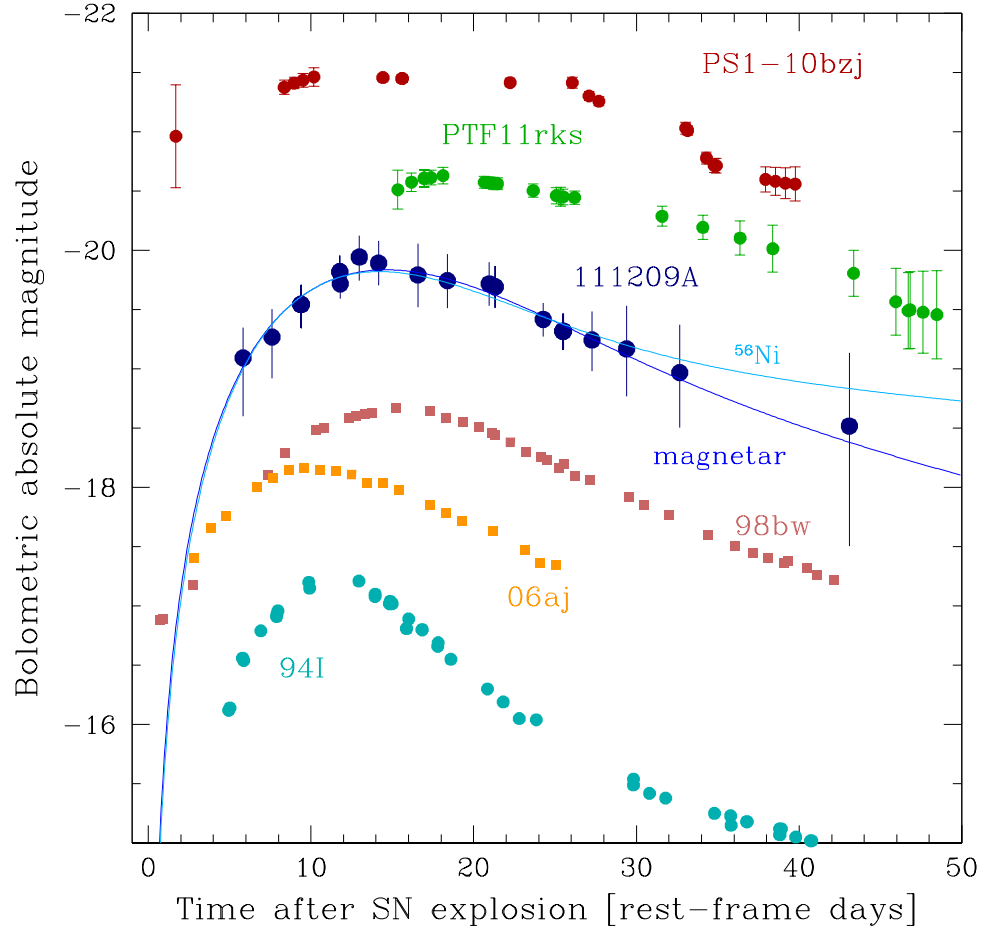
Figure 2.　Bolometric light curves of the "classical" GRB supernovae GRB980425/SN 1998bw and XRF 060218/SN 2006aj, the standard type Ic SN1994I, the super-luminous supernovae PTF11rks and PS1-10bzj (among the fastest declining super-luminous supernovae known so far) and the SN 2011kl associated with the ultra-long GRB111209A (observed duration of ∼10000 seconds). SN2011kl has an intermediate maximum luminosity between the GRB supernovae and the super-luminous supernovae. Solid lines show the best-fitting synthetic light curves computed with a magnetar injection model (dark blue) and ^{56}Ni powering (light blue). Reproduced from Greiner et al., Nature, 523, 189, (2015).

and luminous, a fraction of which may be related to pair instability in the stellar nucleus (Gal-Yam 2012).

The high amount of radioactive nickel (^{56}Ni) that is formally necessary to account for the light curve of SN2011kl ($\sim$1 $M_\odot$) is inconsistent with the low metal content inferred from the optical spectrum, suggesting that an extra component is responsible for powering the supernova. Since the accretion rates implied in a collapsar scenario are incompatible with the GRB duration (the progenitor core mass would exceed many hundreds of solar masses), the magnetar alternative seems viable and even more cogent than it is for the supernovae accompanying "regular" long GRB. The fact that SN2011kl is more luminous than the other GRB-supernovae and thus more similar to super-luminous supernovae, is an added element in favour of magnetar, that was proposed as the engine of super-luminous supernovae (Woosley 2010).

4.   Conclusions

Although it is not yet clear what ultimately causes and triggers blazar multi-wavelength outbursts, the strong correlation between broad emission line luminosity and jet luminosity indicates that the control parameter for both is accretion (Ghisellini et al. 1998; Sbarrato et al. 2012). Accretion may also play a crucial role in GRBs if a fraction or all of them are powered by rotating black holes, as in the collapsar model. The biggest open problem would then consist in understanding how physical properties scale with central black hole mass in the two phenomena, considered that energy dissipation appears to correlate with jet power in a very similar way (Nemmen et al. 2012).

A further complication may descend from the detection of at least one case of a GRB-supernova association, GRB111209A/SN2011kl, where a magnetar scenario (rapidly rotating, highly magnetized proto-neutron star), rather than a collapsar (accreting black hole), seems not only viable but preferred. The fact that both the GRB and the supernova belong to peculiar types (the GRB is ultra-long and the supernova is a factor of 3 more luminous than previously detected GRB supernovae and a factor of 3 less luminous than fast-declining super-luminous supernovae) compounds the issue and points to a novel aspect of GRB-supernova diversity.

More observations in the form of dedicated campaigns and strategically designed multi-wavelength monitoring are necessary to clarify these issues. Specifically, these include mapping of blazar jets with correlated rapid X-ray and TeV variability (see e.g., Albert et al. 2007), the latter becoming possible within the next decade thanks to the sensitive next generation Cherenkov Telescope Array, and accurate optical and high energy observations of ultra-long GRBs.

A very ambitious goal is the construction of a unifying scenario for long GRBs and supernovae, analogous to the one that links FR I and FR II radio-galaxies to BL Lac objects and Flat-Spectrum Radio Quasars, respectively. Since GRBs have jets of a few degrees aperture, if all the long ones, or a large fraction thereof, are related to energetic supernovae, we should be observing – within a given cosmological volume – many more energetic supernovae than GRBs, because the vast majority of GRB jets would be misaligned with respect to our line of sight. The present sensitive all-sky high cadence optical surveys are de-

tecting numerous energetic Ic supernovae (e.g. Mazzali et al. 2013); however, establishing the presence of an accompanying misaligned GRB is difficult. Multi-wavelength relativistic jet models (van Eerten, Zhang, & MacFadyen 2010) predict that a rebrightening in the radio light curve of a GRB afterglow should occur months or years after explosion as the jetted blast wave isotropizes. Lacking a detection in gamma- or X-rays, a misaligned GRB jet should therefore become detectable as enhanced radio emission from the location of its energetic supernova progenitor. This requires however a very sensitive radio array and long uninterrupted exposures of a sizable sample of high kinetic energy supernovae. The newly deployed and developing LOFAR experiment may be suited for this investigation. In the case of short GRBs, an analogous search for transients at low-frequency radio wavelengths (Nakar & Piran 2011) may reveal the counterparts of double neutron star mergers even in the absence of a detected short GRB. In addition, it would contribute to validate any gravitational radiation signal emitted right before the merger.

References

Acero, F., Ackermann, M., Ajello, M., et al. 2015, ApJS, 218, 23

Aharonian, F., Essey, W., Kusenko, A., & Prosekin, A. 2013, Phys. Rev. D, 87, 063002

Albert, J., Aliu, E., Anderhub, H., et al. 2007, ApJ, 669, 862

Amati, L., Guidorzi, C., Frontera, F., et al. 2008, MNRAS, 391, 577

Arsioli, B., Fraga, B., Giommi, P., Padovani, P., & Marrese, P.M. 2015, A&A, 579, A34

Berger, E., Chornock, R., Holmes, T. R., et al. 2011, ApJ, 743, 204

Berger, E., Fong, W., & Chornock, R. 2013, ApJ, 774, L23

Bersier, D., Fruchter, A. S., Strolger, L.-G., et al. 2006, ApJ, 643, 284

Beuermann, K., Hessman, F. V., Reinsch, K., et al. 1999, A&A, 352, L26

Böttcher, M., Reimer, A., Sweeney, K., & Prakash, A. 2013, ApJ, 768, 54

Bonnoli, G., Tavecchio, F., Ghisellini, G., & Sbarrato, T. 2015, MNRAS, 451, 611

Bufano, F., Pian, E., Sollerman, J., et al. 2012, ApJ, 753, 67

Cano, Z., de Ugarte Postigo, A., Pozanenko, A., et al. 2014, A&A, 568, A19

Costa, E., Frontera, F., Heise, J., et al. 1997, Nature, 387, 783

Costamante, L., Ghisellini, G., Giommi, P., et al. 2001, A&A, 371, 512

Costamante, L. 2013, International Journal of Modern Physics D, 22, 1330025

D'Elia, V., Pian, E., Melandri, A., et al. 2015, A&A, 577, A116

Della Valle, M., Malesani, D., Benetti, S., et al. 2003, A&A, 406, L33

Della Valle, M., Chincarini, G., Panagia, N., et al. 2006a, Nature, 444, 1050

Della Valle, M., Malesani, D., Bloom, J. S., et al. 2006b, ApJ, 642, L103

Falomo, R., Pian, E., & Treves, A. 2014, A&A Rev., 22, 73

Fender, R., & Belloni, T. 2004, ARA&A, 42, 317

Fossati, G., Maraschi, L., Celotti, A., Comastri, A., & Ghisellini, G. 1998, MN-RAS, 299, 433

Frail, D. A., Kulkarni, S. R., Nicastro, L., Feroci, M., & Taylor, G. B. 1997, Nature, 389, 261

Frail, D. A., Kulkarni, S. R., Sari, R., et al. 2001, ApJ, 562, L55

Furniss, A., Noda, K., Boggs, S., et al. 2015, ApJ, 812, 65

Fynbo, J. P. U., Sollerman, J., Hjorth, J., et al. 2004, ApJ, 609, 962

Fynbo, J. P. U., Watson, D., Thöne, C. C., et al. 2006, Nature, 444, 1047

Galama, T. J., Vreeswijk, P. M., van Paradijs, J., et al. 1998, Nature, 395, 670

Gal-Yam, A., Fox, D. B., Price, P. A., et al. 2006, Nature, 444, 1053

Gal-Yam, A. 2012, Science, 337, 927

Gehrels, N., Chincarini, G., Giommi, P., et al. 2004, ApJ, 611, 1005

Gehrels, N., Norris, J. P., Barthelmy, S. D., et al. 2006, Nature, 444, 1044

Gendre, B., Stratta, G., Atteia, J. L., et al. 2013, ApJ, 766, 30

Ghisellini, G., Celotti, A., Fossati, G., Maraschi, L., & Comastri, A. 1998, MN-RAS, 301, 451

Ghisellini, G. 1999, Astroparticle Physics, 11, 11

Giommi, P., Padovani, P., & Perlman, E. 2000, MNRAS, 317, 743

Greiner, J., Mazzali, P. A., Kann, D. A., et al. 2015, Nature, 523, 189

Grupe, D., Brown, P. J., Cummings, J., et al. 2006, ApJ, 645, 464

Harrison, F. A., Bloom, J. S., Frail, D. A., et al. 1999, ApJ, 523, L121

Hjorth, J., Sollerman, J., Møller, P., et al. 2003, Nature, 423, 847

Israel, G. L., Marconi, G., Covino, S., et al. 1999, A&A, 348, L5

Itoh, C., Enomoto, R., Yanagita, S., et al. 2002, A&A, 396, L1

Jin, Z.-P., Li, X., Cano, Z., et al. 2015, ApJ, 811, L22

Jorstad, S. G., Marscher, A. P., Smith, P. S., et al. 2013, ApJ, 773, 147

Kasen, D., & Bildsten, L. 2010, ApJ, 717, 245

Kouveliotou, C., Meegan, C. A., Fishman, G. J., et al. 1993, ApJ, 413, L101

Levan, A. J., Tanvir, N. R., Starling, R. L. C., et al. 2014, ApJ, 781, 13

Lichti, G. G., Bottacini, E., Ajello, M., et al. 2008, A&A, 486, 721

MacFadyen, A. I., & Woosley, S. E. 1999, ApJ, 524, 262

Malesani, D., Tagliaferri, G., Chincarini, G., et al. 2004, ApJ, 609, L5

Maraschi, L., Ghisellini, G., & Celotti, A. 1992, ApJ, 397, L5

Mazzali, P. A., Deng, J., Pian, E., et al. 2006a, ApJ, 645, 1323

Mazzali, P. A., Deng, J., Nomoto, K., et al. 2006b, Nature, 442, 1018

Mazzali, P. A., Walker, E. S., Pian, E., et al. 2013, MNRAS, 432, 2463

Mazzali, P. A., McFadyen, A. I., Woosley, S. E., Pian, E., & Tanaka, M. 2014, MNRAS, 443, 67

McBreen, B. 1979, A&A, 71, L19

McBreen, S., Foley, S., Watson, D., et al. 2008, ApJ, 677, L85

Melandri, A., Pian, E., Ferrero, P., et al. 2012, A&A, 547, A82

Melandri, A., Pian, E., D'Elia, V., et al. 2014, A&A, 567, A29

Mesler, R. A., Pihlström, Y. M., Taylor, G. B., & Granot, J. 2012, ApJ, 759, 4

Mészáros, P. 2002, ARA&A, 40, 137

Metzger, B. D., Giannios, D., Thompson, T. A., Bucciantini, N., & Quataert, E. 2011, MNRAS, 413, 2031

Metzger, B. D., Margalit, B., Kasen, D., & Quataert, E. 2015, MNRAS, 454, 3311

Mirabel, I. F., & Rodríguez, L. F. 1999, ARA&A, 37, 409

Modjaz, M., Stanek, K. Z., Garnavich, P. M., et al. 2006, ApJ, 645, L21

Nakar, E., & Piran, T. 2011, Nature, 478, 82

Nemmen, R.S., Georganopoulos, M., Guiriec, S., Meyer, E.T., & Sambruna, R.M. 2012, Science, 338, 1445

Ofek, E. O., Cenko, S. B., Gal-Yam, A., et al. 2007, ApJ, 662, 1129

Padovani, P., Giommi, P., & Rau, A. 2012, MNRAS, 422, L48

Panaitescu, A., & Kumar, P. 2002, ApJ, 571, 779

Pian, E., Vacanti, G., Tagliaferri, G., et al. 1998, ApJ, 492, L17

Pian, E., Mazzali, P. A., Masetti, N., et al. 2006, Nature, 442, 1011

Pian, E., Türler, M., Fiocchi, M., et al. 2014, A&A, 570, A77

Piran, T. 2004, Reviews of Modern Physics, 76, 1143

Rhoads, J. E. 1999, ApJ, 525, 737

Sbarrato, T., Ghisellini, G., Maraschi, L., & Colpi, M. 2012, MNRAS, 421, 1764

Soderberg, A. M., Kulkarni, S. R., Fox, D. B., et al. 2005, ApJ, 627, 877

Soderberg, A. M., Kulkarni, S. R., Price, P. A., et al. 2006, ApJ, 636, 391

Stanek, K. Z., Garnavich, P. M., Kaluzny, J., Pych, W., & Thompson, I. 1999, ApJ, 522, L39

Stratta, G., Gendre, B., Atteia, J. L., et al. 2013, ApJ, 779, 66

Tanvir, N. R., Levan, A. J., Fruchter, A. S., et al. 2013, Nature, 500, 547

Tavecchio, F., Maraschi, L., Pian, E., et al. 2001, ApJ, 554, 725

Urry, C. M., & Padovani, P. 1995, PASP, 107, 803

Usov, V. V. 1992, Nature, 357, 472

van Eerten, H., Zhang, W., & MacFadyen, A. 2010, ApJ, 722, 235

VERITAS Collaboration, Acciari, V. A., Aliu, E., et al. 2009, Nature, 462, 770

Woosley, S. E., & Bloom, J. S. 2006, ARA&A, 44, 507

Woosley, S. E. 2010, ApJ, 719, L204

Highlight contributions

Particle acceleration and magnetic field amplification in hotspots of FR II galaxies: The case study 4C74.26

A.T. Araudo[1], A.R. Bell[2], K.M. Blundell[1]

[1] *University of Oxford, Astrophysics, Keble Road, Oxford OX1 3RH, UK*
[2] *University of Oxford, Clarendon Laboratory, Parks Road, Oxford OX1 3PU, UK*

Abstract. It has been suggested that relativistic shocks in extragalactic sources may accelerate the most energetic cosmic rays. However, recent theoretical advances indicating that relativistic shocks are probably unable to accelerate particles to energies much larger than 1 PeV cast doubt on this. In the present contribution we model the radio to X-ray emission in the southern hotspot of the quasar 4C74.26. The synchrotron radio emission is resolved near the shock with the MERLIN radio-interferometer, and the rapid decay of this emission behind the shock is interpreted as the decay of the downstream magnetic field as expected for small scale turbulence. If our result is confirmed by analyses of other radiogalaxies, it provides firm observational evidence that relativistic shocks at the termination region of powerful jets in FR II radiogalaxies do not accelerate ultra high energy cosmic rays.

1.   Introduction

Radiogalaxies are the subclass of Active Galactic Nuclei (AGN) where jets are clearly detected at radio frequencies, which in turn are classified in type I and II Faranoff-Riley (FR) galaxies. Hotspots are usually detected at the jet termination region of FR II radiogalaxies. These bright radio synchrotron knots have a size $\sim 1 - 10$ kpc and are embedded in larger lobes of shocked plasma. The location of the hotspot is coincident with the downstream region of the jet reverse shock, where particles accelerated by the latter emit non-thermal radiation.

Diffusive shock acceleration (DSA) is a well established mechanism to accelerate particles in astrophysical sources where shock waves are present (Bell 1978a,b). Particles diffuse back and forth across the shock and gain energy in each crossing. Therefore, long times are required to accelerate the most energetic cosmic rays unless the magnetic field around the shock is amplified. The amplified turbulent field scatters particles rapidly so that they cross the shock more frequently achieving a higher energy in the available time. The state-of-the-art of DSA in the hotspots of FR II radiogalaxies is a phenomenological picture where the acceleration process finishes when particles start to radiate their energy or when they can escape from the source, i.e. the energy gained is sufficient for the Larmor radius to exceed the size of the acceleration region (Meisenheimer et al. 1989). Assuming that the magnetic field persists over long distances downstream of the shock, the distribution of non-thermal emitting electrons is a broken power-law where the break frequency is determined by a competition
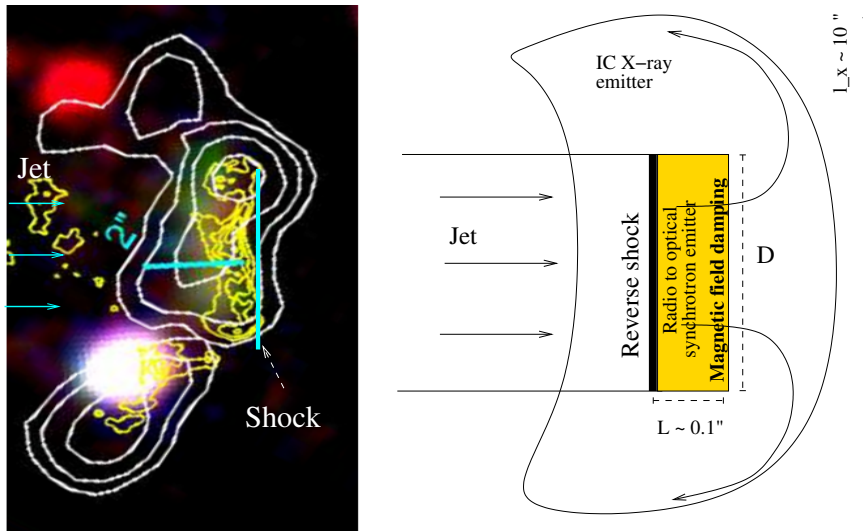
Figure 1.   *Left:* Southern arc adapted from Erlund et al. (2010).
Right: Sketch of the jet termination region (as seen at $\theta_j = 90°$). Particles are accelerated at the reverse shock and radiate in the shock downstream region.

between synchrotron losses and adiabatic expansion (e.g. Brunetti et al. 2003). We will see however that the magnetic field must be highly discrete to explain the very thin radio emission in the southern hotspot of the quasar 4C74.26 (Araudo et al. 2015).

2.   The case study 4C74.26: the southern hotspot

The FR II radiogalaxy 4C74.26 is located at redshift $z = 0.104$ ($\sim$0.5 Gpc from Earth)[1]. This source is the largest known radio quasar, with a projected linear size of 1.1 Mpc and it has a one-sided jet. Two X-ray sources have been detected with the *Chandra* satellite in the termination region of the South jet (Erlund et al. 2007). The brightest X-ray source is called the "X-ray peak" and has no counterpart at other frequencies. On the other hand, the southern X-ray source is coincident with a radio, IR and optical source (Erlund et al. 2010). In the present contribution we focus on this multiwavelength hotspot and assume that this is the jet termination region.

The hotspot X-ray specific luminosity is $L_x \sim 7.9 \times 10^{40}$ erg s^{-1} at frequency $\nu_x = 2.4 \times 10^{17}$ Hz (2 keV). The shape of this emission is arc-like with a characteristic size $l_x \sim 10''$, and encloses a compact radio source, also arc-like and called the "southern arc", as we show in Figure 1 (left). Compact radio emission from the southern arc was detected with the MERLIN high resolution interferometer

---

[1]Throughout the paper we use cgs units and the cosmology $H_0 = 71$ km s^{-1} Mpc^{-1}, $\Omega_0 = 1$ and $\Lambda_0 = 0.73$. One arcsecond represents 1.887 kpc on the plane of the sky at $z = 0.104$.

at a frequency $\nu_{\rm r} = 1.66$ GHz with specific luminosity $L_{\rm r} \sim 1.9 \times 10^{40}$ erg s^{-1}. This emission is located in a region of width $l_{\rm r} < 1''$ on the plane of the sky. In addition, faint and diffuse radiation was detected at IR ($\nu_{\rm ir} = 1.36 \times 10^{14}$ Hz) and optical ($\nu_{\rm opt} = 6.3 \times 10^{14}$ Hz) bands, and located in a region of width $\gtrsim l_{\rm r}$. However, there is a linear structure in both bands that traces the brightest edge of the MERLIN radio emission, and seems to be cupped within it.

The measured radio-to-IR spectral index is $\alpha = 0.75$, typical of synchrotron radiation, and the steep spectrum between IR and optical indicates that the cut-off of the emission is at $\nu_{\rm ir} \leq \nu_{\rm c} \leq \nu_{\rm opt}$ (see Fig. 13 in Erlund et al. 2010). Therefore, the southern arc X-ray emission is not synchrotron[2].

2.1. Inverse Compton X-ray emission

The X-ray emission from hotspots is usually explained as synchrotron self Compton (SSC) or up-scattering of Cosmic Microwave Background (CMB) photons (e.g. Hardcastle et al. 2004, Werner et al. 2012). In the case of the southern arc in 4C74.26, SSC is disfavoured because 1) there is an off-set between the peak of the X-ray and radio emission, and 2) the energy density of synchrotron photons is 8×10^{-15} erg cm^{-3}, much smaller than the energy density of CMB photons $U_{\rm cmb} = 6 \times 10^{-13}$ erg cm^{-3} (Erlund et al. 2010). Therefore, we consider that the X-ray emission from the southern arc is produced by inverse Compton (IC) scattering of CMB radiation.

CMB photons with energy $E_{\rm cmb} \sim 7 \times 10^{-4}$ eV are scattered up to 2 keV X-rays by electrons with Lorentz factor $\gamma_{\rm x} \sim \sqrt{h\nu_{\rm x}/E_{\rm cmb}} \sim 10^3$, where h is the Planck constant. Unless the macroscopic Lorentz factor of the jet is $\gtrsim 10$, $\gamma_{\rm x}$-electrons are non-thermal and follow a power-law energy distribution $N_e = K_e \gamma^{-p}$, with $p = 2\alpha + 1 = 2.5$. The X-ray specific luminosity can be written as $L_{\rm x} \sim N_e(\gamma_{\rm x}) \gamma_{\rm x}^3 / t_{\rm ic}(\gamma_{\rm x}) V_{\rm x}$, where $t_{\rm ic}$ is the IC cooling timescale and $V_{\rm x}$ is the volume of the X-ray emitter. From the previous equation we estimate K_e and therefore, the electron energy density required to explain $L_{\rm x}$ is

$$U_e \sim K_e \left(\frac{\gamma_{\rm min}^{2-p}}{p-2} \right) V_{\rm x} \sim 10^{-9} \left(\frac{\gamma_{\rm min}}{50} \right)^{-0.5} \left(\frac{V_{\rm x}}{300 \, \mathrm{arcsec}^3} \right)^{-1} \mathrm{erg\,cm}^{-3}, \quad (1)$$

where N_e terminates at $\gamma_{\rm min}$. The magnetic field in equipartition with non-thermal particles, i.e. $B_{\rm eq}^2/(8\pi) = (1+a)U_e$, where a takes into account the contribution of non-thermal protons, is

$$B_{\rm eq} \sim 160(1+a)^{0.5} \left(\frac{\gamma_{\rm min}}{50} \right)^{-0.25} \left(\frac{V_{\rm x}}{300 \, \mathrm{arcsec}^3} \right)^{-0.5} \mu\mathrm{G}. \quad (2)$$

Note that $B_{\rm eq} \sim 1.6$ mG if $a = 100$. However, the equipartition field is an upper limit, and the magnetic field in $V_{\rm x}$ is not necessarily the same as that in the MERLIN emitter, as we will see in the next section.

---

[2]Given that the southern hotspot is located at ~ 0.5 Mpc from the nucleus, absorption of the emission by photoionization is ruled-out (see e.g. Ryter et al. 1996).
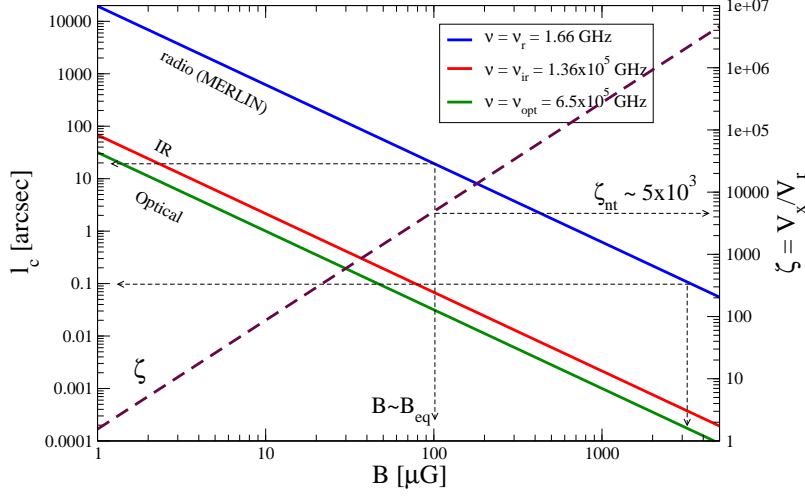
Figure 2. *Left axis* (solid lines): Synchrotron cooling length at radio (1.66 GHz), IR and optical frequencies. *Right axis* (dashed line): X-rays to MERLIN emission volume.

2.2. Synchrotron radio emission

The synchrotron emission at ν_r is produced by electrons with $\gamma_r \equiv \gamma(\nu_r) \sim 1.8 \times 10^3 (B/100\,\mu\text{G})^{-0.5}$, where $\gamma(\nu) \sim 4.5 \times 10^{-4} (\nu/B)^{0.5}$ is the Lorentz factor of electrons emitting synchrotron radiation at frequency ν in a magnetic field B. In a similar way to L_x, we write $L_r \sim N_e(\gamma_r)\gamma_r^3/t_s(\gamma_r)V_r$, where $t_s = 7.5 \times 10^8/(B^2\gamma)$ is the synchrotron cooling timescale and V_r is the volume of the MERLIN emitter. Therefore, $L_x/L_r \sim (\gamma_x/\gamma_r)^{3-p}(U_{\text{cmb}}/U_{\text{mag}})\zeta$, where $U_{\text{mag}} = B^2/(8\pi)$ and $\zeta \equiv V_x/V_r$, and we find that

$$\zeta \sim 4.9 \times 10^3 \left(\frac{B}{100\,\mu\text{G}} \right)^{1.75}. \qquad (3)$$

In Fig. 2 (right axis, dashed line) we can see that $B \sim B_{\text{eq}}$ corresponds to $\zeta_{\text{eq}} = 5 \times 10^3$. Such a large ratio between emitting volumes is not implausible provided the magnetic field is inhomogeneous in the shock downstream region and the synchrotron emitter consists of features smaller than the MERLIN point spread function (FWHM 0.15″) as seen in parts of the MERLIN data. (Note that if $V_x = V_r$, a very small magnetic field ($< \mu$G) would be needed to explain the observed fluxes.) Therefore, X-ray emission is produced in volume $V_x \gg V_r$, as we can see in Fig. 1, and the magnetic field in V_r is much larger than the jet magnetic field of the order of μG (Hardcastle & Krause 2014). As we will discuss in the following, this may be the result of magnetic field amplification.

3.   The (synchrotron) hotspot as a magnetic field damping region

The synchrotron ($l_{\rm s}$) and IC ($l_{\rm ic}$) cooling length of electrons with Lorentz factor γ is $l_{\rm s,ic}(\gamma) = t_{\rm s,ic}(\gamma)v_{\rm sh}/7$, where $v_{\rm sh}/7$ is the velocity of the plasma downstream of the shock. The shock velocity is approximately the same as the jet velocity which we take to be $v_{\rm sh} = c/3$ (Steenbrugge & Blundell, 2008). We use 7 as the shock compression ratio for a non-relativistic shock whose downstream thermal pressure is dominated by relativistic electrons, although 4 may still apply if non-relativistic ions dominate the pressure downstream of the shock. Our conclusions are not sensitive to the exact value of the shock compression ratio.

3.1.   X-ray emitter determined by adiabatic expansion

The IC cooling lenght of X-ray emitting electrons is $l_{\rm ic}(\gamma_{\rm x}) \sim 10^4(3v_{\rm sh}/c)$ arcsec, much larger than $l_{\rm x}$, and therefore IC emission is not the mechanism that determines the size of the X-ray emitter. The synchrotron cooling length $l_{\rm s}$ of $\gamma_{\rm x}$-electrons is also greater than $l_{\rm x}$, unless the magnetic field in the X-ray emitting region is $\sim 360~\mu$G, greater than $B_{\rm eq}$ (unless $V_{\rm x} \sim 60$ arcsec^3). However, such a large value of B in $V_{\rm x}$ would produce a synchrotron flux much greater than that detected by the Very Large Array in the A-configuration (Erlund et al. 2007). Therefore, adiabatic expansion is probably the dominant cooling mechanism as the particles flow out of the hotspot.

3.2.   MERLIN emitter determined by magnetic field damping

The cooling length of electrons emitting synchrotron radiation at frequency ν in a magnetic field B is

$$\frac{l_{\rm s}(\nu)}{[\prime\prime]} \sim 12 \left(\frac{\nu}{\rm GHz}\right)^{-0.5} \left(\frac{B}{100~\mu\rm G}\right)^{-1.5} \left(\frac{v_{\rm sh}}{c/3}\right). \tag{4}$$

In Fig. 2 (left axis, solid lines) we plot $l_{\rm s}(\nu_{\rm r})$, $l_{\rm s}(\nu_{\rm ir})$ and $l_{\rm s}(\nu_{\rm opt})$. Optical and IR emission are almost cospatial, with $l_{\rm s}(\nu_{\rm ir}){\sim}l_{\rm s}(\nu_{\rm opt}){\sim}0.03''(B/100~\mu\rm G)^{-1.5}(3v_{\rm sh}/c)$ and indicating that these particles radiate most of their energy within $l_{\rm r}{}^3$. On the other hand, the synchrotron cooling length of MERLIN emitting electrons is $l_{\rm s}(\nu_{\rm r}) \sim 9.3''(B/100~\mu\rm G)^{-1.5}(3v_{\rm sh}/c) \gg l_{\rm r}$. Even worse, the real hotspot extent downstream of the shock is $L < l_{\rm r}$ if the jet is lying at an angle $\theta_{\rm j} < 90°$ with the line of sight. In particular, $L = (l_{\rm r} - D\cos\theta_{\rm j})/\sin\theta_{\rm j} \sim 0.1''$ when the hotspot is modelled as a cylinder of width L and diameter $D = 3''$, and $\theta_{\rm j} = 73°$ and $l_{\rm r} \sim 1''$ (see the right panel of Fig. 1). In such a case, a very large magnetic field $B_{\rm cool} \sim 2.4\,(3v_{\rm sh}/c)^{2/3}$ mG would be required to match $l_{\rm s}(\nu_{\rm r}) = 0.1''$. This value is greater than $B_{\rm eq}$ for a wide range of $\gamma_{\rm min}$- and $V_{\rm x}$-values, suggesting that the downstream extent of the compact emission detected at $\nu_{\rm r}$ is not the result of fast synchrotron cooling. We suggest that the MERLIN emission region is determined by magnetic field amplification, as we explain below.

---

[3]The diffuse IR and optical emission detected also in hotspots in other sources has been suggested to be the result of reaceleration of non-thermal electrons by second order Fermi acceleration (Brunetti et al. 2003). However, this diffuse emission can be also the result of CMB photons up-scattered by electrons with $\gamma \sim 50$, or synchrotron emission of electrons with $\gamma \sim \gamma_{\rm ir} \sim \gamma_{\rm opt}$ in a region with a smaller magnetic field, outside the MERLIN emitter.

4.   Magnetic field amplification in mildly relativistic shocks

Remarkable advances have been made in the last decade concerning DSA in the non- and ultra-relativistic regimes. In the former case, the realisation that Non Resonant Hybrid instabilities (Bell 2004) in supernova remnants are fast enough to amplify (and maintain) the magnetic field by orders of magnitude (Vink & Laming 2003) and accelerate particles up to the knee ($10^{15.5}$ eV) of the cosmic ray spectrum, has shed light on the origin of Galactic cosmic rays. In the ultra-relativistic case, however, theoretical studies show that Weibel instabilities amplify the magnetic field on a short scale length, producing a rapid decay of the fluctuations and thereby inhibiting particle acceleration to ultra high energies (Sironi et al. 2013, Reville & Bell 2014). The mildly relativistic regime has not been well studied (see however Brett et al. 2013).

In the present contribution we show a mildly relativistic ($v_{\rm sh} \sim c/3$) case study where the synchrotron cooling cannot determine the thickness of the radio emission detected with the high resolution intereferometer MERLIN. Therefore, we suggest that the magnetic field in the southern arc in 4C 74.26 is amplified since $B \sim 100\,\mu$G (required to explain the observations) is much larger than the expected value in the jet upstream of the termination shock (e.g. Hardcastle & Krause 2014). In addition to the thickness of the synchrotron emitter, the cut-off of the synchrotron spectrum can give us an extra piece of information about the magnetic field.

4.1.   Synchrotron cut-off and magnetic field damping

The synchrotron turnover $\nu_{\rm c}$ between $\nu_{\rm ir}$ and $\nu_{\rm opt}$ indicates that the maximum energy of non-thermal electrons is

$$E_{\rm c} = \gamma_{\rm c}\, m_e c^2 \sim 0.9 \left(\frac{\nu_{\rm c}}{\nu_{\rm opt}}\right)^{0.5} \left(\frac{B}{100\,\mu{\rm G}}\right)^{-0.5} \; {\rm TeV}, \qquad (5)$$

where $\gamma_{\rm c} \equiv \gamma_{\rm s}(\nu_{\rm c})$. The standard assumption is that $\gamma_{\rm c}$ is determined by a competition between shock acceleration and synchrotron cooling. By equating $t_{\rm acc}(\gamma_{\rm c}) = t_{\rm s}(\gamma_{\rm c})$, where $t_{\rm acc} \sim 20 D/v_{\rm sh}^2$ is the acceleration timescale for the case of a parallel shock, we find that the electron diffusion coefficient D is much larger than the Bohm value $D_{\rm Bohm}$:

$$\frac{D}{D_{\rm Bohm}} \sim 10^6 \left(\frac{v_{\rm sh}}{c/3}\right)^2 \left(\frac{\nu_{\rm c}}{\nu_{\rm opt}}\right)^{-1}, \qquad (6)$$

and independent of B. Such a large diffusion coefficient is allowed if B is structured on a scale s much smaller than the Larmor radius of the electrons being accelerated, producing $D \sim (r_{\rm g}/s) D_{\rm Bohm}$ and

$$s \sim 2 \times 10^7 \left(\frac{\nu_{\rm c}}{\nu_{\rm opt}}\right)^{1.5} \left(\frac{B}{100\,\mu{\rm G}}\right)^{-1.5} \left(\frac{v_{\rm sh}}{c/3}\right)^{-2} \; {\rm cm}. \qquad (7)$$

In comparison the ion skin-depth is $c/\omega_{\rm pi} \sim 2.3 \times 10^9\,(n/10^{-4}\,{\rm cm}^{-3})^{-0.5}$ cm, where n is the particle density downstream of the shock ($n = 7 n_{\rm j}$, where the $n_{\rm j}$

is the jet density), and

$$\frac{s}{c/\omega_{\text{pi}}} \sim 0.01 \left(\frac{\nu_{\text{c}}}{\nu_{\text{opt}}}\right)^{1.5} \left(\frac{v_{\text{sh}}}{c/3}\right)^{-2} \left(\frac{B}{100\,\mu\text{G}}\right)^{-1.5} \left(\frac{n}{10^{-4}\,\text{cm}^{-3}}\right)^{0.5}. \tag{8}$$

Therefore,

$$B \leq 4.6 \left(\frac{\nu_{\text{c}}}{\nu_{\text{opt}}}\right) \left(\frac{v_{\text{sh}}}{c/3}\right)^{-4/3} \left(\frac{n}{10^{-4}\,\text{cm}^{-3}}\right)^{3} \mu\text{G} \tag{9}$$

is required to satisfy the condition $s \geq c/\omega_{\text{pi}}$ in the case that E_{c} is constrained by synchrotron cooling. Note however that $B \propto n^3 \propto n_{\text{j}}^3$. In Araudo et al. (2016, submitted) we explore this condition in depth.

In the case that the magnetic field is amplified by the Weibel instability, small-scale turbulence ($s \sim c/\omega_{\text{pi}}$) scatters non-thermal electrons during DSA (Sironi et al. 2011). However, the hotspot magnetic field has to survive over distances $\sim$0.2 kpc ($\sim$0.1$''$) downstream of the jet reverse shock, which are much larger than those predicted by numerical simulations. The same discrepancy was found in Gamma-Ray Bursts (e.g. Medvedev et al. 2005, Pe'er & Zhang, 2006). Chang et al. (2008) have shown that the magnetic field generated by Weibel instabilities in ultra relativistic plasmas is maintained constant over a distance $\sim 100\,c/\omega_{\text{p}}$ downstream of the shock, and then decays as $\propto l^{-1}$, where l is the distance downstream of the shock. (See also Lemoine 2015 for a similar study in the non-linear regime.)

5. Conclusions

We model the radio to X-ray emission in the southern hotspot of the FR II radiogalaxy 4C74.26. Our study is based on three key features:

1. The MERLIN emission region is too thin to be the result of fast synchrotron cooling.

2. The radio to IR spectrum ($\alpha = 0.75$) is too flat for the emitting volume to be determined by synchrotron cooling through this wavelength range.

3. The turnover of the synchrotron spectrum at IR/optical frequencies requires $D \gg D_{\text{Bohm}}$ for any reasonable shock velocity.

These three features fit well in a scenario in which the MERLIN radio emission traces out the region where the magnetic field is amplified by plasma instabilities with small length scale. The magnetic field decays quickly behind the shock accounting for the maximum energy of accelerated electrons at $E_{\text{c}} \sim$ TeV. These electrons continue up-scattering CMB photons, thus producing IC X-ray emission downstream of the shock after the MERLIN radio emission has ceased.

The magnetic field in equipartition with non-thermal electrons in the MERLIN emission region is $\sim$100 μG and similar to the values obtained by other authors. An unrealistically large magnetic field $B_{\text{cool}} \sim 2.4\,(3v_{\text{sh}}/c)^{2/3}$ mG would be needed to explain the compact radio emission in terms of synchrotron cooling. If $B \sim 100\,\mu$G in the synchrotron emission region, the maximum energy of non-thermal electrons is $\sim$ TeV, (Eq. 5). If ions are accelerated as well, protons with

energy $\sim$ TeV diffuse also with $D \gg D_{\mathrm{Bohm}}$ and then the maximum proton energy at the termination shock of 4C74.26 is only 100 TeV instead of the 100 EeV indicated by the Hillas parameter. This may have important implications for the understanding of the origins of ultra high energy cosmic rays.

References

Araudo, A. T., Bell, A. R., Blundell, K. M. 2015, ApJ, 806, 243

Araudo, A. T., Bell, A. R., Crilly, A., Blundell, K. M. 2016, MNRAS, 460, 3554

Bell, A. R. 1978, MNRAS, 182, 147

Bell, A. R. 1978, MNRAS, 182, 444

Bell, A. R. 2004, MNRAS, 353, 550

Bret, A., Stockem, A., Fiuza, F., Ruyer, C., Gremillet, L., Narayan, R., Silva, L.O. 2013, Physics of Plasmas, 20, 042102

Brunetti, G.; Mack, K.-H.; Prieto, M. A.; Varano, S. 2003, MNRAS, 345, 40L

Chang, P., Spitkovsky, A., Arons, J. 2008, ApJ, 374, 378

Erlund, M. C., Fabian, A. C., Blundell, K. M., Moss, C., Ballantyne, D. R. 2007, MNRAS, 379, 498

Erlund, M. C., Fabian, A. C., Blundell, K. M., Crawford, C. S., Hirst, P. 2010, MNRAS, 404, 629

Hardcastle, M. J.; Harris, D. E.; Worrall, D. M.; Birkinshaw, M. 2004, MNRAS, 612, 729

Hardcastle, M. J., Krause, M.G.H. 2014, MNRAS, 443, 1482

Lemoine, M. 2015, Journal of Plasma Physics, 81, 455810101

Meisenheimer, K., Roser, H.-J., Hiltner, P. R., Yates, M. G., Longair, M. S., Chini, R., Perley, R. A. 1989, A&A, 219, 63

Pe'er, A., Zhang, B. 2006, ApJ, 653, 454

Reville, B., Bell, A. R. 2014, MNRAS, 439, 2050

Ryter, Ch. E. 1996, Ap&SS, 236, 285

Sironi, L., Spitkovsky, A. 2011, ApJ, 726, 75

Sironi, L., Spitkovsky, A., Arons J. 2013, ApJ, 771, 54

Steenbrugge, K. C., Blundell, K. M. 2008, MNRAS, 388, 1457

Vink, J., Laming, J.M. 2003, ApJ, 554, 758

Werner, M. W., Murphy, D. W., Livingston, J. H., Gorjian, V., Jones, D. L.; Meier, D. L.; Lawrence, C. R. 2012, ApJ, 759, 86

Oral contributions

Exploring the parent population of beamed NLS1s: from the black hole to the jet

M. Berton[1], L. Foschini[2], S. Ciroi[1], A. Caccianiga[2], V. Cracco[1], G. La Mura[1], F. Di Mille[3], M. L. Lister[4], S. Mathur[5], B. M. Peterson[5], J. L. Richards[4], E. Congiu[1], M. Frezzato[1], P. Rafanelli[1]

[1] *University of Padova, vicolo dell'osservatorio 3, 35122, Padova (Italy)*
[2] *INAF - Osservatorio astronomico di Brera, via E. Bianchi 46, 23807, Merate (Italy)*
[3] *Las Campanas Observatory - Carnegie Institution of Washington, Colina el Pino Casilla 601, La Serena (Chile)*
[4] *Purdue University, 525 Northwestern Avenue, West Lafayette, IN 47907, USA*
[5] *Ohio State University, 140 West 18th Avenue, Columbus, OH 43210, USA*

Abstract. The aim of this work is to understand the nature of the parent population of beamed narrow-line Seyfert 1 galaxies (NLS1s), by studying the physical properties of three parent candidates samples: steep-spectrum radio-loud NLS1s, radio-quiet NLS1s and disk-hosted radio-galaxies. In particular, we focused on the black hole mass and Eddington ratio distribution and on the interactions between the jet and the narrow-line region.

1. Introduction

Narrow-line Seyfert 1 galaxies (NLS1s) are a class of active galactic nuclei (AGN) that exhibits some peculiar characteristics. They are tipically classified according to their low full width at half maximum (FWHM) of Hβ, below 2000 km s^{-1}, and their ratio [O III]/H$\beta < 3$ (Osterbrock & Pogge 1985). Along with the presence of strong Fe II multiplets in the optical spectra, such characteristics reveal that these AGN are type 1 sources, where the broad line region (BLR) is directly visible, and with a relatively low black hole mass (10^6-10^8 M$_\odot$), which explains the narrowness of the permitted lines. This "small" black hole, along with the high Eddington ratio characterising these sources (Boroson & Green 1992), led many to think that NLS1s might be young objects still growing (Mathur 2000).

7% of NLS1s are radio-loud (RLNLS1s, Komossa et al. 2006), and some of them exhibit some interesting blazar-like properties, such as high brightness temperature and a flat or even inverted radio spectrum (Yuan et al. 2008). In 2009 the Fermi satellite detected γ-ray emission coming from one of these sources, revealing the presence of a relativistic beamed jet (Abdo et al. 2009a). To date, the known γ-ray emitting NLS1s are 10, and their number is still increasing (e.g. see Yao et al. 2015). This population of flat-spectrum radio-loud NLS1s (F-NLS1s) was extensively studied in Foschini et al. (2015). An important result of their work is that F-NLS1s are likely the low mass tail of γ-ray AGN, as

shown in their Fig. 4. Both of the two blazar classes, BL Lacertae objects and flat-spectrum radio quasars (FSRQs), have indeed a much larger mass, and only FSRQs have an Eddington ratio comparable to that of RLNLS1s.

Once the existence of a beamed population is confirmed, the most obvious following step is to understand the nature of its parent population, hence how do these beamed sources look like when randomly oriented. Assuming a typical bulk Lorentz factor $\sim$10 (Abdo et al. 2009b), 10 γ-ray emitting sources should correspond to more than 2000 misaligned sources (Urry & Padovani 1995).

The first candidates as parent sources are NLS1s with jets viewed at large angles, with a steep radio-spectrum (S-NLS1s) and possibly with an extended radio emission. A few examples can be found in the literature (Gliozzi et al. 2010, Doi et al. 2012, Richards & Lister 2015), but the currently known sources of this kind are anyway quite rare and definitely less than 2000. A fraction of the parent population is therefore missing. An explanation for this is that the high number of flat-spectrum sources with respect to steep-spectrum sources is due to the high brightness induced by the relativistic beaming: F-NLS1s are more common because we can observe them at larger distances. But this is not the only viable option, because there might be more parent sources that appear as completely different objects (Foschini 2011).

In particular, F-NLS1s have a really compact jet and a lack of extended structures at radio frequencies (Foschini et al. 2010) and, when the inclination increases, this jet might become almost invisible. The source would then appear as a radio-quiet NLS1 (RQNLS1). In fact RQNLS1s show a non-thermal radio emission (Giroletti & Panessa 2009), and a bunch of them even harbor a jet (Doi et al. 2013, 2015). Another possibility is based on a different assumption regarding the BLR geometry. If the BLR is disk-like shaped (Decarli et al. 2008, Shen & Ho 2014), when observed pole-on the lines are not broadened by the rotation and appear as narrow. When the inclination increases, the Doppler effect broadens the lines, and the galaxy appears as a broad-line radio-galaxy (BLRG). Increasing again the inclination, the line of sight intercepts the molecular torus, and the galaxy is a narrow-line radio-galaxy (NLRG). Moreover, since many studies revealed that NLS1s are always hosted by disk galaxies (Crenshaw et al. 2003), also radio-galaxies must be disk-hosted (disk RGs). This work summarizes our research in the field. A full discussion can be found in Berton et al. (2015, 2016).

2. Black hole mass

To understand which one of the previous candidates are actually part of the parent population, we built three samples of candidates, to compare their black hole masses and their accretion luminosities with the sample of F-NLS1s of Foschini et al. (2015), and with a control sample of elliptical radio-galaxies derived from the 2 Jy sample of Inskip et al. (2010). We analysed only sources whose optical spectrum could be obtained from the literature or with the Asiago 1.22m telescope.

To calculate the black hole mass we derived the second order momentum σ of Hβ and the stellar velocity dispersion from the core component of the [O III] λ 5007 line (Nelson & Whittle 1996, Greene & Ho 2005). We decided to use line
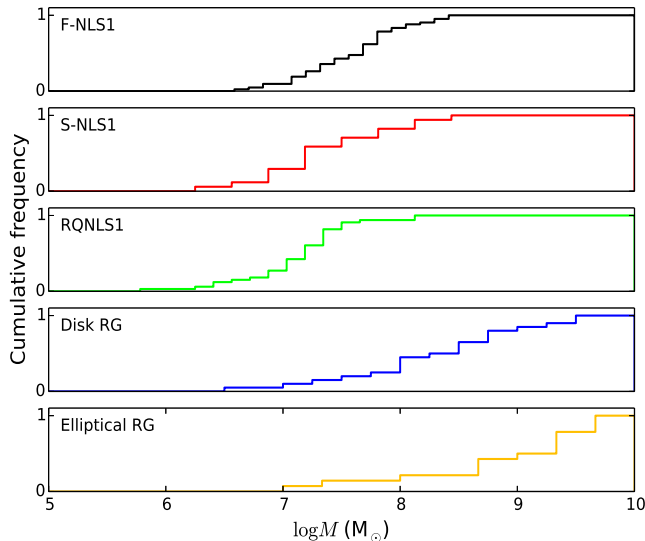
Figure 1. Cumulative distributions of black hole masses. From top to bottom, F-NLS1s, S-NLS1s, RQNLS1s, disk RGs and elliptical RGs.

luminosities instead of continuum luminosity, which is often used to calculate the black hole mass, because lines are less affected by the jet contribution. Moreover, we used σ instead of FWHM, because the former is less affected by inclination and BLR geometry (Collin et al. 2006). In this way we obtained the mass distributions shown in Fig. 1. NLS1s are all located between 10^6 and 10^8 M$_\odot$. F-NLS1s have on average a slightly larger mass than the other two NLS1s samples. Disk RGs span instead over a large interval of masses, while elliptical radio-galaxies are located in the high mass region, above 10^9 M$_\odot$, as expected.

To compare these distributions, we used the Kolmogorov-Smirnov test (K-S), which tests whether two cumulative distributions can be drawn from the same population. An important − and expected − result is that the distributions of steep- and flat-spectrum NLS1s are quite close to each other. This can be interpreted as a sign that these are the same kind of source observed under different angles. The K-S instead cannot provide a conclusive outcome for disk RGs and RQNLS1s. Disk RGs are in the middle between F-NLS1s and elliptical RGs, connecting them with a sort of "bridge". In particular, disk RGs with low black hole mass and high Eddington ratio are well overlapped with the F-NLS1s distribution, suggesting a possible connection between them. We also found that, in presence of a pseudobulge, this connection gets even stronger. Finally, to better understand the role of RQNLS1s, we decided to approach them from a different perspective.
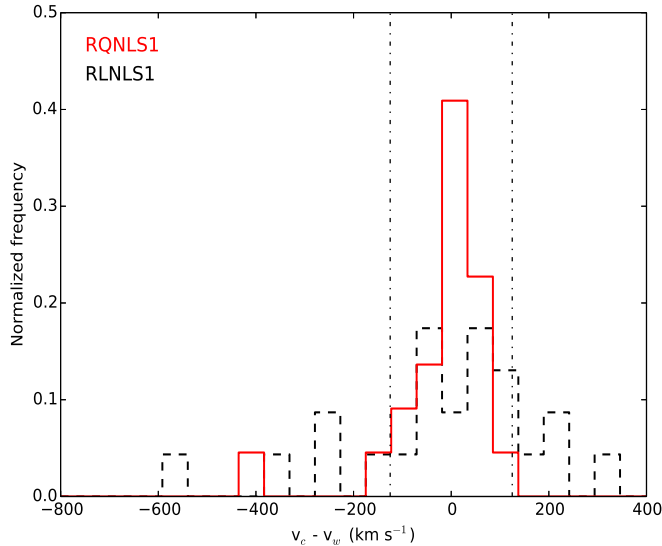
Figure 2.   Normalized histogram of the [O III] lines shift with respect to their restframe wavelength. The reference used is narrow Hβ. Dashed black line is RLNLS1s, solid red line is RQNLS1s. Vertical dash-dotted lines are the limits for blue and red outliers, as in Komossa et al. (2008).

3.   [O III] lines and narrow-line region

[O III] $\lambda\lambda$ 4959,5007 are forbidden lines originated in the narrow-line region (NLR). These lines are typically the brightest high-ionization lines in the optical spectrum. For this reason, they are particularly suitable for studying their kinematic components. [O III] lines often show an outflowing component within the NLR, called the blue wing. In some peculiar sources they also show a blue-shift of both lines. When this velocity shift is larger than 150 km s^{-1}, such sources are known as blue outliers. They are associated with a bulk motion of the NLR toward the observer, possibly induced by an intense radiation pressure coming from the accretion disk or by interaction with a relativistic jet (Zamanov et al. 2002, Komossa et al. 2008).

In our work we analysed the [O III] lines of two samples of NLS1s, one radio-loud including both flat- and steep-spectrum, drawn from a sample of very radio-loud sources selected in Yuan et al. (2008), and one radio-quiet, the same used in Berton et al. (2015) for black hole mass calculation. We used two Gaussians for each line, and measured the velocities of core and blue wings components with respect to the narrow component of Hβ. One of our results is shown in Fig. 2. The histogram represents the velocity shift of the [O III] lines with respect to their restframe wavelength. The distribution of RLNLS1s is wider than that of RQNLS1s ($\sigma_{RL} = 193$ km s^{-1}, $\sigma_{RQ} = 103$ km s^{-1}). This indicates that the [O III] velocities in RLNLS1s can reach higher values than in RQNLS1s.

The number of blue outliers is also higher in radio-loud sources (9 against 2), and the K-S test reveals that the two distribution in Fig. 2 do not arise from the same population (p-value 0.04). We suggest that this might be a sign of an ongoing interaction between the relativistic jet and the NLR clouds in RLNLS1s. In RQNLS1s the NLR is also perturbed, but in a less evident way. This might reveal that, even if some kind of perturbative mechanism is in action, it is something different from, and less effective than, a relativistic jet, and hence that jets may not be tipically harbored in RQNLS1s.

Nevertheless, in spite of their classification as radio-quiet sources, non-thermal emission and jets can be observed in a small fraction of RQNLS1s. There are, however, two possible explanations for this apparent contraddiction. The first one is that radio-loudness is not an absolute parameter, because it strongly depends on the way optical and radio fluxes are measured (Ho & Peng 2001). A radio-quiet classification then does not automatically exclude the presence of a jet. A second possibility is that the jet activity in some NLS1s is intermittent, as suggested in Foschini et al. (2015), and the radio-quiet condition is then only temporary.

4. Future work

Our previous studies revealed that only steep-spectrum RLNS1s and some low mass disk RGs are likely to be included in the parent population. The numerical problem we presented in the introduction is though still open. Is the number of parent sources high enough to constitute the entire parent population?

A very important part of this question can be answered by means of radio luminosity function. The latter is the volumetric density of sources as a function of their radio luminosity. As shown in several works, the great advantage of luminosity functions is that the relativistic beaming can be analytically added to a misaligned function to obtain the observed function of the beamed population (Urry & Shafer, 1984, Urry & Padovani, 1991). This allows to directly compare the two populations, and find a solution for the numerical problem (Urry & Padovani 1995).

We therefore created four complete samples of sources, one for F-NLS1s, and three for parent candidates, calculating their luminosity and evaluating the LFs. We also compared our beamed population with a sample of compact steep-spectrum sources (O'Dea 1998), usually believed to be a class of young radio-galaxies often associated with NLS1s (e.g. Caccianiga et al. 2014). Our results will be presented in the upcoming paper by Berton et al. (in prep.). Finally, to deepen the investigation of the radio-quiet/radio-loud relation in NLS1s, we are carrying out dedicated surveys with VLBA and VLA, that will help us to understand the jet launching mechanism and the origin of this dichotomy.

the University of Arizona, the Brazilian Participation Group, Brookhaven National Laboratory, Carnegie Mellon University, University of Florida, the French Participation Group, the German Participation Group, Harvard University, the Instituto de Astrofisica de Canarias, the Michigan State/Notre Dame/JINA Participation Group, Johns Hopkins University, Lawrence Berkeley National Laboratory, Max Planck Institute for Astrophysics, Max Planck Institute for Extraterrestrial Physics, New Mexico State University, University of Portsmouth, Princeton University, the Spanish Participation Group, University of Tokyo, University of Utah, Vanderbilt University, University of Virginia, University of Washington, and Yale University. This research has made use of the SIMBAD database, operated at CDS, Strasbourg, France.

References

Abdo, A. A., Ackermann, M., Ajello, M., et al., 2009a, ApJ, 699, 976

Abdo, A. A., Ackermann, M., Ajello, M., et al., 2009b, ApJ, 707, L142

Berton, M., Foschini, L., Ciroi, S., et al., 2015, A&A, 578, A28

Berton, M., Foschini, L., Ciroi, S., et al., 2016, A&A, 591, A88

Boroson, T. A. & Green, R. F., 1992, ApJS, 80, 109

Caccianiga, A., Antón, S., Ballo, L., 2014, MNRAS, 441, 172

Collin, S., Kawaguchi, T., Peterson, B. M. & Vestergaard, M., 2006, A&A, 456, 75

Crenshaw, D. M., Kraemer, S. B., & Gabel, J. R., 2003, AJ, 126, 1690

Decarli, R., Dotti, M., Fontana, M., & Haardt, F., 2008, MNRAS, 386, 15

Doi, A., Nagira, H., Kawakatu, N., et al., 2012, ApJ, 760, 41

Doi, A., Asada, K., Fujisawa, K., et al., 2013, ApJ, 765, 69

Doi, A., Wakima, K., Hagiwara, Y., & Inoue, M., 2015, ApJ, 798, L30

Foschini, L., 2011, in Narrow-Line Seyfert 1 Galaxies and their Place in the Universe, Proc. of Science, Vol. NLS1, id.24

Foschini, L., Ghisellini, G., Kovalev, Y. Y., et al., 2011, MNRAS, 413, 1671

Foschini, L., Berton, M., Caccianiga, A., et al., 2015, A&A, 575, A13

Giroletti, M., & Panessa, F., 2009, ApJ, 706, L260

Gliozzi, M., Papadakis, I. E., Grupe, D., et al., 2010, ApJ, 717, 1243

Greene, J. E., & Ho, L. C., 2005, ApJ, 627, 721

Ho, L. C., & Peng, C. Y., 2001, ApJ, 555, 650

Inskip, K. J., Tadhunter, C. N., Morganti, R., et al., 2010, MNRAS, 407, 1739

Komossa, S., Voges, S., Xu, D., et al., 2006, AJ, 132, 531

Komossa, S., Xu, D., Zhou, H., et al., 2008, ApJ, 680, 926

Mathur, S., 2000, MNRAS, 314, 17

Nelson, C. H., & Whittle, M., 1996, ApJ, 465, 96

Osterbrock, D. E., & Pogge, R. W., 1985, ApJ, 297, 166

O'Dea, C. P., 1998, PASP, 100, 493

Richards, J. L., & Lister, M. L., 2015, ApJL, 800, L8

Shen, & Ho, L. C., 2014, Nature, 513, 210

Urry, C. M., & Shafer, 1984, ApJ, 280, 569

Urry, C. M., & Padovani, P., 1995, PASP, 107, 803

Yao, S., Yuan, W., Zhou, H., et al., 2015, MNRAS, 454, 16

Yuan, W., Zhou, H. Y., Komossa, S., et al., 2008, ApJ, 685, 801

Zamanov, R., Marziani, P., Sulentic, J. W., et al., 2002, ApJ, 576, L9

Magnetorotational supernovae and jet formation

G.S. Bisnovatyi-Kogan[1,2], S.G. Moiseenko[1] and N.V. Ardelyan[3]

[1]*Space Research Institute RAS, Profsoyuznaya 84/32, 117997 Moscow, Russia*
[2]*National Nuclear Res. Univ. MEPHI, Kashirskoye Shosse 31, 115409 Moscow, Russia*
[3]*Department of Computational Mathematics and Cybernetics, Moscow State University, Vorobjevy Gory, Moscow B-234, Russia*

Abstract. A magnetorotational mechanism of explosion is at work in core-collapse supernova. The main energy source is the rotational energy of the new born neutron star, and the magnetic field induces the transformation of this energy into the energy of the expanding shock wave. The amount of energy released by this mechanism is enough to explain the observations. The development of the magnetorotational differential instability is studied. A jet is formed at a dipole-like magnetic field configuration.

1. Introduction

Core-collapse SNe explode at the end of evolution of massive stars, with initial mass larger than $\sim 12 M_\odot$. During the core collapse and formation of a neutron star, gravitational energy release $\sim 6 \cdot 10^{53}$ erg, is carried away by neutrinos. The first mechanism (Colgate and White 1966) of the explosion in a core-collapse (CC) SN was based on heating the infalling outer layers by a huge energy flux carried by neutrinos. More accurate calculations revealed that the energy of such explosion is not enough for the explanation of observations, and results of modified neutrino models are still not definite, see e.g. Bisnovatyi-Kogan (2011). Neutrino convection (Epstein, 1979) carries out the inner hot layers, leading to radiation of a more energetic neutrino flux which heats stronger the outer layers, leading to formation of a stronger shock. 2-D calculations do not give a definite answer about the efficiency of neutrino convection, 3-D models give even less powerful explosions. Convective eddies of a larger size are more efficient in heating the envelope by neutrino flux, bringing matter from deeper hotter layers. In 2-dimensional systems the convective energy goes to larger scale eddies, while in a realistic 3-D case the energy goes to smaller eddies. The decrease of the size of convective eddies in realistic 3-D problems makes 3-D models less effective. The magnetorotational mechanism (Bisnovatyi-Kogan, 1970) investigated by many groups shows its efficiency in explanation of CCSN explosions.

2. Magnetorotational mechanism of explosion

In magnetorotational explosion (MRE) the transformation of the rotational energy of the neutron star into explosion energy takes place by means of the mag-
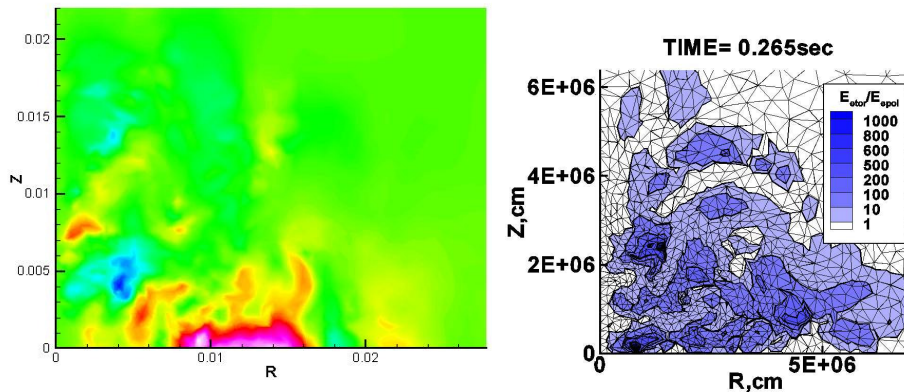
Figure 1.   Toroidal magnetic field distribution at its maximal energy for the quadrupole field (left). The ratio of the toroidal to the poloidal magnetic energy, $E_{\mathrm{tor}}/E_{\mathrm{pol}}$ at $t = 265$ ms for the case $H_0 = 10^9$ Gs, $E_{\mathrm{rot},0}/E_{\mathrm{grav},0} = 1\%$ (right). Reproduced from Bisnovatyi-Kogan et al. (2015).

netic field. In differentially rotating magnetized new born neutron stars the radial component of the magnetic field is twisted, and magnetic pressure becomes very high, producing MHD shock by which the rotational energy is transformed to the explosion energy. Calculations of MRE have been done by Bisnovatyi-Kogan et al. (1976), using one-dimensional MHD equations, for the case of cylindrical symmetry. The calculations show that the outer part of the envelope expands with large velocity, carrying out a considerable part of rotational energy and rotational momentum. MRE has an efficiency about 10% of the rotational energy, the ejected mass is ≈ 0.1 of the star mass, and the explosion energy $\approx 10^{51}$ erg. Ejected mass and explosion energy depend weekly on the initial parameter $\alpha = E_{\mathrm{mag}}/E_{\mathrm{grav}}$. Explosion time is $t_{\mathrm{expl}} \sim \frac{1}{\sqrt{\alpha}}$. Small α values are difficult for calculations with explicit numerical schemes because of the Courant restriction on the time step, The system of equations is "hard", where α determines the "hardness".

3.   2-D calculations

The numerical method used in the simulations is based on the implicit operator-difference, completely conservative scheme on a Lagrangian triangular grid of variable structure, with grid reconstruction. The implicitness of the applied numerical scheme allows for large time-steps (see Ardelyan and Chernigovskii 1984, Ardelyan et al. 1996). The scheme is fully conservative, which includes conservation of mass, momentum and total energy, and correct transitions between different types of energies. MHD equations with self-gravitation, and infinite conductivity have been solved. The problem has an axial symmetry ($\frac{\partial}{\partial \phi} = 0$), and the symmetry with respect to the equatorial plane ($z = 0$). An initial toroidal current J_ϕ was taken at the initial moment producing H_r, H_z. The initial magnetic field of dipole-like symmetry is obtained at opposite directions of

the current in both hemispheres. Neutrino cooling was calculated using a variant of a flux-limited method (Ardelyan et al., 2005).
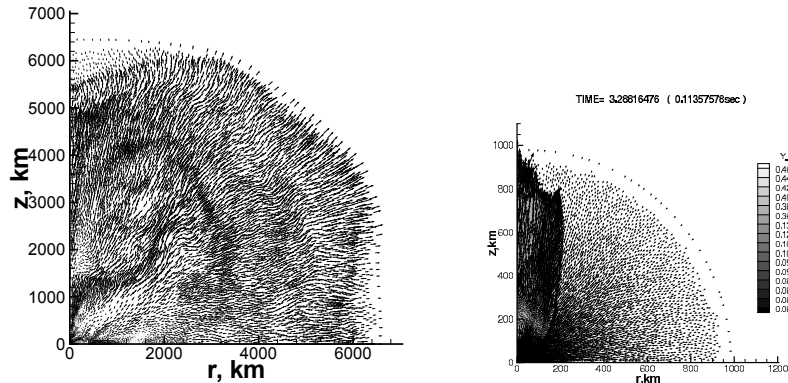
Figure 2.   The velocity field (outflow) for the time moment, $t = 0.25\,s$, from Moiseenko et al. (2006, left). Jet formed for the initial uniform field with $H_{0z} = 10^9$ Gs, $E_{\text{rot},0}/E_{\text{grav},0} = 0.8\%$. The hatched zone corresponds to the outflowing jet, ejected from deep layers of the star with high neutronization, low $Y_e = n_e/n_b$, where n_e is the electron concentration, n_b is a total baryon concentration (free and in nuclei, right) . Left panel reproduced from Bisnovatyi-Kogan et al. (2015).

Magnetic field is amplified due to twisting by the differential rotation, and subsequent development of the magnetorotational instability. The field distribution for initial quadrupole-like magnetic field with $\alpha = 10^{-6}$, at the moment of the maximal energy of the toroidal magnetic field is represented in Fig.1. A maximal value of $B_\phi = 2.5 \cdot 10^{16}$ Gs was obtained. The magnetic field at the surface of the neutron star after the explosion is $B = 4 \cdot 10^{12}$ Gs. The larger part of the gravitational energy, released during the collapse, is carried away by neutrinos. The total energy ejected in the kinetic form is $\sim 0.6 \cdot 10^{51}$ erg, and the total ejected mass is equal to $\sim 0.14 M_\odot$. The simulations were done for the initial poloidal magnetic field of quadrupole (Ardelyan et al. 2005) and of dipole (Moiseenko et al. 2006) symmetry types. The initial ratios between the rotational and gravitational, and also between the internal and gravitational energies of the star had been chosen as: $\frac{E_{\text{rot}}}{E_{\text{grav}}} = 0.0057$, $\frac{E_{\text{int}}}{E_{\text{grav}}} = 0.727$. The ratio between the initial magnetic and gravitational energies was chosen as 10^{-6}. The initial poloidal magnetic field in the center was $\sim 3.2 \times 10^{13}$ Gs. The magnetic field works as a piston for the originated MHD shock. The simulation of the MR supernova explosion for various initial core masses and rotational energies was done by Bisnovatyi-Kogan et al. (2008). The explosive energy increases with the mass of the core, and the initial rotational energy. The energy released in MRE, $(0.5 - 2.6) \times 10^{51}$ erg, is sufficient to explain Types II and Ib supernovae with collapsing cores. Note that magnetorotational explosion (MRE) is supported mainly by the magnetic pressure, which is hardly connected with the scale of eddies, so we may expect the same efficiencies of MRE in 2 and 3-D numerical models.

4.   Magnetorotational differential instability

Magnetorotational differential instability (MRDI) leads to exponential growth of magnetic fields. Different types of MRI have been studied by Velikhov (1959) and Spruit (2002). In our calculations MRDI starts to develop when the ratio of the toroidal to poloidal magnetic energies becomes large, what corresponds to the instability studied by Tayler (1973). In 1-D calculations MRDI is absent because of a restricted degree of freedom, and time of MRE increases with α as $t_{\text{expl}} \sim \frac{1}{\sqrt{\alpha}}$, $\alpha = \frac{E_{\text{mag},0}}{E_{\text{grav},0}}$. Due to development of MRDI the time of MRE depends on α much weaker. The MRE happens when the magnetic energy becomes comparable to the internal energy, at least in some parts of the star. MRDI leads to exponential growth of the magnetic energy. The total time of MRE in 2-D grows **logarithmically** with decreasing of α, $t_{\text{expl}} \sim -\log \alpha$ in 2-D calculations (Ardelyan et al. 2005, Moiseenko et al. 2006), giving the following explosion times t_{expl} (in arbitrary units): $\alpha = 0.01$, $t_{\text{expl}} = 10$, $\alpha = 10^{-12}$, $t_{\text{expl}} = 10^6$ in 1-D, and $\alpha = 10^{-6}$, $t_{\text{expl}} \sim 6$, $\alpha = 10^{-12}$, $t_{\text{expl}} \sim 12$ in 2-D.

5.   Jet formation in MRE

Jet formation in MRE happens at the initial magnetic field of a dipole-like structure, when the ejected mass is collimated along the rotational axis (Moiseenko et al. 2006), see Fig. 2. Simulations of the MR supernova have been made with the equation of state suggested by Shen et al. (1998). A comparison of our results for the initially uniform magnetic field, with the results of Takiwaki et al. (2004) and Takiwaki et al. (2009), for the same initial and boundary conditions, shows good agreement for a strong initial field ($H_0 = 10^{12}$ Gs), while for a weaker field ($H_0 = 10^9$ Gs) we get a mildly collimated jet-like explosion. MRDI is developed in the case of a weaker initial magnetic field, and it is not present in the calculations with stronger field, see Figs. 3,4. In Fig. 2 the ratio of the toroidal magnetic energy to the poloidal one ($E_{\text{tor}}/E_{\text{pol}}$) is represented for the case $H_0 = 10^9$ Gs, and $E_{\text{rot},0}/E_{\text{grav},0} = 1\%$. The toroidal magnetic energy dominates over the poloidal one in the significant part of the region. The MDRI is well-resolved on our triangular grid. At $H_0 = 10^9$ Gs the rotational energy has two maxima. The first contraction is accompanied by the strong growth of the rotational energy and coincides with the first maximum of the density. Development of the magnetorotational instability leads to a rapid growth of the magnetic field, and a large angular momentum flux from the core. It stops the expansion, and leads to the second contraction phase which is not transformed into expansion, because of the rapid decrease of angular momentum in the core.

6.   Asymmetry of the explosion

The symmetry with respect to the equatorial plane. can be violated due to the MRI, the simultaneous presence of the initial dipole and quadrupole -like magnetic fields (Wang et al. 1992), and the initial poloidal and toroidal magnetic fields of opposite symmetries (Bisnovatyi-Kogan and Moiseenko 1992). When rotational and magnetic axes do not coincide the whole picture of the explosion
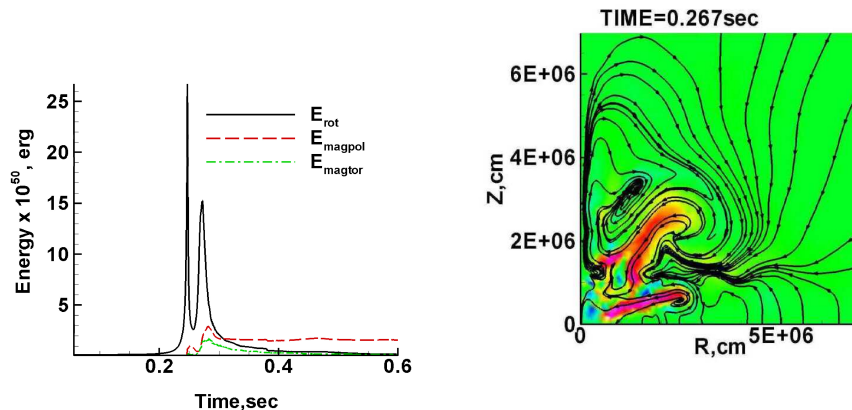
Figure 3. Time evolution of rotational $E_{\rm rot}$ (solid line), magnetic poloidal $E_{\rm mag,pol}$ (dashed line) and magnetic toroidal $E_{\rm mag,tor}$ (dash-dotted line) energies for $H_0 = 10^9$ Gs, $E_{\rm rot,0}/E_{\rm grav,0} = 1\%$ (left). Developed MDRI at $t = 267$ms for the same parameters: contour plot - the toroidal magnetic field, arrow lines - poloidal magnetic field (right). Reproduced from Bisnovatyi-Kogan et al. (2015).

process is three dimensional, but the magnetic field twisting happens around the rotational axis (Mukami et al. 2008). We may expect the kick velocity of the neutron star to be strongly correlated with its spin direction. During the phase of MRE explosion the regular component of magnetic field may exceed temporally 10^{16} Gs (Ardelyan et al. 2005, Moiseenko et al. 2006), when the neutrino cross-section depends on the magnetic field strength, and due to strong anisotropy of the neutrino flux. The kick velocity in this case may reach several thousands km/s (Bisnovatyi-Kogan 1993), as in most rapidly moving radio pulsars (Vlemmings et al. 2005). Analysis of observations of pulsars shows that rotation and velocity vectors of pulsars are aligned, as is predicted by the MR supernova mechanism. This alignment was found by Smirnova et al (1996), and was confirmed by Johnson et al.(2005), Johnson et al.(2007), and Noutsos et al. (2012).

References

Ardeljan, N.V., et al. 1996, A&AS, 115, 573

Ardeljan, N.V., et al. 2005, MNRAS, 359, 333

Ardelyan, N.V. & Chernigovskii, S.V. 1984, Diff. Uravneniya, 20, 1119

Bisnovatyi-Kogan, G.S. 1970, Astron. Zh., 47, 813 [SvA, 1971, 14, 652]

Bisnovatyi-Kogan, G.S. 2011, *Stellar Physics 2: Stellar Evolution and Stability*, Astronomy & Astrophysics Library, Springer-Verlag Berlin Heidelberg

Bisnovatyi-Kogan, G.S. 1993, Astron. Ap. Transactions, 3, 287
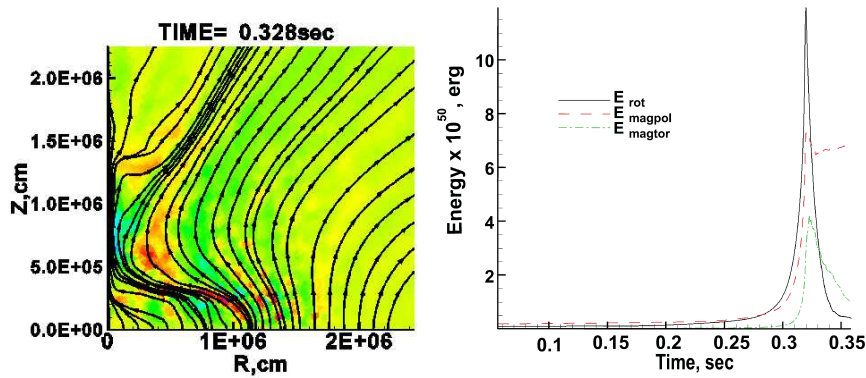
Figure 4. Absence of MDRI for the case $H_0 = 10^{12}$ G, $E_{rot0}/E_{grav0} = 1\%$. Notations are as in Fig.3. Reproduced from Bisnovatyi-Kogan et al. (2015).

Bisnovatyi-Kogan, G.S. & Moiseenko, S.G. 1992, Astron.Zh. 69,563 [SvA 36,285]

Bisnovatyi-Kogan, G.S., et al. 2008, Astronomy Reports, 52, 997

Bisnovatyi-Kogan, G.S., et al. 2015, in *XI Multifrequency Behaviour of High Energy Cosmic Sources Workshop*, Palermo, Italy, PoS(MULTIF2015), 048

Bisnovatyi-Kogan, G.S., Popov, Yu.P. & Samokhin, A.A. 1976, Ap&SS, 41, 287

Burrows, A., et al. 2007, ApJ, 664, 416

Colgate, S.A. & White, R.H. 1966, ApJ, 143, 626

Epstein, R. 1979, MNRAS, 188, 305.

Johnston, S., et al. 2005, MNRAS, 364, 1397

Johnston, S., et al. 2007, MNRAS381, 1625

Mikami, H., et al. 2008, ApJ, 683, 357

Moiseenko, S.G., et al. 2006, MNRAS, 370, 501

Moiseenko, S.G. Bisnovatyi-Kogan, G.S. 2015, Astron. Reports, 59, 573

Noutsos, A., et al. 2012, MNRAS, 423, 2736

Shen, H., et al. 1998, Nuclear Physics A , 637, 435

Smirnova, T.V., Shishov, V.I. & Malofeev, V.M. 1996, ApJ462, 289

Spruit, H.C. 2002, A&A, 381, 923

Takiwaki, T., et al. 2004, ApJ, 616, 1086

Takiwaki, T., Kotake, K., & Sato, K. 2009, ApJ, 691, 1360

Tayler, R. 1973, MNRAS, 161, 365

Velikhov, E.P. 1959, J. Exper. Theor. Phys., 36, 1398 [Sov. Phys. JETP, 9, 995]

Vlemmings, W.H.T., et al. 2005, MmSAI, 76, 531 [astro-ph/0509025]

Wang, J.C L., Sulkanen, M.E., & Lovelace, R.V.E. 1992, ApJ, 390, 46

H.E.S.S. Observations of Extragalactic Jet Sources

M. Böttcher[1], on behalf of the H.E.S.S. Collaboration

[1]*Centre for Space Research, North-West University, Potchefstroom, South Africa*

Abstract. The High Energy Stereoscopic System (H.E.S.S.) is the world's largest currently operating Atmospheric Cherenkov Telescope Array. This paper presents highlights of recent results from H.E.S.S. observations of extragalactic jet sources. It will focus on variability studies of the well-known blazars Mrk 501 (discovering minute-scale variability at energies > 2 TeV) and PKS 2155-304, the multiwavelength analysis of the recently discovered blazar PKS 1440-389, and observations of the gravitationally lensed blazar PKS 1830-211, including a brief discussion of the implications of its non-detection by H.E.S.S.

1. Introduction

The High Energy Stereoscopic System (H.E.S.S.) is an array of 5 Cherenkov Telescopes (4×12 m and 1×28 m diameter), located in the Khomas Highland near Windhoek, Namibia, 1800 m above sea level (Aharonian et al. 2006). It observes very-high-energy (VHE: $E > 100$ GeV) γ-rays indirectly by imaging the Cherenkov light from electromagnetic showers produced by VHE γ-rays in the atmosphere. It is operated by an international collaboration of over 200 scientists from 12 countries. The original array of four 12-m telescopes (CT1 – CT4), inaugurated in 2002, constitutes the first phase of operations (H.E.S.S. I, from 2002 - 2012). The addition of the fifth (28-m) telescope (CT5 — which is the largest single Cherenkov telescope in the world) in 2012 ushered in the second phase (H.E.S.S. II), and extended the sensitivity of the array significantly towards lower energies, compared to H.E.S.S. I (see Zaborov et al. 2015 for a more detailed description).

The capabilities of H.E.S.S. II can be exploited in two complementary analysis approaches:

1. CT5 Mono Analysis: CT5 can be used in standalone mode, without consideration of data from CT1 – CT4. This mode yields the lowest possible energy threshold of $E_{\mathrm{thr}} < 100$ GeV.

2. H.E.S.S. II Hybrid Analysis: Considering data from all five telescopes yields the best achievable sensitivity (because of superior background rejection), but at the cost of a slightly higher energy threshold compared to CT5 Mono Analysis.

Figure 1 shows a comparison of the VHE γ-ray spectra of the well-known VHE γ-ray blazar PKS 2155-304, obtained from H.E.S.S. I observations in 2010
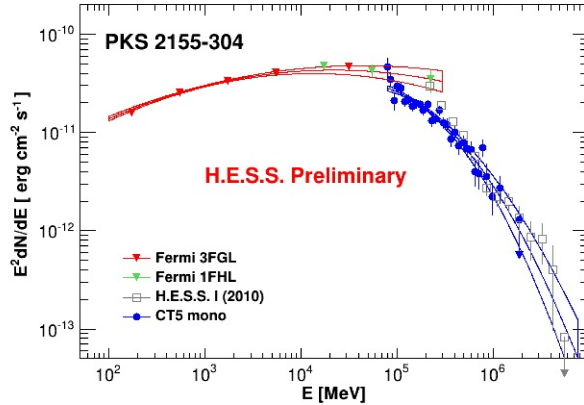
Figure 1.   Comparison between H.E.S.S. I and CT5 Mono Analyses, and the *Fermi*-LAT spectrum of the blazar PKS 2155-304. The figure shows excellent agreement between H.E.S.S. I and CT5 as well as significant energy overlap between *Fermi*-LAT and CT5. Reproduced from Zaborov et al. (2015).

(open squares) to CT5 Mono observations (filled circles). It illustrates that (a) there is excellent agreement between H.E.S.S. I and CT5 analyses, and (b) CT5 allows for significant energy overlap with *Fermi*-LAT at $\sim 80 - 300$ GeV. The flux mismatch is a result of the well-known, significant flux variability (e.g., Aharonian et al. 2007), considering the drastically different integration times and non-simultaneity of the *Fermi*-LAT and H.E.S.S. observations.

H.E.S.S. observations of extragalactic targets are focusing on the following key science projects:

1. ToO observations and long-term monitoring of known VHE AGN (primarily blazars, but also radio galaxies, such as Cen A). Science drivers for such observations include diagnostics of particle acceleration, particle content, and the location of the γ-ray emission region in relativistic jets, as well as searches for signatures of physics beyond the standard model (Lorentz Invariance Violation / Axion-Like Particles).

2. Discovery of potential new VHE sources (including radio galaxies, radio-quiet AGN and non-active galaxies). Science drivers include the expansion of the extragalactic VHE source catalogue to enable population studies and probes of the Extragalactic Background Light (EBL), as well as the search for the origin of ultra-high-energy ($E \overset{>}{\sim} 10^{19}$ eV) cosmic rays (UHECRs).

3. Search for VHE emission from gravitationally lensed blazars (at large redshifts, otherwise likely inaccesible to VHE observations because of severe EBL attenuation).

4. Search for VHE γ-ray emission from gamma-ray bursts (GRBs) — both prompt GRBs and early afterglows.

5. Multimessenger astronomy (including follow-up observations of VHE neutrino events and gravitational-wave triggers).

6. Search for Dark Matter annihilation signatures (in particular, observations of dwarf spheroidal galaxies).

Due to length/time restrictions, this paper will focus on a few recent results and highlights from sub-programs 1. - 3. above. For a recent update on the H.E.S.S. GRB program, see, e.g., Parsons et al. (2015), while more information on the H.E.S.S. multimessenger program can be found in Schüssler et al. (2015), and on the dark matter program in Abramowski et al. (2014a). Recent results of new EBL constraints based on H.E.S.S. observations of blazars can be found in Lorentz et al. (2015).

2. Variability Studies of Known VHE Blazars

There are several well-known VHE γ-ray emitting blazars accessible from the southern hemisphere with sufficiently bright quiescent levels to allow for meaningful long-term monitoring with H.E.S.S. With its 13 years of continuous operations, these on-going H.E.S.S. monitoring observations provide light curves of unprecedented duration and detail for several blazars.
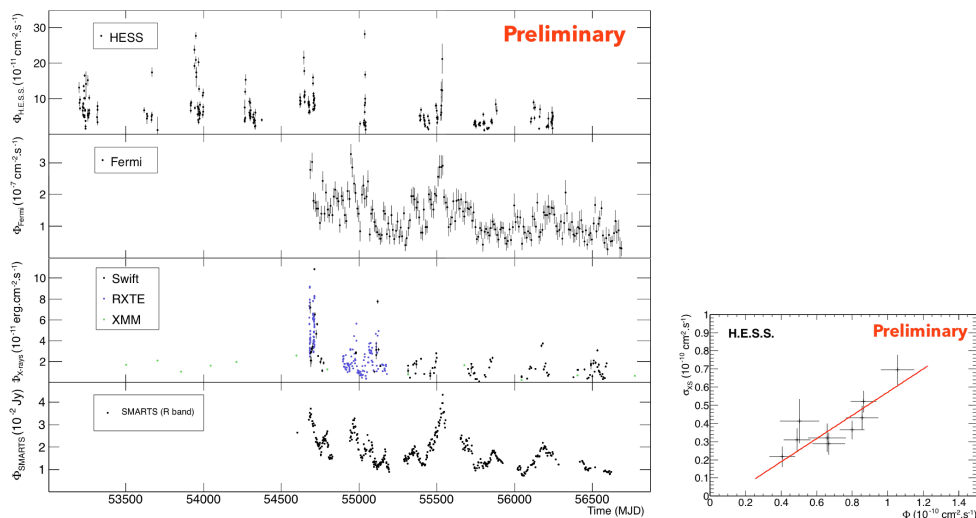
Figure 2. *Left:* The long-term ($\sim$ 12 years) multi-wavelength light curve of PKS 2155-304. *Right:* H.E.S.S. excess variability amplitude as a function of underlying flux level from the long-term light curve of PKS 2155-304. Reproduced from Chevalier et al. (2015).

The prominent high-frequency-peaked BL Lac object (HBL) PKS 2155-304 is a prime example (see, e.g., Abramowski et al. 2014b). Figure 2 (left) shows the H.E.S.S. VHE γ-ray, *Fermi*-LAT HE γ-ray, X-ray, and optical (R-band) light curve of this blazar, indicating the large range of flux states in which H.E.S.S. has detected the source, and the generally close correlation between the variability patterns in these frequency bands, on long time-scales. A study of the excess variability amplitude of the VHE γ-ray variability of PKS 2155-304 as a function

of its short-term average flux state (shown in Figure 2, right) reveals a linear correlation, which indicates a multiplicative process driving the γ-ray variability of this blazar.
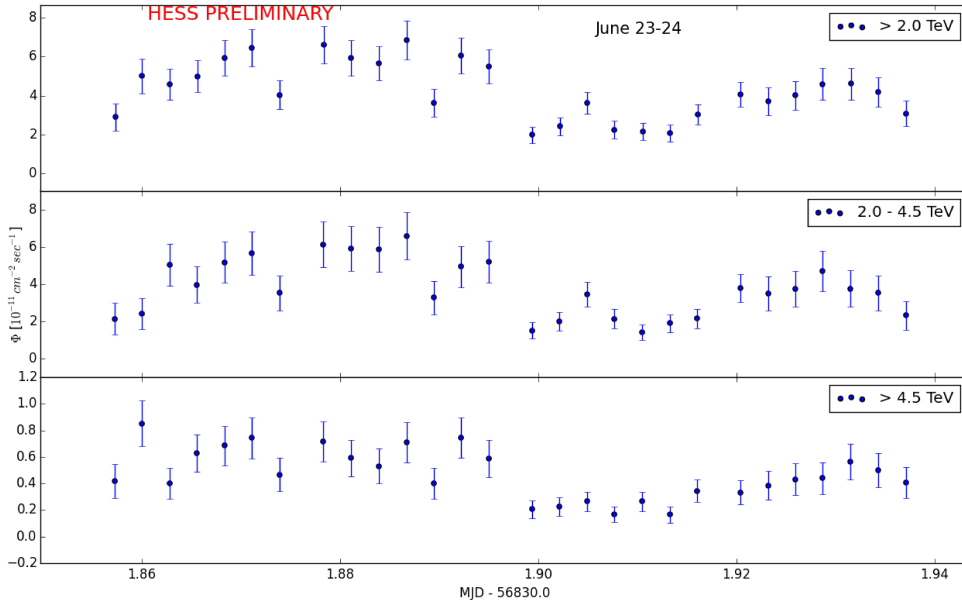
Figure 3.   Four-minute binned light curve of the HBL Mrk 501 at $E > 2$ TeV during June 2014, revealing variability on ~ 10 minute time scales. Reproduced from Chakraborty et al. (2015).

Another prominent, VHE-bright blazar which was subject to several co-ordinated observing campaigns including H.E.S.S. is the HBL Mrk 501. This blazar (as PKS 2155-304) has been known to show very rapid ($\sim$ few minutes) variability in VHE γ-rays, based on low-zenith-angle (and, hence, low-energy threshold, $E \gtrsim 150$ GeV) observations with MAGIC (Albert et al. 2007). In that case, the variability is strongly dominated by the signal of photons near the low-energy threshold, i.e., $E < 1$ TeV. High-zenith-angle observations (with energy threshold $E > 2$ TeV) by H.E.S.S. were performed during major flaring activity of Mrk 501 in June 2014. These led, for the first time, to the detection of rapid ($\lesssim 10$ min.) variability clearly associated with $E > 2$ TeV photons (Fig. 3). This result is particularly interesting as it rules out a cosmic-ray induced origin of the multi-TeV emission, at least in the case of Mrk 501, which has been invoked to explain an apparent deficit in EBL induced $\gamma\gamma$ attenuation for moderate-redshift ($z \lesssim 0.5$) blazars (e.g., Essey et al. 2010).

3.   New Discovery: PKS 1440-389

One of the most recent new blazar discoveries by H.E.S.S. is the BL Lac object PKS 1440-389. H.E.S.S. observations were motivated by the hard *Fermi*-LAT spectrum with a photon index of $\Gamma_{\mathrm{LAT}} = 1.77 \pm 0.06$. The redshift of this source
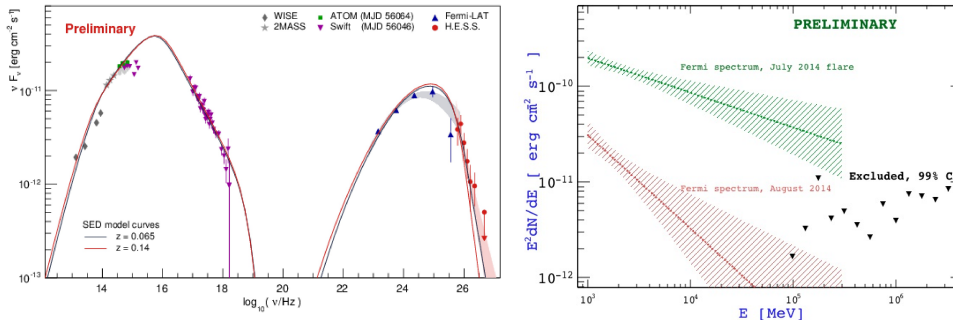
Figure 4. *Left:* Spectral energy distribution of PKS 1440-389, with two single-zone, leptonic SSC fits for redshifts $z = 0.065$ and $z = 0.14$. Reproduced from Prokoph et al. (2015). *Right: Fermi*-LAT spectra (quiescent and flaring) of PKS 1830-211, compared to 99 % CL upper limits from H.E.S.S., indicating a significant deficit of VHE emission compared to the flaring-state LAT spectrum. Reproduced from Glicenstein et al. (2015).

is uncertain. While a preliminary redshift of $z = 0.065$ appeared in an early version of the 6dF Galaxy Survey, it is no longer listed in the final version. Shaw et al. (2013) determined redshift limits of $0.14 < z < 2.2$. H.E.S.S. observed PKS 1440-389 for a total of ~ 12 hr in the period Feb. 29 – May 27, 2012, which led to a detection with 9.1 σ significance. No evidence for significant γ-ray variability was found, and a simple single-zone leptonic SSC model (using the code of Böttcher et al. 2013) can fit the simultaneous SED (Figure 4 left) with parameters corresponding to a particle-dominated jet in which the ratio of powers carried in magnetic fields and relativistic electrons is $L_B/L_e \sim 0.1$.

4.   The Gravitationally Lensed Blazar PKS 1830-211

Two *Fermi*-LAT detected γ-ray blazars (QSO B0218+357 and PKS 1830-211) are known to be gravitationally lensed by foreground galaxies. While the lensed images can not be spatially resolved by γ-ray observations, the light-travel time delay between the two images, in conjunction with the variable nature of these objects, can be exploited to look for the lensing-delayed counterpart of a γ-ray flare (Barnacka et al. 2011, Cheung et al. 2014). The lensing magnification along with the prospect of predicting the lensing-delayed second γ-ray flare, given the known time delay between the two images, motivated VHE observations of both of these blazars. In the case of QSO B0218+357 ($z = 0.94$), this led to the discovery of VHE γ-ray emission by MAGIC (Sitarek et al. 2015), making it the most distant known VHE γ-ray emitter at the time.

H.E.S.S. observations of the other lensed γ-ray blazar, PKS 1830-211, were triggered by the *Fermi*-LAT detection of a flare on July 27, 2014, which prompted H.E.S.S. observations in August 2014, around the time of the known radio delay of $\Delta t \sim 26$ days. Further motivation for H.E.S.S. observations was provided by

studies of Barnacka et al. (2014b) that excess $\gamma\gamma$ absorption by intervening systems (the lensing galaxy or individual stars within it) is not expected to occur, thus enabling us to take full advantage of the expected lensing magnification to observe this $z = 2.5$ blazar. The H.E.S.S. observations did not result in a significant detection, and the resulting 99 % CL upper limits are compared to the *Fermi*-LAT spectra during the flare (green) and simultaneous to the H.E.S.S. observations (red) in Figure 4 (right). The comparison to the LAT flaring spectrum indicates a significant deficit of VHE γ-ray emission. This may be (at least partially) explained by strong EBL $\gamma\gamma$ absorption, but may also indicate a slightly different location of the VHE emission region compared to the HE emission region, which might lead to different time delays in the two energy regimes (Barnacka et al. 2014a).

References

Abramowski, A., et al., 2014a, Phys. Rev. D., vol. 90, id. 112012

Abramowski, A., et al., 2014b, A&A, 571, A39

Aharonian, A. A., et al., 2006, A&A, 457, 899

Aharonian, A. A., et al., 2007, ApJ, 664, L71

Albert, J., et al., 2007, ApJ, 669, 862

Barnacka, A., Glicenstein, J.-F., & Moudden, Y., 2011, A&A, 528, L3

Barnacka, A., et al., 2014a, ApJ, 788, 139

Barnacka, A., Böttcher, M., & Sushch, Iu., 2014b, ApJ, 790, 147

Böttcher, M., et al., 2013, ApJ, 768, 54

Chakraborty, N., et al., 2015, in proc. of 34th ICRC, PoS(ICRC2015), 872

Cheung, C. C., et al., 2014, ApJL, 782, L14

Chevalier, J., et al., 2015, in proc. of 34th ICRC, PoS(ICRC2015), 829

Essey, W., et al., 2010, Phys. Rev. Lett., vol. 104, id. 141102

Glicenstein, J.-F., et al., 2015, in proc. of 34th ICRC, PoS(ICRC2015), 737

Lorentz, M., et al., 2015, in proc. of 34th ICRC, PoS(ICRC2015), 777

Parsons, R. D., et al., 2015, in proc. of 34th ICRC, PoS(ICRC2015), 853

Prokoph, H., et al., 2015, in proc. of 34th ICRC, PoS(ICRC2015), 862

Schüssler, F., et al., 2015, in proc. of 34th ICRC, PoS(ICRC2015), 726

Shaw, M. S., et al., 2013, ApJ, 764, 135

Sitarek, J., et al., 2015, in proc. of 34th ICRC, PoS(ICRC2015), 825

Zaborov, D., et al., 2015, in proc. of 34th ICRC, PoS(ICRC2015), 808

---

[1]Any opinion, finding, and conclusion or recommendation expressed in this material is that of the authors, and the NRF does not accept any liability in this regard.

Coupling hydrodynamics and radiation calculations for star-jet interactions in AGN

V. M. de la Cita[1], V. Bosch-Ramon[1], X. Paredes-Fortuny[1], D. Khangulyan[2] and M. Perucho[3,4]

[1]*Departament d'Astronomia i Meteorologia, ICCUB, Universitat de Barcelona (IEEC-UB), Martí i Franquès 1, E-08028 Barcelona, Spain*
[2]*Department of Physics, Rikkyo University 3-34-1, Nishi-Ikebukuro, Toshima-ku, Tokyo 171-8501, Japan*
[3]*Departament d'Astronomia i Astrofísica, Universitat de València, Av. Vicent Andrés Estellés s/n, 46100 Burjassot (València), Spain*
[4]*Observatori Astronòmic, Universitat de València, C/ Catedràtic José Beltran, 2, 46980, Paterna (València), Spain*

Abstract. Stellar populations can contribute to the non-thermal emission of radio-loud active galactic nuclei via the interaction with the relativistic jets. The shock produced between the stellar wind and the jet can accelerate particles and produce high-energy emission. We have performed 2D axisymmetric hydrodynamical simulations of the jet-stellar wind interaction and obtained the hydrodynamical properties of the emitting flow. With this information we study the evolution of the non-thermal particles accelerated in the collision and their IC and synchrotron radiation. We present here the results of these computations: detailed radiation maps and spectral energy distributions for different scenarios, depending on the position of the star in the jet, the magnetic field, and the viewing angle. We have studied two representative scenarios: the steady state of the jet-wind interaction; and the case in which a transient instability develops, enlarging the interaction region.

1. Introduction

The interaction between the winds of stars and jets in active galactic nuclei (AGN) has been proposed to play an important role in the evolution of the latter (e.g. Komissarov 1994; Bowman et al. 1996; Hubbard & Blackman 2006; Bosch-Ramon et al. 2012; Perucho et al. 2014). In addition, the shock created in the interaction between AGN jets and stellar atmospheres is thought to produce significant non-thermal emission, potentially detectable from Earth, in both blazar and non-blazar AGN (e.g. Bednarek & Protheroe 1997; Barkov et al. 2010, 2012a,b; Khangulyan et al. 2013; Bosch-Ramon et al. 2012; Araudo et al. 2013; Bosch-Ramon 2015; Bednarek & Banasinski 2015). Although the extent of the dynamical and radiative impact of these interactions is not well known, there are already observational hints of this kind of scenarios (e.g. Müller et al. 2014) and also evidence supporting that some high-energy phenomena observed in AGN could be interpreted in the context of jet-star interactions (e.g. Barkov et al. 2010, 2012a,b; Khangulyan et al. 2013).

We study a single star-jet interaction under different conditions. To do so, we first perform a relativistic hydrodynamic (RHD) simulation in 2 dimensions, taking advan-

tage of the cylindrical symmetry of the problem (at first order aproximation). This simulation is focused on a relatively small volume close to the interacting star, where the shock is formed. Then we compute the inverse Compton (IC) and syncrotron radiation of the non-thermal particle population in the relativistic regime. This emission is calculated in a variety of scenarios, letting vary, namely, the magnetic field, the observational angle, and the height of the star with respect to the base jet. Our results are in coincidence with the previous, less accurate estimates by Bosch-Ramon (2015), and confirm the potential importance of star-jet interactions in the total X-ray and γ-ray emission budget in AGN.

2.   Hydrodynamics and radiation

2.1.   Hydrodynamical setup

We have performed a simulation using a finite-difference code based on a high-resolution shock-capturing scheme that solves the equations of RHD in two dimensions in a conservation form (Martí et al. 1997). The code is paralelized using open message passing (Open MP; Perucho et al. 2005). We let vary, namely, the magnetic field, the observational angle and the height of the star with respect to the base jet. The details of this simulation are detailed in de la Cita et al. (2016). Here we present the physical scenario in an abridged way.

We have assumed a collisionless, adiabatic and relativistic ideal gas in which the magnetic field does not play an important role dynamically. The physical size of the domain is $r \in [0, l_r]$ with $l_r = 2 \times 10^{15}$ cm, and $z \in [0, l_z]$ with $l_z = 1.5 \times 10^{15}$ cm, and the grid has 400×300 cells. The star is placed at $(r_0, z_0) = (0, 0.3 \times 10^{15})$ cm, and its spherical wind (taken homogeneous, with a density profile $\propto 1/R^2$) is injected in a stellar radius of $r_{\text{in}} = 7 \times 10^{13}$ cm, with a velocity of $v_{\text{wind},\star} = 2 \times 10^8$ cm and stellar mass-loss rate $\dot{M}_\star = 10^{-9} \text{M}_\odot \text{yr}^{-1}$. These parameters have been chosen to correspond to those of a high-mass star with modest mass-loss rate. The thrust of this wind (dynamically, the most relevant stellar parameter) also corresponds to that of a red giant. The jet is injected at the bottom of the grid, with a total jet power inside the grid of $L_{\text{jet}} \approx 4 \times 10^{37}$ erg s^{-1} ($\sim 10^{44}$ erg s^{-1} for a 1 pc jet radius) and a jet Lorentz factor of $\Gamma = 10$. The star is considered to cross the jet at a height of 10 pc, although the results obtained for this case can be extrapolated to different heights, as we discuss in Sect. 3.2.

In order to compute the emission from non-thermal particles, we divide the fluid into streamlines, getting 77 lines segmented into 200 cells each, so we have reduced the original 3-dimensional problem into a number of 1-dimensional emitters. To recover the 3D information, we assigned a random azimuthal angle ϕ to each of the 77×200 cells after the radiation computation, getting a 3D emitter more similar to the object of interest.

2.2.   Non-thermal radiation computation

From the streamlines we get dynamical information about the fluid. Using this information we can calculate how the non-thermal population will evolve. For this work we developed a code that computes, for each streamline, the location where particles are accelerated and the luminosity injected through these particles. Then, the code calculates the steady particle energy distribution, and finally derives the synchrotron and
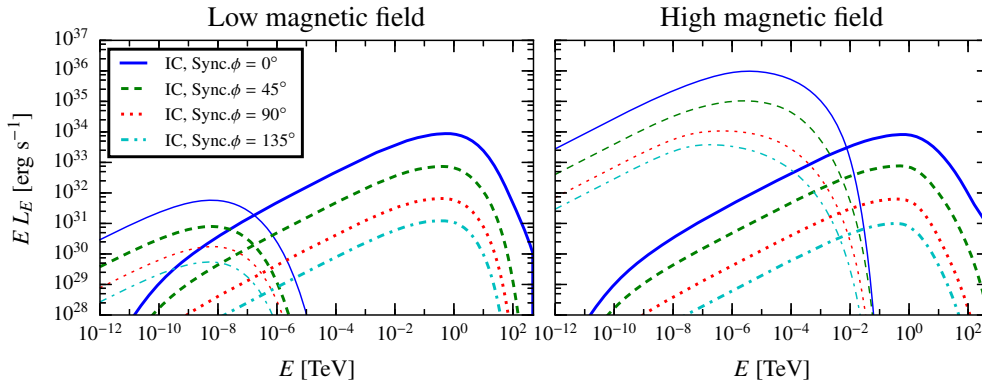
Figure 1.   Synchrotron (thin) and IC (thick line) SEDs for the jet-star interaction in the steady state, taking $z_{int} = 10$ pc and for $\phi = 0°$, $45°$, $90°$ and $135°$. In the left pannel we have a low magnetic field with $\chi_B = 10^{-4}$ and on the right one a high magnetic field with $\chi_B = 1$.

IC radiation as seen from the observer. When the radiation coming from each line is known, the total spectral energy distribution (SED) can be obtained and emission maps derived. A full description of the method can be found in de la Cita et al. (2016).

Here we stress some key points in the setup of our code: 1. The injection of non-thermal particles is done anywhere a shock takes place, considering tha this happens when the internal energy increases and the fluid velocity decreases. The rate of energy injection in the form of non-thermal particles in the cell volume in the fluid frame is taken to be a fraction (in our case, $\chi_{NT} = 1$) of the generated internal energy per second in the cell, i. e., the time derivative of the 00-component of the enery momentum tensor times the volume in the fluid frame. The spectral energy distribution of the injected particles is a power law of index -2 with a cut-off at the maximum energy of the accelerated particles. 2. The magnetic field is taken as a fraction χ_B of the matter energy flux at the beginning of the line, and it is considered perpendicular to the streamline. We let it evolve throughout the streamline, but it never gets strong enough to play a relevant dynamical role. And 3. The low-energy photon field considered for the IC computation is the typical of a red giant placed in the star position, with a black body of temperature $T_\star = 3 \times 10^3$ K and $L_\star = 3 \times 10^{36}$ ergs s^{-1}.

3.   Results

We have computed the IC and syncrotron emission for a number of scenarios, letting vary the viewing angle and the magnetic field. The viewing angle is taken as the angle formed by the line of sight and the jet velocity, and it plays a very important role due to the relativistic nature of the fluid. The luminosity is enhanced when the fluid is pointing towards the observer, given that the observed luminosity is boosted as: $\epsilon L(\epsilon) = \delta^4 \epsilon' L'(\epsilon')$ where the luminosity L and the spectral energy ϵ have a prime where they represent the quantities in the fluid frame, and $\delta = 1/\Gamma(1 - \beta \cos\theta_{obs})$ is the Doppler boosting factor.
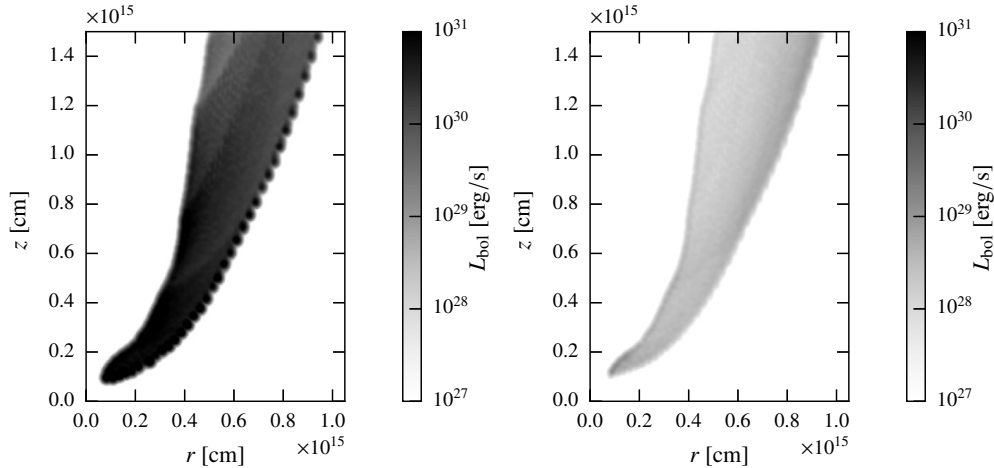
Figure 2.   Map in the *rz*-plane for the IC (left) and the synchrotron (right),
bolometric luminosity per cell, for the jet-star interaction in the steady state.
The adopted parameters are $\phi = 0$, $\chi_B = 10^{-4}$ and $z = 10$ pc.

Concerning the magnetic field B, we have taken two extreme cases for the χ_B
factor, being $\chi_B = 10^{-4}$ the low B case and $\chi_B = 1$ the high B case. We have considered
this last case to illustrate the impact of a high magnetic field; note that this case is
actually not realistic, as the magnetic field would be dynamically relevant.

In Fig. 1 the spectral energy distribution (SED) of the two cases for the magnetic
field are shown, each considering 4 different viewing angles. In the case of a low
magnetic field, the IC radiation dominates the spectrum, but for higher magnetic fields
the synchrotron emission can play an important role at GeV energies. In both low and
high B the IC contribution remains similar. The total emission is always larger for
smaller viewing angles, given that most of the cells have a strong velocity component
in the direction of the jet. Apart from the SEDs, a specific case has been chosen to
build a map of the emission, to give an idea of the emitter structure. This map is shown
in Fig. 2 and presents an emitter much larger than the size of the wind shock stand-
off distance. Whereas the total observer luminosity within the grid is $L_{IC} = 5 \times 10^{34}$
erg s^{-1}, the luminosity in the region with a radial coordinate smaller than the contact
discontinuity radius is ~ 100 times smaller.

3.1.   Perturbed state

Apart from the steady state reached by the RHD simulation, some instabilities may
grow making the shocked area much larger. A detailed description of the nature, origin
and development of such instabilities is addressed in de la Cita et al. (2016). Here we
note that under this perturbed state the shock region can become few times larger than
in the steady state scenario, increasing the emitting region and thus potentially the total
output non-thermal luminosity. In Fig. 3 the SEDs of several cases are shown, as well
as a map of the IC radiation. On one hand, the IC SED does not change significantly
compared with the steady state, due to the fact that the target photon field decays as
$1/r^2$ with r centred in the star. On the other hand, the synchrotron emission is enhanced
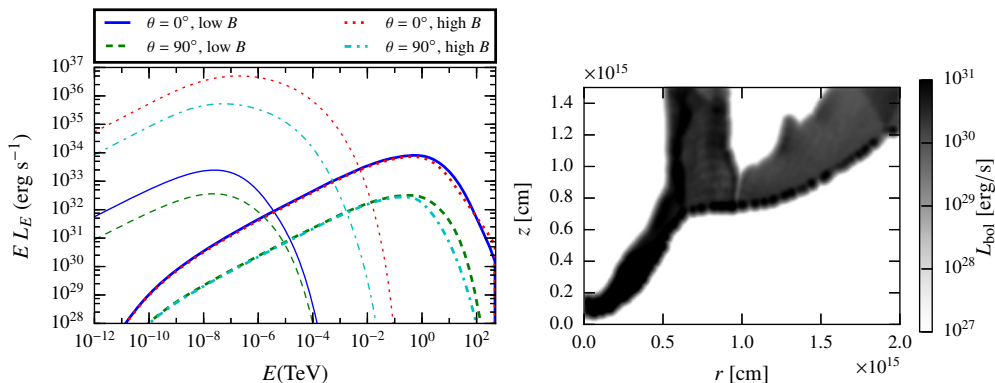
Figure 3.   On the left, synchrotron (thin) and IC (thick line) SEDs for the jet-star interaction in the perturbed state, taking $z_{int} = 10$ pc, $\chi_B = 10^{-4} - 1$, and $\phi = 0° - 90°$ are shown. On the right, an IC map of the perturbed state, with $z_{int} = 10$ pc, $\chi_B = 10^{-4}$, and $\phi = 0°$, equivalent to those in Fig. 2 is shown.

due to the larger area of the shock. These changes in luminosity are expected to be transient, since the life of the perturbations is relatively short.

3.2.   Scalability of the results

All the computations have been made placing the star at a jet height of $z = 10$ pc, but the results can be scaled with z since the total non-thermal luminosity is approximately proportional to $1/z$, as it is shown in Fig. 4.

4.   Conclusions

The results obtained are in agreement with the previous work by Bosch-Ramon (2015), as the effective emitter size is expected, predicted to be much larger than the size of the star. Also it is noted that the emission levels strongly depend on the viewing angle, due to the relativistic nature of the jet. Providing estimates for the emission levels expected from one jet-star interaction under different conditions, this work allows the computation of the integrated non-thermal luminosity of a typical stellar population crossing an AGN jet.

Figure 4.   Synchrotron (thin) and IC (thick line) SEDs for the jet-star interaction in the steady state, taking $\phi = 0°$, $\chi_B = 10^{-4}$, and for $z_{int} = 1$, 10, 100 and 1000 pc.

References

Araudo, A. T., Bosch-Ramon, V., & Romero, G. E. 2013, MNRAS, 436, 3626

Barkov, M. V., Aharonian, F. A., Bogovalov, S. V., Kelner, S. R., & Khangulyan, D. 2012a, ApJ, 749, 119

Barkov, M. V., Aharonian, F. A., & Bosch-Ramon, V. 2010, ApJ, 724, 1517

Barkov, M. V., Bosch-Ramon, V., & Aharonian, F. A. 2012b, ApJ, 755, 170

Bednarek, W. & Banasinski, P. 2015, ApJ, 807, 168

Bednarek, W. & Protheroe, R. J. 1997, MNRAS, 287, L9

Bosch-Ramon, V. 2015, A&A, 575, A109

Bosch-Ramon, V., Perucho, M., & Barkov, M. V. 2012, A&A, 539, A69

Bowman, M., Leahy, J. P., & Komissarov, S. S. 1996, MNRAS, 279, 899

de la Cita, V. M., Bosch-Ramon, V., Paredes-Fortuny, X., Khangulyan, D., & Perucho, M. 2016, A&A, 591, A15

Hubbard, A. & Blackman, E. G. 2006, MNRAS, 371, 1717

Khangulyan, D. V., Barkov, M. V., Bosch-Ramon, V., Aharonian, F. A., & Dorodnitsyn, A. V. 2013, ApJ, 774, 113

Komissarov, S. S. 1994, MNRAS, 269, 394

Martí, J. M., Müller, E., Font, J. A., Ibáñez, J. M., & Marquina, A. 1997, ApJ, 479, 151

Müller, C., Kadler, M., Ojha, R., et al. 2014, A&A, 569, A115

Perucho, M., Martí, J. M., & Hanasz, M. 2005, A&A, 443, 863

Perucho, M., Martí, J. M., Laing, R. A., & Hardee, P. E. 2014, MNRAS, 441, 1488

High-energy emission as signature of magnetic field amplification in neutron star mergers

N. Fraija[1], W. H. Lee[1], P. Veres[2] and R. Barniol Duran[3]

[1]*Instituto de Astronomía, Universidad Nacional Autónoma de México, Apdo. Postal 70-264, Cd. Universitaria, México DF 04510.*
[2] *Center for Space Plasma and Aeronomic Research (CSPAR), University of Alabama in Huntsville, Huntsville, AL 35899, USA.*
[3] *Department of Physics and Astronomy, Purdue University, 525 Northwestern Avenue, West Lafayette, IN 47907, USA.*

Abstract. The merger of a binary neutron star system is suggested as the central engine of short gamma-ray bursts (sGRBs). For the merger process, simulations predict that magnetic field is amplified beyond magnetar field strength by Kelvin-Helmholtz instabilities. With the Large Area Telescope (LAT), bursts have been detected that show a temporally extended component in coincidence with a short-lasting peak at the end of the prompt phase. We show that the presence of these LAT components in a sGRB could provide evidence of magnetic field amplification in the neutron star merger.

1. Introduction

The most popular progenitor model associated with short gamma-ray bursts (sGRBs) is the merger of compact object binaries; a neutron star binary or a neutron star–black hole (NS–BH; Eichler et al. 1989; Lee et al. 2004, 2005b). During the merger, simulations have exhibited an amplification of magnetic field strength, achieving values as high as 10^{15} G. The growth emerges from the transfer of hydrodynamical kinetic energy to electromagnetic energy via Kelvin-Helmholtz instabilities and turbulent amplification (Price & Rosswog 2006; Giacomazzo et al. 2009).

In the afterglow phase, the relativistic ejecta encounters the circumburst medium generating external shocks, forward and reverse shocks. A strong short-lived reverse shock propagates back into the ejecta, explaining the γ-ray, X-ray, optical and/or radio flares present at the end of the prompt phase (Kobayashi 2000; Kobayashi et al. 2004; Fraija et al. 2012; Fraija 2015). The long-lived forward shock leading to a continuous softening of the afterglow spectrum describes the temporarily extended emissions in multiwavelengths (Panaitescu 2007).

GRB110731A and GRB130427A were detected from the optical to the GeV energy range (Ackermann et al., 2013; 2014). Analysis on the prompt phase at the LAT energy range (> 100 MeV) revealed a temporally extended flux lasting hundreds of seconds in coincidence with a short-lasting bright peak. Fraija (2015) and Fraija et al. (2016a) showed that both components could be interpreted as synchrotron and SSC emissions from the forward and reverse shocks, respectively, provided that the reverse shock evolves in a thick-shell regime and the central

engines were entrained with a significant magnetic field. In this work we propose that the presence of high-energy components in sGRBs could offer evidence of the magnetic field amplification during the merger of two neutron stars.

2.   Dynamics of external Shock Model

In the external shock model, afterglow emission is generated when an expanding relativistic shell encounters the circumburst medium and consequently, forward and reverse shocks are produced (Uhm & Belodorodov 2007). Relativistic electrons at both shocks are accelerated and cooled down by synchrotron and Compton scattering emission. In the following subsections we will develop the dynamics of forward and reverse shocks. We hereafter use the observable quantities: a total energy $E = 5 \times 10^{52}$ erg, a luminosity distance from the source $D = 3 \times 10^{27}$ cm, an homogeneous density $n = 0.1$ cm^{-3}, a duration of the GRB $T_{90} = 1$ s (Berger 2014), and the values of cosmological parameters $H_0 = 71$ km s^{-1} Mpc^{-1}, $\Omega_m = 0.27$, $\Omega_\lambda = 0.73$. Also we will use primes (unprimes) to define the quantities in a comoving (observer) frame and the universal constants $c=\hbar=1$ in natural units. The subscripts f and r refer throughout this paper to the forward and reverse shock, respectively and the convention $Q_x = Q/10^x$ will be adopted in cgs units.

2.1.   Forward shock dynamics

The dynamics of the afterglow for a spherical ultrarelativistic and adiabatic shell propagating into a homogenous density is analyzed through the radius shock $R = 3^{1/3}(4\pi\, m_p)^{-1/3}\, n^{-1/3}\, \Gamma^{-2/3}\, E^{1/3}$ and the deceleration time $t_{dec} = 3^{1/3}(32\,\pi\, m_p)^{-1/3}\,(1+z)\, n^{-1/3}\, E^{1/3}\, \Gamma^{-8/3}$, where Γ is the bulk Lorentz factor, m_p is the proton mass and z is the redshift.

Synchrotron emission. Electrons are accelerated to a power law distribution by the first order Fermi mechanism, $N(\gamma_e)\, d\gamma_e \propto \gamma_e^{-p}\, d\gamma_e$, with $\gamma_e \geq \gamma_{m,f} = \epsilon_e \Gamma m_p (p-2)/(m_e(p-1))$ where m_e is the electron mass and $\epsilon_e = U_e/(4\,\Gamma^2\, n\, m_p)$ the electron equipartition parameter defined as fraction of the energy density U_e that goes to accelerate electrons. The total energy density (U) is also equipartitioned to amplify the magnetic field $\epsilon_{B,f} = U_{B,f}/U$ (with $U_{B,f} = B_f'^2/8\pi$), hence the magnetic field can be written as $B_f' = (32\pi m_p)^{1/2}\, \epsilon_{B,f}^{1/2}\, n^{1/2}\, \Gamma$.

  Considering the time scale for synchrotron cooling $t_{e,syn} \simeq 3 m_e (16\sigma_T)^{-1}\,(1+z)\, \epsilon_{B,f}^{-1}\, n^{-1}\, \Gamma^{-3}\, \gamma_e^{-1}$ and the deceleration time, the cooling electron Lorentz factor can be written as $\gamma_{e,c,f} = 3\, m_e (16\, \sigma_T\, m_p)^{-1}(1+z)\, \epsilon_{B,f}^{-1}\, n^{-1}\, \Gamma^{-3}\, t^{-1}$, where σ_T is the Thomson cross section. Comparing the acceleration $t_{acc} \simeq 2\pi\, m_e q_e^{-1}(1+z)\, \Gamma^{-1}\, B_f'^{-1}\gamma_e$ and synchrotron time scales, the maximum electron Lorentz factor achieved is $\gamma_{e,max,f} = 2(18\pi\, q_e^2 m_p)^{1/4}\sigma_T^{-1/2}\, \epsilon_{B,f}^{1/4}\, n^{1/4}\, \Gamma^{1/2}$, with q_e the elementary charge. From the electron Lorentz factors and deceleration time scales, the synchrotron spectral breaks are (Fraija et al. 2016a)

$$E_{\gamma,\mathrm{a,f}}^{syn} \quad \simeq \quad 3.21 \times 10^{-6}\,\mathrm{eV}\,\left(\frac{1+z}{2}\right)^{-1}\, \epsilon_e^{-1}\, \epsilon_{B,f}^{1/5}\, n_{-1}^{3/5}\, E_{52.7}^{1/5}\,,$$

$$
\begin{aligned}
E_{\gamma,\mathrm{m,f}}^{syn} &\simeq 1.19 \times 10^9 \,\mathrm{eV} \left(\frac{1+z}{2}\right)^{1/2} \epsilon_e^2 \,\epsilon_{B,f}^{1/2} \,E_{52.7}^{1/2} \,t_0^{-3/2}, \\
E_{\gamma,\mathrm{c,f}}^{syn} &\simeq 23.13 \,\mathrm{eV} \left(\frac{1+z}{2}\right)^{-1/2} (1+x_f)^{-2} \,\epsilon_{B,f}^{-3/2} \,n_{-1}^{-1/2} \,E_{52.7}^{-1/2} \,t_0^{-1/2}, \\
E_{\gamma,\mathrm{max,f}}^{syn} &\simeq 180.38 \times 10^9 \,\mathrm{eV} \left(\frac{1+z}{2}\right)^{-5/8} n_{-1}^{-1/8} \,E_{52.7}^{1/8} \,t_0^{-3/8}.
\end{aligned} \tag{1}
$$

The lightcurve in the LAT energy range generated by the ultra-relativistic electrons in the fast-cooling regime ($E_{\gamma,\mathrm{m,f}}^{syn} < E_\gamma^{syn} < E_{\gamma,\mathrm{max,f}}^{syn}$) is

$$
(EF_\nu)_{\gamma,\mathrm{f}}^{syn} = 3.67 \times 10^{-5} \,\frac{\mathrm{erg}}{\mathrm{cm^2\,s}} \left(\frac{1+z}{2}\right)^{1.1} \epsilon_{B,f}^{0.1} \,\frac{\epsilon_e^{1.4} \,n_{-1}^{\frac{1}{4}}}{D_{27.3}^2 \,E_{52.7}^{0.1} \,t_0^{1.3} \left(E_{\gamma,8}^{syn}\right)^{0.2}}. \tag{2}
$$

2.2. Reverse shock dynamics

For the reverse shock, a simple analytic solution can be derived taking two limiting cases, the thick- and thin-shell case, by using a critical Lorentz factor defined by

$$
\Gamma_c = 1.15 \times 10^3 \left(\frac{1+z}{2}\right)^{3/8} E_{52.7}^{1/8} \,n_{-1}^{-1/8} \,T_{90,0}^{-3/8}. \tag{3}
$$

For $\Gamma > \Gamma_c$ (thick shell) the shell is significantly decelerated by the reverse shock, otherwise, $\Gamma < \Gamma_c$ (thin shell), the reverse shock cannot decelerate the shell effectively. Irrespective of the evolution of the reverse shock, the synchrotron spectral evolution between reverse and forward shock is related by $E_{\gamma,\mathrm{m,r}}^{syn} \sim \mathcal{R}_B^{-1} \mathcal{R}_M^{-2} E_{\gamma,\mathrm{m,f}}^{syn}$, $E_{\gamma,\mathrm{c,r}}^{syn} \sim \mathcal{R}_B^3 E_{\gamma,\mathrm{c,f}}^{syn}$ and $F_{\gamma,\mathrm{max,r}}^{syn} \sim \mathcal{R}_B^{-1} \mathcal{R}_M F_{\gamma,max,f}^{syn}$, where

$$
\mathcal{R}_B = \frac{B_f'}{B_r'}, \quad \text{and} \quad \mathcal{R}_M = \frac{\Gamma_d^2}{\Gamma}, \tag{4}
$$

with Γ_d the bulk Lorentz factor at the shock crossing time t_d.

In the thick-shell regime, the reverse shock becomes relativistic during its propagation and the ejecta is significantly decelerated. The bulk Lorentz factor at the shock crossing time $t_d \simeq T_{90}$ is given by $\Gamma_d \sim \Gamma_c$. Eventually, the shock crossing time could be shorter than T_{90} depending on the degree of magnetization of the ejecta (Zhang & Kobayashi 2005). Numerical analysis performed by Fan et al. (2004) revealed that for the particular value of the magnetization parameter $\sigma \simeq 1$, the shock crossing time becomes $t_d \simeq T_{90}/6$.

Synchrotron emission. Assuming that electrons are accelerated in the reverse shock to a power-law distribution and the energy density is equipartitioned between electrons and magnetic field, then the minimum electron Lorentz factor $\gamma_{\mathrm{e,m,r}} = \epsilon_e(p-2)m_p\Gamma/((p-1)m_e\Gamma_d)$ and magnetic field is

$$
B_r' = (32\pi m_p)^{1/2} \,\epsilon_{B,r}^{1/2} \,n^{1/2} \,\Gamma. \tag{5}
$$

From the characteristic cooling time of synchrotron radiation and dynamical time scale, the cooling electron Lorentz factor is $\gamma_{e,c,r} = 3\,m_e(16\,\sigma_T\,m_p)^{-1}(1+z)\,(1+$

$x_r)^{-1}\,\epsilon_{B,r}^{-1}\,n^{-1}\,\Gamma^{-3}\,T_{90}^{-1}$. By considering $\gamma_{e,a,r} \simeq \gamma_{e,m,r}$ (Sari & Esin 2001) and from eq. (4), we rescale the synchrotron self-absorption energy between forward and reverse shocks as $E_{\gamma,a,r}^{syn} \sim \mathcal{R}_B^{-2/5}\,\mathcal{R}_M^{-2}\,E_{\gamma,a,f}^{syn}$. Additionally, from synchrotron break energy relations (forward and reverse shock), eqs. (1) and (4), we can write the synchrotron spectral breaks as

$$
\begin{aligned}
E_{\gamma,a,r}^{syn} &\simeq 1.86 \times 10^{-18}\,\text{eV}\,\left(\frac{1+z}{2}\right)^{-5/2}\epsilon_e^{-1}\,\epsilon_{B,r}^{1/5}\,\Gamma^2\,E_{52.7}^{-3/10}\,n_{-1}^{11/10}\,T_{90,0}^{3/2}, \\
E_{\gamma,m,r}^{syn} &\sim 6.94 \times 10^{-4}\,\text{eV}\,\left(\frac{1+z}{2}\right)^{-1}\epsilon_e^2\,\epsilon_{B,r}^{1/2}\,\Gamma^2\,n_{-1}^{1/2}, \\
E_{\gamma,c,r}^{syn} &\sim 2.58\,\text{eV}\,\left(\frac{1+z}{2}\right)^{-1/2}(1+x_r)^{-2}\,\epsilon_{B,r}^{-3/2}\,n_{-1}^{-1}\,E_{52.7}^{-1/2}\,T_{90,0}^{-1/2}.
\end{aligned}
\tag{6}
$$

Here, $x_r = (-1 + \sqrt{1 + 4\eta\epsilon_e/\epsilon_{B,r}})/2$ is the ratio of the SSC to synchrotron luminosity, where η for slow-cooling and fast-cooling regime is $(\gamma_{e,c,r}/\gamma_{e,m,r})^{2-p}$ and $\eta = 1$, respectively (Sari & Esin 2001).

SSC emission. Accelerated electrons can upscatter photons from low to high energies as $E_{\gamma,m,r}^{ssc} \sim \gamma_{e,m,r}^2\,E_{\gamma,m,r}$, $E_{\gamma,c}^{ssc} \sim \gamma_{e,c,r}^2\,E_{c,r}$ and $F_{\gamma,\max,r}^{ssc} \sim k\tau\,F_{\max,r}$ where $k = 4(p-1)/(p-2)$ and $\tau = (4\pi r_d^2)^{-1}\sigma_T N(\gamma_e)$ is the optical depth of the shell. From electron Lorentz factors and the synchrotron spectral breaks (eq. 6), we get the break SSC energies

$$
\begin{aligned}
E_{\gamma,a,r}^{ssc} &\simeq 9.33 \times 10^{-19}\,\text{eV}\,\left(\frac{1+z}{2}\right)^{-13/4}\epsilon_e\,\epsilon_{B,r}^{1/5}\,\Gamma^4\,E_{52.7}^{-11/20}\,n_{-1}^{27/20}\,T_{90,0}^{9/4}, \\
E_{\gamma,m,r}^{ssc} &\sim 5.83 \times 10^{-4}\,\text{eV}\,\left(\frac{1+z}{2}\right)^{-7/4}\epsilon_e^4\,\epsilon_{B,r}^{1/2}\,\Gamma^4\,n_{-1}^{3/4}\,E_{52.7}^{-1/4}\,T_{90,0}^{3/4}, \\
E_{\gamma,c,r}^{ssc} &\sim 9.44 \times 10^{22}\,\text{eV}\,\left(\frac{1+z}{2}\right)^{3/2}(1+x_r)^{-4}\,\frac{1}{\epsilon_{B,r}^{7/2}\,n_{-1}^3\,E_{52.7}^{1/2}\,\Gamma^6\,T_{90,0}^{5/2}}.
\end{aligned}
\tag{7}
$$

Considering the SSC spectrum in the fast-cooling regime, the SSC flux reaches the peak $F_{\gamma,\text{peak},r}^{ssc} \sim (E_{\gamma,r}^{ssc}/E_{\gamma,c,r}^{ssc})^{-1/2}\,F_{\gamma,\max,r}^{ssc}$ at (Kobayashi & Zhang 2003):

$$
(EF_\nu)_{\gamma,\text{peak}}^{ssc} \sim 1.25 \times 10^{11}\,\frac{\text{erg}}{\text{cm}^2\,\text{s}}(1+x_r)^{-2}\left(\frac{1+z}{2}\right)^3\frac{E_{52.7}^{3/2}\,(E_{\gamma,r,8}^{ssc})^{1/2}}{\epsilon_{B,r}^{3/4}n_{-1}^{3/4}D_{27.3}^2\,\Gamma^5\,T_{90,0}^{5/2}}.
\tag{8}
$$

3. Results and Conclusions

We plot the synchrotron and SSC spectral breaks of the forward and reverse shocks as a function of equipartition parameters ($\epsilon_{B,f/r}$ and ϵ_e), considering the typical values of the magnetic ($10^{-5} \leq \epsilon_{B,f(r)} \leq 1$) and electron ($\epsilon_{e,f} = 0.25$) parameters (Santana et al. 2014) for $\Gamma = 1200$ (left panel) and $\Gamma = 3000$ (right panel), as shown in Figure 1.
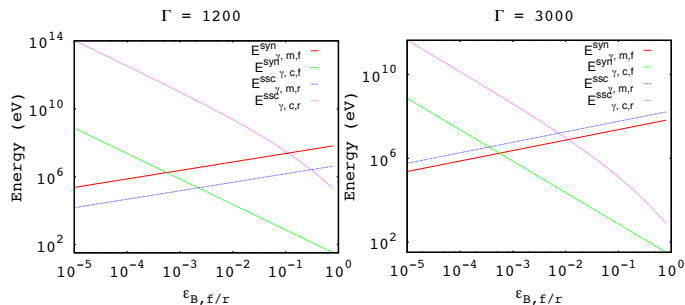
Figure 1. Break photon energies of synchrotron and SSC emission as a function of $\epsilon_{B,f/r}$ from the forward and reverse shocks, respectively. Taking into account the values of $\Gamma_c = 1.15 \times 10^3$, we consider the values of $\Gamma = 1200$ (left panel) and $\Gamma = 3000$ (right panel).

When we consider $\Gamma = 1200$, the break energies behave as $E^{syn}_{\gamma,\mathrm{m,f}} < E^{syn}_{\gamma,\mathrm{c,f}}$ ($E^{syn}_{\gamma,\mathrm{c,f}} < E^{syn}_{\gamma,\mathrm{m,f}}$ and $E^{ssc}_{\gamma,\mathrm{m,r}} < E^{ssc}_{\gamma,\mathrm{c,r}}$ ($E^{ssc}_{\gamma,\mathrm{c,r}} < E^{ssc}_{\gamma,\mathrm{m,r}}$) for $\epsilon_{B,f/r} \sim 10^{-5}$ ($\epsilon_{B,f/r} > 0.5$) and when $\Gamma = 3000$ is assumed, a shift of parameter ($\epsilon_{B,f/r} > 0.01$) is obtained for the break energies $E^{syn}_{\gamma,\mathrm{c,f}} < E^{syn}_{\gamma,\mathrm{m,f}}$ and $E^{ssc}_{\gamma,\mathrm{c,r}} < E^{ssc}_{\gamma,\mathrm{m,r}}$. Therefore, for small values of ϵ_B, the synchrotron and SSC emissions are at slow-cooling regime whereas for large values of ϵ_B both emissions are at fast-cooling regime. Also when the bulk Lorentz factor increases (from $\Gamma = 1200$ to $\Gamma = 3000$) the characteristic break energies change (from $E^{ssc}_{\gamma,\mathrm{m,r}} < E^{syn}_{\gamma,\mathrm{m,r}}$ to $E^{ssc}_{\gamma,\mathrm{m,r}} > E^{syn}_{\gamma,\mathrm{m,r}}$) for any value of ϵ_B.

Using the method of Chi-square χ^2 minimization as implemented in the ROOT software package (Brun & Rademakers 1987), we obtain the values of parameters $\epsilon_{B,f(r)}$ and ϵ_e that could describe the temporally extended flux superposed with the short-lasting bright peak at the LAT energy range, considering a typical LAT flux density (from $\sim 10^{-6}$ to $\sim 10^{-5}\,\mathrm{erg\,cm^{-2}\,s^{-1}}$ at 100 MeV) and a spectral index of electron distribution $p = 2.4$ reported in most of the bursts detected by Fermi-LAT (Ackermann et al. 2010, 2011, 2013). The temporally extended flux is explained by synchrotron radiation from forward shock and the short-lasting bright peak with SSC emission from the reverse shock.

We can see that the difference between the synchrotron and SSC spectral breaks achieved in forward and reverse shocks, respectively, are explained through the energy distribution given to magnetic field. Comparing the magnetic equipartition parameters that best describe the emission at forward and reverse shocks, we can see that magnetic fields in both shocks are related by $B_f \simeq 10^{-1} B_r$. The previous result suggests that the magnetic field in the reverse-shock region is stronger (~ 10 times) than in the forward-shock region, indicating that the ejecta is magnetized and hence, the magnetic field amplification during the merger of NS - NS.
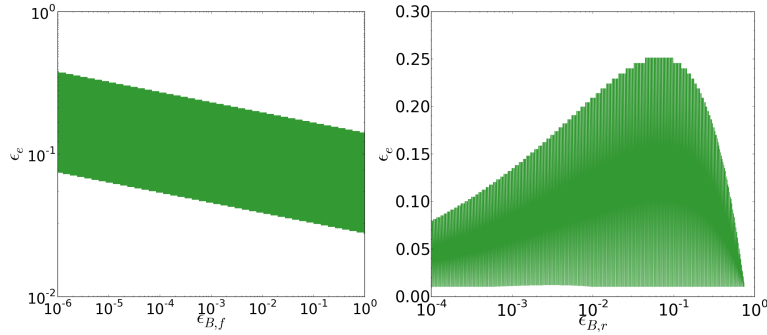
Figure 2. Left: Values of equipartition parameters (ϵ_e and $\epsilon_{B,f}$) that explain the temporarily extended LAT flux through synchrotron radiation from the forward shock. Right: Values of ϵ_e and $\epsilon_{B,r}$ that describe the short-peak bright LAT peak through SSC emission from reverse shock.

References

Ackermann, M. et al., 2010, ApJ, 716, 1178

Ackermann, M. et al., 2011, ApJ, 729, 114

Ackermann, M. et al., 2013, ApJ, 763, 71

Ackermann, M. et al., 2014, Science, 343, 42

Berger, E., 2014, ARA&A, 52, 43

Brun, R. & Rademakers, F. 1997, Nuc. Instr. and Met. in Phys. Res.A, 389, 81

Eichler, D., Livio, M., Piran, T., & Schramm, D. N. 1989, Nature, 340, 126

Fan, Y. Z., Wei, D. M., & Wang, C. F. 2004, A&A, 424, 477

Fraija, N., M. M. Gonzalez & Lee, W. 2012, ApJ, 751, 33

Fraija, N. 2015, ApJ, 804, 105

Fraija, N., Lee, W. & Veres, P. 2016a, ApJ, 818, 190

Fraija, N., Lee, W., Veres, P. & Barniol Duran R. 2016b, ApJ, 831, 1

Giacomazzo, B., Rezzolla, L., & Baiotti, L. 2009, MNRAS, 399, L164

Kobayashi, S. 2000, ApJ, 545, 807

Kobayashi, S., Mészáros, P., & Zhang, B. 2004, ApJ, 601, L13

Lee, W. H., Ramirez-Ruiz, E., & Page, D. 2004, ApJ, 608, L5

Lee, W. H., Ramirez-Ruiz, E., & Page, D. 2005b, ApJ, 632, 421

Panaitescu, A. 2007, MNRAS, 379, 331

Price, D. J., & Rosswog, S. 2006, Science, 312, 719

Santana, R., Barniol Duran, R., & Kumar, P. 2014, ApJ, 785, 29

Sari, R., Piran, T. & Narayan, R. 1998, ApJ, 497, 17

Sari, R. & Esin, A. 2001, ApJ, 548, 787

Uhm, Z. L., & Beloborodov, A. M. 2007, ApJ, 665, L93

Zhang, B., & Kobayashi, S. 2005, ApJ, 628, 315

Non-linear variability in microquasars in relation with the winds from their accretion disks

A. Janiuk[1], M. Grzedzielski[1], P. Sukova[1], F. Capitanio[2], S. Bianchi[3],
W. Kowalski[1]

[1]*Center for Theoretical Physics, Polish Academy of Sciences, Al.
Lotnikow 32/46, 02-668 Warsaw, Poland*
[2]*INAF-Instituto di Astrofisica e Planetologia Spaziali, via del Fosso del
Cavaliere 100, 00133 Rome, Italy*
[3]*Dipartimento di Matematica e Fisica, Università degli Studi Roma Tre,
via della Vasca Navale 84, 00146 Roma, Italy*

Abstract.

The microquasar IGR J17091-3624, which is the recently discovered
analogue of the well known source GRS 1915+105, exhibits quasi-periodic
outbursts, with a period of 5-70 seconds, and regular amplitudes, referred
to as "heartbeat state". We argue that these states are plausibly explained
by accretion disk instability, driven by the dominant radiation pressure.
Using our GLobal Accretion DIsk Simulation hydrodynamical code, we
model these outbursts quantitatively. We also find a correlation between
the presence of massive outflows launched from the accretion disk and the
stabilization of its oscillations. We verify the theoretical predictions with
the available timing and spectral observations. Furthermore, we postu-
late that the underlying non-linear differential equations that govern the
evolution of an accretion disk are responsible for the variability pattern
of several other microquasars, including XTE J1550-564, GX 339-4, and
GRO J1655-40. This is based on the signatures of deterministic chaos
in the observed lightcurves of these sources, which we found using the
recurrence analysis method. We discuss these results in the frame of the
accretion disk instability model.

1. Introduction

In black hole accretion disks, two main types of thermal-viscous instabilities may
arise: (i) the radiation pressure instability and (ii) the partial hydrogen ioniza-
tion instability. They can lead to (i) the short term limit-cycle oscillations in
black hole X-ray binaries (from tens to hundreds of seconds), to the intermittent
activity of quasars (timescales from tens to thousands of years), or (ii) to the
X-ray novae eruptions (timescales from months to years), and to the long-term
activity cycles in AGN (timescales about millions of years), respectively. Both
these types of instabilities are known in theoretical astrophysics for about 40
years (Lightman & Eardley 1974, Smak 1984). In both cases, the variability
and cyclic outbursts of the accretion disk are governed by the nonlinear equa-
tions of hydrodynamics. However, as long as for the partial hydrogen ionization
instability the observations of Dwarf Novae systems have already confirmed the

theoretical predictions in many ways, the radiation pressure instability occurrence has been the subject of extensive debate. In particular, the only certain candidate for this instability being in action in the case of Galactic microquasars is the source GRS 1915+105. Nevertheless, there are many other systems, in which the mean accretion rate is high enough (i.e., more than about 10% of Eddington rate) to allow for the occurrence of the hot, radiation pressure dominated regions in the innermost accretion flow. Consequently, the non-linear variability of the observed flux at short timescales should be observed also in other sources.

It has been shown that the accretion disk can be stabilized partially or completely against these instabilities by several mechanisms. First, the very strong jet or wind outflow can reduce the amplitudes of oscillations and outbursts (Janiuk & Czerny 2011). Also, a modified heating prescription, in which the viscous stress tensor scales not with the total pressure, but with a geometrical mean of the gas and total pressures, is an obvious stabilizer (Czerny et al. 2009). In eccentric binaries, the influence of a companion star may lead to the decrease of a mean accretion rate and hence stabilize the disk at some parts of the binary orbit (Kunert-Bajraszewska & Janiuk 2011). Finally, the stochastic viscous fluctuations can be a viable mechanism to stabilize the cyclic variability of the accretion disk (Janiuk & Misra 2012). Here we neglect the three latter possibilities, and we study the accretion disk, influenced by the radiation pressure, while some part of the locally dissipated energy flux is used to eject a wind from the disk's surface. We show that the competing roles of the instability and wind outflow lead to the long-term trend, in which the heartbeat oscillations of the X-ray luminosity are weaker, or cease completely, when the wind is strong.

2. Accretion disk model

We use our own numerical code GLADIS (GLobal Accretion Disk InStability) which simulates the behavior of an accretion disk in the frame of a 1,5-dimensional hydrodynamics (Janiuk et al. 2002). We assume a geometrically thin, Keplerian α-disk under the pseudo-Newtonian Paczynski-Wiita potential. The structure of the disk is solved according to the continuity and energy equations, in the latter the viscous heating is balanced by radiative and advective cooling. For a given mean accretion rate (i.e., the mass accreted from the companion star in an X-ray binary, which is a parameter in our model), some part of the disk is dominated by radiation pressure. Hence, the local accretion rate, density, temperature, and disk thickness, oscillate. This behavior is shown in quantitative way in Figure 1.

Also, some fraction of energy that is locally dissipated and transferred vertically to the disk surface, is used to eject the wind, when the local disk luminosity instantaneously approaches the Eddington limit. In particular, we adopt a simple mathematical prescription for $f_{\mathrm{out}} = 1 - 1/(1 + A\dot{m}^2)$, with $\dot{m}(r,t) = L/L_{\mathrm{Edd}}$ (Nayakshin et al. 2000). We are then able to compute the mass loss rate from the disk, as equal to the ratio of the locally generated energy flux, to the energy change per particle, which is given by the virial energy. The total mass loss, $\dot{M}_{\mathrm{w}}$, is the one integrated over the disk surface, between some radius R_{min} and size of the disk R_{max} (see Janiuk et al. 2015, for further details).
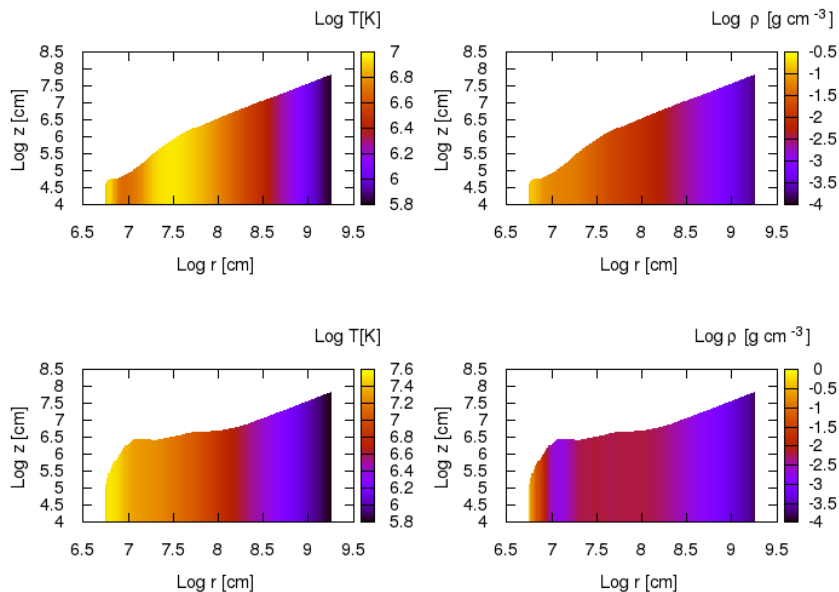
Figure 1.   Profiles of the temperature (left) and density (right) of the disk between the outbursts (top row) and at its outbursts maximum (bottom row). Colors present the quantities in a log-scale, in the r-z plane. Parameters of the simulation: mass of black hole 6 $M_\odot$, accretion rate 0.1 Eddington, viscosity $\alpha = 0.1$. Also, a wind, with dimensionless strength coefficient $A = 15$, was assumed.
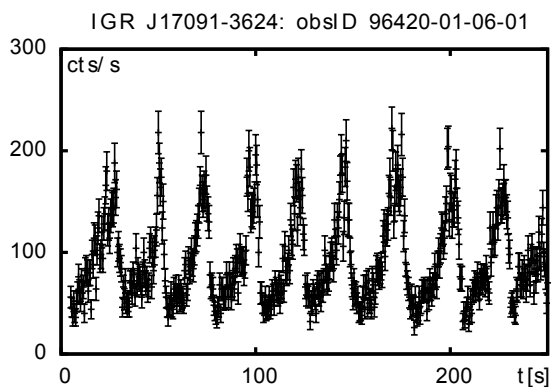
Figure 2.   X-ray lightcurve of the microquasar IGR J17091-3624 in its heartbeat state, taken from the PCA RXTE observations from April 4, 2011. Data in the 2-10 keV energy band, were extracted from the event files with time resolution of 0.5 s.

3.   Observations

3.1.   Case study of IGR J17091-3624. Variability and wind

The outburst of the microquasar IGR J17091-3624 observed in 2011 was one of its brightest (Capitanio et al. 2012). According to Altamirano et al (2011), in this source, in comparison to GRS 1915+105, two clear differences occur: (i) the time scales can be different (IGR J17091-3624 tends to be faster), and (ii) the average count rate (or flux) of the source can be much higher (factor 10-50) in GRS 1915+105. If the period of the oscillations is proportional to some power of the mass of the compact object then the black hole in IGR J17091-3624 could be a factor of a few less massive than the $14 \pm 4.4 M_\odot$ of GRS 1915+105. In our modeling, we assume the black hole mass to be 6 Solar masses.

In Figure 2, we show an X-ray lightcurve of this source, which is representative for the heartbeat oscillation. The amplitude of these flares is well modeled with our instability code, provided that we incorporate a moderate wind with its 'strength' parameter on the order of $A = 15$. The mass loss rate computed from such model is consistent with the upper limit, derived from the *Chandra* observations (see Janiuk et al. 2015 for details). In the non-heartbeat state, the wind is required by the model fitting in the *Chandra* spectra, which allowed us to constrain the winds velocity v, its ionization parameter ξ and filling factor f. In Table 1, we summarize these results, together with the mass loss rate and the radial extension of the wind launching zone, derived from our numerical model. In the non-heartbeat state, the wind strength parameter A has to be much larger, so that it suppresses the oscillations of the disk completely.

Table 1.   Wind parameters. Observations vs. model in the 'heartbeat' (HB) and 'non-heartbeat' (NHB) states in the microquasar IGR J17091-3624. Two wind components, w1 and w2, were detected in the NHB *Chandra* data (see Janiuk et al. 2015 for details). Notes: $\dot{M}_{\mathrm{w},16} = \dot{M}_\mathrm{w}/10^{16}\,\mathrm{g\,s^{-1}}$, $n_{15} = n/10^{15}\,\mathrm{cm^{-3}}$, $v_3 = v/10^3\,\mathrm{km\,s^{-1}}$.

State	Wind	Observations				Model			
		v_3	$\log \xi$	n_{15}	f 10^{-3}	$\dot{M}_{\mathrm{w},16}$	R_min $[R_\mathrm{g}]$	R_max $[R_\mathrm{g}]$	A
NHB	w1	9.7±0.8	3.4 ± 0.3	5.1	1.5	27	950	4200	300
	w2	15.7±0.6	3.8 ± 0.2	13	3.7	42	380	4700	300
HB	w1	-	-	≤ 0.5	-	2.5	950	4900	15
	w2	-	-	≤ 1	-	3.9	380	5900	15

3.2.   Other X-ray binaries. Non-linear variability

For the X-ray sources other than the two above-mentioned microquasars, no detailed analysis was performed before, with respect to their possible non-linear variability induced by the thermal-viscous instability in the accretion flow. As proposed by Janiuk & Czerny (2011), at least eight of the known black hole binaries have their accretion rates high enough for their disks to be unstable. In the recent work by Sukova et al. (2016), we studied several of these sources. We analyzed quantitatively their observed lightcurves, in order to find the traces of deterministic chaos type of behavior. If found, it indicates that the non-
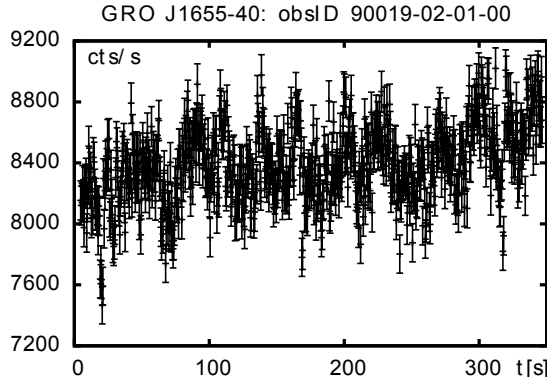
Figure 3.   X-ray lightcurve of the microquasar GRO J1655-40 in its outburst from 2005. The source's spectral state was classified as Soft-Intermediate, according to Miller et al. (2008). The data in the energy range 2-10 keV, from PCA/RXTE, taken on March 13, 2005, were extracted in Std1 mode, with time resolution of 0.5 s.

linear hydrodynamical process is acting behind the observed variability, and is governed by a finite set of differential equations. Therefore, the global behavior of the accretion flow, rather than some stochastic processes, is responsible for the shape of the observed lightcurves. We suggest that the disk instability is operating also in the accretion flow (possibly affected by the presence of a non-thermal corona above the disk), even if the regular 'heartbeat' flares are not directly visible in the lightcurves.

An exemplary lightcurve of GRO J1655-40, one of the sources which we studied in our sample, is shown in Figure 3. In this case, our method, based on the recurrence analysis, gave a significant result for deterministic chaos type of behavior. Basic object of the method is the recurrence matrix, defined as

$$\mathbf{R}_{i,j}(\epsilon) = \Theta(\epsilon - \parallel \vec{x}_i - \vec{x}_j \parallel), \qquad i,j = 1, ..., N, \tag{1}$$

where $\vec{x}_i = \vec{x}(t_i)$ are (N) points of the reconstructed trajectory, Θ is the Heaviside step function, and ϵ is a threshold parameter. It can be visualized in the recurrence plot (for details, see Sukova et al. 2016). We compared the results between real and surrogate data (the latter have the same power spectra, but variability is stochastic). The significance of chaos is defined as a weighted difference between the logarithm of the second order Renyi's entropy of the data series and its surrogates sample. Our method was tested with simulated trajectories of complicated non-linear systems, i.e., motion of the test particle in the field of a black hole, given by Einstein equations (see article Sukova & Janiuk, in these proceedings). Its chaotic orbit shows high significance of non-linear dynamics (Semerak & Sukova 2012). Highly significant results were obtained also for the microquasars XTE J550-564, and GX 339-4. The non-linear behavior of the lightcurve during some of the observations gives the evidence, that the accretion flow in these sources is governed by a low number of non-linear equations. A possible explanation is that the accretion disc is prone to the thermal-viscous instability and the induced limit-cycle oscillations.

4.   General picture and conclusions

IGR J17091-3624 is another microquasar, after GRS 1915+105, that in some states exhibits the limit-cycle oscillations of its X-ray luminosity. These oscillations are plausibly explained by the intrinsic thermal-viscous instability of the accretion disk, induced by the radiation pressure. The fast, ionized wind ejected from the accretion disk on the cost of a fraction of dissipated energy is a viable mechanism to completely stabilize the disk in other states, or to govern the moderate amplitude of the disk oscillations.

In other black hole X-ray binaries, i.e. GRO J1655-40, XTE J1550-564, and GX 339-4, the hints of a non-linear variability were also found, using the novel method, which adapts the recurrence analysis for the study of a deterministic chaos process. We applied this analysis to observations of six black hole X-ray binaries observed by the RXTE satellite, in their soft and intermediate states. We also tested this method on the sample of observations of the microquasar IGR J17091-3624, in its various spectral states defined as in Pahari et al. (2014). Significant results for the "heartbeat" state were obtained, which confirmed our previous findings for this source.

We suggest a possible geometrical configuration of the accretion flow in IGR J17091-3624, and possibly other microquasars where an ionized wind is detected (e.g. GRO J1655-40). The radiation pressure dominated accretion disk is stabilized by a quasi-static corona in its inner parts, and by an unbound wind ejected at its outer radii. The wind (possibly with multiple components), may be partially collimated and be narrower in the part where the spectral features are produced.

References

Altamirano D., et al., 2011, ApJ, 742, L17

Capitanio F., Del Santo M., Bozzo E., et al, 2012, MNRAS, 422, 3130

Czerny B., et al. 2009, ApJ, 698, 840

Janiuk, A., Czerny B., Siemiginowska A., 2002, ApJ, 576, 908

Janiuk A. & Czerny B., 2011, MNRAS, 414, 2186

Janiuk A. & Misra R., 2012, A&A, 540, A114

Janiuk A., Grzedzielski M., Capitanio F., Bianchi S., 2015, A&A, 574, 92

Kunert-Bajraszewska M. & Janiuk A., 2011, ApJ, 736, 125

Lightman A.P., Eardley D.M., 1974, ApJL, 187, 1

Miller J.M., Raymond J., Reynolds C.S., 2008, ApJ, 680, 1359

Nayakshin S., Rappaport S., Melia F., 2000, ApJ, 535, 798

Pahari M., Yadav J. S., Bhattacharyya S.. 2014, ApJ, 783, 141

Semerak O. & Sukova P., 2012, MNRAS, 425, 2455

Smak J., 1984, Acta Astron., 34, 161

Sukova et al., 2016, A&A, 586, 143

3D variable GRB jets and their photospheric light curve

D. López-Cámara[1], D. Lazzati[2] and B. J. Morsony[3]

[1] *Instituto de Astronomía, Universidad Nacional Autónoma de México,*
Apdo. Postal 70-264, Cd. Universitaria, México DF 04510, México
[2] *Department of Physics, Oregon State University, 301 Weniger Hall,*
Corvallis, OR 97331, USA
[3] *Department of Astronomy, University of Maryland, 4296 Stadium*
Drive, College Park, MD 20742-2421, USA

Abstract. The bursting and quiescent activity observed in many GRB remains to be fully understood, thus is significant to study the effects that a pulsed central engine has on the prompt GRB emission variability with numerical simulations. In this study, for the first time ever, numerous models of a variable jet drilling through the stellar envelope and then through the ISM is followed using 3D numerical simulations. Since there is a correlation between the variability and the observed peak isotropic luminosity, we calculate the light curve for each model and discuss how the variability in the central engine affects the photospheric emission. Finally, we also deliberate how our results compare with observations from Swift and other instruments.

1. Introduction

No GRB is the same as any other. All GRB presents temporal variability (Walker et al. 2000), some GRBs present pulses separated by quiescent time intervals lasting from fractions of a second to several tens of seconds (Ramirez-Ruiz & Fenimore 2000, Ramirez- Ruiz & Merloni 2001). The variability is believed to be due to internal shocks (Sari & Piran 1997), while the quiescent epochs can be explained by dormant periods of the inner engine (Drago & Pagliara 2007) or even an indication of a complete turn-off of the central motor (Ramirez-Ruiz et al. 2001). Also, a significant fraction of the long GRBs ($\sim$85%) seems to be the result of several pulses (Borgonovo et al. 2007). The pulsed behavior and quiescent periods observed in the GRBs light curve remain to be fully understood.

Nakar & Piran (2002) (NP02) analyzed the GRB dataset from the BATSE 4B catalogue, specifically the temporal behavior of the 68 brightest long GRBs. The total number of pulses and dormant epochs in these bright bursts was in total 1330 and 1262 (respectively). NP02 find that the pulses follow a lognormal distribution while the intervals does not and conclude that the pulses and quiescent epochs come from different mechanisms. Whether the pulses and dormant periods can be due to the same mechanism or not remains to be fully studied. Thus, we performed a series of two- and three-dimensional simulations where a variable relativistic jet emerging from the interior of its correspondent progenitor star, evolves through the interstellar medium (ISM) until it reaches at a far away position ($\sim$10^{12}cm) where its light curve is calculated. From the total of

the pulses and dormant periods a synthetic dataset was built and compared with real data from GRB observations. We find that both the pulsed behavior and quiescent epochs can be produced by the same mechanism.

2. Initial setup and numerical models

A series of three- and two- dimensional (3D and 2D respectively) simulations, with a temporally variable jet (set at the inner boundary) were performed. In each, the variable jet drilled through a pre-SN progenitor (model 16TI from Woosley & Heger 2006) and then through the ISM where the photospheric luminosity was calculated (at $y=2.2\times10^{11}$cm). The 3D numerical setup was very similar to that from López-Cámara et al. (2013) except for the jet which had equal active and dormant epochs (Δ=0.1s, 0.5s, 1s, 2s). In order to be able to compare with the observations we performed a set of 2D simulations. The characteristics of the 3D and 2D models are shown in Table 1.

Table 1.   Model characteristics

Model	Dimension	Δ(s)	t_{max}(s)	t_{bo}(s)
m0.1	3D (2D)	0.1	17.40 (50.00)	5.02 (5.60)
m0.5	3D (2D)	0.5	15.20 (50.00)	7.80 (10.07)
m1.0	3D (2D)	1.0	17.13 (50.00)	6.73 (11.93)
m2.0	3D (2D)	2.0	13.33 (50.00)	6.80 (12.34)
mon	3D	always on	7.80	5.27
mrand*	2D	random	50.00	-

*Note: 20 models

The numerical domain covered the top half of the pre-SN progenitor star as well as the ISM it is immersed in. The boundaries were set at 1×10^{9} cm and 2.56×10^{12} cm along the polar axis and $\pm6.4\times10^{11}$ cm in the equatorial plane (XZ-axis). The finest resolution was 7.81×10^{6} cm, comparable to the resolution of previous 3D GRB-jet studies (López-Cámara et al. 2013, Wang et al. 2008), and 2D GRB-jet studies (Morsony et al 2010, Lazzati et al. 2013a).

3. Results and Discussion

The evolution of the 3D model with Δ=0.5s is shown in the left panel of Figure 3 (density stratification maps). The break out time (t_{bo} for it is 7.8s and whose the global morphology that all the 3D variable jet models had. The pulsed behavior in is distinguishable as density jumps in the jet and the active regions (pulses) have lower densities ($\rho=10^{-6}$ g cm^{-3}) than the dormant periods ($\rho=10^{-4}$ g cm^{-3}). In the right panel of Figure 3 the Lorentz factor (Γ) contours overlapped with the density stratification maps of the XY plane for the variable 3D models is shown. All the 3D models evolve mildly relativistically inside the progenitor ($\Gamma \sim 1$), break out of the progenitor, and evolve relativistically through the ISM ($\Gamma \sim 50$) before the cocoon surpasses the numerical domain. The break out times (t_{bo}, shown in table 1) are consistent with the both previous 3D numerical studies (López-Cámara et al. 2003, Wang et al. 2008), 2D
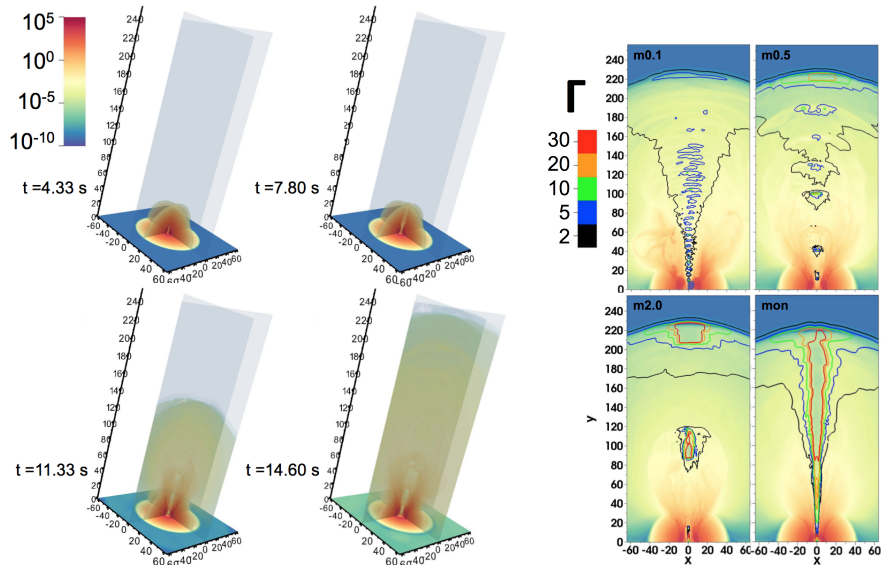
Figure 1. *Left:* Density stratification maps (g cm^{-3}) for model m0.5 at different time frames. The axis are scaled to 10^{10} cm. *Right:* Lorentz factor contours overlapped with the density stratification maps (same density stratification map as for the left panel). Adapted from López-Cámara et al. (2016).

numerical studies (Zhang et al. 2003, Zhang et al. 2004, Morsony et al 2010, Lazzati et al. 2013a, Nagakura et al. 2011, Mizuta & Ioka 2013), and with the analytic model of Bromberg et al. (2011). Moving along the ISM the pulsed behavior in also distinguishable as high-Lorentz ($\Gamma{>}5$) versus the low-Lorentz ($\Gamma{<}5$) of the dormant periods. ns (pulses) have lower densities ($\rho{=}10^{-6}$ g cm^{-3}) than the dormant periods ($\rho{=}10^{-4}$ g cm^{-3}).

Analyzing the active regions from the Lorentz contour maps, m0.1 having regions with values of the pulses average Lorentz larger than $\Gamma{>}2$ while m2.0 had $\Gamma{>}30$, there seems to be a correlation between tΔ and the average obtained value of Γ. To verify the latter, in the top panel from Figure 3, we show the pulses average Γ value along the polar axis once the jet has reached y$_{obs}{=}2{\times}10^{11}$ cm for all the 3D models (including a one $\pm\sigma$ error bar). Clearly there is a correlation between the duration of the pulses and Γ values. Also, we calculated the average FWHM duration for all the pulses, see the bottom panel of Figure 3. As for Γ, there is a correlation between the value of the average FWHM and Δ.

In order to compare the results from the numerical simulations with real data from GRB observations, we need to create a synthetic dataset from the numerical models. Unfortunately constructing such a large dataset from 3D simulations is out of the computational possibilities. Thus we performed two extra sets of 2D simulations, the first set to compare how the global morphology compared with that from the 3D models, and the second set to build the synthetic dataset. The 2D simulations were run with the same initial conditions, boundary
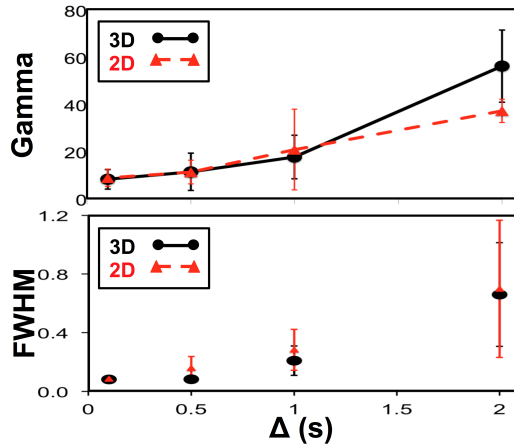
Figure 2. Upper panel: Average Lorentz factor ($\pm 1\sigma$ error bars) for the 3D and the 2D models with non random Δ. Bottom panel: Average FWHM ($\pm 1\sigma$ error bars) for the 3D and the 2D models with non random Δ. Adapted from López-Cámara et al. (2016).

conditions, as that from the XY slice of the 3D models (see Table 1 for more details). In order to compare with the 3D models, the first set of simulations had the same Δ values as those used in the 3D runs. Not only did the 2D simulations have comparable t_{bo} (the 3D models propagate slightly faster through the stellar progenitor), have the same Γ behavior inside and outside the progenitor, and show a very similar correlation between Δ and Γ (within $\pm 1\sigma$ of each other), and Δ and the FWHM (also within $\pm 1\sigma$, see Figure 3). To further view the latter, in the left panel of Figure 3, we show the photospheric light curve (LC) of the 3D and 2D models from which the FWHM were obtained and see that they resemble very much. In both 3D and 2D models, mostly due to turbulence, the pulses FWHM are shorter and the quiescent epochs are longer than the input temporal Δt distribution (though in the 3D models it is more evident). The right panel of Figure 3, shows how very similar the Schlieren maps (which maps the turbulence) for the case when $\Delta=0.5$s for both 2D and 3D models. Thus, the 2D models reproduce the global morphology and we can continue to build the 2D synthetic dataset in order to compare our variable jet models with the observations.

Nakar & Piran (2002) (NP02) analyzed the temporal behavior of the 68 brightest long GRBs from the BATSE 4B catalogue and found that the active periods follow a lognormal distribution while the dormant periods do not. In order to create a synthetic data from variable GRBs and compare with the dataset from NP02 we ran a second set of 2D simulations, twenty 2D variable jet simulations each one with random pulse and dormant epoch durations. In total we had 240 pulses and 246 quiescent epochs (NP02 had 1330 pulses and 1262 quiescent intervals). The normalized histogram of the Δ distribution of the pulses and quiescent epochs is shown in Figure 3. It can be seen that both the initial active and dormant epoch distribution fraction are similar ($\sim$0.2-0.3) and
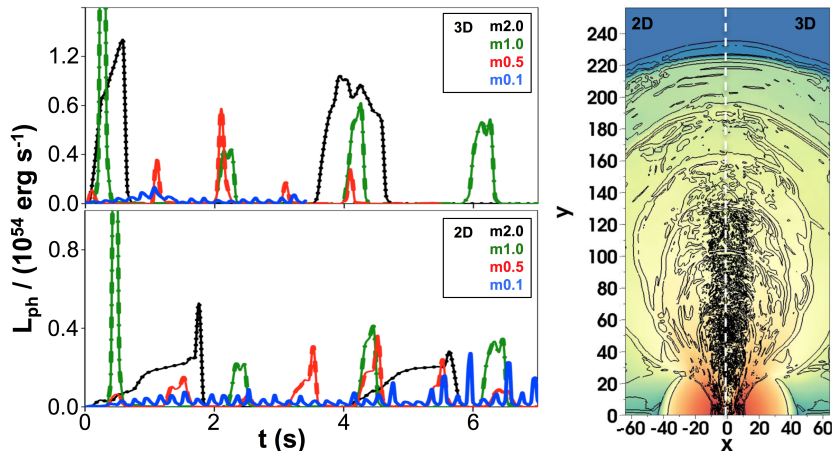
Figure 3. *Left:* Photospheric light curves of the 3D and 2D variable jet models. Adapted from López-Cámara et al. (2016). *Right:* Schlieren map of a 3D GRB jet once it has broken out of the progenitor.

range between Δ=0-4s. As was already discussed, the pulses FWHM broaden while the dormants periods grow. Hence, a large fraction of the pulses have shorter timescales while the dormant periods broaden in comparison with the input distribution for both cases. The pulses output distribution have a spike at Δ<2s, while the quiescent intervals reach values that range as large as Δ=4s-8s.

4. Conclusions

In this study, for the first time ever, numerous 3D models of a variable jet drilling through the stellar envelope and then through the ISM are followed. We find that the variable 3D jet models break out of the progenitor, that the active periods are low density - high Lorentz compared to the dormant periods which show higher density - lower Lorentz values.

We find that, independently of 2D or 3D, there is a correlation between the average Lorentz factor of the pulses, as well as the FWHM, and the duration of the pulses. Except for the fact that in the 3D models the pulses duration observed far from the progenitor broaden while the dormant periods last longer, we find that the 2D models resemble the global morphology of the 3D models. We calculate the photospheric light curves and discuss how the variability in the central engine affects the photospheric emission.

We find room for having different distributions for the pulses and dormant intervals produced by the same mechanism. This difference is a consequence of the variable jet drilling through a very massive stellar envelope.
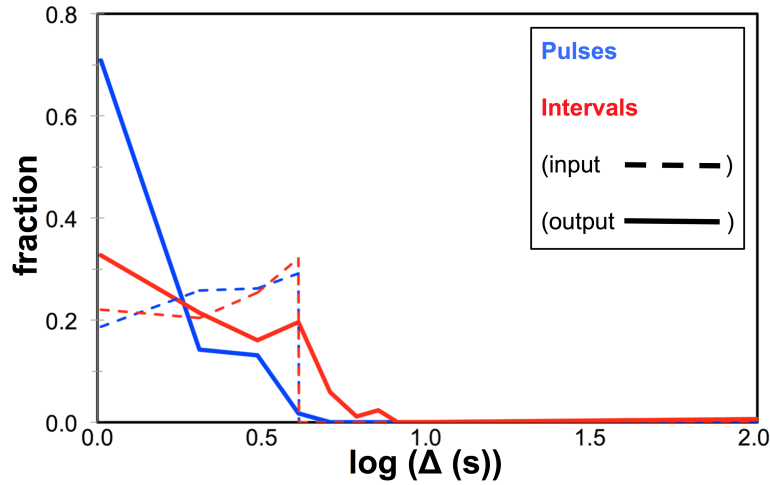
Figure 4.   Histogram of the pulse (blue) and dormant intervals (red) distribution (initial distribution is shown with dashed lines, and the final distribution as solid lines).

References

Borgonovo, L., et al. 2007, A&A, 465, 765

Bromberg, O., et. al. 2011, ApJ, 740, 100

Drago, A., & Pagliara, G. 2007, ApJ, 665, 1227

Lazzati, D., et al. 2013, ApJ, 765, 103

López-Cámara, D., et al. 2013, ApJ, 767, 19

López-Cámara, D., et al. 2016, ApJ, 826, 180

Morsony, B. J., et. al. 2010, ApJ, 723, 267

Mizuta, A., & Ioka, K. 2013, ApJ, 777, 162

Nagakura, H., et. al. 2011, ApJ, 731, 80

Nakar E., & Piran T. 2002, MNRAS, 331, 40

Ramirez-Ruiz E., Fenimore E. E., 2000, ApJ, 539, 712

Ramirez-Ruiz, E., & Merloni, A. 2001, MNRAS, 320, L25

Ramirez-Ruiz E., et. al. 2001, MNRAS, 324, 1147

Sari, R., & Piran, T. 1997, MNRAS, 287, 110

Walker, K. C., et. al. 2000, ApJ, 537, 264

Wang, P., et. al. 2008, ApJS, 176, 467

Woosley S. E., & Heger A. 2006, ApJ, 637, 914

Zhang, W., et al. 2003, ApJ, 586, 356

Zhang, W., et al. 2004, ApJ, 608, 365

Physical properties of the gamma-ray binary LS 5039 through low and high frequency radio observations

B. Marcote[1,2], M. Ribó[1†], J.M. Paredes[1] and C.H. Ishwara-Chandra[3]

[1]*Departament d'Astronomia i Meteorologia, Institut de Ciències del Cosmos, Universitat de Barcelona, IEEC-UB, Barcelona, Spain*
[2]*Joint Institute for VLBI ERIC, The Netherlands*
[3]*National Centre for Radio Astrophyisics, TIFR, Pune, India*
[†] *Serra Húnter Fellow*

Abstract. LS 5039 is a gamma-ray binary displaying synchrotron emission at GHz radio frequencies with a small variability and without signatures of being orbitally modulated. A detailed study in the 0.15–15 GHz range has been carried out by analyzing VLA, GMRT and WSRT observations, obtaining an average spectrum and two quasi-simultaneous spectra. We have observed a persistent radio emission on day, week and year timescales, with a variability below 25% and with no signatures of orbital modulation at all frequencies except at 150 MHz, where the source remains undetected. The spectra reveal a power-law emission at high frequencies ($\gtrsim 1$ GHz) and a turnover at about 0.5 GHz. We explain these spectra with a simple model of one-zone synchrotron emitting region. Synchrotron self-absorption and Razin effect explain the absorption at low frequencies ($\lesssim 1$ GHz). With this model we have obtained an estimate of the physical properties of the radio emitting region of LS 5039, and derived a high mixing of the stellar wind within the relativistic plasma of the radio outflow.

1. Introduction

Gamma-ray binaries are binary systems composed of a young massive star and a compact object that display a Spectral Energy Distribution dominated by the MeV-GeV photons (Dubus 2013). Only five gamma-ray binaries have been discovered up to now. LS 5039 is one of these sources, and is composed of an O6.5 V star and a compact object with a mass of 1–5 $M_\odot$ orbiting it every 3.9 d (Casares et al. 2005). The light-curves of LS 5039 from X-rays to TeV are orbitally modulated. However, at radio frequencies we do not observe any evidence of orbital modulation. The GHz radio emission is non-thermal and persistent with a variability below 30%, which is much smaller than the one observed in any other gamma-ray binary (Martí et al. 1998, Ribó et al. 1999, Clark et al. 2001). At low

frequencies ($\lesssim 1$ GHz) only a few observations have been published up to now. On the one hand, Pandey et al. (2007) reported a power-law spectrum with a negative spectral index of $\alpha \approx -0.8$ between 235 and 610 MHz (with α defined as $S_\nu \propto \nu^\alpha$, where S_ν is the flux density). On the other hand, Godambe et al. (2008) and Bhattacharyya et al. (2012) reported the presence of a turnover at ~ 1 GHz.

This discrepancy would require a much larger variability at low than at high frequencies ($\gtrsim 1$ GHz), which is surprising. To perform a detailed study of the source at low and high frequencies we decided to reduce and analyze all the available low-frequency data, two high-frequency monitorings and conduct coordinated observations at low and high frequencies.

2.   Radio observations and results

We have analyzed two archival monitorings at 1.4, 5, 8.5, and 15 GHz frequencies with the Very Large Array (VLA), all the available archival data at low frequencies (150, 235 and 610 MHz) from the Giant Metrewave Radio Telescope (GMRT), and we have conducted a coordinated campaign with the GMRT and the Westerbork Synthesis Radio Telescope (WSRT) in 2013 to observe the source simultaneously in the range 0.15–5 GHz. All these data are spread over 15 yr (see a detailed table of all these data in Marcote et al. 2015).

LS 5039 is clearly detected at all frequencies with flux density values between ~ 10 and 50 mJy, except at 150 MHz. At this low frequency the source is undetected up to a 3-σ noise level of 7 mJy. At all frequencies at which the source is detected we observe a persistent emission with a small variability below 25%. This variability is observed on day, week and year timescales, and does not show any signature of being orbitally modulated.

Figure 1 shows the obtained average spectrum considering all the analyzed data. We observe a power-law spectrum at high frequencies and the presence of a turnover at around ~ 0.5 GHz. Figure 2 shows the quasi-simultaneous spectra obtained from the coordinated campaign with the GMRT and WSRT in 2013. these spectra are similar to the average spectrum shown in Figure 1, although there are significant differences between all of them. The spectrum from 2013 July 19 exhibits a stronger emission at all frequencies, and the emission from 610 MHz to 5 GHz can be fit with a pure power-law. However, the spectrum from 2013 July 21 exhibits a curved profile along this frequency range.

3.   Modeling

We have considered a simple model to explain the obtained spectra and to derive the physical properties of the radio emitting region. Moldón et al. (2012) observed LS 5039 at VLBI scales, reporting that most of the emission is produced in a compact unresolved core. This allows us to consider
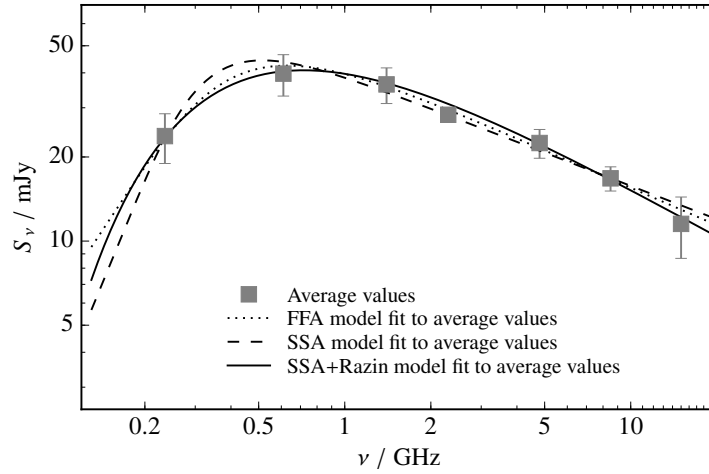
Figure 1.   Average flux density values as a function of the frequency considering all the analyzed data. Error bars represent the standard deviations at each frequency. The obtained spectrum has been fit with three different absorption models: FFA, SSA, and SSA plus Razin effect. Reproduced from Marcote et al. (2015).
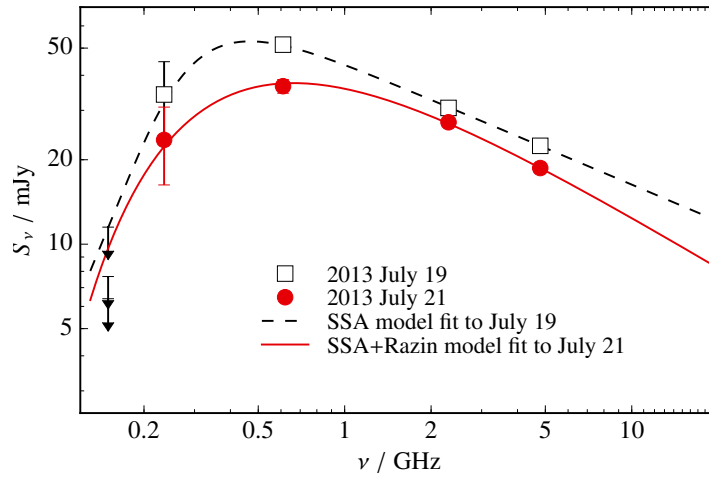
Figure 2.   Quasi-simultaneous spectra of LS 5039 obtained with coordinated GMRT and WSRT observations in 2013. The data at 150 MHz were obtained on 2013 July 18, 20 and 22. The source is not detected at this frequency and the arrows represent the 3-σ upper-limits. The most accurate model fit is shown at each spectrum. Reproduced from Marcote et al. (2015).

as a first approximation a one-zone model for the emitting region. In addition, the absence of orbital modulation in the radio emission of LS 5039 (Marcote et al. 2015, and references therein) implies that the geometry of the region must remain qualitatively similar along the orbit. As a first approximation, we have considered a spherically symmetric emitting region. The high-frequency spectrum of LS 5039 is dominated by synchrotron emission (Paredes et al. 2000), and we have assumed the presence of different absorption mechanisms to explain the low-frequency cutoff: synchrotron self-absorption (SSA), free-free absorption (FFA), and Razin effect, and combinations between them.

Figure 1 shows the average spectrum and the fit models. We observe that either a FFA, SSA or SSA plus Razin effect produce a similar profile that explains the observed spectrum. A model with SSA plus Razin effect produces the most accurate fit (considering statistical analysis over their χ^2 values), although we cannot statistically reject any of the other ones. In the case of the simultaneous spectra, Figure 2 shows the fit models that reproduce the data. Whereas the spectrum on 2013 July 19 can be explained by a pure SSA model, the spectrum on 2013 July 21 requires the presence of the Razin effect. A pure SSA model can not reproduce the low and the high-frequency data simultaneously.

In summary, the three obtained spectra (the average spectrum and the 2013 campaign spectra) can be explained by a simple one-zone model considering a synchrotron self-absorption mechanism. However, the presence of the Razin effect is required in one of the spectra and is favored in another one.

4.   Discussion

The fit models present a coupling between different physical parameters of the radio emitting region. However, we can consider one additional restriction to decouple some of them. The models with SSA produce a lower χ^2 value compared with the models with FFA. Therefore, SSA seems to dominate over FFA. This implies that the emitting region must be optically thin to the FFA. Considering the fit parameters, which contain coupled physical properties, and this restriction to the free-free opacity, we can estimate some of the physical parameters for the radio emitting region.

Figure 3 shows the relationship between these physical parameters. We have considered reasonable values for the radius of the radio emitting region and derived the expected values for the electron density, the magnetic field, and the mass-loss rate. Given that we do not expect significant changes in the emitting region at different orbital phases (an orbital modulation is not observed at radio frequencies), we have considered the three fit models to estimate these physical properties. The presence of the Razin effect, which is produced by the thermal plasma from the stellar wind, can impose limits to the total electron density of the emitting region (see
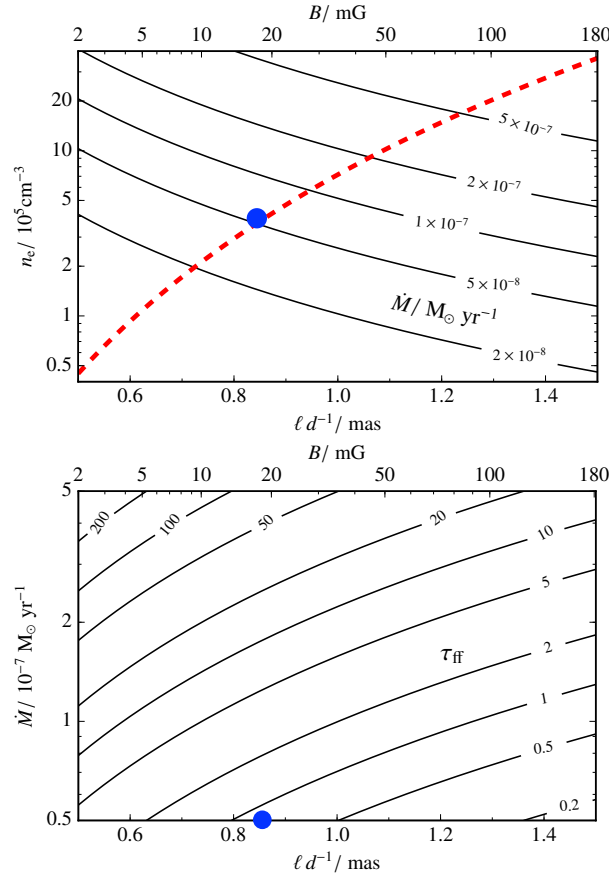
Figure 3. *Top*: electron density, n_{e}, for the non-relativistic plasma as a function of the angular radius of the emitting region, $\ell\,d^{-1}$, and of the magnetic field, B, for different mass-loss rates, $\dot{M}$. The dashed line denotes the electron density values inferred from the fit Razin effect contribution. Only electron density values above this line are realistic. *Bottom:* mass-loss rate as a function of the angular radius and of the magnetic field for different free-free opacities, τ_{ff}. Only values $\tau_{\mathrm{ff}} \lesssim 1$ can be considered according to the obtained fits. The blue marker represents the mean values that produce a coherent picture for the radio emitting region. Reproduced from Marcote et al. (2015).

Figure 3, red dashed line). Simultaneously, a small value for the free-free opacity imposes limits to the mass-loss rates. As a result, we obtain a coherent picture for the radio emitting region assuming an angular radius of ~ 0.85 mas ($\ell \sim 2.5$ AU at 3 kpc), $B \sim 20$ mG, $n_e \sim 4 \times 10^5$ cm^{-3}, and $\dot{M} \sim 5 \times 10^{-8}$ M$_\odot$ (see Marcote et al. 2015 for a full discussion).

The derived total electron density is close to the thermal electron density of the non-relativistic plasma, which implies a mixing close to $\sim 100\%$ of the non-relativistic plasma inside the synchrotron radio emitting relativistic plasma. The derived mass-loss rate is in agreement with recent results obtained by Casares et al. (in prep.), implying that the wind is clumpy. The presence of the Razin effect, reported here for first time in a gamma-ray binary, is typically found in colliding wind binaries, and it could give further support to the scenario of a young non-accreting pulsar given that both scenarios consider the wind interaction between the two components of the system.

References

Bhattacharyya, S., et al., 2012, MNRAS, 421, L1

Casares, J., et al., 2005, MNRAS, 364, 899

Clark J. S., et al., 2001, A&A, 376, 476

Dubus, G., 2013, A&AR, 21, 64

Godambe, S., et al., 2008, MNRAS, 390, L43

Marcote, B., et al., 2015, MNRAS, 451, 4578

Martí, J., Paredes, J. M., Ribó, M., 1998, A&A, 338, L71

Moldón, J., Ribó, M., Paredes, J. M., 2012, A&A, 548, A103

Pandey, M., et al., 2007, A&A, 463, 567

Paredes, J. M., et al., 2000, Science, 288, 2340

Ribó, M., et al., 1999, A&A, 347, 518

Mass-loading of bow shock pulsar wind nebulae

G. Morlino[1], M. Lyutikov[2] and M. Vorster[2]

[1]*INFN – Gran Sasso Science Institute, viale F. Crispi 7, 67100
L'Aquila, Italy*
[2]*Department of Physics, Purdue University, 525 Northwestern Avenue,
West Lafayette, IN 47907-2036, USA*

Abstract. We investigate the dynamics of bow shock nebulae created
by pulsars moving supersonically through a partially ionized interstellar
medium. A fraction of interstellar neutral hydrogen atoms penetrating
into the tail region of a pulsar wind will undergo photo-ionization due
to the UV light emitted by the nebula, with the resulting mass loading
dramatically changing the flow dynamics of the light leptonic pulsar wind.
Using a quasi 1-D hydrodynamic model of relativistic flow we find that
if a relatively small density of neutral hydrogen, as low as 10^{-4} cm^{-3},
penetrate inside the pulsar wind, this is sufficient to strongly affect the
tail flow. Mass loading leads to the fast expansion of the pulsar wind tail,
making the tail flow intrinsically non-stationary. The shapes predicted for
the bow shock nebulae compare well with observations, both in Hα and
X-rays.

1. Introduction

It has been estimated that between 10% and 50% of pulsars are born with kick
velocities $V_{\rm NS} \gtrsim 500$ km s^{-1}. These pulsars will escape from their associated
supernova remnants into the cooler, external interstellar medium (ISM) in less
than 20 kyr (Cordes & Chernoff 1998; Arzoumanian et al. 2002). As this time
scale is sufficiently short, the pulsars are still capable of producing powerful rel-
ativistic winds. Furthermore, comparison with typical sound speeds in the ISM,
$c_{s,\rm ISM} = 10 - 100$ km s^{-1}, shows that the pulsars are moving with highly super-
sonic velocities. The interaction of the pulsar's wind with the ISM produces a
bow shock nebula with an extended tail. If a pulsar is moving through a partially
ionized medium, the bow shock nebula can be detected by the characteristic Hα
emission resulting from the collisional and/or charge-exchange excitation of neu-
tral hydrogen atoms in the post-shock flows and the subsequent emission via
bound-bound transitions (Chevalier et al. 1980). To date, nine such bow shock
nebulae emitting Hα have been discovered, including three around γ-ray pulsars
(Brownsberger & Romani 2014).

Hydrodynamic (and hydromagnetic) models of bow shock nebulae predict
the formation of a smooth two shock structure (Bucciantini 2002) schematically
shown in Fig.1 (left panel): a forward shock in the ISM separated by a contact
discontinuity from a termination shock in the pulsar wind. In the head of the
nebula the contact discontinuity is situated at a distance given by Eq.(1), corre-
sponding to the position where the ram pressure of the ISM balances the pulsar

wind pressure. The flow structure in the head of the nebula is reasonably well understood, especially in the limit of strong shocks (Wilkin 1996).

In contrast to these numerical models, Hα, radio and X-rays observations show that the morphologies of bow shock nebulae are significantly more complicated. More specifically, observations reveal that the tails of bow shock nebulae have a highly irregular morphology: Fig.1 (right panel) shows four such examples. All these nebulae have a characteristic *"head-and-shoulder"* structure, with the smooth bow shock in the head not evolving into a quasi-conical or quasi-cylindrical shape, but instead showing a sudden sideways expansion(s). Arguably the most famous example is the *Guitar nebula* powered by the pulsar PSR B2224+65 (see right panel in Fig.1). As the name suggests, this nebula has a guitar-like shape with a bright head, a faint neck, and a body consisting of several larger bubbles.

These peculiar tail shapes have been interpreted as the result of density variations in the ISM (Romani et al. 1997; Vigelius et al. 2007). However, several observations seem to suggest that the peculiar morphological features could result from the internal dynamics of the pulsar wind, rather than through inhomogeneities in the ISM. First of all, all tails show *similar* morphological variations. Moreover a common characteristic of these bow shock nebulae is that they are all highly symmetric with respect to the direction of motion of the pulsar - this is not expected in general if variations are due to the external medium. Finally, in many cases morphological features in Hα, radio and X-rays are quasi-periodic. It has also been proposed that the morphology of the Guitar nebula could be explained by (unidentified) instabilities in the jet-like flow of pulsar material away from the bow shock (van Kerkwijk & Ingle 2008), even if the magnetic field tension could stabilize the pulsar wind tale (Bucciantini et al. 2005).

In the present paper we illustrate the effect of neutral hydrogen on the tail region of these nebulae and we suggest that the mass loading of neutral hydrogen in the pulsar wind can explain the peculiar morphology observed at Hα, radio and X-ray energies. The detailed analysis of this hypothesis has been presented in (Morlino et al. 2015). In order to focus on the effect of mass loading on the evolution of bow shock nebulae, complications introduced by magnetic field pressure (and topology) are neglected in the present paper.

2. Interaction of neutrals

In order for mass loading to play a role in the dynamic evolution of bow shock nebulae, neutrals are required to cross the distance between the bow shock and the contact discontinuity, Δ, and penetrate into the wind region (see Fig.1). Hence the interaction length inside the shocked ISM must be larger than Δ, which has been estimated to be $\Delta = 5/16\, d_0$ (Chen et al. 1996; Bucciantini et al. 2005), where d_0 is the distance between the pulsar and the contact discontinuity (CD) (formed between the shocked ISM and the shocked wind). The distance d_0 is obtained by equating the wind pressure with the bulk pressure of the ISM:

$$d_0 = \left(\frac{\mathcal{L}_w}{4\pi V_{\mathrm{NS}}^2 \rho_{\mathrm{ISM}} c}\right)^{1/2} = 1.3 \times 10^{16} \mathcal{L}_{w,34}^{1/2}\, V_{300}^{-1}\, n_{\mathrm{ISM},-1}^{-1/2}\,\mathrm{cm}\,, \qquad (1)$$
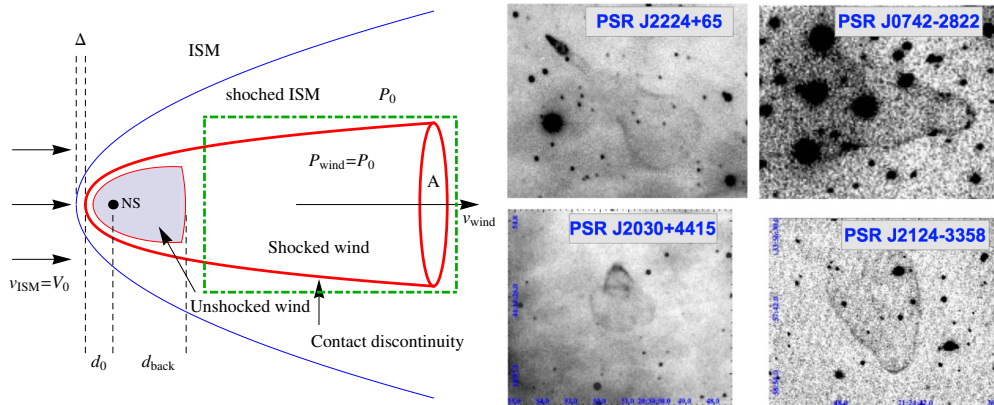
Figure 1. *Left*: schematic illustration of a bow shock nebula propagating through fully ionized ISM, as seen in the rest frame of the pulsar. The dot-dashed box identify the region studied in §2. *Right*: montage of Hα images of optical bow shocks associated with pulsar wind nebulae. Shown are J2224+65, the so-called *Guitar nebula* (Chatterjee & Cordes 2002), J0742-2822, J2030+4415, and J2124-3348 (Brownsberger & Romani 2014). Reproduced from Morlino et al. (2015).

where $\mathcal{L}_w = 10^{34} \mathcal{L}_{w,34} \, \mathrm{erg \, s^{-1}}$ is the pulsar wind luminosity, $V_{\mathrm{NS}} = 300 \, V_{300} \, \mathrm{km \, s^{-1}}$ is its peculiar velocity, and $\rho_{\mathrm{ISM}} = m_p n_{\mathrm{ISM}}$ is the density of the dragged component of the ambient medium, expressed in units of $n_{\mathrm{ISM}} = 0.1 \, n_{\mathrm{ISM},-1} \, \mathrm{cm^{-3}}$.

After crossing the bow shock, neutral atoms can interact with the shocked protons. The interaction length is given by

$$\lambda = \frac{V_{\mathrm{NS}}}{X_{\mathrm{ion}} n_{\mathrm{ISM}} r_c \langle \sigma v_{\mathrm{rel}} \rangle} \,, \tag{2}$$

where X_{ion} is the ionization fraction of the ISM, r_c is the compression ratio of the bow shock, σ is the relevant cross section of the process under consideration, and $\langle \sigma v_{\mathrm{rel}} \rangle$ is the collision rate averaged over the ion distribution function. Using the fiducial values $n_{\mathrm{ISM}} = 0.1 \, \mathrm{cm^{-3}}$ and $V_{\mathrm{NS}} = 300 \, \mathrm{km \, s^{-1}}$, together with an ionization fraction of 90% and $r_c = 4$ (the typical value for strong shocks), leads to the following estimates for the mean free paths (Morlino et al. 2015): $\lambda_{\mathrm{ion},p} \approx 3.0 \times 10^{20} \, \mathrm{cm}$, $\lambda_{\mathrm{ion},e} \approx 2.2 \times 10^{16} \, \mathrm{cm}$, and $\lambda_{\mathrm{CE}} \approx 1.5 \times 10^{15} \, \mathrm{cm}$, for the ionization due to collisions with protons, electrons and charge-exchange (CE), respectively. Note that $\lambda_{\mathrm{ion},e}$ has been calculated under the assumption that the electrons downstream of the shock equilibrate rapidly with protons, thereby acquiring the same temperature. If this assumption does not hold, the collisional length scale for ionization due to electrons can become much larger. In addition, these values of λ are to be taken as lower limits as they are valid just ahead of the nebula, where the compression ratio and the temperature obtain their maximum values.

From these estimates it follows that only a negligible fraction of the neutral hydrogen will be collisionally ionized by electrons, whereas a significant fraction

of neutrals will undergo CE. The neutrals resulting from a CE event will tend to be dragged with the shocked protons along a direction parallel to the contact discontinuity. Nevertheless, the CE process produces a diffusion of neutrals in the nose of the nebula and it may still be possible for the newly formed neutrals to enter the wind region, provided that their diffusion velocity perpendicular to the contact discontinuity is of the same order or larger than their velocity parallel to the contact discontinuity. This is a complication that will not be addressed in the present paper but is essential to estimate the correct amount of neutrals that can penetrate into the wind.

Although a large number of neutrals will be lost due to CE, a minimum fraction of neutrals proportional to $\exp[-\Delta/(\lambda_{CE} + \lambda_{ion})]$ will cross the shocked ISM region without suffering any interaction and will enter the pulsar wind in their original state. These neutrals will not influence the wind structure until they are ionized, either through collisions with relativistic electrons and positrons, or through photo-ionization with photons emitted by the nebula or by the pulsar. In Morlino et al. (2015) we showed that photo-ionization due to UV photons emitted by the nebula is the dominant process, while collisional ionization can be neglected.

3. Hydrodynamical model

To study the effect of mass loading in the tail of bow shock nebulae, we solve, in a quasi 1-D approximation, the steady-state conservation equations for mass, momentum and energy. We restrict our attention to the region enclose in the dot-dashed rectangle of Fig.1, meaning that any internal structures are neglected, in particular the free wind region and the termination shock. For the sake of simplicity the presence of the bow shock is also neglected, but we will comment on possible effects of mass loading on the shape of the bow shock. It is further assumed that the external medium has a spatially independent velocity, V_0, pressure, P_0, and density, ρ_0. The quasi 1-D approximation implies that the transverse cross section, A, of the flow can change, but that all the characteristic quantities of the wind, *i.e.*, the velocity, u, density, ρ and pressure, P, are assumed to be a function of the position x only.

The relativistic equations for the conservation of particle number, energy and momentum, for a 1-D system, written in the rest frame of the neutron star are

$$\partial_x \left[n_{e,p} u A \right] = \dot{n} A' \,, \tag{3}$$

$$\partial_x \left[w \gamma_w u A \right] = q c^2 \gamma_0 A' \,, \tag{4}$$

$$\partial_x \left[w u^2 A \right] + c^2 A \partial_x P = q c^2 \gamma_0 A' V_0 \,. \tag{5}$$

Here $n_{e,p}$ is the numerical density of electrons (protons), w is the total wind enthalpy and γ_w and γ_0 are the Lorentz factors of the wind and the neutrals, respectively. A' represent the effective area crossed by neutrals. For the sake of clarity we discuss here only the case where the neutrals penetrate everywhere in the nebula, which imply $A' = A$. The mass loading term is given by $q = \dot{n}(m_e + m_p) \approx \dot{n} m_p$, where $\dot{n}$ is the number of hydrogen atoms ionized per unit time and unit volume and is determined by the photo-ionization due to UV

photons. Hence $\dot{n} = n_N n_{\mathrm{ph}} \bar{\sigma}_{\mathrm{ph}} c$, where $\bar{\sigma}_{\mathrm{ph}}$ is the photo-ionization cross section averaged over the photon distribution whose density is n_{ph}, while n_N is the density of neutrals entering inside the wind. Both n_{ph} and n_N are assumed to be constant inside the wind.

The pulsar wind after the termination shock is only marginally relativistic with a bulk Lorentz factor $\gamma_w \approx 1$. Furthermore, the neutrals are non-relativistic, hence $\gamma_0 \approx 1$, while the steady-state assumption requires the pressure to be constant everywhere, *i.e.*, $P = P_0$ and $\partial_x P = 0$ (we are assuming a subsonic flow).

In order to close the system (3)-(5), an expression for the enthalpy is required. It is generally believed that the shocked pulsar wind predominantly consists of electron-position pairs with highly relativistic temperatures, and we assume that when mass loading occurs there is no energy transfer between electron and protons. In other words, electrons and protons do not reach a thermal equilibrium, but evolve independently with different temperatures. This implies that the electron gas is always highly relativistic, hence the rest mass contribution to enthalpy can be neglected, *i.e.*, $w_e = \epsilon_e + P_e = 4P_e = 4P_0$. On the other hand, protons are non-relativistic, hence their thermal energy is always negligible with respect to their rest mass energy, and their enthalpy is $w_p = \rho_p c^2$. The total enthalpy of the wind is thus $w = w_p + w_e = \rho_p c^2 + 4P_0$.

Using all the simplifications outlined above one can obtain an analytical solution for the wind dynamics (Morlino et al. 2015). It turns out that the cross section and the proton density can be expressed as a function of the flow speed only:

$$A(u) = u_1 A_1 / u \,, \tag{6}$$

$$\rho_p(u) = 4P_0/c^2 \, (u_1 - u)/(u - V_0) \,, \tag{7}$$

where the subscript $_1$ identifies the values of quantities at the initial position $x = x_1$ right behind the backward shock. Notice that, as a consequence of the mass loading, the usual conservation equation $\rho u A = const$ does not hold any more, being replaced by $uA = const$. The flow speed can be expressed as a function of x in an implicit form as follows

$$\frac{x}{\lambda_{\mathrm{ML}}} = \frac{u}{u - V_0} - \frac{u_1}{u_1 - V_0} + \ln\left[\frac{u_1 - V_0}{u - V_0}\right] \,, \tag{8}$$

where we have introduced the mass loading length scale

$$\lambda_{\mathrm{ML}} = \frac{4P_0(u_1 - V_0)}{qc^2} \simeq \frac{4P_0}{\rho_N c^2} \frac{u_1}{n_{\mathrm{ph}} \bar{\sigma}_{\mathrm{ph}} c} \,. \tag{9}$$

The last equality holds because $u_1 \approx c \gg V_0$. Eq.(9) reveals the meanings of λ_{ML}: this is the typical length scale such that the enthalpy of the loaded mass, $\rho_N c^2$, times $\lambda_{\mathrm{ML}}/\lambda_{\mathrm{interaction}}$, equals the enthalpy of the wind, $4P_0$. Choosing realistic values for the parameters associated with bow shock nebulae emitting Hα shows that $\lambda_{\mathrm{ML}} \sim 10^{15}$ cm (Morlino et al. 2015), even if this value can vary by orders of magnitude, essentially due to the fact that the values of the neutral density inside the wind and the luminosity of the PWN tail are difficult to estimate.
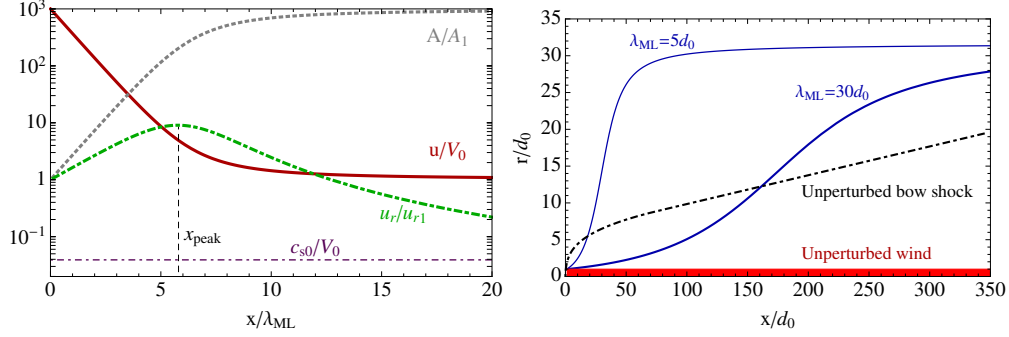
Figure 2.   *Left*: structure of a pulsar wind when mass loading occurs. The various lines represent the wind speed divided by V_0 (solid line), wind cross section (dotted line) and radial expansion speed (dot-dashed line) both normalized to their initial values. The sound speed of the ISM, c_{s0}, also normalized to V_0, is shown for comparison (thin dot-dashed line). *Right*: comparison between two mass loaded wind profiles, calculated using $\lambda_{\mathrm{ML}} = 5d_0$ (thin lines) and $\lambda_{\mathrm{ML}} = 30d_0$ (thick lines), and the profile of the unperturbed bow shock, calculated using the thin shock approximation (dot-dashed line; Wilkin 1996). The shaded region, with radius $r = d_0$, shows the unperturbed pulsar wind, i.e. without the mass loading effect. Adapted from Morlino et al. (2015).

The behavior of A and u as a function of the normalized distance is shown in the left panel of Fig.2, where we chose $V_0 = 300$ km s^{-1}, $u_1 = c$ and $n_0 = 0.1$ cm^{-3}. As one would expect, the loaded mass slows down the wind on a typical length scale of λ_{ML} and, because of Eq.(6), the cross section expands. For distances $x \gg \lambda_{\mathrm{ML}}$ we have $u \to V_0$ and $A/A_1 \to u_1/V_0$. Because $u_1 \approx c \gg V_0$, the wind cross section can expand up to a factor $\approx 10^3$.

In the right panel of Fig.(2) we compare our solutions for the wind profile with the unperturbed wind and with the unperturbed bow shock profile as predicted by Wilkin (1996). For $\lambda_{\mathrm{ML}} \lesssim 100d_0$ the modified wind crosses the bow shock, implying that the bow shock shape will be strongly affected.

The left panel of Fig.2 also reports the velocity of the expansion in the radial direction, derived from the evolution of A and u with r, i.e. $u_r \equiv \frac{dr}{dt} = \frac{V_0}{2\sqrt{\pi A}} \frac{dA}{du} \frac{du}{dx}$. It is easy to show that the value of u_r at the origin is $u_{r1} = V_0 d_0/(2\lambda_{\mathrm{ML}})$, while for very large distances one has $u_r \to 0$. Moreover the radial expansion speed has a peak at the position $x_{\mathrm{peak}} = \lambda_{\mathrm{ML}} (0.25 + \ln[u_1/(4V_0)])$ where its value is $u_{r,\mathrm{peak}} = 0.3 \, u_{r1} \sqrt{u_1/V_0}$. This behavior has two important consequences. The first one is that for $\lambda_{\mathrm{ML}} \lesssim 100d_0$ the expansion speed is larger than the sound speed in the ISM when the wind crosses the unperturbed bow shock profile. In other words, when the pulsar wind expands beyond the unperturbed bow shock, the expansion is supersonic and one expects a strong modification of the bow shock. By contrast, for $\lambda_{\mathrm{ML}} \gtrsim 100d_0$ the expansion of the wind in the ISM is subsonic, and one therefore expects a less pronounced deformation of the bow shock profile. The second consequence is that for distances

close to x_{peak}, u_r can be even larger than u. When the latter condition is realized the quasi 1-D approximation is no longer valid and our model can no longer be used. Based on the above arguments one may speculate that the system becomes non-stationarity at that location, giving rise to a periodic structure of expanding bubbles, similar to those observed in the Guitar Nebula. However, addressing this scenario using only analytical models is a complicated matter, requiring the use of full 2-D numerical simulations.

References

Arzoumanian, Z., Chernoff, D. F., & Cordes, J. M. 2002, ApJ, 568, 289

Brownsberger, S. & Romani, R. W. 2014, ApJ, 784, 154

Bucciantini, N. 2002, A&A, 387, 1066

Bucciantini, N., Amato, E., & Del Zanna, L. 2005, A&A, 434, 189

Chatterjee, S. & Cordes, J. M. 2002, ApJ, 575, 407

Chen, Y., Bandiera, R., & Wang, Z.-R. 1996, ApJ, 469, 715

Chevalier, R. A., Kirshner, R. P., & Raymond, J. C. 1980, ApJ, 235, 186

Cordes, J. M. & Chernoff, D. F. 1998, ApJ, 505, 315

Morlino, G., Lyutikov, M. & Vorster, M. 2015, MNRAS, 454, 3886

Romani, R. W., Cordes, J. M., & Yadigaroglu, I.-A. 1997, ApJL, 484, L137

van Kerkwijk, M. H. & Ingle, A. 2008, ApJL, 683, L159

Vigelius, M., Melatos, A., Chatterjee, S., Gaensler, B. M., & Ghavamian, P. 2007, MNRAS, 374, 793

Wilkin, F. P. 1996, ApJL, 459, L31

Superorbital variability of the gamma-ray binary LS I +61 303 studied with MAGIC

J.M. Paredes[1], A. López-Oramas[2], D. Hadasch[3], O. Blanch[2],
D.F. Torres[4] for the MAGIC Collaboration, J. Casares[5] and A. Herrero[5]

[1] *Departament d'Astronomia i Meteorologia, Institut de Ciències del Cosmos, Universitat de Barcelona, IEEC-UB, Martí i Franquès 1, E-08028 Barcelona, Spain*
[2] *IFAE, Campus UAB, E-08193 Bellaterra, Spain*
[3] *Japanese MAGIC Consortium, ICRR, The University of Tokyo, Japan*
[4] *ICREA and Institute for Space Sciences (CSIC-IEEC), E-08193 Barcelona, Spain*
[5] *Instituto de Astrofísica de Canarias, E-38200 La Laguna, Tenerife, Spain; Universidad de La Laguna, Dpto. Astrofísica, E-38206 La Laguna, Tenerife, Spain*

Abstract. The gamma-ray binary LS I +61 303 has been detected from radio up to very high–energy gamma rays. Its emission is likely originated by the interaction of the stellar wind and a relativistic outflow. The broadband emission shows a periodicity of about 26.6 days, coincident with the orbital period. A long-term periodicity of 1667 ± 8 days was discovered in radio and confirmed in optical and high–energy gamma rays. Here we will present the results of a four-year campaign performed by MAGIC together with archival data. In this campaign, we search for a long-term signature in the VHE emission from LS I +61 303. We will focus on the search for super orbital modulation of the VHE emission, similarly to the one observed at other wavelengths, and on the search for (anti-)correlation between the TeV emission and the extension of the circumstellar disk, measured using optical data.

1. Introduction

Of those currently known, LS I +61 303 is one of the most powerful and complex gamma-ray binaries. This system is comprised of a young main sequence B0 Ve star and a compact object orbiting it with a period of $P_{\rm orb} = 26.4960 \pm 0.0028$ d (Gregory 2002) and an eccentricity of $e = 0.72 \pm 0.15$ (Casares et al. 2005). The system is located at 2.0 ± 0.2 kpc (Frail & Hjellming 1991), and the periastron passage takes place in the orbital phase range 0.23–0.28 (Casares et al. 2005; Aragona et al. 2009), using $\rm JD_0 = 2\,443\,366.775$. Extended emission at mas scales ($\sim$1–100 AU) has been reported at GHz frequencies, showing morphological changes along the orbit (Massi et al. 2004; Dhawan et al. 2006; Moldón 2012).

The emission of LS I +61 303 is orbitally modulated from radio to gamma-rays. At radio frequencies, the spectrum is produced by synchrotron emission. The 1–10 GHz radio light-curve of the source shows a clear outburst on each

orbital cycle that increases the $\lesssim 50$ mJy steady flux density emission up to $\sim$100–200 mJy. These outbursts are periodic, although changes in their shape and intensity have been reported from cycle to cycle (Paredes et al. 1990; Ray et al. 1997). A similar periodicity ($\sim$26.5 d) has been detected at optical and infrared bands (Mendelson & Mazeh 1989; Paredes et al. 1994), at X-rays (Paredes et al. 1997; Torres et al. 2010), at high energies (HE; 100 MeV–20 GeV) by *Fermi-LAT* (Abdo et al. 2009), and at very high energies (VHE; 20 GeV–TeV) by MAGIC (Albert et al. 2009).

A long-term modulation is also observed, from radio to HE wavelengths, the so-called superorbital modulation, with a period of $P_{\rm so} = 1\,667 \pm 8$ d or $\simeq$4.6 yr (Gregory 2002). This modulation was first found at GHz radio frequencies (Paredes 1987; Gregory et al. 1989; Paredes et al. 1990), affecting the amplitude of the non-thermal periodic outbursts and the orbital phases at which the onset and peak of these outbursts take place, drifting from orbital phases of $\sim$0.45 to $\sim$0.95 (Gregory 2002). The source exhibits the minimum activity at GHz frequencies during the superorbital phase range of $\phi_{\rm so} \sim 0.2$–0.5, whereas the maximum activity takes place at $\phi_{\rm so} \sim 0.78$–0.05 (using the same JD$_0$ quoted above). This $\simeq$4.6 yr modulation has also been observed at optical (Zamanov et al. 2013), X-rays (Chernyakova et al. 2012; Li et al. 2014), and HE by *Fermi-LAT* (Ackermann et al. 2013). In order to determine if this modulation is also present at VHE energies, we carried out a multi-year campaign with MAGIC.

The origin of the superorbital modulation was proposed to be related to periodic changes in the circumstellar disc and the mass-loss rate of the Be star (Zamanov et al. 2013), although other interpretations within the framework of a precessing jet have been also discussed (see Massi & Torricelli-Ciamponi 2014, and references therein).

2. Observations

A four-year (August 2010–September 2014) campaign was carried out with the MAGIC telescopes together with the Liverpool optical telescope. With the aim of detecting a possible long-term modulation, LS I $+61$ 303 was observed with MAGIC during the orbital phase range $\phi_{\rm orb} = 0.5$–0.75, where the TeV emission outburst peak is present. Furthermore, in order to search for (anti-)correlation between the Be star mass-loss rate and the TeV emission, contemporaneous observations with MAGIC and Liverpool telescope were performed during the orbital phase range $\phi_{\rm orb} = 0.75$–1.0, where the TeV emission does not present yearly periodic variability (Aleksic et al 2012). For technical details of the observations and the analysis and data reduction see Ahnen et al. (2016).

3. Results

The VHE spectrum for the different campaigns follows a power-law with spectral index α. Figure 1 shows the dependence of α with the phase of the superorbital period of 1667 days. The values of α obtained are compatible with a constant value of 2.43 ± 0.04. The spectral index also does not show variability for each of the different observational campaigns, for orbital intervals $\phi_{\rm orb} = 0.5$–0.75 and $\phi_{\rm orb} = 0.75$–1.0, and for epochs when the source was in high– or low–flux states.
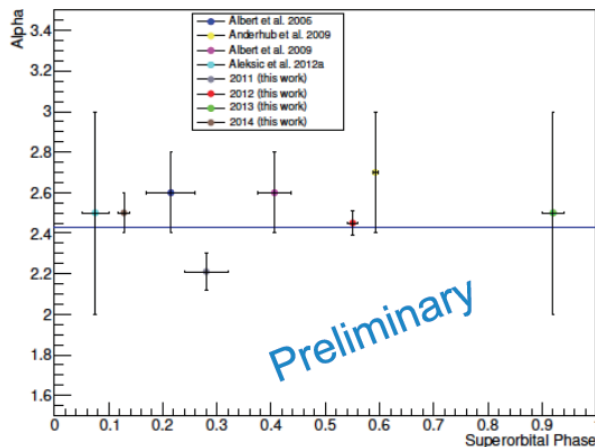
Figure 1. Spectral index dependence of all MAGIC campaigns with the superorbital period (1667 d). The average value of all MAGIC data is represented by the blue line.

In order to have enough data to search for superorbital modulation at VHE, we have added to our four-year campaign archival data from MAGIC obtained since its detection in 2006 (Albert et al. 2008; Anderhub et al. 2009; Albert et al. 2009; Aleksic et al. 2012), and data from VERITAS (Acciari et al. 2008, 2009, 2011; Aliu et al. 2013). Figure 2 shows the peak integrated flux above 300 GeV for each orbit folded into the superorbital period. The data were fit with a sinusoide and a constant function, being the probability for a constant flux negligible (4.5×10^{-12}), and for a sinusoidal signal 8%. This seems to indicate that there is a superorbital signature in the TeV emission of LS I +61 303 and that it is compatible with the 4.5-year radio modulation seen at other frequencies.

We have explored possible correlations between the H_α parameters (EW, FHWM, profile centroid velocity) measured by the Liverpool telescope, and the TeV flux measured by MAGIC, for data in the orbital phase range $\phi_{\mathrm{orb}} = 0.75$–1.0. No significant correlation was found from the statistical test performed on the sample within this phase interval. Figure 3 shows the EW, FHWM, and profile centroid velocity as a function of the TeV flux.

4. Discussion and Conclusions

In this paper we presented the first detection of superorbital variability in the TeV regime using new MAGIC data and archival MAGIC and VERITAS data. The detection of superorbital variability at TeV/VHE energies is consistent with the predicted long-term behavior of the flip-flop model (Zamanov et al. 2001, Torres et al. 2012, Papitto et al. 2012) that considers LS I +61 303 as a pulsar-Be star binary that changes (driven by the influence of matter) from a propeller regime in periastron to an ejector regime in apastron. This result also confirms the earlier observational hints for this phenomenology discovered using smaller samples of TeV data (Li et al. 2012).
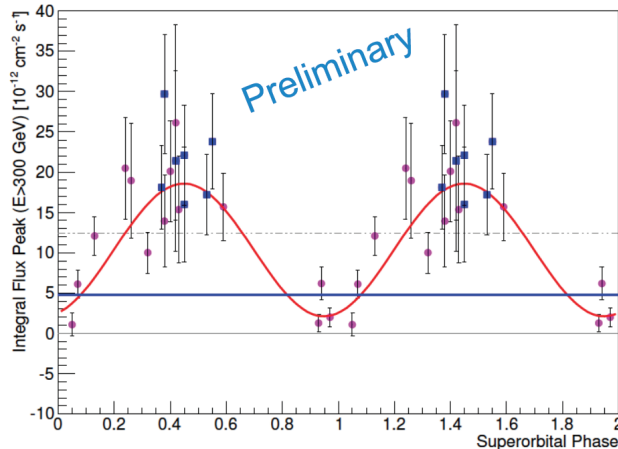
Figure 2.   VHE peak flux emitted during orbital phases $0.5 - 0.75$ in different orbital periods folded into the superorbital 1667 d period. MAGIC data are magenta dots and VERITAS data blue squares. The solid red line represents the fit with a sinusoidal function and the blue line the fit with a constant. The 10% of the Crab Nebula flux is represented by a grey dashed line whereas the grey solid line marks the zero level.

No statistically significant correlation between the H_α parameters and the TeV emission has been found. However, this lack of (anti-)correlation could be due to the fast and extreme changes in the H_α data of the source (Zamanov et al. 2013), and the vastly different integration times (minutes vs. several hours) in both frequencies may blur finding any possible trend.

References

Abdo et al. 2009, ApJ 701, L123

Acciari, V. A., Aliu, E., Arlen, T., et al. 2009, ApJ, 700, 1034

Acciari, V. A., Aliu, E., Arlen, T., et al. 2011, ApJ, 738, 3

Acciari, V. A., Beilicke, M., Blaylock, G., & et al. 2008, ApJ, 679, 1427

Ackermann et al. 2013, ApJ, 773, L35
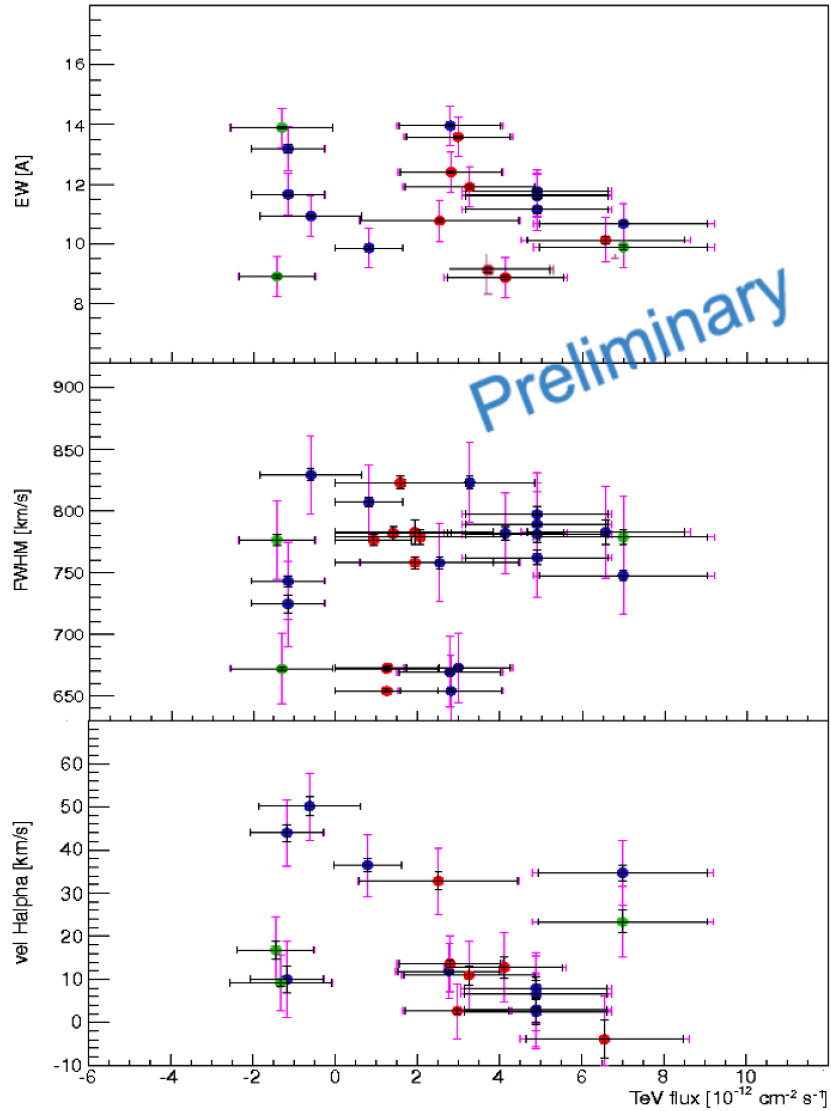
Figure 3. Correlations between the TeV flux obtained by MAGIC and the H$_\alpha$ parameters (EW, FWHM and velocity) measured by the Liverpool telescope, for the extended orbital interval 0.75 – 1.0. Optical data corresponds to 10 minutes observation whereas TeV data has a variable integration time. The different color means that the optical and TeV data were taken nightly (blue), contemporary (red) and strictly simultaneous (green).

Albert, J., Aliu, E., Anderhub, H., et al. 2008, ApJ, 684, 1351

Albert et al. 2009, ApJ 693, 303

Aleksic et al 2012, ApJ 746, 80

Aliu, E., Archambault, S., Behera, B., et al. 2013, ApJ, 779, 88

Ahnen et al 2016, A&A, 591, A76

Anderhub, H., Antonelli, L. A., Antoranz, P., et al. 2009, ApJ, 706, L27

Aragona, C., McSwain, M. V., Grundstrom, E. D., et al. 2009, ApJ, 698, 514

Casares, J., Ribas, I., Paredes, J. M., et al. 2005, MNRAS, 360, 1105

Chernyakova et al. 2012, ApJ 747, L29

Dhawan, V., Mioduszewski, A., & Rupen, M. 2006, in Proceedings of the VI Microquasar Workshop: Microquasars and Beyond (Como, Italy, PoS(MQW6)052)

Gregory, P. C. 2002, ApJ, 575, 427

Gregory, P. C., Xu, H.-J., Backhouse, C. J., & Reid, A. 1989, ApJ, 339, 1054

Frail, D. A. & Hjellming, R. M. 1991, ApJ, 101, 2126

Li, J., Torres, D. F., Zhang, S., et al. 2012, ApJ, 744, L13

Li, J., Torres, D. F., & Zhang, S. 2014, ApJ, 785, L19

Massi, M., Ribo, M., Paredes, J. M., et al. 2004, A&A, 414, L1

Massi, M. & Torricelli-Ciamponi, G. 2014, A&A, 564, A23

Mendelson & Mazeh 1989, MNRAS 239, 733

Moldón, J. 2012, PhD thesis, Universitat de Barcelona

Papitto, A., Torres, D. F., & Rea, N. 2012, ApJ, 756, 188

Paredes, J. M. 1987, PhD thesis, Universitat de Barcelona

Paredes, J. M., Estalella, R., & Rius, A. 1990, A&A, 232, 377

Paredes et al. 1994 A&A 288, 519

Paredes et al. 1997 A&A 320, L25

Ray, P. S., Foster, R. S., Waltman, E. B., et al. 1997, ApJ, 491, 381

Torres et al. 2010, ApJ 719, L104

Torres, D. F., Rea, N., Esposito, P., et al. 2012, ApJ, 744, 106

Zamanov, R., Marti, J., & Marziani, P. 2001, in The Second National Conference on Astrophysics of Compact Objects, 50

Zamanov, R., Stoyanov, K., Marti, J., et al. 2013, A&A, 559, A87

Numerical simulations of the collision of an inhomogeneous stellar wind and a relativistic pulsar wind in a binary system

X. Paredes-Fortuny[1], V. Bosch-Ramon[1], M. Perucho[2] and M. Ribó[1, †]

[1] *Dept. d'Astronomia i Meteorologia, Institut de Ciènces del Cosmos (ICCUB), Universitat de Barcelona (IEEC-UB), Martí i Franquès 1, E08028 Barcelona, Spain*
[2] *Departament d'Astronomia i Astrofísica, Universitat de València, Av. Vicent Andrés Estellés s/n, 46100 Burjassot (València), Spain*
[†] *Serra Húnter Fellow*

Abstract. Binary systems hosting a massive star and a non-accreting pulsar present strong interacting winds. The stellar wind can be clumpy resulting in an unstable two-wind interaction region, which can strongly influence the non-thermal emission of the binary system. We performed axisymmetric relativistic hydrodynamical simulations of the interaction between a relativistic pulsar wind (Lorentz factors up to 6) and an inhomogeneous stellar wind with different degrees of inhomogeneity. The simulations show that the stellar wind inhomogeneities can significantly reduce the two-wind interaction region size. In addition, the whole interaction region is quite unstable, and presents a complex spatial and temporal pattern, with the shocked pulsar wind structure strongly changing under small perturbations. All of this can lead to strong variations in the non-thermal output from these binary systems.

1. Introduction

The collision of a relativistic pulsar wind and a stellar wind in a binary system produces a shock structure bow-shaped towards the wind with the lowest thrust, this is expected to result in particle acceleration and non-thermal emission. Stellar winds may be inhomogeneous to different degrees. There are many sources of stellar wind inhomogeneity, producing smaller or larger clumps: instabilities in the inner wind region of hot stars of spectral types O and B (e.g., Lucy & Solomon 1970), dynamical effects of rotation, magnetic fields, or non-radial pulsations (e.g., Cranmer & Owocki 1996), and the truncation of the Be star equatorial decretion disk in binary systems (e.g., Okazaki et al. 2011). This clumpy wind can distort the overall two-wind interaction structure, and therefore affect the non-thermal output from the binary system (e.g., Bosch-Ramon 2013). We study the impact of the clumps on the colliding wind region using numerical simulations.
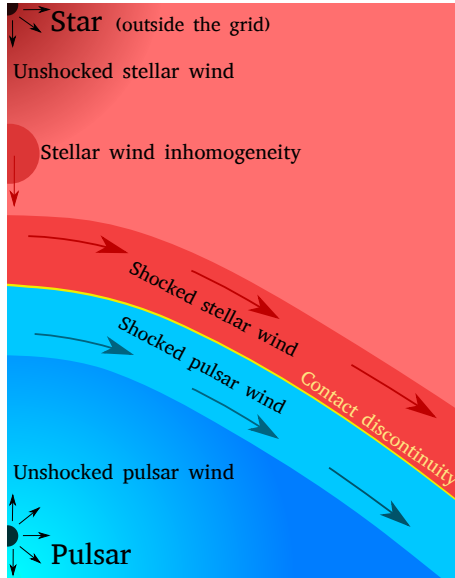
Figure 1.   Cartoon of the numerical set-up of the axisymmetric simulation of the collision of an inhomogeneous stellar wind and a relativistic pulsar wind. The inhomogeneous stellar wind is characterized by a single clump in the z axis. Adapted from Paredes-Fortuny et al. (2015).

2.   Clump impact on the colliding wind region

We conducted axisymmetric numerical Relativistic Hydrodynamical (RHD) simulations aimed to study the interaction of a relativistic pulsar wind and an inhomogeneous stellar wind for different degrees of inhomogeneity. We characterized the inhomogeneous stellar wind by a single clump placed at the axis joining the two stars. The numerical simulations were performed using a parallelized finite-difference code based on a high-resolution shock-capturing scheme that solves the equations of RHD in a conservation form (Martí et al. 1997, Perucho et al. 2005). See Fig. 1 for a sketch of the numerical set-up.

We simulated an ideal gas with single particle species and an adiabatic coefficient value of $\hat{\gamma} = 1.444$, between the value of a non-relativistic and a relativistic ideal gas. The grid size is of $l_r = 2.4 \times 10^{12}$ cm $l_z = 4.0 \times 10^{12}$ cm, with a resolution of 150×250 cells (a compromise between physical and numerical limitations, see Paredes-Fortuny et al. 2015 for an extended discussion). The star and the pulsar are located at $(r_0^{\mathrm{star}}, z_0^{\mathrm{star}}) = (0, 4.8 \times 10^{12})$ cm and $(r_0^{\mathrm{pulsar}}, z_0^{\mathrm{pulsar}}) = (0, 0.4 \times 10^{12})$ cm, respectively, yielding a star-pulsar separation of $d_{\mathrm{star-pulsar}} = 4.4 \times 10^{12}$ cm, similar to the typical orbital separation of gamma-ray binaries (see, e.g., Dubus 2013 and references therein). The left boundary is set to reflection, while the lower and right boundaries are set to outflow. The stellar wind is injected at the top of the grid as a boundary condition, and the pulsar wind is injected at a radius of 2.4×10^{11} cm (15 cells). The stellar mass-loss rate is $\dot{M} = 10^{-7}$ M$_\odot$ yr^{-1}, the pulsar spindown luminosity and

the pulsar wind Lorentz factor are $L_{\mathrm{sd}} = 10^{37}$ erg s^{-1} and $\Gamma = 6$, respectively, and the pulsar-to-stellar wind thrust ratio is $\eta \sim 0.2$, values representative of gamma-ray binaries hosting a pulsar and an OB star.

We simulated different degrees of inhomogeneity, each inhomogeneity degree is characterized by a single over-dense region with the same speed as the homogeneous stellar wind placed at the axis joining the two stars, this clump is introduced when the steady state has been reached. We parametrized the inhomogeniety degree with the clump radius, R_{C}, and the density contrast, χ, with respect the homogeneous stellar wind at the injection point. We simulated 3 cases ranging different clump sizes and density contrasts (see Table 1).

χ	R_{C}	Description
10	$8 \cdot 10^{10}$ cm	light and small
10	$4 \cdot 10^{11}$ cm	light and large
30	$8 \cdot 10^{10}$ cm	dense and small

Table 1. Summary of the simulated stellar wind inhomogeneities, being χ the density contrast with respect the homogeneous stellar wind, and R_{C} the clump radius.

3. Results

The (quasi-)steady state of the interaction of a relativistic pulsar wind with a homogeneous stellar wind, i.e., prior to the injection of any clump, is shown in Fig. 2. The prefix *quasi* is used because the system does not reach a stationary steady state. Instead, it reaches a meta-stable steady state with periodic temporal patterns (waves) in the two-wind interaction region. Despite such irregularities might have a numerical origin due to the presence of a coordinate singularity at the axis, it is expected that instabilities quickly grow if perturbations are present by Kelvin-Helmholtz instability, as has already been demonstrated in 2D planar simulations (e.g., Bosch-Ramon et al. 2012; Lamberts et al. 2013). This suggests that these systems are prone to suffer such instabilities. In addition, the dynamical effects of the clump impact will overcome any (quasi-)steady state instability (see Paredes-Fortuny et al. 2015 for an extended discussion).

The density maps showing the effect of the clump impact on the two-wind interaction region for the light and small, light and large, and dense and small clumps are shown from top to bottom in Fig. 3, respectively. From Fig. 3 we see that the compression of the two-wind interaction region is larger for denser/larger clumps. After the clump has reached the minimum distance to the pulsar, the clump is shocked, then the pulsar wind pushes the clump backwards, and finally the clump material is evacuated with the shocked flow.

4. Discussion

The arrival of clumps can have very strong impact on the whole interaction structure, and its role triggering instabilities more important than any possible numerical perturbation. In addition, the clumps trigger Rayleigh-Taylor/Richtmyer-
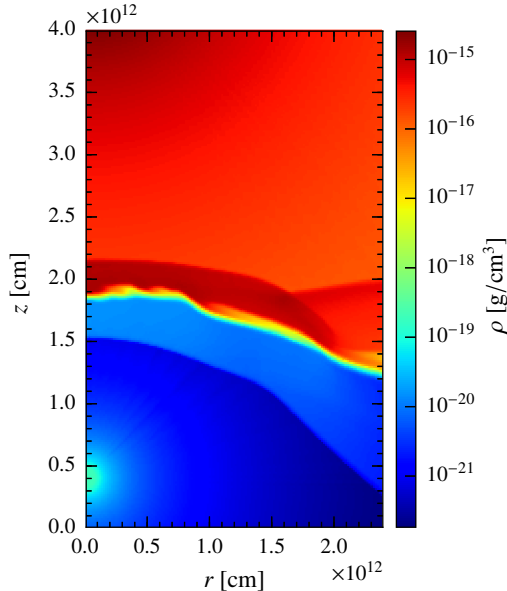
Figure 2. Density map of the (quasi-)steady state at $t \sim 6 \times 10^4$ s. The pulsar is placed at $(r_0^{\text{pulsar}}, z_0^{\text{pulsar}}) = (0, 0.4 \times 10^{12})$ cm, and the star is located at $(r_0^{\text{star}}, z_0^{\text{star}}) = (0, 4.8 \times 10^{12})$ cm (outside the grid).

Meshkov and (mainly) Kelvin-Helmholtz instabilities leading to quick changes of the shocked two-wind region (see also Bosch-Ramon et al. 2015). The clumps with a modest inhomogeneity degree produce non-negligible variations of the interaction structure and enhance the instability growth. On the other hand, the clumps with a high inhomogeneity degree produce strong variations in the size of the two-wind interaction structure. Both cases generate quick and global variations in the shocked pulsar wind, affecting to the location of the pulsar wind termination shock, and therefore reducing the emitter size and increasing the magnetic field density (Bosch-Ramon 2013). The relativistic flow variations on small spatial and temporal scales downstream of the pulsar wind shock would lead to a complex radiative pattern in time and direction caused by Doppler boosting (e.g., Khangulyan at al. 2014).

In the gamma-ray binary PSR B1259−63 the impact of a piece of disk of the optical Be star on the two-wind interaction region has been suggested as an explanation for the flare observed by Fermi ∼ 30 days after periaston passage (Abdo et al. 2011). This might have led to efficient Compton scattering by GeV electrons on local X-ray photons (Dubus & Cerutti 2013; Khangulyan et al. 2012 for IR photons), as a result of the strong enhancement of the synchrotron photon density. In addition, the clump impact might explain the short flares occurring on scales of seconds to hours found in X-ray lightcurves of LS 5039 and LS I +61 303 (e.g., Bosch-Ramon et al. 2005; Paredes et al. 2007; Smith et al. 2009; Li et al. 2011), and the short X-ray variability in supergiant fast X-ray transients (e.g., Walter & Zurita Heras 2007).
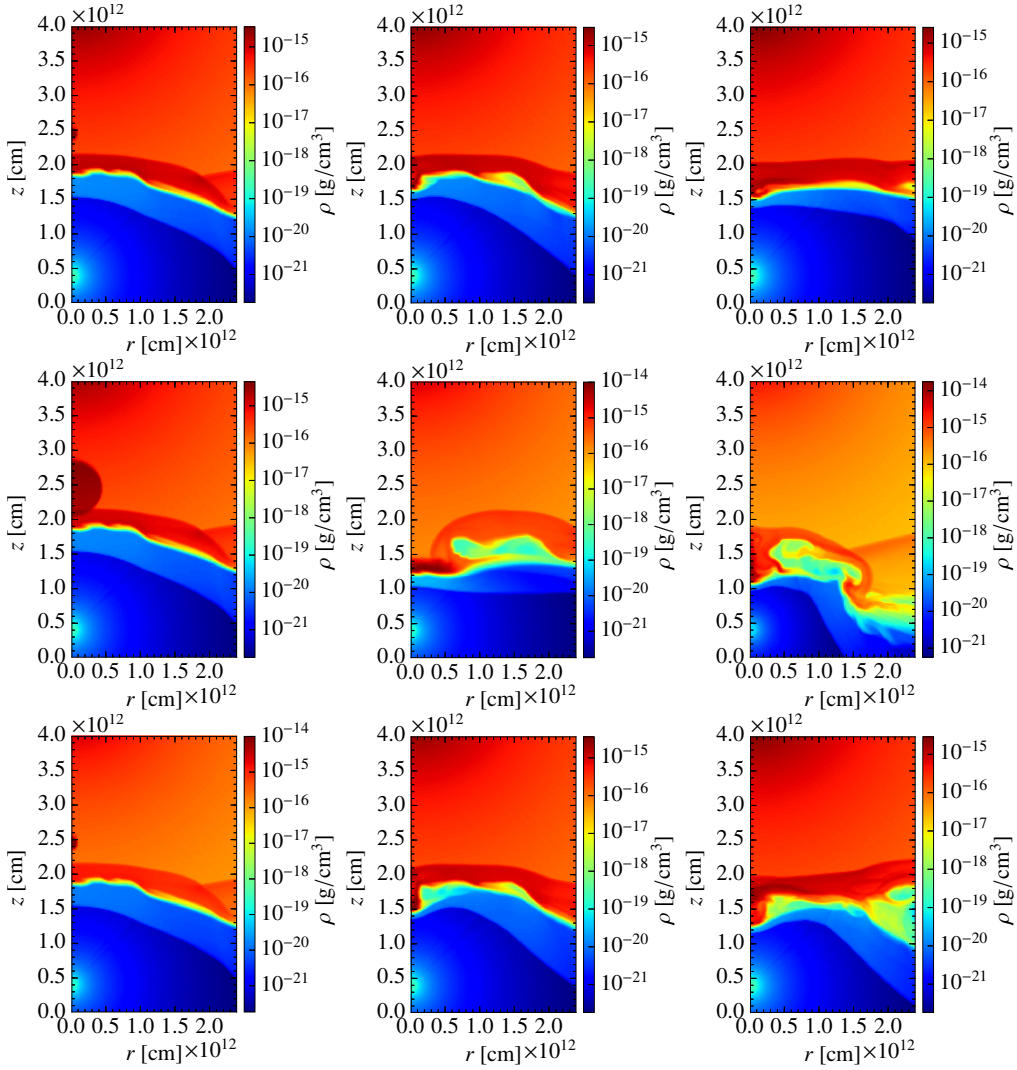
Figure 3. From top to bottom, density map for the light and small, light and large, and dense and small clumps, respectively. From left to right, clump evolution at different increasing times. The pulsar is placed at $(r_0^{\text{pulsar}}, z_0^{\text{pulsar}}) = (0, 0.4 \times 10^{12})$ cm, and the star is located at $(r_0^{\text{star}}, z_0^{\text{star}}) = (0, 4.8 \times 10^{12})$ cm (outside the grid).

References

Abdo, A. A., Ackermann, M., Ajello, M., et al. 2011, ApJ, 736, L11

Bosch-Ramon, V., Paredes, J. M., Ribó, M., et al. 2005, ApJ, 628, 388

Bosch-Ramon, V., Barkov, M. V., Khangulyan, D., & Perucho, M. 2012, A&A, 544, A59

Bosch-Ramon, V. 2013, A&A, 560, A32

Bosch-Ramon, V., Barkov M. V., Perucho M., 2015, A&A, 577, A89

Cranmer, S. R. & Owocki, S. P. 1996, ApJ, 462, 469

Dubus, G. 2013, A&ARev., 21, 64

Dubus, G. & Cerutti, B. 2013, A&A, 557, A127

Khangulyan, D., Aharonian, F. A., Bogovalov, S. V., & Ribó, M. 2012, ApJ, 752, L17

Khangulyan, D., Bogovalov, S. V., & Aharonian, F. A. 2014, International Journal of Modern Physics Conference Series, 28, 60169

Lamberts, A., Fromang, S., Dubus, G., & Teyssier, R. 2013, A&A, 560, A79

Li, J., Torres, D. F., Zhang, S., et al. 2011, ApJ, 733, 89

Lucy, L. B. & Solomon, P. M. 1970, ApJ, 159, 879

Martí, J. M., Müller, E., Font, J. A., Ibáñez, J. M., & Marquina, A. 1997, ApJ, 479, 151

Okazaki, A. T., Nagataki, S., Naito, T., et al. 2011, PASJ, 63, 893

Paredes, J. M., Ribó, M., Bosch-Ramon, V., et al. 2007, ApJ, 664, L39

Paredes-Fortuny, X., Bosch-Ramon, V., Perucho, M., & Ribó, M. 2015, A&A, 574, A77

Perucho, M., Martí, J. M., & Hanasz, M. 2005, A&A, 443, 863

Smith, A., Kaaret, P., Holder, J., et al. 2009, ApJ, 693, 1621

Walter, R. & Zurita Heras, J. 2007, A&A, 476, 335

Estimating GRB detection rate with MIRAX

A.V. Penacchioni[1,2], J. Braga[3], M.A. Castro[3], J.R. Sacahui[4], F. D'Amico[3]

[1] *University of Siena, Rettorato, via Banchi di Sotto 55, 53100 Siena, Italy*
[2] *ASI Science Data Center (ASDC), Via del Politecnico snc, 00133 Rome, Italy*
[3] *Instituto Nacional de Pesquisas Espaciais (INPE), São José dos Campos, Brazil*
[4] *Instituto de Investigación, Escuela de Ciencias Físicas y Matemáticas, Universidad de San Carlos de Guatemala, Guatemala*

Abstract. MIRAX (Monitor e Imageador de Raios X) is a satellite mission designed to monitor the hard X-ray and soft gamma-ray part of the sky (5 - 200 keV). Its principal instrument is an X-ray camera that makes use of a coded mask and solid-state (CZT) detectors. With its wide field of view (20×20 degrees) MIRAX will study variable sources such as accreting neutron stars (NS), black holes (BH), active galactic nuclei and both short and long gamma-ray bursts (GRBs). In this work we present an estimation on how many GRBs MIRAX will be able to detect during its low-earth near equatorial orbit (90 min). We perform Monte Carlo simulations with GEANT4 to reproduce the interaction of the cosmic diffuse background with the detector material, and image reconstructions for different known GRB sources at different positions in the field of view. We also compute MIRAX sensitivity curve over the energy detection range, and estimate the redshift range for which a GRB will be detectable by MIRAX as a function of the flux.

1. Introduction

Gamma-ray bursts (GRBs) are short and intense flashes of radiation observed in the γ-ray and X-ray band. With a radiated energy $\sim 10^{53}$ erg they constitute the most energetic events in the Universe. GRBs present a typical duration of a few seconds (Gehrels et al. 2009) and have been associated with massive star forming regions.

The GRB prompt emission spectrum in the keV - MeV range is typically best fitted by the so-called Band function, which consists of two power laws joined smoothly at a given break energy (Band et al. 1993). However, some bursts present a clear deviation from this function.

Based on their duration, two types of bursts have been clearly differentiated: the long GRBs with durations longer than 2 s and the short GRBs with durations shorter than 2 s (Kouveliotou et al. 1993). The difference between the two classes seems to be related to the nature of the progenitor. Long GRB progenitors are believed to be directly related to the death of massive stars, while Short GRB
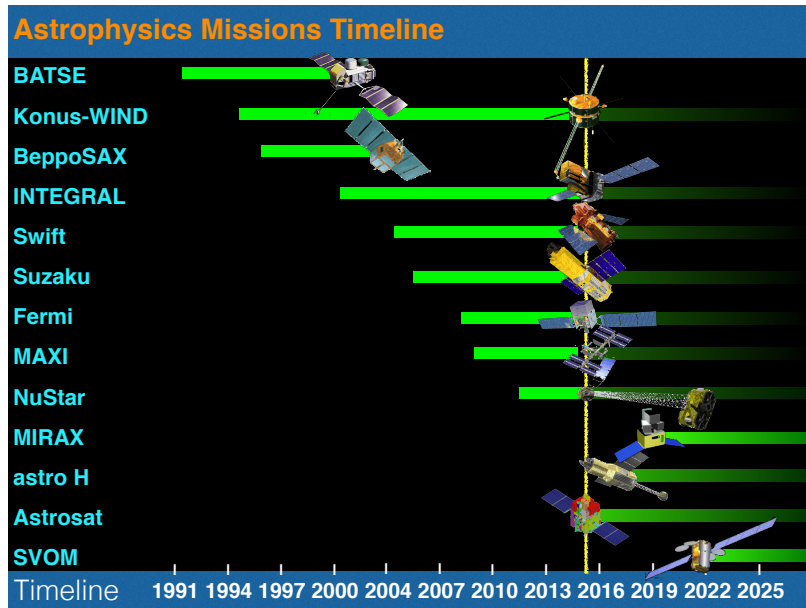
Figure 1.   Past, present and future missions for GRB science. Reproduced from Sacahui et al. (2016).

progenitors are suspected to be compact object binary mergers (NS-NS or NS-BH). If short GRBs are in fact related to compact object mergers, they are expected to play an extremely important role as electromagnetic counterparts of gravitational wave sources detected by Advanced LIGO, and hopefully Virgo, detectors (Camp et al. 2015).

GRBs are important tools to study properties of the high redshift Universe. Because of their importance, many instruments on space missions (Gehrels et al. 1994; Gehrels & Swift 2004; Meegan et al. 2009; Atwood et al. 2009) have studied GRBs over the last ∼ 25 years. In this context, it is crucial that future missions continue to contribute to this field.

Many important GRB missions such as Swift and Fermi are approaching the end of their lives, and we are possibly entering in a dark period for GRB observations (see Figure 1). The MIRAX (Monitor e Imageador de RAios-X) experiment, scheduled to be launched in ∼ 2020, will play a crucial role by virtue of its wide field and wide band X-ray/low energy γ-ray coverage. MIRAX will have the capability to detect transient events such as GRBs and will complement other observatories operating at higher energies such as HAWC and CTA (HAWC collaboration et al. 2012; Bouvier et al. 2011) in order to better understand these phenomena.

2.   The MIRAX mission

MIRAX is a hard X-ray mission which is part of the space science program at the Brazilian National Institute for Space Research (INPE) (Braga et al. 2004).
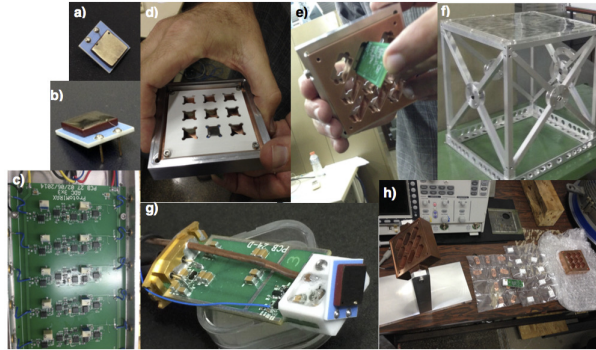
Figure 2. Different components of the protoMIRAX experiment: a) and b) CZT detectors; c) ADC converter; d) and e) 3×3 prototype support for the detectors; f) X-ray camera support with the coded-mask; g) CZT detector connected to the electronic circuit; h) all the components being mounted in the laboratory.

This mission constitutes the first Brazilian-led space observatory dedicated to astrophysics. The MIRAX camera will be tested in late 2016 in protoMIRAX, a balloon experiment (Penacchioni et al. 2015) that will fly at an altitude of ~ 42 km. In protoMIRAX the camera will be mounted in a balloon gondola with an attitude control and pointing systems, which will provide a 500kbps telemetry and command capability for real-time operation and data acquisition. The camera includes a coded mask (Gottesman & Fenimore 1989) based on an extended (2×2) pattern of a 13×13 Modified Uniformly Redundant Array (MURA). The mask elements are made of lead with 20 mm $\times$ 20 mm of area and 1mm thickness. The mask will be placed 650 mm away from a position-sensitive detector plane. The detector plane is made of an array of 13×13 CZT (Cadmium Zinc Telluride) planar detectors with dimensions 10 mm $\times$ 10 mm $\times$ 2 mm, which will give an energy coverage of ~ 10 - 200 keV for MIRAX and 30 - 200 keV for protoMIRAX (the lower detection energy for protoMIRAX is 30 keV instead of 10 keV due to the atmospheric absorption, since it is a balloon experiment). Each detector is separated from its neighbours by a 10-mm gap.

With such a design the camera will have a $1°45'$ angular resolution and a fully-coded field of view (FCFOV) of $\sim 20° \times 20°$. The MIRAX scanning geometry, with pointing direction off- set $25°$ to the south of zenith, has been chosen to emphasize the Galactic bulge and adjoining southern Galactic plane, but also covers a large portion of the extragalactic sky. A detailed explanation on the X-ray camera, the detectors, the scientific data acquisition subsystem, the coded mask, etc, can be found in Braga et al. 2015.

Figure 2 shows some of the components that are part of the protoMIRAX experiment, including a 3×3 prototype. All of them (except for the detectors) were made at INPE and will be assembled in the balloon gondola to fly in 2016.
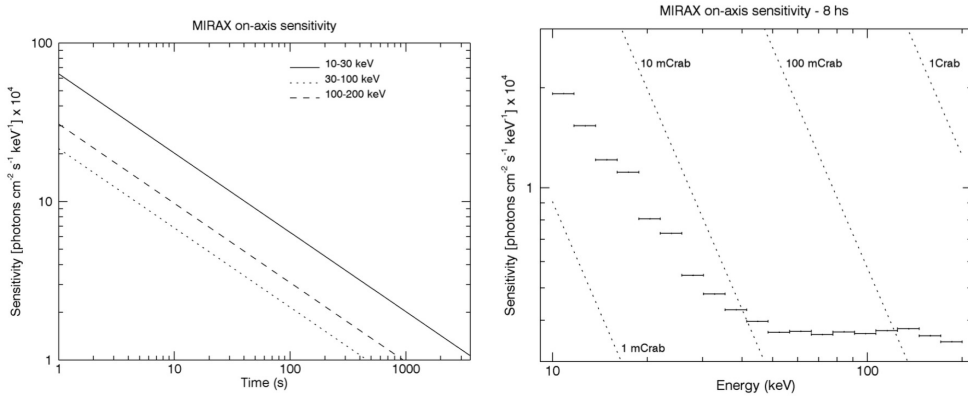
Figure 3. *Left:* MIRAX on-axis sensitivity curve for 8 hours of observation. Spectra in terms of Crab units and shown for comparison. *Right:* Sensitivity curve for MIRAX as a function of time, in different energy bands: 10-30 keV (solid line), 30-100 keV (dotted line) and 100-200 keV (dashed line). Reproduced from Sacahui et al. (2016).

3. MIRAX sensitivity

The sensitivity of the experiment in terms of the minimum detectable flux (F_{min}) with a particular statistical significance is calculated as:

$$F_{min} = \frac{N_\sigma}{\epsilon \, \Delta E} \sqrt{\frac{B}{A_{geo} \, T}} \; \text{photons} \, \text{cm}^{-2} \, \text{s}^{-1} \, \text{keV}^{-1}, \qquad (1)$$

where ϵ is the detector efficiency, ΔE is the energy interval (in keV) under consideration, A_{geo} is the detector geometrical area, T is the integration time in seconds, and B is the background level in counts $\text{cm}^{-2} \, \text{s}^{-1}$ that was derived from simulations (Castro et al. in preparation). For this work we consider a signal to noise ratio $N_\sigma = 5$.

Figure 3 shows MIRAX on-axis sensitivity curve for 8 hours of observation and as a function of time, in different energy bands.

4. Time variability and GRB rate expected with MIRAX

MIRAX will be able to detect variability in X-rays from fractions of a second (for short GRBs prompt emission) up to several minutes (long GRBs prompt emission and afterglows for both families). Figure 4 shows a plot of the X-ray luminosity as a function of variability (in seconds). The coloured boxes indicate the luminosity range and the time variability of short GRBs, long GRBs and their afterglows, while the dashed lines indicate the maximum distance at which this time variability will be detected by MIRAX for a given X-ray luminosity.

The number of GRBs expected to be detected per year by MIRAX can be calculated as follows. According to Lien et al. 2015, there are 4571^{+829}_{-1584} GRBs per year that are beamed towards us in the whole Universe. MIRAX FoV is
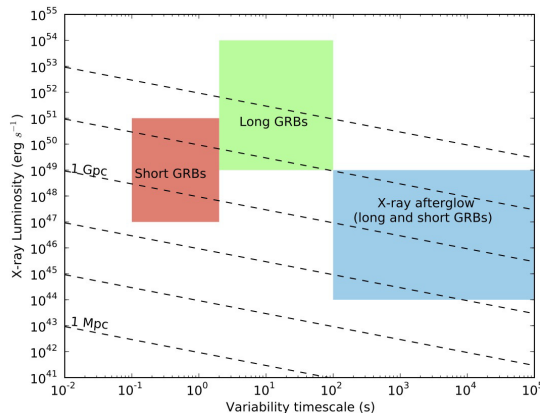
Figure 4. Maximum distance at which GRB time-variability will be detected by MIRAX according to their typical X-ray luminosities. The red box represents the typical time variability (of the order of fractions of a second) and luminosity range for short GRBs (prompt emission), while the green and blue boxes represent the same for long GRBs prompt emission (of the order of seconds) and their afterglows (from minutes to days), respectively. Reproduced from Sacahui et al. (2016).

$20° \times 20°$, which corresponds to 0.121 sr. For this fraction of the sky that will be covered by MIRAX, we expect to detect 44^{+8}_{15} GRBs yr^{-1}.

5. Conclusions

MIRAX is expected to be the first Brazilian-led astronomical satellite project, with strong international partnership with the United States and Europe. It will open a new high-energy astrophysics observational window for the Brazilian community. Among MIRAX science objectives is its capability of providing simultaneous spectral and temporal coverage of the evolution of a large number of Galactic accreting BH and NS systems, including a detailed characterisation of the spectral state transitions in these systems. MIRAX will also be able to measure AGN variability and detect extragalactic objects like GRBs with an advantage given by its wide-band spectral capability. In the case of short-hard GRBs, there is the very exciting possibility to perform simultaneous measurements with Advanced LIGO to search for gravitational waves. In the case of long GRBs, we will be able to measure the incident flux with sub-second resolution (depending on the source luminosity) and produce detailed light curves, which will show the late prompt emission and early afterglow decay, sometimes reaching the X- ray plateau.

In this paper, we show that MIRAX will be able to detect ~ 44 GRBs/year with good sensitivity and produce wide band spectra and light curves for the prompt emission and the early X-ray afterglow.

References

Atwood, W. B., Abdo, A. A., Ackermann, M., et al. 2009, ApJ, 697, 1071

Band, D., Matteson, J., Ford, L., et al. 1993, ApJ, 413, 281

Bouvier, A., Gilmore, R., Connaughton, V., et al. 2011, arXiv:1109.5680

Braga, J., Rothschild, R., Heise, J., et al. 2004, Advances in Space Research, 34, 2657

Braga, J., D'Amico, F., Avila, M. A. C., et al. 2015, A&A, 580, A108

Camp, J., Blackburn, L., Briggs, M., et al. 2015, arXiv:1506.02628

Castro, M.A., Braga, J., D'Amico, F., Penacchioni, A. & Sacahui, J.R. in preparation

Gehrels, N., Chipman, E., & Kniffen, D. 1994, The Astrophysical Journal Supplement Series, 92, 351

Gehrels, N. & Swift. 2004, in Bulletin of the American Astronomical Society, Vol. 36, American Astronomical Society Meeting Abstracts, 116.01

Gehrels, N., Ramirez-Ruiz, E., & Fox, D. B. 2009, Annual Review of Astronomy and Astrophys, 47, 567

Gottesman, S. R. & Fenimore, E. E. 1989, 28, 4344

HAWC collaboration, Abeysekara, A. U., Aguilar, J. A., et al. 2012, Astroparticle Physics, 35, 641

Kouveliotou, C., Meegan, C. A., Fishman, G. J., et al. 1993, ApJ, 413, L101

Lien, A., Sakamoto, T., Gehrels, N., et al. 2015, ApJ, 806, 276

Meegan, C., Lichti, G., Bhat, P. N., et al. 2009, ApJ, 702, 791

Penacchioni, A. V., Braga, J., Castro, M. A., & D'Amico, F. 2015, Journal of High Energy Astrophysics, 5, 22

Sacahui, J.R. et al. 2016, Journal of High Energy Astrophysics, 9-10, 16

Spectral energy distribution, polarization, and synthetic radio maps of Cygnus X-1: a lepto-hadronic jet model

C. Pepe,[1] G.S. Vila[1] and G.E. Romero[1,2]

[1]*Instituto Argentino de Radioastronomía (IAR-CONICET), C.C. 5,
(1894) Villa Elisa, Buenos Aires, Argentina*
[2]*Facultad de Ciencias Astronómicas y Geofísicas, Universidad Nacional
de La Plata (FCAG-UNLP), Paseo del Bosque S/N, (1900) La Plata,
Buenos Aires, Argentina*

Abstract. In this work we combine SEDs, radio maps and polarization observations to understand the emission mechanisms in Cygnus X-1. Our radiative model indicates that the MeV emission originates in the jet and that all the very high-energy emission is from hadronic origin. We also performed a synthetic radio map that suggests that our description of the magnetic field should be improved, since it leads to a very compact emission region. In order to choose the most suitable magnetic field geometry, we investigated the polarization in X-rays and we found that a very simple geometry can explain the high levels of polarization reported by other authors.

1. Introduction

Cygnus X-1 (Cyg X-1) is probably the most widely monitored microquasar (MQ) in the Galaxy. The binary system, located at 1.86 kpc from Earth (Reid et al. 2011), is composed of a high-mass star (spectral type O9.7 Iab and mass $\sim 20\ M_\odot$) and a black hole of 14.8 $M_\odot$ (Orosz et al. 2011).

A very complete broadband spectral energy distribution (SED) is available for Cyg X-1 in the hard state (for a compilation of the data see Zdziarski et al. 2014), including gamma-ray detections and upper limits at GeV energies and above (Albert et al. 2007, Malyshev et al. 2013). The origin of the soft gamma rays ($\sim$ MeV), in particular, is still unknown: there is no agreement about whether they originate in the jets or somewhere else in the accretion flow. This is one of the issues we assess in this work.

Jets in Cyg X-1 have been resolved in the radio band (Stirling et al. 2001). The outflow is extremely collimated and mildly relativistic. The extension and geometry of the radio emission region may provide complementary, useful information about the conditions in the jets, such as the size and location of the acceleration region of relativistic particles, and the magnetic field.

Finally, while polarization data at low energies have been long available for Cyg X-1 (see Russell et al. 2013 for a compilation), high levels of polarization in the X rays/soft gamma rays have been measured recently for the first time (Laurent et al. 2011, Rodríguez et al. 2015). Polarization studies of the jet radiation can help settle the issue of the origin of the MeV tail.
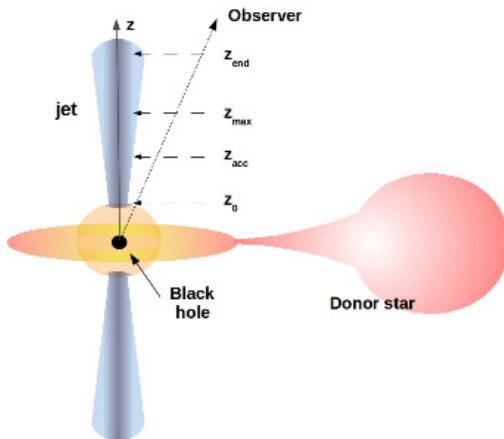
Figure 1.   Basic sketch of the binary and the jet (not to scale). Credit:
Pepe et al, A&A, 584, A95, 2015, reproduced with permission ©ESO.

In this work, we combine these three different sources of data (non-thermal
SED, radio images and polarization measurements) to obtain information about
the conditions in the jets of Cyg X-1. In Sections 2 and 3, we briefly review the
radiative model - developed in detail in Pepe et al. (2015) - and its application to
the generation of synthetic radio maps. In Section 4, we present our preliminary
results for the degree of polarization of the jet synchrotron emission. Finally, in
Section 5 we discuss our conclusions and perspectives for future work.

2.   Radiative processes

In this section we describe the modelling of the radiative output of Cyg X-1. The
reader is referred to Pepe et al. (2015) for details. We adopt a conical shape for
the jet, see Fig. 1. The jet base is located at a distance $z_0 = 1.1 \times 10^8$ cm from
the compact object. Relativistic particles are injected in a region that starts at
$z_{acc} = 2.2 \times 10^8$ cm and extends up to $z_{max} = 8.6 \times 10^{11}$ cm. The jet ends
(for computing purposes) at $z_{end} = 1.0 \times 10^{15}$ cm. The magnetic field at the
base, $B_0 = 5.0 \times 10^7$ G, is estimated from equipartition between the magnetic
and kinetic energy densities and it decays as $B(z) = B_0(z_0/z)$. Given the total
power of the jet L_{jet}, a power

$$L_{rel} = q_{rel}L_{jet} \qquad q_{rel} = 0.1 \tag{1}$$

is transferred to the relativistic particles in the acceleration region, which, in
turn, is distributed between electrons and protons as $L_p = aL_e$ with $a = 0.07$.
     Relativistic particles are injected in the jet according to the injection func-
tion

$$Q(E, z) = Q_0 \, E^{-\Gamma} \, \exp\left[-E/E_{max}(z)\right]. \tag{2}$$

Here, Q_0 is a normalization constant obtained from the total power injected in each particle species and Γ is the spectral index. The injection function is different from zero only in the region $z_{\mathrm{acc}} \leq z \leq z_{\mathrm{max}}$ and for $E \geq E_{\mathrm{min}}$. The cutoff energy E_{max} is calculated equating the total particle energy loss rate and the acceleration rate (e.g. Aharonian 2004); we adopt $E_{\mathrm{min}} = 120 m_0$, where m_0 is the rest mass of the particles.

Radiative cooling is calculated for all particles. Leptons cool via synchrotron, relativistic Bremsstrahlung and inverse Compton. For this last process we consider three different photon targets: electron synchrotron radiation (SSC), the radiation field of the companion star (IC-Star) and the X-ray photons from the accretion disk (IC-Disk). Protons cool via synchrotron, proton-proton (pp) and proton-photon ($p\gamma$) interactions. In the case of pp collisions the targets are the thermal protons in the jet and in the stellar wind (pp-Star). The number density of protons in the wind is calculated from the continuity equation and the standard velocity profile of massive stars. The photons for $p\gamma$ interactions are those of the radiation field of the companion star and the synchrotron field of primary electrons. All particles cool via adiabatic losses. In the case of electrons, synchrotron losses are dominant until the end of the jet, while in the case of protons adiabatic losses govern the cooling nearly all along the jet.

Once the cooling rates and the injection functions are calculated, we solve the steady-state transport equation for the particle distributions $N(E, z)$,

$$v_{\mathrm{conv}} \frac{\partial N}{\partial z} + \frac{\partial}{\partial E} \left(\frac{dE}{dt} \bigg|_{\mathrm{tot}} N \right) = Q(E, z), \tag{3}$$

for both protons and electrons. The convection velocity is on the order of the jet bulk velocity, $v_{\mathrm{conv}} \approx v_{\mathrm{jet}}$. The resulting electron and proton distributions are shown in Fig. 2. Energetic protons can be found well outside the acceleration region, but electrons cool almost immediately after they leave the acceleration region.
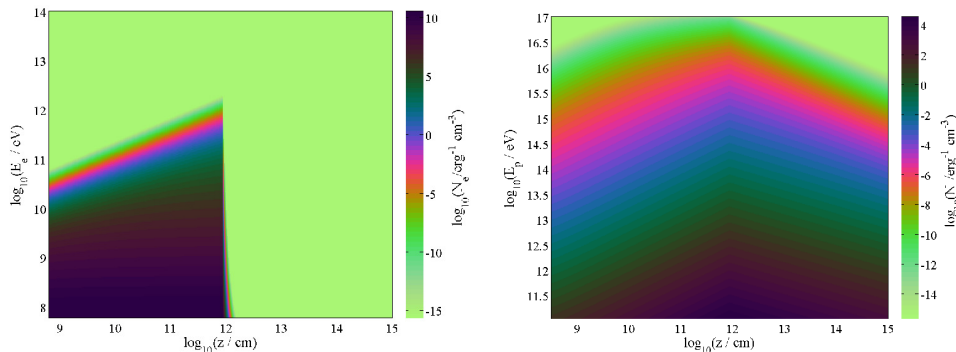

Figure 2.   Steady-state distribution of electrons (left) and protons (right). Credit: Pepe et al, A&A, 584, A95, 2015, reproduced with permission ©ESO.

Once the particle distributions are known, we then obtain the specific luminosity in the observer reference frame (in erg s^{-1} sr^{-1}) at photon energy E_γ as

$$L_\gamma(E_\gamma) = E_\gamma \int_V q_\gamma \, dV, \qquad (4)$$

where V is the volume of the emission region and q_γ the volume emissivity. In Fig. 3 we show our best-fit SED as well as the broadband data for Cyg X-1. In this model, the non-thermal emission from radio wavelengths to the the MeV tail is well described as synchrotron radiation from electrons in the jet. Note that all the emission above 10 GeV is exclusively of hadronic origin. Furthermore, it is very close to the detections limits of MAGIC and CTA. If this emission were detected, it would be an indicator of the presence of protons in the outflows of Cyg X-1.[1]
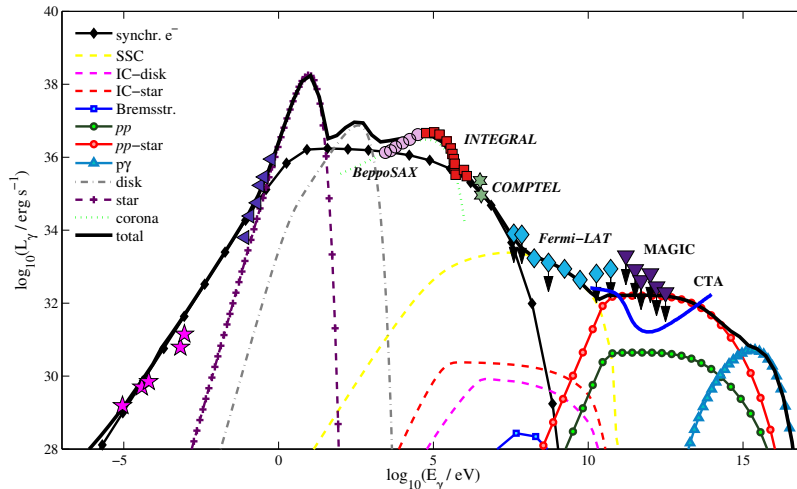
Figure 3.   Best-fit spectral energy distribution for Cygnus X-1. Down-pointing arrows indicate upper limits. The data are not simultaneous. Some relevant parameters are $L_{jet} = 3.6 \times 10^{37}$ erg/s, $\Gamma = 2$ and $v_{\rm jet} = 1.8 \times 10^{10}$ cm s^{-1}. See Pepe et al. (2015) for details on the sources of the data. Credit: Pepe et al, A&A, 584, A95, 2015, reproduced with permission ©ESO.

3. Radio maps

In this section we describe the procedure and results of our modelling of the radio emission region. We integrate the volume emissivity q_γ along the line of sight and then convolve it with a bidimensional Gaussian function of full width

---

[1]So far, heavy nuclei have been detected in the jets of only two MQs: SS 433 and 4U 1630C47.
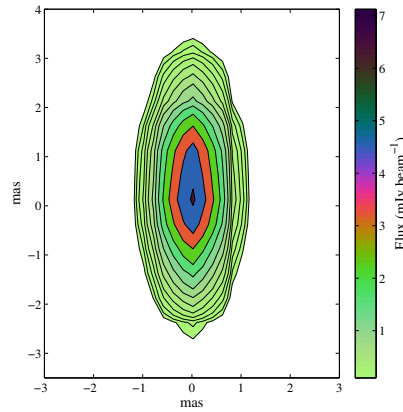
Figure 4.   Image of the jet at 8.4 GHz after convolution with a Gaussian beam of 2.25×0.86 mas^2. The origin of coordinates is chosen to coincide with the position of the flux maximum. Contours are spaced in factors of $\sqrt{2}$; the lowest contour corresponds to 0.1 mJy beam^{-1}. Credit: Pepe et al, A&A, 584, A95, 2015, reproduced with permission ©ESO.

at half maximum (FWHM) of 2.25×0.86 mas^2 to mimic the effect of an array with a beam as in Fig. 3 of Stirling et al. (2001); the chosen separation between pointings was of one beam radius in each direction. The result is shown in Fig. 4. The flux levels are comparable to those measured by Stirling et al. (2001); the extension of the emitting region, however, is smaller. This may be an indication that our modelling of the acceleration region (size and/or position) and/or the magnetic field should be revised.
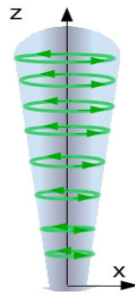
Figure 5.   A toroidal magnetic field geometry is explored.   The z direction is parallel to the jet axis.

4.   Synchrotron polarization

Polarization depends directly on the magnetic field strength and configuration. Hence, we study the polarization of the emitted radiation as a means of testing

our description of the magnetic field in the jet. We particularly focus on the polarization of the MeV radiation in order to compare our results with the recent measurements in that energy range. We follow Korchakov & Sirovatskii (1962) for the calculation of the degree of polarization. We compute the Stokes parameters from first principles, i.e., for completely general shapes of the magnetic field and particle distributions. We explore a simple geometry for the magnetic field; see Fig. 5. The magnetic field intensity decays with the coordinate z as stated in Section 2. Our calculations indicate levels of polarization $\rho \sim 75\%$, comparable to those reported by Laurent et al. (2011) and Rodriguez et al. (2013).

5.   Conclusions

In this paper we present our latest results for the modelling of the broadband emission of Cyg X-1. Our model indicates that the most energetic emission of this source is dominated by hadronic processes and that the MeV tail has a leptonic origin in the jets. We also obtain a flux of synchrotron radio emission consistent with observations. However, the compactness of the synthetic radio source indicates that our description of the magnetic field and/or the acceleration zones needs to be improved. Our first investigations of the polarization of the radiation in the MeV band show that a very simple field geometry can account for the observed level of polarization. In future works, we expect to further exploit the radio and polarization measurements to improve our modelling of the jets. In this regard, we will improve our description of the jet magnetic field by considering more realistic geometries and explore other configurations for the particle (re-)acceleration zones.

References

Aharonian, F. A. 2004, *Very high energy cosmic gamma radiation: a crucial window on the extreme Universe*, World Scientific Publishing, Singapore

Albert, J., Aliu, E., Anderhub, H., et al. 2007, ApJ, 665, L51

Fender, R. P., Pooley, G. G., Durouchoux, P., et al. 2000, MNRAS, 312, 853

Korchakov, A. A. & Sirovatskii, S. I. 1962, Soviet Astronomy, 5, 678

Laurent, P., Rodriguez, J., Wilms, J., et al. 2011, Science, 332, 438

Malyshev, D., Zdziarski, A. A., & Chernyakova, M. 2013, MNRAS, 434, 2380

Orosz, J. A., McClintock, J. E., Aufdenberg, J. P., et al. 2011, ApJ, 742, 84

Pepe, C., Vila, G. S. & Romero, G.E., 2015, A&A, 584, A95

Reid, M. J., McClintock, J. E., et al. 2011, BAAS, Vol. 43, 217, 223.01

Rodriguez, J., Grinberg, V., Laurent, P., et al. 2015, ApJ, 807, 17

Russell, D. M. & Shahbaz, T. 2014, MNRAS, 438, 2083

Sabatini, S., Tavani, M., Striani, E., et al. 2010, ApJ, 712, L10

Stirling, A. M., Spencer, R. E., et al. 2001, MNRAS, 327, 1273

Zdziarski, A. A., Pjanka, P., et al. 2014, MNRAS, 442, 3243

High Energy Processes in Protostellar Jets

A. Rodríguez-Kamenetzky[1], C. Carrasco-González[2], A. Araudo[3],
J.M. Torrelles[4], G. Anglada[5], J. Martí[6], L.F. Rodríguez[2], C. Valotto[1]

[1]*Instituto de Astronomía Teórica y Experimental
(IATE-CONICET-UNC)*
[2]*Instituto de Radioastronomía y Astrofísica (UNAM)*
[3]*University of Oxford, Department of Physics*
[4]*Institut de Ciències de l'Espai (CSIC-IEEC) and Institut de Ciències
del Cosmos (UB-IEEC)*
[5]*Instituto de Astrofísica de Andalucía (CSIC)*
[6]*Universidad de Jaén, Dept. de Física, EPS de Jaén*

Abstract. In the last years the presence of synchrotron emission has been proposed in a handful of protostellar jets. However, it is yet unclear how this "slow" jets could be able to accelerate particles up to relativistic velocities in order to emit detectable synchrotron emission. One of the most likely possibilities is that particles are accelerated in strong shocks of the jet against the dense envelopes surrounding the protostar. Particle acceleration has been studied in several astrophysical systems (AGN's, microquasars, SN, massive binaries, etc.), nevertheless, in YSO is a fairly new phenomenon. Here, we present the analysis of high sensitivity continuum and linearly polarized images at several frequencies of one of the most characteristic non-thermal protostellar jets: The Triple Radio Source in Serpens.

1. Introduction

Radio emission from protostellar jets is well known to be of thermal nature with a characteristic positive spectral index at centimeter wavelengths (Anglada et al. 1998). However, in the last years a handful of protostellar radio jets has been detected showing negative spectral indices, suggestive of non-thermal emission (Rodríguez et al. 1989, Martí et al. 1993, Garay et al. 1996, Rodríguez et al. 2005, Wilner et al. 1999, Girart et al. 2002). Several authors proposed that the non-thermal nature of this emission could be related to synchrotron emission. This possibility was recently confirmed after the detection of linearly polarized emission in of the HH 80-81 massive protostellar jet (Carrasco-Gonzalez et al. 2010). This discovery triggered an observational campaign to study the synchrotron emission in a sample of protostellar jets.

The Serpens star-forming region, located at a distance of $\sim$415 pc (Dzib et al. 2010), contains one of the first protostellar radio jets proposed to be a synchrotron emitter: the Triple Radio Source in Serpens. Protostellar jets usually show a simple morphology at radio frequencies, consisting of an elongated source with a positive spectral index interpreted as free-free emission from ionized material tracing out the base of the large-scale jet (Anglada et al. 1998). The triple

source in Serpens also shows this central free-free radio source, but it also shows non-thermal radio knots located at larger distances from the central protostar (Rodríguez et al. 1989, Curiel et al. 1993). The most likely scenario to explain the presence of these non-thermal radio knots is that they are tracing strong shocks against the ambient medium where it is possible to accelerate particles that emit synchrotron radiation. In this situation, particles could gain energy by diffusing back and forth across a shock front (e.g., Drury 1991). This process, known as diffusive shock acceleration (DSA), allows that particles originally moving at a few hundreds of kilometers per second can reach relativistic velocities. However, this phenomenon only seems to be possible in some protostellar jets.

In this proceeding, we present a brief analysis of new and archive data at radio wavelengths of the Triple Radio Source in Serpens, and discuss the results in the context of particle acceleration and synchrotron emission production. Detailed analysis and discussion are reported in Rodríguez-Kamenetzky et al. (2016).

2. Observations

Observations of the Triple Radio Source in Serpens were made with the Karl G. Jansky Very Large Array (VLA) of the National Radio Astronomy Observatory (NRAO)[1]. We observed the continuum emission in the S, C, and X bands in B configuration during June 12 and 16, 2012 (project code: 12A-240). For each band, we observed a total continuum bandwidth of 2 GHz covering the frequency ranges 2-4 GHz, 4.5-6.5 GHz, and 8-10 GHz, in S, C, and X bands, respectively. The phase center of our observations was α(J2000)=$18^h29^m49.8^s$, δ(J2000)=$+01°15'20.6''$. We also analyzed VLA archive data taken at C band in the A configuration at 8 epochs spanning 18 years, from 1993 to 2011. Calibration of the data was performed with the data reduction package CASA (Common Astronomy Software Applications[2]; version 4.1.0) following standard VLA procedures.

3. Results

The Triple Radio Source in Serpens shows a morphology consisting of a central thermal (positive spectral index) radio continuum source, and two outer non-thermal lobes (negative spectral indices). The outer knots show proper motions of the order of a few hundred kilometers per second, suggesting they are tracing out the motion of the jet against the ambient medium (Rodríguez et al. 1989, Curiel et al. 1993).

In Figure 1 we show the continuum image (contours) obtained by using all the B configuration data in S, C and X bands, as well as a spectral index map (color scale) obtained from the multifrequency synthesis cleaning. In this figure,

---

[1]The NRAO is a facility of the National Science Foundation operated under cooperative agreement by Associated Universities, Inc.

[2]https://science.nrao.edu/facilities/vla/data-processing

the jet-like morphology of the Serpens triple source is clearly seen. We identify four compact components: a central elongated source (C) and three outer knots (NW, NW_C and SE). The three components C, NW_C, y NW are connected by extended emission, whereas no similar extended emission is detected connecting the central source to the SE component. The SE knot appears splitted in two different components labeled as SE_N and SE_S (separated by $\sim 1.2''$), clearly seen in the higher angular resolution images. In the following we discuss the characteristics of the radio jet.

3.1. Spectral Indices and Spectral Energy Distributions

In order to study the nature of the radio emission in the triple source in Serpens, we obtained a spectral index map (Figure 1), and the spectral energy distribution (SED) for each of the compact components in the jet. Both, the spectral index map and the SEDs show a difference between the nature of the emission of the central component, the lobes, and the extended emission. The central source shows a clear positive spectral index (~ 0.3), suggesting partially optically thick free-free emission and in good agreement with those of thermal radio jets (e.g. Anglada et al. 2015). In contrast, the rest of the emission shows flat ($\alpha \sim 0$) or negative spectral indices, which suggests optically thin free-free emission and non-thermal emission, respectively. From the SEDs we obtained $\alpha = 0.28 \pm 0.02$ for the central source, and $\alpha \simeq -0.35$ for the external knots, in agreement with the spectral index map.

3.2. Polarization

We searched for linearly polarized emission at the observed wavelengths in our new VLA observations. These are the most sensitive data obtained so far in the Serpens region that allow polarization calibration. However, we did not detect linearly polarized emission from regions with negative spectral indices in the Triple Radio Source in Serpens (in none of the 2 GHz images we made). From this negative result, we estimated an upper limit for the polarization degree of 10%. This low value be due to a very disordered magnetic field in shock regions, or to strong Faraday depolarization effects, implying a high electronic density of the jet material. New, more sensitive observations should be needed in order to discern if linearly polarized emission is present in this protostellar radio jet.

3.3. Proper Motions

We study the kinematics of the different knots in the Serpens radio jet by analysing the multiepoch high angular resolution archive data at 6 GHz. Measuring their displacements in each epoch and assuming a distance of 415 pc to the Serpens molecular cloud, we estimated the tangential (i.e., in the plane of the sky) velocities of the knots. We found that the NW and SE_S tangential velocities are similar (~ 200 km s^{-1}), while the SE_N is moving faster (~ 300 km s^{-1}). The velocities of these three knots seem to be constant during the analyzed epochs. We also derived the position angles (P.A.s) for the motion of each component. Components NW, NW_C and SE_S seem to be moving with similar P.A.s in the range 132-136 degrees. In contrast, component SE_N seems to move in a different direction with a P.A. of 126 degrees. We also note that the central source appears elongated in all epochs with a PA of 119 ± 1
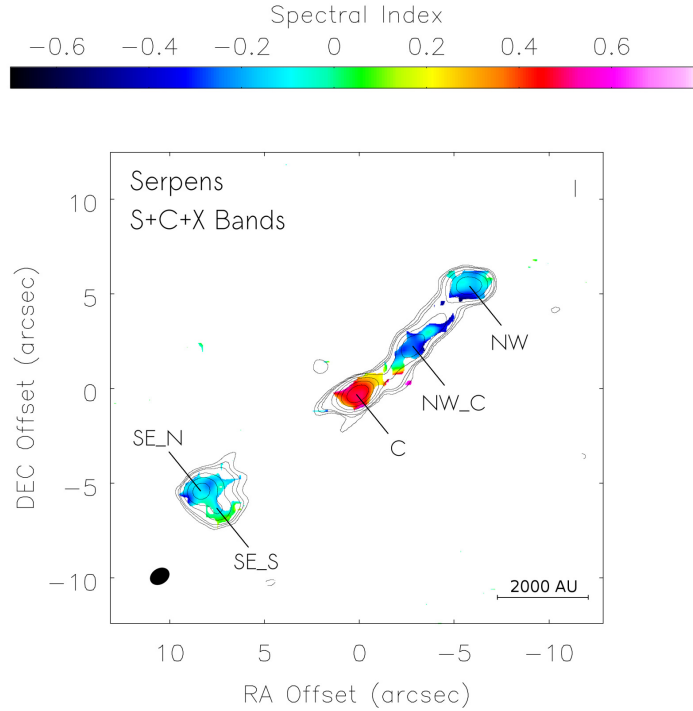
Figure 1.   Spatial distribution of spectral indices obtained from multifrequency synthesis cleaning in the frequency range of S, C, and X bands (color scale). The pixels shown are those with an error in the spectral index less than 0.1. This map suggest a clear difference in the emission nature from the powering source and the jet. White contours represent the radio continuum emission with total intensity corresponding to 4, 6, 8, 16, 31, 64, and 128 times the root mean square of the image. The synthesized beam size is $1.07'' \times 0.80''$ with a PA of $-58°$ (bottom left). The four components discussed in the paper are labeled. Reproduced from Rodríguez-Kamenetzky et. al (2016).

degrees, which is closer to the value obtained for the motion of SE_N. We interpret this behaviour as consistent with precession of the jet and episodic ejection phenomena.

4.   Discusion: On the particle acceleration and synchrotron emission

The intriguing aspect of particle acceleration in protostellar jets is to understand how these relatively slow jets are able to accelerate particles up to relativistic velocities. In the following, we discuss about the physical properties of the Triple Radio Source in Serpens and their relationship to the particle acceleration phenomenon.
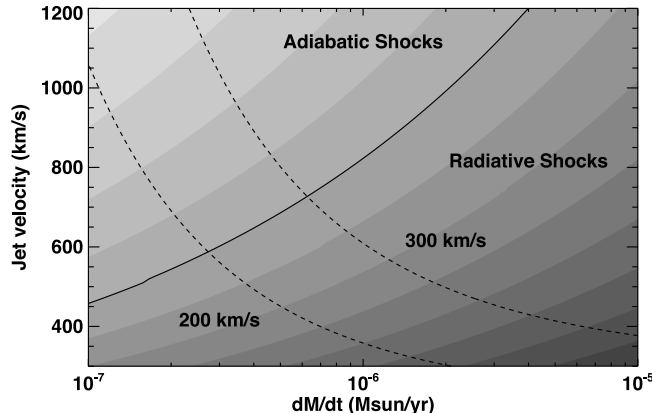
Figure 2. In order to identify jet conditions resulting in adiabatic shocks, the $d_{cool,rs}/r_{jet}$ ratio is plotted for different combinations of $\dot{M}$ and v_{jet} (grey scale). The solid line (corresponding to $d_{cool,rs} = r_{jet}$) separates regions where adiabatic and radiative shocks can take place, whereas dashed lines correspond to v_{bs}= 200 and 300 km s^{-1}. From this plot it can be inferred that a mass-loss rate $\dot{M} \lesssim 5 \times 10^{-7} M_{\odot}$ yr^{-1} and jet velocity $v_{jet} \gtrsim 500$ km s^{-1} are needed for the Mach disk to be an adiabatic shock. Reproduced from Rodríguez-Kamenetzky et. al (2016).

In Section 3.3 we have derived the proper motions ($\sim$200-300 km s^{-1}) of non-thermal ($\alpha \sim -0.35$) radio knots. We interpret the emission of these knots as synchrotron produced where the jet impacts against the ambient medium. Therefore, if the molecular cloud is denser than the jet at the position of the shock, the jet velocity should be larger than the velocities observed in the synchrotron radio knots since the material of the jet should slow down in the shock.

Synchrotron emission at 6 cm is produced by relativistic electrons with Lorentz factors $\gamma_6 \sim 60(B/mG)^{-1.5}$ in a magnetic field B. These particles can be accelerated in the bow shock with the ambient medium or in the jet reverse shock (Mach disk). The acceleration mechanism depends on the nature of the shocks, radiative or adiabatic (i.e. non-radiative). A way to discern whether the shocks are radiative or adiabatic is by comparing the thermal cooling distance d_{cool} with the radius of the jet at the position of the shock, r_{jet} (Blondin et al. 1989).

For the shocks against the molecular cloud we found $d_{cool,bs}/r_{jet} = 0.02$, implying a radiative origin for its emission. We also studied the necessary conditions in the reverse shock in order for it to be adiabatic. We explored different combinations of mass-loss rate and jet velocity, i.e. $10^{-7} \leq \dot{M} \leq 10^{-5}$ M$_{\odot}$ yr^{-1} and $400 \leq v_{jet} \leq 1200$ km s^{-1}. Then, given v_{jet} and $\dot{M}$, we calculate the number density of the jet n_{jet}, the bow-shock velocity v_{bs} and the reverse shock velocity v_{rs}. In this way, we can study if a given pair of v_{jet} and $\dot{M}$ results in an adiabatic or radiative reverse shock.

The results of the above procedure are shown in Figure 2. In this Figure, we show a line that separates the combinations of $\dot{M}$ and v_{jet} that result in an adiabatic reverse shock (i.e. $d_{cool,rs} > r_{jet}$) from those that result in radiative

reverse shocks. We also show two lines corresponding to $v_{bs} = 200$ and $300 \mathrm{~km~s^{-1}}$, the observed velocities of the bow-shocks. We can see that, in order to be the Mach disc a non-radiative shock, and the bow-shocks to move with the observed velocities, the jet should have a mass-loss rate $\dot{M} \lesssim 5 \times 10^{-7} \mathrm{~M_\odot~yr^{-1}}$ while the jet material should move at velocities $v_{jet} \gtrsim 500 \mathrm{~km~s^{-1}}$. This suggests that a jet with a typical mass-loss rate for an intermediate-mass protostar is able to accelerate particles via the DSA mechanism if the velocity of the jet is high enough.

5. Conclusions

We have presented an analysis of new and archive VLA observations of the Triple Radio Source in Serpens. Our results suggest that particle acceleration via DSA could be possible in jets from intermediate-mass protostars. The jet does not need to show very extreme characteristics, as a high mas-loss rate, but it seems to be only necessary that the jet reaches moderately high velocities ($\sim 600 \mathrm{~km~s^{-1}}$) at certain epochs.

From our analysis of the proper motions of the non-thermal radio knots we found that the jet is precessing and that non-thermal bow-shocks are excited only at certain epochs. This leads us to think that most of the time, the jet parameters do not meet the necessary conditions to produce efficiently relativistic particles in shocks.

Because of the episodic nature of the bow-shock, we speculate that periodic interactions of the driving source of the jet with a close companion could increase the jet velocity (and maybe also, to produce a slight increase in the mass-loss rate), giving rise to synchrotron emission in the shocks against the ambient medium.

References

Anglada, G., Villuendas, E., Estalella, R., et al. 1998, AJ, 116, 2953

Anglada, G., Rodríguez, L. F., & Carrasco-Gonzalez, C. 2015, Advancing Astrophysics with the Square Kilometre Array (AASKA14), PoS, 121

Blondin, J. M., Konigl, A., & Fryxell, B. A. 1989, ApJ, 337, L37

Carrasco-González, C., et al. 2010, Science, 330, 1209

Curiel, S., et al. 1993, ApJ, 415, 191

Drury, L. O. 1991, MNRAS, 251, 340

Dzib, S., Loinard, L., Mioduszewski, A. J., et al. 2010, ApJ, 718, 610

Garay, G., Ramirez, S., Rodriguez, L. F., et al. 1996, ApJ, 459, 193

Girart, J. M., et al. 2002, Rev. Mex. Astron. Astrofis., 38, 169

Martí, J., Rodríguez, L. F., & Reipurth, B. 1993, ApJ, 416, 208

Rodríguez, L. F., Curiel, S., Moran, J. M., et al. 1989, ApJ, 346, L85

Rodríguez, L. F., Garay, G., Brooks, K. J., & Mardones, D. 2005, ApJ, 626, 953

Rodríguez-Kamenetzky, A., et al. 2016, ApJ, 818, 27

Wilner, D. J., Reid, M. J., & Menten, K. M. 1999, ApJ, 513, 775

Extreme BL Lacs: probes for cosmology and UHECR candidates

F. Tavecchio and G. Bonnoli

INAF-OAB, Via Bianchi 47, 23807, Merate, Italy

Abstract. High-energy observations of extreme BL Lac objects, such as 1ES0229+200 or 1ES 0347–121, recently focused interest both for blazar and jet physics and for the implication on the extragalactic background light and intergalactic magnetic field estimate. Moreover, their enigmatic properties have been interpreted in a scenario in which their primary high-energy output is through a beam of high-energy hadrons. However, despite their possible important role in all these topics, the number of these extreme highly peaked BL Lac objects (EHBL) is still rather small. Aiming at increase their number, we selected a group of EHBL candidates considering those undetected (or only barely detected) by the LAT onboard *Fermi* and characterized by a high X-ray versus radio flux ratio. We assembled the multi-wavelength spectral energy distribution of the resulting 9 sources, using available archival data of *Swift*, *GALEX*, and *Fermi* satellites, confirming their nature. Through a simple one-zone synchrotron self-Compton model we estimate the expected very high energy flux, finding that in the majority of cases it is within the reach of present generation of Cherenkov arrays or of the forthcoming CTA.

1. Introduction

Intense emission of gamma rays is a distinctive feature of blazars, active galactic nuclei (AGN) dominated by the relativistically boosted non–thermal continuum from a relativistic (typical bulk Lorentz factors $\Gamma = 10 - 20$) jet pointing toward the observer. The spectral energy distribution (SED) of blazars displays two broad bumps, whose peak frequency appears to anti-correlate with the emitted luminosity – the so-called *blazar sequence* (Fossati et al. 1998, but see Giommi et al. 2005). The low energy (from radio to optical-UV bands) emission is clearly associated to synchrotron radiation from relativistic electrons (or pairs). The nature of the mechanisms responsible for the high-energy component, instead, is still debated. The most popular view adopts the so-called leptonic scenario (e.g. Ghisellini et al. 1998), in which the high energy radiation is interpreted as inverse-Compton emission by the same leptons responsible for the synchrotron component. Alternatively, hadronic models interpret the high-energy emission as either the by-product of cascades initiated by ultra-relativistic hadrons or synchrotron emission from high-energy protons (e.g. Muecke et al. 2003).

A quite interesting feature of blazars is the intense very high energy (VHE, $E > 100$ GeV) emission, characterizing in particular the subclass of BL Lac objects. The great majority of known TeV BL Lac objects have the maximum of the the high-energy component peaking in the 1-100 GeV band. Therefore,

typical VHE spectra of BL Lacs are soft. However, there is a (still) small group of TeV BL Lacs for which the maximum is located well above 1 TeV (e.g. Tavecchio et al. 2011). These so-called *extreme* HBL (Costamante et al. 2001) represent a challenging case for the standard leptonic scenario, apparently requiring a quite special physical set-up (e.g. Katarzyński et al. 2005, Tavecchio et al. 2009, Lefa et al. 2011). Besides the importance for blazar emission models, the extremely hard gamma-ray emission offer the ideal tool to probe absorption by the intervening extragalactic background light (EBL, e.g., Costamante 2013 and references therein), or to measure the tiny intergalactic magnetic field permeating the extragalactic space (e.g. Tavecchio et al. 2010, Neronov & Vovk 2010). In this context, EHBL offer also an useful tool to probe possible deviations of the gamma-ray propagation, related either to the mixing of photons with new particles (axion-like particles, e.g. De Angelis et al. 2011) or to the violation of the Lorentz invariance et high energy (e.g. Tavecchio & Bonnoli 2016).

Leptonic models do not naturally explain the quite limited variability of the VHE emission of EHBL, at odds with the extreme (both in amplitude and in time-scale) variability characterizing the high-energy emission of the average BL Lac population. This evidence is instead naturally reproduced in an alternative view, postulating that the observed very high energy (VHE) emission is the left-over of electromagnetic cascades, occurring in the intergalactic space, possibly triggered by a beam of high-energy hadrons produced in the jet of the EHBLs. In fact, high-energy hadrons (proton for simplicity) accelerated and beamed by the jet would interact with low energy background photons, producing neutral pions that, in turn, decay in ultra-high energy photons, which initiate a cascade. In this framework, misaligned jets of EHBL residing within the GZK horizon could contribute to the flux of ultra-high energy cosmic rays at the Earth since, in principle, the maximum energy attainable by protons in these jets is of the order of 10^{19} eV (Tavecchio 2014). A nice testable prediction of the model sketched above is that the existence of an observable hard tail above 10 TeV (energies at which, instead, due to the severe absorption leptonic models do not predict any detectable signal), see e.g. Murase et al. (2012).

The known EHBL are still quite a few. One reason for this situation is the strong bias of *Fermi*-LAT against the detection of EHBL which in the GeV band are characterized by a quite weak emission. With the aim of enlarging the sample of these extremely interesting sources, we started a program of selection of candidates EHBL based on the peculiar properties of the multifrequency SED of these sources. In the following we outline the selection procedure and the results. For more details we refer the reader to the paper by Bonnoli et al. (2015).

2.   Enlarging the EHBL population

A distinctive property of the SED of EHBL is to display a low radio flux together with a relatively bright X-ray emission. This feature provides an affective way to separate EHBL from the population of "normal" BL Lac objects. We exploit this strategy starting from a list of 71 BL Lac (Plotkin et al. 2011) resulting from the correlation of SDSS and FIRST surveys and by optical spectrum dominated by the host galaxy emission. We further select the sources with measured X-ray
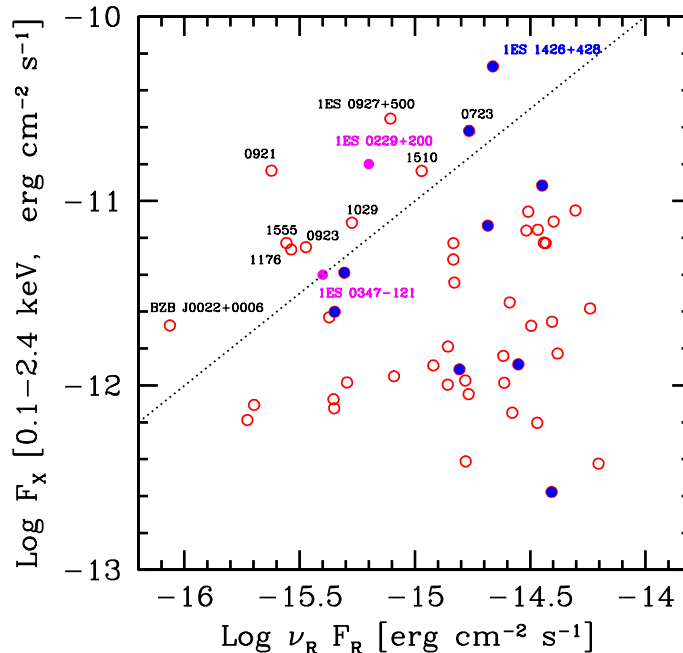
Figure 1. F_X–F_R plot for the sample of BL Lacs described in the
text. Red open circles represent the full sample; the blue circles are the
sources detected by LAT in the 1FGL catalogue. The 12 sources above
the black dotted diagonal line have a high ($F_X/F_R > 10^4$) ratio of X–
ray vs. radio flux. The magenta filled circles are the two archetypal
TeV detected, but GeV faint extreme BL Lacs, 1ES 0229+200 and 1ES
0347-121. Reproduced from Bonnoli et al. (2015).

flux (by *ROSAT*) and we restrict the redshift to $z < 0.4$, so that the absorption
of TeV gamma rays is not too large, obtaining a total of 50 BL Lacs.

The X-ray *vs.* the radio flux of the sources are shown in Fig. 1. According to
our criterion, we select the EHBL candidates among the sources residing in the
left upper corner of the plot (low radio flux, large X-ray flux), above the dotted
line. This choice is consistently supported by the fact that two prototypical
EHBL (1ES 0229+200 and 1ES 0347-121) appear in this region (magenta points).
Eliminating the already known EHBL, we obtained a total of 9 new candidates,
whose nature is further investigated using the SED.

We assembled the SED exploiting archival data (especially by *Swift* and
GALEX) and asking dedicated *Swift* pointings for RBS 0923 and RBS 1176, for
which previous observations were not available. *Swift* observations are crucial
for characterizing these sources, since UVOT and XRT data allow us to outline
the UV-X-ray continuum, a key band for the identification of EHBL. Indeed,
the shape of the low-energy (i.e. synchrotron) SED component of all the sources

confirm the EHBL nature of all selected candidates. In particular, for most of the sources the *Swift*/UVOT and *GALEX* data track the UV tail of the host galaxy, sometimes showing a hint of the expected hard jet emission at the highest frequencies. As expected, the slope of the X-ray spectra (which, we remark, was not used in the selection procedure) are on average flat (photon index around 2), indicating that the peak of the synchrotron component occurs in this band.

2.1.   Some interesting cases

In Fig. 2 we show the SED of two particularly interesting sources, together with a prediction of their VHE emission based on the one-zone synchrotron-self Compton model. We report two cases, corresponding to two values of the magnetic field ($B = 0.1$ and 0.01 G, red and blue lines respectively), expected to bracket the range valid for these sources. Modelling the synchrotron component, tracked by the UV-X-ray data, we derive the electron distribution which, in turn, allows us to specify the SSC component. The intrinsic SSC emission (solid line) is then corrected to take into account the absorption of gamma-rays through the interaction with the EBL (dashed lines).

RBS 1176 (left panel), displays a peculiar X-ray spectrum, with a rather hard slope at low energies. While it cannot be excluded that the lack of soft photons is related to absorption (intervening or internal), it is tempting to interpret the spectral break as directly linked to the electron distribution. In fact, the break can be well reproduced by assuming that the electrons follow a power law in energy, with a very large minimum energy $E_{\min} = 0.2$ TeV, so that the hard low-energy X-ray continuum is reproduced by the $\nu^{1/3}$ low-energy tail of the synchrotron emission of electrons with $E_{\min}$. In this case (black line in Fig. 2), the predicted SSC component would peak at energies well above 10 TeV, but the predicted flux would be vary low, due to the very small flux of the target low-energy synchrotron photons. The comparison with the CTA sensitivity curve (calculated for 50 hours of exposure and 5σ significance), shows that, in this case, the detection at VHE would be unlikely, also because the relatively large redshift causes a quite pronounced drop of the observed VHE flux.

The right panel of Fig. 2 instead shows a quite promising source, RBS 0921. The bright and hard X-ray continuum (indicating that the peak of the synchrotron component occurs at energies larger then several keV) translates into a relatively bright VHE component, possibly detectable even with current Cherenkov arrays such as MAGIC (light blue curve).

3.   Discussion and prospects

A generalization of our criterion, for instance relaxing the condition of the redshift, will allow us to extend the selection procedure to larger samples of BL Lacs (or, possibly, radio-loud AGN). A larger number of EHBL is especially important for improving our understanding about the far-IR EBL, IGMF and the extragalactic gamma-ray background. Exploiting the capability of *NuStar*, SKA, and CTA will also be particularly revealing. Even before the construction of the full CTA, the planned ASTRI/CTA mini–array (Vercellone et al. 2013) could be used in this direction. It is arguable that HAWC and later on LHAASO will effectively survey them in the local Universe.
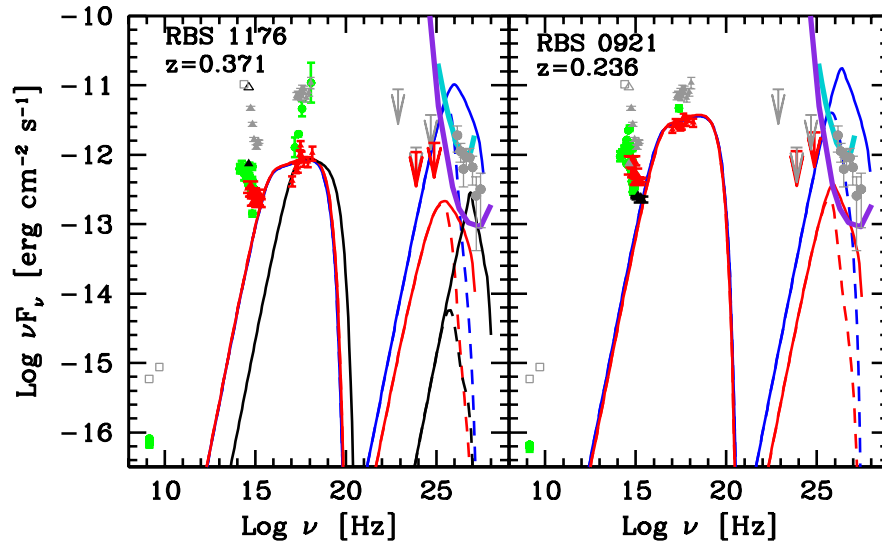
Figure 2. SED of two EHBL candidates selected in Bonnoli et al. (2015). Green symbols report historical data, red symbols show *Swift*/UVOT, XRT and *Fermi*/LAT data, black symbols display *GALEX* data. Background grey symbols show the SED of the prototypical EHBL 1ES 0229+200 for comparison. Two different models of the SED are reported, corresponding to low ($B = 0.01$ G, blue lines) and high ($B = 0.1$ G, red lines) magnetic field. Dashed lines show the model after absorption with the EBL. Green data in the optical-UV band trace the emission from the host galaxy, not accounted by our model. Light blue and violet curves report the differential sensitivities (5σ, 50 hours of exposure, 5 bins per energy decade) of MAGIC and CTA respectively. Adapted from Bonnoli et al. (2015).

An interesting topic to be addressed is the position of EHBLs within the general BL Lac population and, especially, the nature of their parent population. In the framework of the standard one-zone leptonic model the physical conditions within the EHBL jets appear to be different from that of the other EHBL, with rather low magnetic fields and large particle energies. It is not clear whether and how these differences are related to the other striking difference of EHBL, i.e. the very limited variability. The differences of EHBL could be somewhat related to the different parent population. By construction, the parent population are expected to have very faint radio emission (radio luminosities around $L_r \sim 10^{40}$ erg s^{-1}) indicating very weak radio jets (see Giroletti et al. 2004). Considering that at least a fraction of the radio flux comes from the beamed jet synchrotron component, we argue that the intrinsic radio luminosity drops below the lower end of the FRI radiogalaxy power range, making EHBLs suitable candidates for the aligned counterparts of the weak radiogalaxies population (dubbed FR 0) studied by Baldi & Capetti (2010), Baldi et al. (2015).

References

Baldi R. D., Capetti A., 2010, A&A, 519, A48
Baldi R. D., Capetti A., Giovannini G., 2015, A&A, 576, A38
Bonnoli G., et al. 2015, MNRAS, 451, 611
Costamante, L., Ghisellini, G., Giommi, P., et al. 2001, A&A, 371, 512
Costamante L., 2013, IJMPD, 22, 1330025
De Angelis, A., Galanti, G., & Roncadelli, M. 2011, Phys. Rev. D, 84, 105030
Fossati, G. et al. 1998, MNRAS, 299, 433
Ghisellini G., et al. 1998, MNRAS, 301, 451
Giroletti, M., et al. 2004, ApJ, 613, 752
Giommi, P. et al. 2005, A&A, 434, 385
Katarzyński, K., Ghisellini, G., Tavecchio, F., et al. 2005, A&A, 433, 479
Lefa, E., Rieger, F. M., & Aharonian, F. 2011, ApJ, 740, 64
Mücke, A., et al. 2003, Astroparticle Physics, 18, 593
Murase, K., et al. 2012, ApJ, 749, 63
Neronov, A., & Vovk, I. 2010, Science, 328, 73
Plotkin R. M., et al. 2011, MNRAS, 413, 805
Tavecchio, F., et al. 2009, MNRAS, 399, L59
Tavecchio, F., Ghisellini, G., Foschini, L., et al. 2010, MNRAS, 406, L70
Tavecchio, F., et al. 2011, MNRAS, 414, 3566
Tavecchio, F. 2014, MNRAS, 438, 3255
Tavecchio, F., Bonnoli, G. 2016, A&A, 585, 25
Vercellone, S., et al. 2013, arXiv:1307.5671

Review of the latest results from the Pierre Auger Observatory

Hernan Wahlberg [1] for the Pierre Auger Collaboration[2]

[1]*IFLP - Physics Department, Universidad Nacional de La Plata*
C.C. 67-1900 La Plata, Argentina.
[2] *Observatorio Pierre Auger, Av. San Martn Norte 304, 5613*
Malargüe, Argentina .
Full author list: http://www.auger.org/archive/authors_ 2015_ 09.html

Abstract. The Pierre Auger Observatory, located in the province of Mendoza, Argentina, was built for detecting and studying ultra-high energy cosmic rays. The Observatory was designed as a hybrid detector covering an area of 3000 km^2 and it has been taking data for more than ten years. In this report a selection of the latest results is presented. These include the observation of the flux evolution and suppression at the highest energies, inferred trends on composition with energy, bounds on photons and neutrinos, and arrival direction studies.

1. Introduction

The Pierre Auger Observatory (Aab et al. 2015) is located in the Province of Mendoza, Argentina. The design of the instrument is based on a hybrid system, a combination of a large surface-detector array (SD) and a fluorescence detector (FD), used to study cosmic rays with energies in excess of 10^{17} eV. The surface detector array, covering an area of over 3000 km^2, comprises 1660 stations, which are arranged on a triangular grid with 1500 m spacing. It samples the electromagnetic and muonic components of extensive air showers (EAS) at a given observation level, with a duty cycle of nearly 100%. The fluorescence detector consists of 27 optical telescopes overlooking the array. On clear moonless nights, these are used to observe the longitudinal development of the shower produced by the primary particle in the atmosphere, by detecting the fluorescence light produced by charged particles along the shower trajectory. The duty cycle of the FD is $\sim$ 13%. Extensions over the base design and future upgrades are summarised in Ghia (2015). The properties of ultra-high energy cosmic rays are studied through the EAS they produce in the atmosphere. These are detected by the complementary surface and fluorescence detectors. In this report a selection of the latest results obtained by the Observatory from data collected since 2004 is presented. Data from a total of 188 000 showers were collected, with a total exposure exceeding 50 000 km^2 sr yr, on a a wide range of sky coverage.
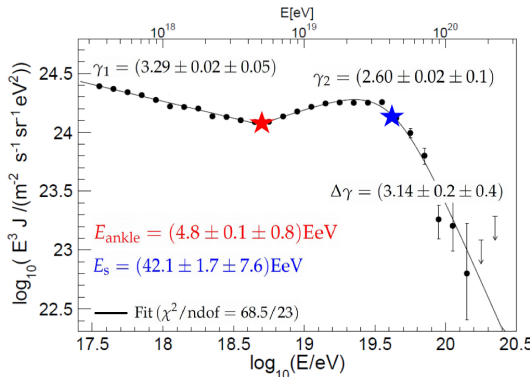
Figure 1. The combined energy spectrum of cosmic rays as measured by the Auger Observatory, fitted with a flux model (reproduced from Valiño 2015). Only statistical uncertainties are shown. The systematic uncertainty on the energy scale is 14%. The number of events is given above the points, which are positioned at the mean value of $\log_{10}(\mathrm{E/eV})$. Stars mark the positon of E_{ankle} and E_s as described in the text. The upper limits correspond to the 84% C.L.

2. Analysis and Main Results

2.1. Energy spectrum

The FD allows the measurement of the electromagnetic energy released by the shower in the atmosphere as a function of the atmospheric depth (X). The total primary energy is then derived by integrating this longitudinal profile dE/dX over the X-range and adding an estimate of the so-called invisible energy carried into the ground by high-energy muons and neutrinos. The hybrid measurement is based on the selection and reconstruction of showers observed by the FD in co-incidence with at least one SD station, which enables an accurate determination of the shower geometry and consequently of the energy of the primary particle.

The characteristic features of the energy spectrum (Valiño 2015), shown in Figure 1, have been quantified by fitting a model that describes the spectrum by a power law below the ankle $J(E) = J_0(E/E_{ankle})^{-\gamma_1}$ and a power law with a smooth suppression at the highest energies $J(E) \propto (E/E_{ankle})^{-\gamma_2}[1 + (E/E_s)^{\Delta\gamma}]^{-1}$. The results show a spectral index of 2.6 above 4.8×10^{18} eV and a clear steepening of the cosmic-ray flux above an energy around 4.2×10^{19} eV. The dominant systematic uncertainty of the spectrum comes from the overall uncertainty in the energy scale of 14%.

2.2. Mass composition

In this section three different techniques used in the Pierre Auger Observatory to measure mass sensitive observables are presented.

Depth of shower maximum $(X_{\max})$: The measurement of the longitudinal profile of the energy deposit in the atmosphere is described in detail in Porcelli
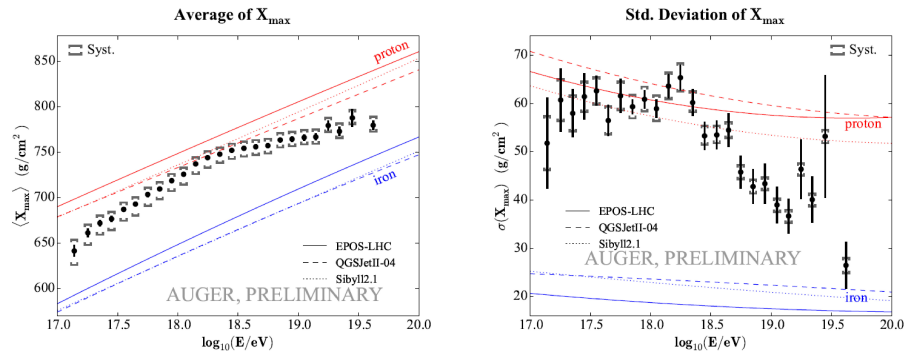
Figure 2. The mean (left) and standard deviation (right) of the measured $X_{\max}$ distributions as a function of energy, compared to air-shower simulations for proton and iron primaries (reproduced from Porcelli 2015).

(2015). In this analysis, hybrid events have been used. The longitudinal profile of the energy deposit is reconstructed from the light recorded by the FD using the fluorescence and Cherenkov yields. The light collected by the telescopes is corrected for the attenuation between the shower and the detector using data from atmospheric monitoring devices. The longitudinal shower profile is finally reconstructed as a function of the atmospheric depth, and $X_{\max}$ is obtained by fitting the profile with a Gaisser-Hillas function. The results for $\langle X_{\max} \rangle$ and its fluctuations $\sigma(X_{\max})$ are shown in Figure 2. Between $10^{17.0}$ and $10^{18.3}$eV, $\langle X_{\max} \rangle$ increases by around 85 g/cm^2 per decade of energy (Figure 2, left). This value, being larger than the one expected for a constant mass composition (~ 60 g/cm^2/decade), indicates that the mean primary mass is getting lighter. Around $10^{18.3}$ eV the observed rate of change of $\langle X_{\max} \rangle$ becomes significantly smaller (~ 26 g/cm^2/decade) indicating that the composition is becoming heavier. The fluctuations start to decrease at around the same energy $\sim 10^{18.3}$ eV as shown in Figure 2 (right).

Muon Production Depth (MPD): The time of the signals recorded by the SD can be used to obtain information about the longitudinal development of the hadronic component of extensive air showers in an indirect way. It is shown in Collica (2015) that it is possible to reconstruct the MPD, i.e., the distance to the production of the muon measured parallel to the shower axis, by converting the time distribution of the signal recorded by the SD stations into muon production distances using an approximate relation between production distance, transverse distance and time delay. From the MPDs, an observable can be defined, $X_{\max}^{\mu}$, as the depth along the shower axis where the number of produced muons reaches a maximum. Figure 3 shows the variations of $\langle \ln A \rangle$ with energy that is extracted from a comparison with each of two hadronic interaction models tuned with the latest LHC data.

Signal Time Asymmetry: It is well known that the first portion of the signal in each SD detector is dominated by the muon component which arrives earlier and over a period of time shorter than the electromagnetic (photons and electrons)
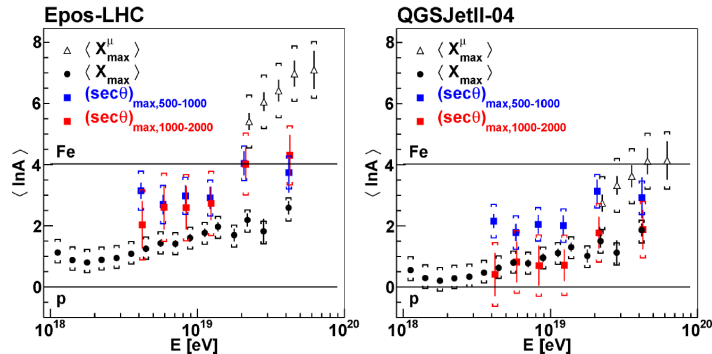
Figure 3. $\langle \ln A \rangle$ vs E as predicted by Epos-LHC and QGSJetII-04. Results from the time asymmetry method in both r-intervals are compared with those from the elongation curve and the MPD method (reproduced from Minaya 2015).

particles (EM). This is because muons travel in almost straight lines whereas the electromagnetic particles suffer multiple scattering. Due to the absorption of the EM component, the number of these particles at ground level depends, for a given energy, on the distance to the shower maximum and therefore on the primary mass. In consequence, the time profile of particles reaching the ground is sensitive to the cascade development as the higher the production height, the narrower the time pulse. Equivalently, for inclined showers, both the magnitude and risetime of the signals depend on the azimuth since particles reaching late detectors traverse longer atmospheric paths than those arriving at early detectors. The method uses the above mentioned azimuthal asymmetry to describe the shower profile (Minaya 2015) and has been carried out independently for two intervals from the shower core, i.e., 500-1000m and 1000-2000m.

Figure 3 shows the variations of $\langle \ln A \rangle$ with energy summarising the results from the measurements of X_{max}, MPD and asymmetry. The values of $\langle \ln A \rangle$ derived from the Epos-LHC model are consistent for the two distance ranges for the asymmetry. However this is not the case for QGSJetII-04 as can be seen in the figure. In an overall comparison neither model provides an accurate description when taking into account the different shower parameters.

2.3.   Search for photons and neutrinos

Limits to the flux of neutrinos: Neutrinos, unlike protons and heavier nuclei, can generate showers initiated deep into the atmosphere. The main signature of these deep showers in the SD is a significant electromagnetic component spread in time over hundreds of nanoseconds, especially in the region on the ground at which the shower arrives earlier. On the other hand, hadron-induced showers start high in the atmosphere, and for very inclined showers their electromagnetic component is fully absorbed and only high energy muons and their radiative and decay products reach the surface, concentrated within a few tens of nanoseconds. The criteria for selecting showers initiated by neutrinos can be found in Bleve (2015) and references therein. Figure 4 (left) shows upper

limits to the diffuse flux of UHE neutrinos at 90% C.L. in integrated and differential forms. These limits are compared with cosmogenic neutrino models, the Waxman-Bahcall bound, and limits from IceCube and ANITA. All neutrino limits and fluxes are converted to single flavour. As can be seen in the figure, cosmogenic models assuming a pure primary proton composition at the sources with strong evolution (FRII-type) of the sources and constrained by the GeV observations of Fermi-LAT are disfavoured. The current Auger limit is approaching the fluxes predicted under a range of assumptions for the composition of the primary flux, source evolution, and model for the transition from galactic to extragalactic cosmic rays. A 10-fold increase in the exposure will be needed to reach the most optimistic predictions in the case of a pure iron composition at sources, out of the range of the current configuration of the Observatory.

Limits to the photon flux: Showers induced by photons are characterised by a lower content of muons and larger average depth of maximum longitudinal development than showers initiated by nuclei with the same energy. This is due to the radiation length being more than two orders of magnitude smaller than the mean free path for photo-nuclear interactions, causing a reduced transfer of energy to the hadron/muon channel, and to the development of the shower being delayed by the typically small multiplicity of electromagnetic interactions. At large distances from the axis, photon showers produce typically smaller signals than expected from the lateral distribution of nuclear showers. This feature, together with the risetime of the signal in the station, are suitable variables for the search for photons (Bleve 2015). The limits to the integral flux are shown in Figure 4 (right) . The figure also shows results from Telescope Array (TA), Yakutsk (Y), Haverah Park (HP), AGASA (A) and predictions from several top-down and cosmogenic photon models. The limits to the diffuse flux of photons obtained with the Auger Observatory are the most stringent for E > 10 EeV and start to constrain the most optimistic predictions of cosmogenic photon fluxes under the assumption of a pure proton composition at the sources.

2.4. Arrival directions

Intrinsic and large angular scale anisotropy studies: The search for intrinsic anisotropies in the distribution of arrival directions of cosmic rays with energies above 40 EeV is performed by computing the angular auto-correlation function, and by looking at potential excesses in circular windows across the exposed sky. Both tests gave results that are compatible with isotropic expectations (Aublin 2015). Rayleigh analyses are also performed both in right ascension and in azimuth angle, and the dipole components are obtained along the equatorial plane and along the rotation axis of the Earth. In the energy band E >8 EeV a dipole component with amplitude (0.073±0.015) and pointing in the direction $(\alpha;\delta)=(95°±13°,39°±13°)$ is found, above isotropic expectations (Samarai 2015).

Search for cross-correlations with astrophysical sources: For the cross-correlation with astrophysical sources, a scan is done over events energies from 40 EeV up to 80 EeV and in angular scale, between 1 and 30 degrees. For sources in the catalogs, a maximum distance cut D is imposed, that can vary from 10 Mpc up to 200 Mpc. For each value of D, the fraction of isotropic simulations having an equal or higher number of pairs than the data is computed, and a search for its
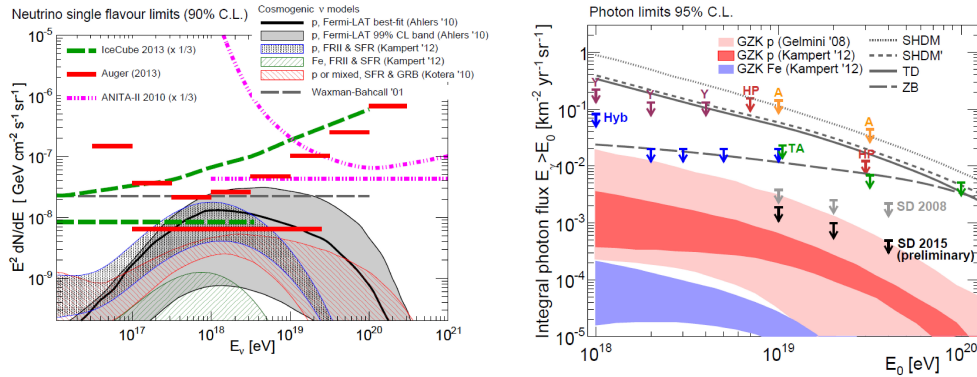
Figure 4.   Left: upper limits to the diffuse flux of UHE neutrinos at
90% C.L. in integrated (horizontal lines) and differential forms. Limits
described in this work (red lines) are compared with cosmogenic neu-
trino models. Right: Upper limits at 95% C.L. to the diffuse flux of
UHE photons derived from recent Auger data (black) shown together
with previous results from the Pierre Auger Observatory with hybrid
(Hyb) and SD data (reproduced from Bleve 2015).

minimum f_{min} is carried out. The associated post-trial probability is determined
as the fraction of isotropic realisations that lead to a lower than or equal value of
f_{min} under a similar scan. The cross-correlation from three complementary astro-
physical catalogues has been performed, namely the 2MRS catalogue of galaxies,
the Swift-BAT X-ray catalogue of AGNs, and a catalogue of radio galaxies with
jets, together with a specific analysis of the arrival directions around the Cen
A radio galaxy. The results are summarised in Aublin (2015). The penalised
chance probabilities, accounting for the scan on parameters are of the order of
a few percent, reach the 1% level when selecting only the brightest AGNs of the
Swift-BAT catalogue or with the Cen A radio galaxy. From the results it could
be noted that all minima, despite not being statistically significant, occur for a
value of the maximum distance of approximately 80-90 Mpc.

References

Aab A., et al. (The Pierre Auger Collab.) 2015, Nucl. Instrum. Meth. A 798, 172

Aublin J., for the Pierre Auger Collab. 2015, Proc. 34th ICRC, PoS(ICRC2015)310

Bleve C., for The Pierre Auger Collab. 2015, Proc. 34th ICRC, PoS(ICRC2015)1103

Collica L., for The Pierre Auger Collab. 2015, Proc. 34th ICRC, PoS(ICRC2015)336

Ghia P.L., for the Pierre Auger Collab. 2015, Proc. 34th ICRC, PoS(ICRC2015)034

Minaya I.A., for The Pierre Auger Collab. 2015, Proc. 34th ICRC, PoS(ICRC2015)405

Porcelli A., for The Pierre Auger Collab. 2015, Proc. 34th ICRC, PoS(ICRC2015)420

Samarai I.A., for the Pierre Auger Collab. 2015, Proc. 34th ICRC, PoS(ICRC2015)372

Valiño I., for The Pierre Auger Collab. 2015, Proc. 34th ICRC, PoS(ICRC2015)271

Poster contributions

Ultra high energy cosmic rays as a probe of black strings

R. C. Anjos[1], C. H. Coimbra-Araújo[1]

[1] *Universidade Federal do Paraná - Setor Palotina, Departamento de Engenharias e Exatas, Brazil*

Abstract. Ultrahigh energy cosmic rays (UHECRs) are problably originated in extragalactic sources as, e.g., Active Galactic Nuclei (AGNs). In the present work it is proposed an approach to calculate bounds on the AGN luminosity fraction that can be converted in such UHECRs. This result comes from two separated points of view: (i) the intrinsic mechanism powered by central black holes to produce the AGN luminosity and (ii) the observation of UHECRs and gamma-rays from ground experiments to reconstruct proton luminosities of a given AGN source.

1. Introduction

AGNs are active galaxies that have a supermassive black hole (SMBH) in its center, surrounded by an accretion disk with the formation of perpendicular jets. The accretion mechanism produces, by friction, by inverse Compton and by other radiative processes, enormous bolometric luminosities. The injection of only a moderate fraction of their bolometric luminosity would suffice to reproduce the observed cosmic ray flux above 10^{19} eV. Nevertheless, cosmic ray flux from AGNs problably has its origin from jet luminosities (Coimbra & Anjos 2015).

This limits the potential number of AGNs as cosmic ray sources in the nearby Universe (unless the highest energy cosmic rays are heavy nuclei: Lemoine & Sigl 2002). For protons, only the most powerful flat spectrum radio quasars, which are thought to be the jet-on analogs of FR II radio galaxies with relativistic jets, show a magnetic luminosity in excess of 10^{45} ergs s^{-1}. BL Lac objects or TeV blazars, thought to be the analogs of FR I radio galaxies (such as Cen A) typically exhibit magnetic luminosities L_B of the order of 10^{44} ergs s^{-1} or less. Shocks in the jets and the hot spots of the most powerful FRII radio-galaxies may nevertheless offer the requisite conditions for proper accelerations (Takahara 1990; Rachen & Biermann 1993).

In the present work, it will be investigated the bolometric luminosity that comes from the accretion mechanism. It will be argued that the jet contribution comes as a quantity that is proportional to the bolometric luminosity, i.e., a fraction L_{CR}^{Theory} of such luminosity, assuming that any geometrically thick or hot inner region of an accretion flow can lead magnetic field fluctuations to produce powerful jets (Coimbra & Anjos 2015). Perturbations due to extradimensional effects will therefore be calculated to derive possible variations in the luminosity (Anjos et al. 2016).

The method described in Supanitsky & Souza (2013) and Anjos et al. (2014) is a productive tool for the obtainment of the upper limits of the cosmic-ray lumi-

nosity. The method has been used with the upper limit of the GeV-TeV gamma-ray flux measured by space and ground instruments, as *Fermi*-LAT (2010), VERITAS (2009), H.E.S.S (2008) and MAGIC (2010). The method connects a measured upper limit on the integral flux of GeV-TeV gamma-rays and the UHECR cosmic-ray luminosity (L_{CR}^{UL}) of a source by the equation,

$$L_{CR}^{UL} = \frac{4\pi D_s^2 (1 + z_s)\langle E\rangle_0}{K_\gamma \int_{E_{th}}^{\infty} dE_\gamma \ P_\gamma(E_\gamma)} \ I_\gamma^{UL}(> E_\gamma^{th}),$$ (1)

where $I_\gamma^{UL}(> E_\gamma^{th})$ is the upper limit on the integral gamma-ray flux for a given confidence level and energy threshold, K_γ is the number of gamma-rays generated from the cosmic-rays particles, $P_\gamma(E_\gamma)$ is the energy distribution of the gamma-rays arriving on Earth, E_γ is the energy of gamma-rays, $\langle E\rangle_0$ is the mean energy, D_s is the comoving distance and z_s is the redshift of the source. The method allows to calculate upper limits on the proton and total luminosities for energies above 10^{18}eV.

This method illustrates techniques to study the origin of UHECR from gamma rays at GeV-TeV energies, and it has been used to calculate the upper limits to thirty sources (AGNs) so far, with redshift smaller than 0.048 and UHECR spectra measured by the Pierre Auger (2013) and Telescope Array (2011; TA) observatories. The construction of the CTA Observatory will allow the calculus of the upper limits on the UHECR luminosity to many sources applying this model.

2. Luminosity of black strings and cosmic rays

The luminosity L_{acc}^{Theory} of AGNs due to BH accretion is given by

$$L_{acc}^{Theory} = \epsilon \dot{M} c^2 = \frac{GM\dot{M}}{6R},$$ (2)

where $\dot{M}$ denotes the accretion rate and depends on some specific model of accretion, $R = R_{Sbrane}$, R_{+Kerr} or $R_{+Kerrbrane}$ are the horizons for a static BH with extra dimension correction, a rotating BH without extra dimension and a rotating BH with extra dimension correction, respectively and M is the BH mass. The luminosity of AGNs is produced essentially by the accretion mechanism i.e., AGN activity is related to the growth, via accretion, of central supermassive black holes (SMBHs).

We can consider that the jet contribution comes as a quantity proportional to the bolometric luminosity, namely, a fraction, assuming that any geometrically thick or hot inner region of an accretion flow can lead magnetic field fluctuations to produce powerful jets. We write the fraction of the total luminosity that goes into UHECR as $L_{CR}^{Theory} = \eta_{CR} L_{acc}^{Theory}$ (see Anjos et al. 2016 for a more thorough discussion).

3. Conclusions

We calculated the luminosity due to accretion of nine sources. The luminosities calculated based on theory were compared to an upper limit on the UHECR luminosity. The comparison resulted in the determination of upper limits on the energy conversion from accretion to UHECR. The theoretical estimations of this conversion efficiency represent an important information about of the energy balance in BH.

References

Anjos, R.C. et al 2016, JCAP, 03, 14

Anjos, R.C.; Souza, V. and Supanitsky, A.D. 2014, JCAP, 07, 049

Bondi, H. 1952, Mon. Not. Roy. Astron. Soc., 112, 195

Coimbra-Araujo, C.H.; Anjos, R.C. 2015, PRD, 92, 103001

Galante, N., for the VERITAS Collaboration. 2009, arXiv: 0912.3850

H.E.S.S Collaboration. 2008, A&A, 478, 387

Lemoine, M., Sigl, G. 2002, "Physics and Astrophysics of Ultra High Energy Cosmic Rays Hardcove", Springer

Rachen, J.P., Biermann, P.L. 1993, A&A, 272, 161

Supanitsky, A.D. and Souza, V. 2013, JCAP, 12, 023

Takahara, F. 1990, Prog. Theor Phys. 83, 1071

Telescope Array Collaboration. 2011, Experimental Astronomy, 32, 193

The Fermi-LAT Collaboration. 2010, ApJ, 715, 429

The MAGIC Collaboration. 2010, ApJL, 723, 2

The Pierre Auger Collaboration. *Proceedings of the 33rd International Cosmic Ray Conference*, Rio de Janeiro, Brazil, 2013, arXiv: 1307.5059

Optical polarimetry of blazars detected at TeV γ-rays

S. A. Cellone[1,2], J. A. Combi[2,3], I. Andruchow[1,2], G. E. Romero[2,3] and J. Martí[4]

[1]*Instituto de Astrofísica La Plata (IALP), CONICET-UNLP, Argentina*
[2]*Facultad de Ciencias Astronómicas y Geofísicas, UNLP, Argentina*
[3]*Instituto Argentino de Radioastronomía (IAR), CONICET, Argentina*
[4]*Departamento de Física, Universidad de Jaén, Spain*

Abstract. We present results from an optical polarimetric study of blazars that have been detected at very high-energy (VHE) γ-rays. We look for short time-scale fluctuations (i.e., *microvariability*) either/both in their polarisation percent or position angle in the B and R optical bands. Spurious effects introduced by light contamination from the host galaxy, especially due to seeing FWHM variations, are quantitatively analysed.

1. Background and aims

This study is part of an effort to characterise the optical photo-polarimetric variability behaviour of γ-ray emitting blazars (Andruchow et al. 2003, 2011). In particular, *microvariability* (i.e., variations at time-scales of minutes to hours) should probe the innermost and/or smallest emitting regions in the relativistic jet, thus shedding light on mechanisms operating at the zones where the VHE emission is expected to originate.

Since γ-photons are efficiently absorbed by the extragalactic background light (EBL), most blazars detected at VHE are not very distant ($z < 0.5$). Their relatively bright and resolved host galaxies thus introduce a depolarising effect, which may lead to systematic errors in photo-polarimetric light-curves when seeing conditions vary with time. We show some preliminary results focusing on this effect, providing a means to quantitatively evaluate it.

2. Observations and polarimetric light-curves

We obtained polarimetric data in the optical B and R bands of two high-synchrotron peaked (HSP) blazars: 1ES 1011+496 ($z = 0.212$) and 1ES 1218+304 ($z = 0.184$), which have been detected at very high energy (VHE) γ-rays by MAGIC (Albert et al. 2006, 2007). Our observations span three nights for each blazar, with a temporal resolution ~ 45 minutes. We used the instrument CAFOS at the CAHA 2.2 m tel., Calar Alto, Spain, in its polarimetric mode (Patat & Romaniello 2006).

Figure 1 displays the polarimetric light-curves for each blazar, with different symbols for data before and after subtracting the host-galaxy contribution (see Sect. 3).
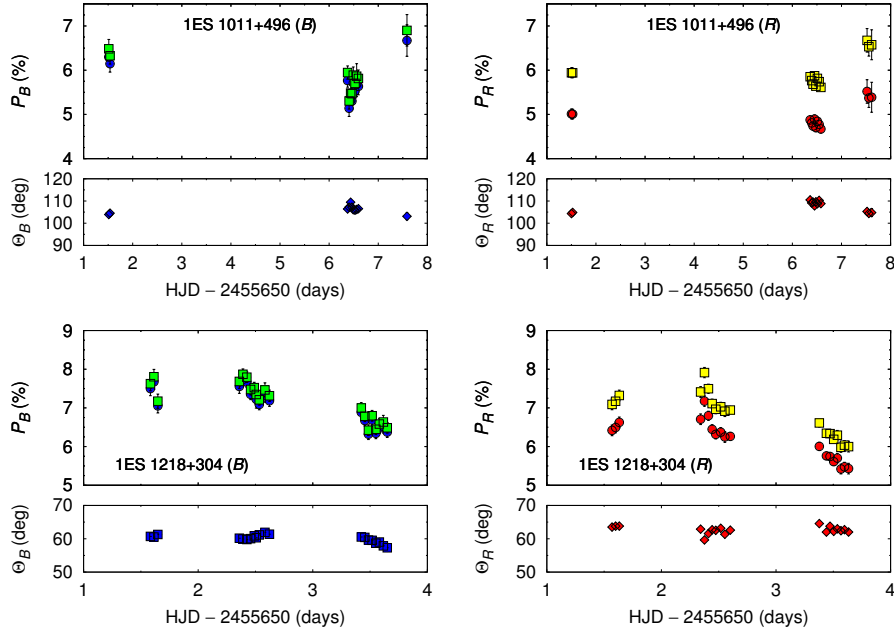
Figure 1.   Polarisation percent (P) and position angle (Θ) before (blue/red circles) and after (green/yellow squares) subtracting the host-galaxy contribution (see Sect. 3).   The uppermost panels correspond to 1ES 1011+496; the lowermost ones to 1ES 1218+304 (*left*: *B*-band; *right*: *R*-band).

The blazars in our VHE detected sample show significant polarisation in both bands: $5\% \leq \langle P \rangle \leq 10\%$. Mild (if any) *intra-night* variations in P and electric-vector position angle (Θ) can be seen in their polarimetric light-curves, while significant (although rather low-amplitude) *inter-night* variations in P are evident. A similar behaviour was detected in total flux (not shown). Position angles (Θ), in turn, remained almost stable along the whole observing run.

3.   The host galaxy problem

Polarimetric observations of low-redshift blazars can be systematically affected by the host galaxy, which is usually bright and spatially resolved. The main effect is polarisation dilution by the unpolarised galaxy starlight; this effect differs from one photometric band to other, thus leading to colour-dependent errors. A more subtle effect is spurious variability caused by seeing fluctuations: since seeing affects differently the brightness profiles of the nucleus and the host galaxy, its variations will lead to changes in the relative starlight contribution, and hence different depolarisation factors (see Andruchow et al. 2008).

Polarisation dilution by the host galaxy starlight is illustrated in Figure 2, which shows P and Θ as a function of photometric apertures for the blazar
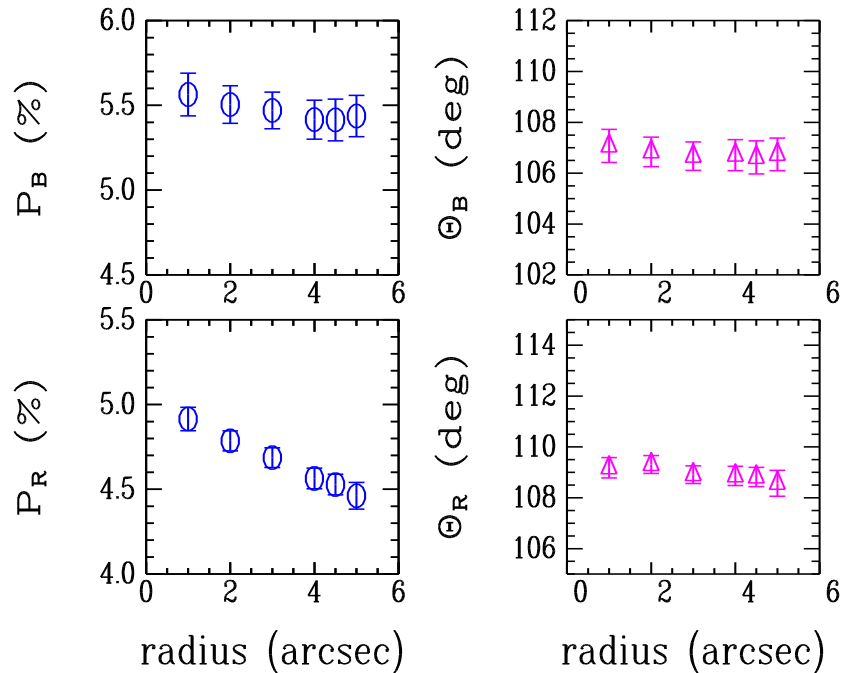
Figure 2. Polarisation percent (P, *left panels*) and position angle (Θ, *right panels*) vs. aperture radius for 1ES 1011+496 (*upper panels: B*-band, *lower panels: R*-band).

1ES 1011+496. Larger apertures include a larger fraction of the host galaxy light, so P decreases while Θ remains stable. The polarisation dilution effect is stronger in R than in B because of the galaxy's red colour.

In order to quantitatively evaluate host-galaxy effects on optical polarimetric measurements of blazars, we performed a simple experiment: we simulated observations of the blazar 1ES 1011+496, assuming an intrinsic polarisation of the active nucleus $P_{\mathrm{AGN}} = 10\%$, in both B and R bands, and a nuclear flux in agreement with our observations. We simulated seeing effects by convolving our synthetic data with Gaussians spanning an appropriate range in FWHM. For the host galaxy, we used the R-band fluxes given by Nilsson et al. (2007), and we assumed $B - R = 2.26$ mag, expected value for the K-corrected colour of an E galaxy at $z \simeq 0.2$ (e.g. Buzzoni 2005).

The results are displayed in Figure 3, where our simulated polarisation measurements are shown against seeing FWHM, for different values of the photometric aperture. It is clear that measured P decreases with larger seeing FWHM, because the (pointlike) nucleus is more affected than the (extended) host galaxy. Smaller apertures maximise the effect, which is larger in R than in B, leading to incorrect results in frequency dependent polarisation (P_B/P_R).

Note that observations taken under different atmospheric conditions and processed wit different apertures could not be directly comparable. On the other hand, if seeing FWHM changes along a given observing run, spurious variability results will be obtained, which in this example can grow up to ∼ few percent in
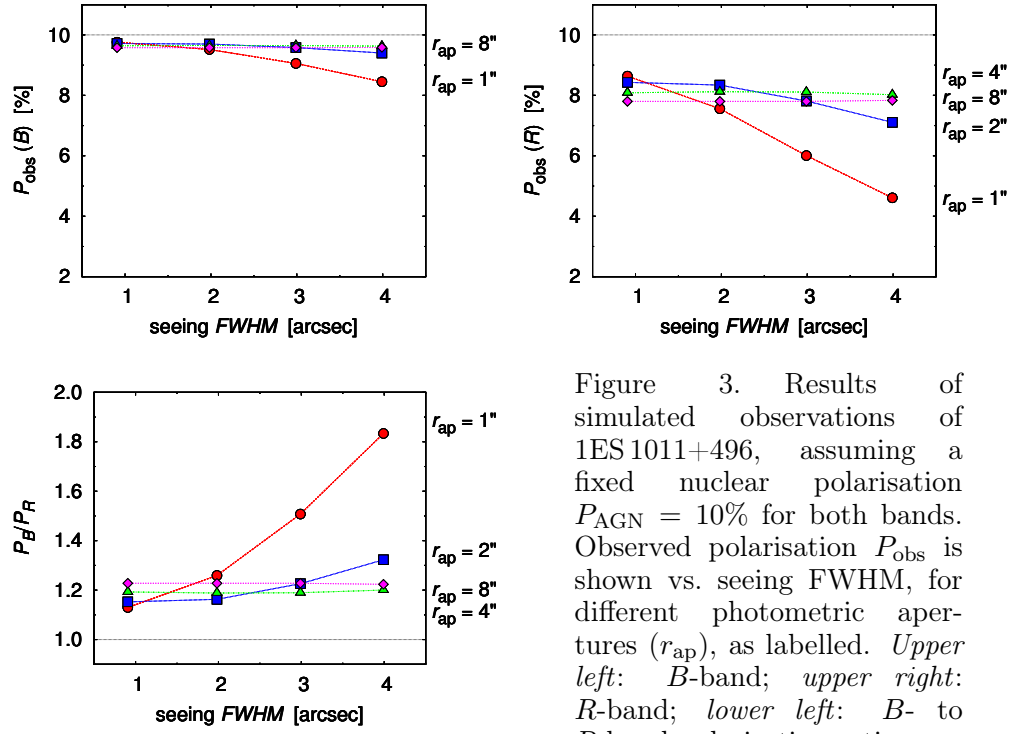
Figure 3. Results of simulated observations of 1ES 1011+496, assuming a fixed nuclear polarisation $P_{\rm AGN} = 10\%$ for both bands. Observed polarisation $P_{\rm obs}$ is shown vs. seeing FWHM, for different photometric apertures ($r_{\rm ap}$), as labelled. *Upper left*: *B*-band; *upper right*: *R*-band; *lower left*: *B*- to *R*-band polarisation ratio.

P, especially if a small aperture is used. Also note that small apertures minimise the depolarisation effect if seeing is small and stable, but they maximise spurious results if seeing worsens.

In order to obtain results that can be compared between different studies, it is thus necessary to correctly subtract the starlight contribution from the host galaxy. Our group is now undertaking an effort to quantitatively evaluate those effects on a sample of blazars detected at TeV γ-rays; this needs accurate modelling of their host galaxies in different photometric bands.

References

Albert, J., et al. 2006, ApJ, 642, L119

Albert, J., et al. 2007, ApJ, 667, L21

Andruchow, I., Cellone, S. A., Romero, G. E., Dominici, T. P., Abraham, Z. 2003, A&A, 409, 857

Andruchow, I., Cellone, S. A., Romero, G. E. 2008, MNRAS, 388, 1766

Andruchow, I., Combi, J. A., Muñoz-Arjonilla, A. J., Romero, G. E., Cellone, S. A., Martí, J. 2011, A&A, 531, A38

Buzzoni, A. 2005, MNRAS, 361, 725

Nilsson, K., Pasanen, M., Takalo, L. O., et al. 2007, A&A, 475, 199

Patat, F., Romaniello, M. 2006, PASP, 118, 146

Connecting AGN jet luminosities and ultra high energy cosmic ray luminosities

C. H. Coimbra-Araújo[1] and R. C. Anjos[1]

[1]*Departamento de Engenharias e Exatas, Universidade Federal do Panará, R. Pioneiro, 2153, 85050-000, Palotina, Brazil*

Abstract. In the present work it is investigated the magnetic luminosity produced by Kerr black holes in active galactic nuclei (AGNs). Some comparison is made between the results for some black hole masses with spins in the range $0.44 < a < 0.80$ and the upper limit of ultra high energy cosmic ray (UHECR) luminosities, calculated from observed integral flux of GeV-TeV gamma rays for nine UHECR AGN candidates with the same masses considered theoretically. We find that the calculated theoretical range of magnetic luminosities from AGNs coincides with the calculated UHECR luminosity. It is argued that this result can possibly shed some light in the phenomenology of AGN magnetic properties in manner to explain some of the requisite conditions to proper accelerate the highest energy cosmic rays.

1. Introduction

The main extragalactic candidates for accelerating particles to the highest energies are active galactic nuclei (AGNs) (Henri et al. 1999), the most powerful radiogalaxies (Takahara 1990, Rachen & Biermann 1993), and also gamma ray bursts, fast spinning newborn pulsars, interacting galaxies, large-scale structure formation shocks and some other objects (Kotera & Olinto 2011).

The reconstruction of cosmic ray luminosities, from Earth laboratory observations, can possibly shed some light on radiative bounds of UHECR potential sources, as can be seen in Supanitsky & de Souza (2013) and in Anjos et al. (2014), where it is shown that the methods of UHECR propagation from the source to Earth and the measured upper limit on the integral flux of GeV-TeV gamma-rays can infer upper limits of proton and total UHECR (iron) luminosities. This comes from the fact that gamma-rays can be produced as a result of the cosmic ray propagation and contribute to the total flux measured from the source.

In the present work, nine AGN are investigated as UHECR sources (see Table 1). It is calculated upper limits of UHECRs luminosities to be compared to the theoretical magnetic/jet luminosity of those AGNs.

2. Upper limits of UHECR luminosities

Space and ground instruments, as FERMI-LAT (2010), VERITAS (Galante 2009), H.E.S.S and MAGIC (2010) provide upper limits on the GeV-TeV gamma-

ray integral flux. The method described in Supanitsky & de Souza (2013) and Anjos et al. (2014) connects those measured upper limits with the source UHECR cosmic ray luminosity (L_{CR}^{UL}) by

$$L_{CR}^{UL} = \frac{4\pi D_s^2(1 + z_s)\langle E\rangle_0}{K_\gamma \displaystyle\int_{E_{th}}^{\infty} dE_\gamma \; P_\gamma(E_\gamma)} \; I_\gamma^{UL}(> E_\gamma^{th}), \tag{1}$$

where $I_\gamma^{UL}(> E_\gamma^{th})$ is the upper limit on the integral gamma-ray flux for a given confidence level and energy threshold, K_γ is the number of gamma rays generated from the cosmic ray particles, $P_\gamma(E_\gamma)$ is the energy distribution of the gamma-rays arriving on Earth, E_γ is the energy of gamma-rays, $\langle E\rangle_0$ is the mean energy, D_s is the comoving distance and z_s is the redshift of the source. This method allows one to calculate upper limits on the proton and total luminosities for energies above 10^{18} eV. Also, it illustrates techniques to study the origin of UHECRs from multi-messenger GeV-TeV gamma-rays and it has been used to calculate at least upper limits for thirty sources (AGNs), with redshift smaller than 0.048 and UHECR spectra measured by the Pierre Auger (Schulz 2013) and Telescope Array (TA) (Bergman 2013) observatories. For this same method, CTA (2011) Observatory will also allow, in the future, a range of new UHECR luminosity calculations.

3. Central black holes and the magnetic luminosity of AGNs

In what follows it is described the production of UHECR luminosities based on the possible relation between magnetic flux accumulation and jet production efficiency. Considering a system with a rotating central BH, the necessary condition to use Blandford-Znajek mechanism is that $\Phi_d > \Phi_{BH,\max}(\dot{M})$, i. e., the net poloidal magnetic flux Φ_d trapped in the disk is larger than the maximum that can be confined on the BH caused by pressure of the accreting plasma. Satisfied this condition, the rate of energy extraction from the rotating BH via the Blandford-Znajek mechanism yields the magnetic luminosity

$$\begin{aligned} L_B &\simeq 4 \times 10^{-3}\Phi_{BH,\max}^2(\dot{M})\frac{\Omega_{BH}^2}{c}f_a(\Omega_{BH}) \\ &= 10(\phi/50)x_a^2 f_a(x_a)\dot{M}c^2, \end{aligned} \tag{2}$$

where Ω_{BH} is the angular velocity of the black hole and

$$x_a = r_g\frac{\Omega_{BH}}{c} = [2(1 + \sqrt{1 - a^2})]^{-1}a, \tag{3}$$

with

$$f_a(x_a) \simeq 1 + 1.4x_a^2 - 9.2x_a^4, \tag{4}$$

where a is the dimensionless angular momentum parameter ($a = J/Mc$, with J the BH angular momentum), ϕ is a dimensionless factor which, according to numerical simulations (see, e.g., McKinney et al. 2012), is typically of order 50, and r_g is the gravitational radius $r_g = GM/c^2$.

4.   Results

As AGN jets can be the main extragalactic sources of UHECRs, one can write the UHECR luminosity L_{CR}^{Theory} as a fraction η of the magnetic luminosity:

$$L_{CR}^{Theory} = \eta L_B. \qquad (5)$$

For example, bounds on the fraction η_{pr} of L_B to be converted in relativistic protons, as a function of BH spin a, come from eqs. (1), (2) and (5) as

$$\eta(a)_{pr} = \frac{L_{pr}^{UL}}{10(\phi/50)x_a^2 f_a(x_a)\dot{M}c^2}. \qquad (6)$$

For the spin range $0.44 < a < 0.8$ where most black holes are expected to lie, the fraction η_{pr} varies from $\sim 5\%$ to 40% for $a = 0.45$ and from 2% to 10% for $a = 0.8$, see Fig. 1.
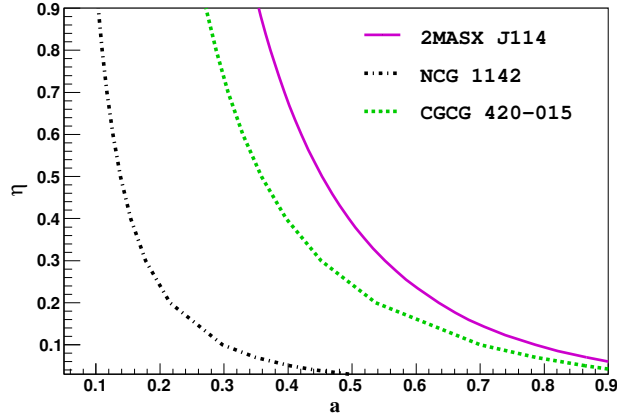

Figure 1. η_{pr} as a function of the parameter a. For all plots it was considered $\dot{M}$ as the Bondi accretion rate .

Table 1 shows the range $L_{CR,\min}^{Theory} - L_{CR,\max}^{Theory} = \eta_{pr,\min}L_B - \eta_{pr,\max}L_B$ for nine AGN sources, assuming a fixed spin of $a = 0.7$. The column L_{pr}^{UL} is the calculated upper limit of the proton luminosity for each source from eq. (1), and it has dependence only with observational [GeV-TeV gamma rays + cosmic rays] constraints, i.e., it has no dependence with BH mass or BH spin of the AGN.

5.   Conclusions

The present work compared ultra high energetic cosmic ray luminosities with a theoretical luminosity derived from intrisic AGN properties, as its mass and central black hole spin. An important remark is that luminosity calculation from method (1) does not require any AGN property, since they come uniquely from observed integral flux of GeV-TeV gamma-rays of UHECR AGN sources. In this

Source name	L_{pr}^{UL} (Proton) [erg s^{-1} × 10^{45}]	$L_{CRmin}^{Theory} - L_{CRmax}^{Theory}$ [erg s^{-1} × 10^{45}]
NGC 985	1.03	0.77 - 2.79
NGC 1142	0.49	0.97 - 3.52
2MASX J07595347+2323241	1.01	0.72 - 2.61
CGCG 420-015	0.95	0.83 - 2.99
MCG-01-24-012	0.65	0.28 - 1.02
2MASX J11454045-1827149	1.30	0.19 - 0.70
LEDA 170194	1.48	0.75 - 2.73
NGC 5995	0.90	0.15 - 0.54
Mrk 520	0.98	0.49 - 1.77

Table 1.   Comparison between cosmic ray luminosity L_{pr}^{UL} (protons) from the method derived from eq. (1) and the theoretically calculated range $L_{CRmin}^{Theory} - L_{CRmax}^{Theory}$ of cosmic ray luminosities, from nine sources. Here it is considered the case for $a = 0.7$.

aspect, both for proton and iron luminosities it is possible to find phenomenological bounds on the conversion fraction of magnetic luminosities into energetic particles.

References

Anjos, R. C., Supanitsky, A. D., de Souza, V. 2014, JCAP, 07, 049

Bergman, D. for the Telescope Array Collaboration 2013, *Proceedings of the 33rd International Cosmic Ray Conference*, Rio de Janeiro, Brazil, 2013

CTA Consortium 2011, *Experimental Astronomy*, 32, 193

Galante, N. for the VERITAS Collaboration 2009, *Fermi Symposium*, 2, arXiv:0912.3850.

Henri, G., Pelletier, G., Petrucci, P.-O., Renaud, N. 1999, Astropart. Phys., 11, 347

Kotera, K., Olinto, A. V. 2011, ARA&A, 49, 119

McKinney, J. C., Tchekhovskoy, A., Blandford, R. D. 2012, MNRAS, 423, 3083

Rachen, J. P., Biermann, P. L. 1993, A&A, 272, 161

Supanitsky, A. D, de Souza, V. 2013, JCAP, 12, 023

Takahara, F. 1990, Prog. Theor Phys. 83, 1071

The Fermi-LAT Collaboration 2010, ApJ, 715, 429

The MAGIC Collaboration 2010, ApJ, 723, L207

Schulz, A. for The Pierre Auger Collaboration 2013, *Proceedings of the 33rd International Cosmic Ray Conference*, Rio de Janeiro, Brazil, 2013, arXiv:1307.5059

Relativistic particle content in the most massive colliding-wind binary in the Galaxy

del Palacio, S.[1], Romero, G.E.[1,2], Bosch-Ramon, V.[3], and Benaglia, P.[1,2]

[1]*Instituto Argentino de RadioastronomÃa (CONICET)*
[2]*Facultad de Ciencias Astronómicas y Geofísicas, Universidad Nacional de La Plata*
[3]*Departament d'Astronomia i Meteorologia, Institut de Ciències del Cosmos (ICC), Universitat de Barcelona (IEEC-UB)*

Abstract. The wind-collision region of the system HD 93129A was recently resolved. This system is the most massive known binary in our Galaxy. We aim to gain insight into the physics taking place in such a system, particularly in the acceleration process(es). We explored the broadband non-thermal emission for different injection spectra of relativistic particles accelerated in the wind-collision region. We developed a model that computes the evolution of the particle energy distribution taking into account different energy losses while the particles stream along the fluid lines in the shocked region. Such model was able to reproduce the available radio data. Also, for different scenarios we predicted the evolution of the cosmic-rays energy distribution and the radiative output in future epochs, when the stars come closer. With further observational data it will be possible to determine the injection spectrum and acceleration efficiency of relativistic particles in HD 93129A.

1. Introduction

Early-type stars produce powerful stellar winds with high mass-loss rates and hypersonic terminal velocities. In massive colliding-wind binaries (CWBs), the stellar winds collide generating strong shocks where efficient particle acceleration can take place. In this wind-collision region (WCR) the most promising acceleration mechanism is first-order diffusive shock acceleration (DSA). The relativistic particles interact with the ambient magnetic, photon and/or matter fields, producing non-thermal (NT) radiation (e.g., Eichler & Usov 1993, Benaglia & Romero 2003). So far η-Carinae and WR 11 are the only CWB detected at high-energies (HE), and we intend to predict whether HD 93129A is a promising candidate to join the family of γ-ray emitting, massive star binaries.

The system HD 93129A is among the earliest, hottest, most massive and luminous binaries in the Galaxy. It is located at 2.3 kpc, in the Carina arm, and it is composed of an O2 If* star (the primary) and an O3.5 V star (the secondary). Recent VLBI observations resolved the NT emitting region associated to the WCR (Benaglia et al. 2015). The wind momentum rate, flux densities at different frequencies, an unusually soft spectral index, a very large projected system size, and high mass-loss rates were derived. The available data at radio-frequencies allows a characterisation of the injection spectrum of rela-

tivistic particles in the WCR. A preliminary determination of orbital parameters suggests that the periastron passage will occur in the next few years.

2.   Particle Distribution

The WCR presents wide, hypersonic, and adiabatic shocks, where NT particles are expected to accelerate via DSA. These particles are responsible of the observed NT radio emission. Radio observations show a cutoff in the Spectral Energy Distribution (SED) at $1-2$ GHz, and they also indicate that the particle energy distribution of electrons that emit at $3-10$ GHz has a power-law index of $\alpha \sim 3.2$, which is peculiarly low considering that the expected index for DSA in a strong shock is $\alpha = 2$. To obtain a cutoff in the SED around $\nu \sim 1$ GHz due to a cutoff in the electron energy distribution at a minimum Lorentz factor $\gamma_{\mathrm{min_e}}$, one needs $B\,\gamma_{\mathrm{min_e}}^2 \sim 10^3$. The evolved particle distribution has the same spectral index as the injected distribution, as advection dominates over the particle cooling time except for the most energetic particles.

   The radio observations do not provide any information of the higher energy electron distribution, so it is possible that such distribution stiffens at energies above the radio-emitting ones. Considering that the micro-physics of the DSA process for the less energetic particles is still unknown (uncertainties in the shock precursor, different compression ratios, non-linear effects in the shocks, etc.; see e.g. Drury 1983), the resultant particle distribution could be soft at low energies (say $E < 1$ GeV, see e.g. Berezhko et al. 2009 for similar conclusions in SN 1006), while other acceleration processes might act besides DSA, such as magnetic reconnection (Falceta-Gonçalves et al 2012), and harden the spectra at higher energies.

   The normalisation of the particle energy distribution depends on the cosmic-ray acceleration efficiency, and the energy budget, which is limited by the amount of kinetic energy flux perpendicular to the shock surface. Such a flux is only $3-10\%$ of the total wind luminosity, and the amount of that luminosity we assumed is converted into NT energy is $f_{\mathrm{NT}} \sim 10-40\%$. Summing all, the NT luminosity is roughly $L_{\mathrm{NT}} \sim 10^{36}$ erg s^{-1}. We notice that secondary particles produced in p-p interactions are not expected to play an important role unless the scenario is hadronic dominated, $f_{\mathrm{NT}} > 20\%$, and the magnetic field in the WCR is almost in equipartition with the post-shock thermal energy; such scenario was not analysed in this work. We explored the parameter space of i, $\dot{M}$, f_{NT}, $\gamma_{\mathrm{min_e}}$, $\gamma_{\mathrm{stiff_e}}$, and B_{WCR}, subject to physical and observational constraints, and focused in analysing the models that maximise the HE luminosity. These models are summarised in Tab. 1. In all cases equipartition of energy between electrons and protons was considered.

3.   Results

We calculated the particle energy distribution for the models summarised in Tab. 1; we show the electron distributions in Fig. 1. We proceeded to calculate the resultant luminosities from the different radiative processes (synchrotron, relativistic Bremsstrahlung, and IC for electrons; p-p interactions for protons) for different epochs. The results are shown in Fig. 2, along with some instru-

Model	i	$\dot{M}_1$	f_{NT}	$\gamma_{\min_e}$	$\gamma_{\mathrm{stiff}_e}$	B_{WCR}	B_*
A	$15°$	$3 \times 10^{-5} M_\odot/\mathrm{yr}$	30%	4	-	~ 1.4 G	150 G
B	$15°$	$1 \times 10^{-5} M_\odot/\mathrm{yr}$	10%	180	7×10^3	~ 0.7 G	30 G
C	$75°$	$1 \times 10^{-5} M_\odot/\mathrm{yr}$	10%	200	6×10^3	~ 0.2 G	50 G

Table 1.   Parameters of the best fit models. The stellar surface magnetic field values represent only upper limits, as no magnetic field amplification (besides the adiabatic compression) was considered.
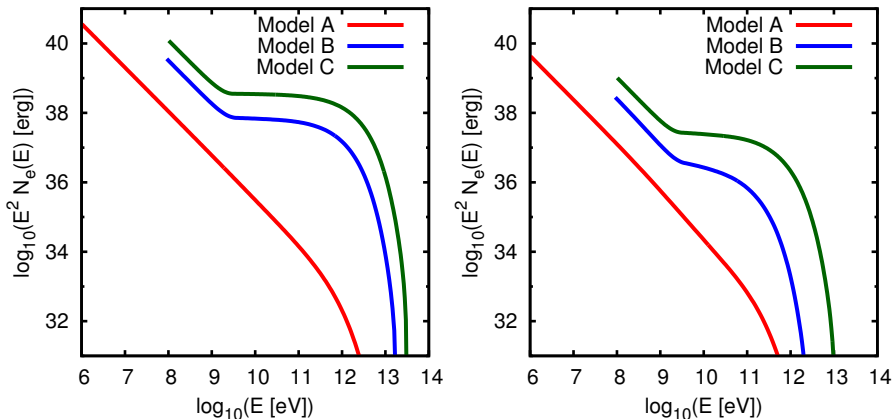

Figure 1.   Electron distribution for different scenarios and different epochs. The *left* panel corresponds to a binary separation of D (epoch of radio observations), and the *right* panel to a binary separation of $0.1D$ (roughly periastron passage).

ment sensitivities. Figure 2 (*left*) shows that if the inclination of the orbit (i) is small, then it is possible to explain the low-energy cutoff in the SED by means of free-free absorption in the stellar wind (Model A). However, such scenario is in tension with the observational data, as it requires very high stellar mass-loss rates, and also the preliminary orbital fits favour high inclinations instead. A low-energy cutoff in the particle distribution works to explain the low-energy cutoff in the SED independently of whether the system inclination is low (Model B) or high (Model C). With the above considerations as an input for the particle distribution, we predict the behaviour of the system in the HE domain. It is important to notice that the NT emission from IR to soft X-rays is completely overcome by the thermal emission from the stars and/or the WCR, so the signatures of relativistic particles in the SED are limited to radio and potentially to hard X-rays and γ-rays.

4.   Conclusions

Our leptonic model leads to good spectral fits. However, due to the limited knowledge on the physical parameters of the source, the model degeneracy and limited observations, it is not possible to unambiguously determinate the best fit for the non-thermal spectra. Future observations of this system at frequencies
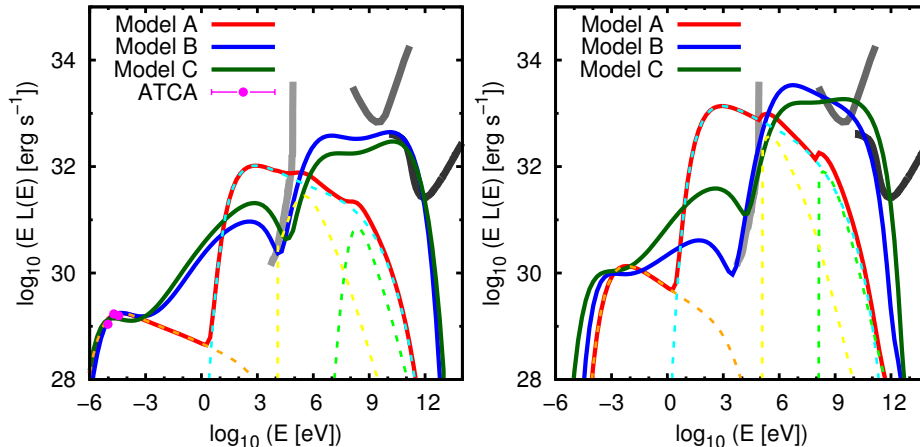
Figure 2.   Broadband SED for the different scenarios. For illustrative purposes, we show the individual components from synchrotron (orange), IC (cyan), relativistic Bremsstrahlung (yellow), and *p-p* (light green) emission in Model A. *Left*: binary separation D (epoch of radio observations). *Right*: binary separation $0.1D$ (periastron passage). We show instrument sensitivity curves for 1-Ms *NuSTAR* (grey), 4-yr *Fermi* (dark grey), and 50-h CTA (black).

below 10 GHz can disentangle the nature of the radio absorption/suppression mechanism. Moreover, observations in the hard X-ray range ($10 - 100$ keV) would provide tighter constraints to the free parameters in our model, such as the injected particle energy distribution, the magnetic field strength, and the acceleration efficiency. We predict that for certain possible cases, this source will be detectable by *Fermi* and/or CTA during periastron passage.

References

Benaglia, P., & Romero, G. E. 2003, A&A, 399, 1121

Benaglia, P., Marcote, B., Moldón, J., et al. 2015, A&A, 579, 99

Berezhko, E. G., Ksenofontov, L.T., & Völk, H. J. 2009, A&A, 505, 169

Drury, L. O. 1983, RPPh, 46, 973

Eichler, D. & Usov, V. 1993, ApJ, 402, 271

Falceta-Goncalvez, D., & Abraham, Z., 2012, MNRAS, 423,1562

Multiwavelength survey of a sample of flat-spectrum radio-loud narrow-line Seyfert 1 galaxies

L. Foschini[1], M. Berton[2], A. Caccianiga[1], S. Ciroi[2], V. Cracco[2], B. M. Peterson[3], E. Angelakis[4], V. Braito[1], L. Fuhrmann[4], L. Gallo[5], D. Grupe[6], E. Järvelä[7,8], S. Kaufmann[9,10], S. Komossa[4], Y. Y. Kovalev[11,4], A. Lähteenmäki[7,8], M. M. Lisakov[11], M. L. Lister[12], S. Mathur[3], J. L. Richards[12], P. Romano[13], A. Sievers[14], G. Tagliaferri[1], J. Tammi[7], O. Tibolla[10,15], M. Tornikoski[7], S. Vercellone[13], G. La Mura[2], L. Maraschi[1], P. Rafanelli[2]

[1]*INAF Osservatorio Astronomico di Brera, Merate (LC), Italy;*
[2]*Dipartimento Fisica & Astronomia Università di Padova, Padova, Italy;*
[3]*Dept Astronomy & Center for Cosmology & AstroParticle Physics, The Ohio State University, Columbus, OH, USA;*
[4]*Max-Planck-Institut für Radioastronomie, Bonn, Germany;*
[5]*Dept Astronomy & Physics, Saint Mary's University, Halifax, Canada;*
[6]*Space Science Center, Morehead State University, Morehead, KY, USA;*
[7]*Aalto University Metsähovi Radio Observatory, Kylmälä, Finland;*
[8]*Aalto University Dept Radio Science & Engineering, Aalto, Finland;*
[9]*Landessternwarte, Universität Heidelberg, Heidelberg, Germany;*
[10]*MCTP-UNACH, Tuxtla Gutiérrez, Chiapas, México.*
[11]*Astro Space Center of the Lebedev Physical Institute, Moscow, Russia;*
[12]*Dept Physics & Astronomy, Purdue Univ., West Lafayette, IN, USA;*
[13]*INAF Istituto di Astrofisica Spaziale e Fisica Cosmica, Palermo, Italy;*
[14]*Institut de Radio Astronomie Millimétrique, Granada, Spain;*
[15]*ITPA, Universität Würzburg, Würzburg, Germany.*

Abstract. We report on a multiwavelength survey of a sample of 42 flat-spectrum radio-loud narrow-line Seyfert 1 galaxies (RLNLS1s). This is the largest known sample of this type of active galactic nucleus (AGN) to date. We found that 17% of sources were detected at high-energy gamma rays ($E > 100$ MeV), and 90% at X-rays ($0.3 - 10$ keV). The masses of the central black holes are in the range $\sim 10^{6-8} M_\odot$, smaller than the values of blazars. The disk luminosities are about $1 - 49\%$ of the Eddington value, with one outlier at 0.3%, comparable with the luminosities observed in flat-spectrum radio quasars (FSRQs). The jet powers are $\sim 10^{42-46}$ erg s^{-1}, comparable with BL Lac Objects, yet relatively smaller than FSRQs. However, once renormalized by the mass of the central black hole, the jet powers of RLNLS1s, BL Lacs, and FSRQs are consistent each other, indicating the scalability of the jets. We found episodes of extreme variability at high energies on time scales of hours. In some cases, dramatic spectral and flux changes are interpreted as the interplay between the relativistic jet and the accretion disk. We conclude that, despite the distinct observational properties, the central engines of RLNLS1s are similar to those of blazars.

1. The Survey

As soon as the *Fermi* Large Area Telescope (LAT, Atwood et al. 2009) revealed high-energy γ-ray emission from a handful of radio-loud narrow-line Seyfert 1 galaxies (RLNLS1s, Abdo et al. 2009a,b,c, Foschini et al. 2010), we searched for more information about this type of AGN. Unlike their radio-quiet siblings, RLNLS1s were poorly observed and studied, probably because they are faint at all wavelengths. However, some pioneering surveys were carried out by Zhou & Wang (2002), Komossa et al. (2006), Whalen et al. (2006), and Yuan et al. (2008), the latter comprising 23 RLNLS1s with radio loudness at 1.4 GHz greater than 100. After the *Fermi* discovery of high-energy γ rays, Foschini (2011) performed a study on 76 NLS1s (46 radio loud, 30 radio quiet) based on archival data, where there was a clear lack of information in some frequency bands. In particular, only 60% of sources were detected in the *ROSAT* All Sky Survey (X-rays).

To optimize our efforts, we focussed on a subsample of RLNLS1s, mainly characterized by the flat or inverted radio spectral index ($\alpha_{\rm r} < 0.5$, $S_\nu \propto \nu^{-\alpha_{\rm r}}$), although we have taken into account also those sources with a single-frequency radio detection[1]. In addition to what was available in public archives, we obtained new observations with the X-ray satellites *Swift* (25 sources) and *XMM-Newton* (3 sources). We studied also optical spectra from the Sloan Digital Sky Survey (SDSS), complemented with new observations (2 sources) from the Asiago Astrophysical Observatory (Italy). In addition, extensive multifrequency radio observations with high sampling rate of four γ-detected RLNLS1s are reported by Angelakis et al. (2015), while Lähteenmäki et al. (in preparation) is performing a high-frequency ($22 - 37$ GHz) radio survey. Infrared properties (*WISE*) have been analysed in detail by Caccianiga et al. (2015). The parent population, which comprises the sources with the jet viewed at large angles, was studied by Berton et al. (2015a). A more thorough discussion can be found in Foschini et al. (2015).

The distributions of masses of the central black holes and the luminosities of the accretion disks are shown in Fig. 1, together with a sample of blazars (FSRQs and BL Lac Objects) for comparison. It is evident that RLNLS1s cover a previously unexplored part of that parameter space. This is crucial in the unification of powerful relativistic jets from stellar-mass black holes and neutron stars to AGN, as shown by Foschini (2014).

We found some interesting observational characteristics of RLNLS1s. About 17% of the sources (7/42) were detected at MeV–GeV energies[2], with an average spectral index $\alpha_\gamma \sim 1.6$, similar to FSRQs (~ 1.4). We detected about 90% of

---

[1] We calculated the radio spectral index between 1.4 and 5 GHz when possible. When the latter measurement was missing, we used any other frequency available. Half of the sources (21/42) had only one detection at 1.4 GHz. After the publication of our work, Richards & Lister (2015) observed at 9 GHz one of these sources (J0953 + 2836) and calculated a spectral index of $\alpha_{1.4-9\,{\rm GHz}} = 0.5$, which is still matching our requirements.

[2] After the publication of our work, D'Ammando et al. (2015) reported about the γ-ray detection of one source of our sample, J1644 + 2619, thus increasing the detection rate to 19% (8/42). Three new γ-ray detections of RLNLS1s – not included in the present sample – were reported by Komossa et al. (2015), Liao et al. (2015), Yao et al. (2015).
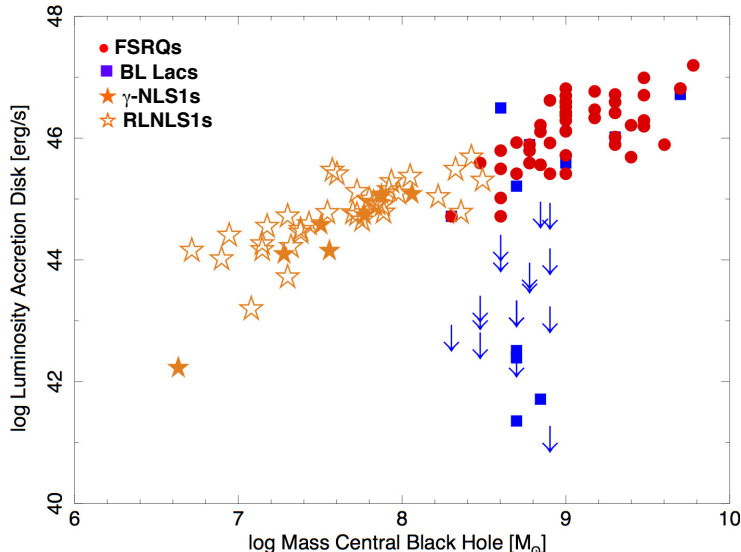
Figure 1. The parameter space of the luminosity of the accretion disk and the mass of the central black hole for AGN with powerful relativistic jets. FSRQs (red filled circles), BL Lacs (blue filled squares, blue arrows for upper limits), RLNLS1s (orange stars; γ-ray detections are indicated with filled orange stars). Cf. Foschini et al. (2015).

the sources (38/42) at X-rays (keV energies), but three of the four undetected objects were never observed at X-rays and we found an upper limit in the RASS only. The X-ray spectral index of RLNLS1s is similar to broad-line Seyfert 1s ($\alpha_{\mathrm{X,RLNLS1}} \sim 1.0$, $\alpha_{\mathrm{X,BLS1}} \sim 1.1$) and in the middle between FSRQs and BL Lac Objects ($\alpha_{\mathrm{X,FSRQ}} \sim 0.6$, $\alpha_{\mathrm{X,BL\,Lac}} \sim 1.3$). The spectral energy distributions (SEDs) of RLNLS1s showed that the X-ray emission could be due to inverse-Compton emission either from the relativistic jet (non thermal) or the corona of the accretion disk (thermal). This could explain why the average spectral index is softer than that of FSRQs, where the X-ray emission is dominated by the jet only. Infrared colours are typical of synchrotron emission, although there is a significant overlap with the starburst region in the *WISE* color-color diagram (see also Caccianiga et al. 2015).

Violent intraday variability – even on hour timescales – has been observed in many sources in the sample at all wavelengths. In some cases, where a dense multiwavelength coverage was available, we observed strong spectral changes in the SED that could be explained by the jet-disk interplay. Radio measurements indicate changes only in the Very Large Baseline Interferometer (VLBI) core, and in a few cases, when compared to γ-ray lightcurves, suggested a link between the rotation of the electric vector position angle (EVPA) and the emission at high energy.

The calculated jet power is in the range $10^{42.6-45.6}$ erg s^{-1}, generally lower than blazars, yet consistent if normalised by the mass of the central black hole. We conclude that RLNLS1s are similar to other AGN with a powerful relativistic

jets. Specifically, they seem to be the low-power tail of the FSRQ distribution. The small number of sources known today is likely due to either their low observed luminosities or an on-off behaviour of the jet. Future observatories with better sensitivities (e.g. SKA, Berton et al. 2015b), should reveal more sources of this type.

References

Abdo, A. A., et al. (LAT Coll.) 2009a, ApJ, 699, 976

Abdo, A. A., et al. (LAT Coll.) 2009b, ApJ, 707, 727

Abdo, A. A., et al. (LAT Coll.) 2009c, ApJ, 707, L142

Angelakis, E., Fuhrmann, L., Marchili, N., et al. 2015, A&A, 575, A55

Atwood, W. B., et al. (LAT Coll.) 2009, ApJ, 697, 1071

Berton, M., et al. 2015a, These Proceedings

Berton, M., et al. 2015b, in: "The Many Facets of Extragalactic Radio Surveys: Towards New Scientific Challenges", 20-23 October 2015, Bologna (Italy).

Caccianiga, A., Antón, S., Ballo, L., et al. 2015, MNRAS, 451, 1795

D'Ammando, F., et al., 2015, MNRAS, 452, 520

Foschini, L. 2011, in "Narrow-Line Seyfert 1 Galaxies and Their Place in the Universe", Proceedings of Science, vol. NLS1, id 24

Foschini, L. 2014, IJMP CS, 28, 1460188

Foschini, L., et al. (LAT Coll.) 2010, in "Accretion and Ejection in AGNs: A Global View", ASP Conf. Series, vol. 427, p. 243

Foschini, L., Berton, M., Caccianiga, A., et al., 2015, A&A, 575, A13

Komossa, S., Voges, W., Xu, D., et al. 2006a, AJ, 132, 531

Komossa, S., Xu, D., Fuhrmann, L., et al., 2015, A&A, 574, A121

Liao, N.-H., Liang, Y.-F., Weng, S.-S., et al., 2015, `arXiv:1510.05584`

Lister, M. L., Aller, H. D., Aller, M. F., et al. 2009, AJ, 137, 3718

Lister, M. L., Aller, M. F., Aller, H. D., et al. 2013, AJ, 146, 120

Richards, J. L., & Lister, M. L. 2015, ApJ, 800, L8

Whalen, D. J., et al. 2006, AJ, 131, 1948

Yao, S., Yuan, W., Zhou, H., et al., 2015, MNRAS, 454, L16

Yuan, W., Zhou, H. Y., Komossa, S., et al. 2008, ApJ, 685, 801

Zhou, H., & Wang, T. 2002, Chin. J. Astron. Astrophys., 2, 501

Hadronic processes in the low-luminosity radio galaxy IC310

N. Fraija[1], A. Marinelli[2], A. Galván-Gámez[1] and E. Aguilar-Ruiz[1]

[1]*Instituto de Astronomía, Universidad Nacional Autónoma de México, Circuito Exterior, C.U., A. Postal 70-264, 04510 México D.F., México. (*nifraija@astro.unam.mx, g.antonio@ciencias.unam.mx, eaguilar@astro.unam.mx*)*
[2]*I.N.F.N. & Physics Institute Polo Fibonacci Largo B. Pontecorvo, 3 - 56127 Pisa, Italy. (*antonio.marinelli@pi.infn.it*)*

Abstract. The active radio galaxy IC310 is one of brightest objects of the Perseus cluster in the radio wavelengths and X-rays. This source has been detected in radio, X rays and γ rays. Recently, a γ-ray flux at TeV energies was detected by the MAGIC Telescopes. We introduce a lepto-hadronic model to describe the spectral energy distribution (SED), radio to GeV photons as synchrotron self-Compton (SSC) emission and TeV photons as the result of the decay of neutral pions resulting from pγ interactions. For the pγ interactions, we assume that the seed photons are those around the second SSC peak. We show that this hadronic model describes successfully the TeV γ-ray photons at low state of this radio galaxy. Additionally, we compute the number of neutrinos expected to be detected in the IceCube neutrino telescope.

1. Introduction

The radio galaxy IC310, also called B0313+411 and J0316+4119, located in the Perseus Cluster at a redshift of $z = 0.00189$ (Bernardi et al. 2002) is one of brightest objects of the Perseus cluster in the radio and X-ray bands. Due to its kiloparsec-scale radio morphology, it has been classified as a head-tail or, more specifically, narrow-angle tail radio galaxy (Feretti et al. 1998). This radio galaxy is one of the four closest AGN (after Cen A, M87 and NGC1275) observed in VHE γ-rays (> 150 GeV). It has been detected above 30 GeV by Fermi-LAT (Neronov et al. 2010) and above 260 GeV by MAGIC telescopes (Aleksic et al. 2010). The detection above 120 GeV took place between 2008 November and 2010 February Aleksic et al. 2014). The indications for flux variability on time scales of months and years, and a hard spectrum in high and low state ($F \propto E^{-\alpha}$ with $\alpha \sim 2.0$) were reported. The variability time scale of years was confirmed by the non-detection of the source reported in 2010 August - 2011 February (Aleksic et al. 2014). In this paper, we propose that the SED of IC 310 can be described as synchrotron self-Compton (SSC) emission and pion decay products from proton-photon interactions. We calculate the number of neutrinos expected from these interactions on the IceCube neutrino telescope.

2.   Theoretical model

In the following subsections we are going to describe the SSC emission and pion decay products.

2.1.   SSC emission

Fermi-accelerated electrons in the emitting region are described by a broken power-law written as (Fraija et al. 2012)

$$N_e(\gamma_e) = N_{0,e} \begin{cases} \gamma_e^{-\alpha_e} & \gamma_{e,m} < \gamma_e < \gamma_{e,b}, \\ \gamma_{e,b}\gamma_e^{-(\alpha_e+1)} & \gamma_{e,b} \le \gamma_e < \gamma_{e,max}, \end{cases} \tag{1}$$

where $N_{0,e}$ is the proportionality electron constant, α_e is the spectral power index of the electron population and $\gamma_{e,i}$ are the electron Lorentz factors. We assume that the emitting region is endowed with a magnetic field, then electrons are cooled down by synchrotron radiation in accordance with the cooling time scale $t'_c = \frac{3m_e}{4\sigma_T} U_B^{-1} \gamma_e^{-1}$, with $U_B = \frac{B^2}{8\pi}$, m_e the electron mass and $\sigma_T = 6.65 \times 10^{-25}$ cm^2 the Compton cross section. Comparing the previous synchrotron time scale with the dynamic scale $t'_d \simeq r_d/\delta_D$, being r_d the radius of emitting region, the break Lorentz factor is

$$\gamma_{e,b} = \frac{3\,m_e}{4\,\sigma_T} (1+Y)^{-1} \delta_D U_B^{-1} r_d^{-1}, \tag{2}$$

where δ_D is the Doppler factor, $Y \equiv \frac{\eta U_e}{(1+Y)U_B}$ is the Compton parameter with $U_e = m_e \int \gamma_e N_e(\gamma_e)d\gamma_e$. Here $\eta = (\gamma_{e,b}/\gamma_{e,m})^{2-\alpha_e}$ is for slow cooling and $\eta = 1$ for fast cooling with $\gamma_{e,m} = \frac{(\alpha_e-2)}{m_e(\alpha_e-1)} \frac{U_e}{N_e}$. Taking into account the cooling processes for electron distribution, the observed spectra for electron synchrotron radiation is (Fraija and Marinelli 2016, Fraija et al. 2012)

$$\left[\epsilon^2 N(\epsilon)\right]_{\gamma,syn} = A_{syn,\gamma} \begin{cases} (\frac{\epsilon_\gamma}{\epsilon_{\gamma,m}^{syn}})^{4/3} & \epsilon_\gamma < \epsilon_{\gamma,m}^{syn} \\ (\frac{\epsilon_\gamma}{\epsilon_{\gamma,m}^{syn}})^{-(\alpha_e-3)/2} & \epsilon_{\gamma,m}^{syn} < \epsilon_\gamma < \epsilon_{\gamma,c}^{syn} \\ (\frac{\epsilon_{\gamma,c}^{syn}}{\epsilon_{\gamma,m}^{syn}})^{-(\alpha_e-3)/2}(\frac{\epsilon_\gamma}{\epsilon_{\gamma,c}^{syn}})^{-(\alpha_e-2)/2}, & \epsilon_{\gamma,c}^{syn} < \epsilon_\gamma < \epsilon_{\gamma,max}^{syn}, \end{cases} \tag{3}$$

where $A_{syn,\gamma}$ and $\epsilon_{\gamma,i}^{syn}$ are the normalization constant and synchrotron spectral breaks, respectively.

Fermi-accelerated electrons in the emitting region can upscatter synchrotron photons up to higher energies by $\epsilon_{\gamma,(m,c,max)}^{ssc} \simeq \gamma_{e,(m,c,max)}^2 \epsilon_{\gamma,(m,c,max)}^{syn}$. Considering the synchrotron spectrum (eq. 3), the Compton scattering spectrum is obtained in Fraija and Marinelli (2016).

2.2.   Pion decay products

We consider a proton population described as a simple power law $\left(\frac{dN}{dE}\right)_p = A_p E_p^{-\alpha_p}$ (Fraija 2004a), with A_p the proportionality constant and α_p the spectral power index of the proton population. Fermi-accelerated protons lose their

energies by electromagnetic channels and hadronic interactions. Electromagnetic channels such as proton synchrotron radiation and inverse Compton will not be considered here, we will only assume that protons will be cooled down by pγ interactions at the emission region in the jet. Charged (π^+) and neutral (π^0) pions are created from pγ interaction through the following channels $p\,\gamma \longrightarrow \Delta^+ \longrightarrow p\,\pi^0$ (branching ratio 2/3) and $n\,\pi^+$ (branching ratio 1/3) In the pγ interaction model, we consider that Fermi-accelerated protons interact with the photon population at the second-peak SED photons ($\epsilon_{pk,ic}$). Taking into account that photons released in the energy range ϵ_γ to $\epsilon_\gamma + d\epsilon_\gamma$ by protons in the range E_p and $E_p + dE_p$ are $f_{\pi^0}\, E_p\, (dN/dE)_p\, dE_p = \epsilon_{\pi^0,\gamma}\, (dN/d\epsilon)_{\pi^0,\gamma}\, d\epsilon_{\pi^0,\gamma}$, the photo-pion spectrum is reported in Fraija and Marinelli 2016. On the other hand, pγ interactions produce neutrinos as the $\pi^\pm$ decay product ($\pi^\pm \rightarrow \mu^\pm + \nu_\mu/\bar{\nu}_\mu \rightarrow e^\pm + \nu_\mu/\bar{\nu}_\mu + \bar{\nu}_\mu/\nu_\mu + \nu_e/\bar{\nu}_e$). Assuming that the neutrino spectrum produced by the photo hadronic interactions is $\frac{dN_\nu}{dE_\nu} = A_\nu \left(\frac{E_\nu}{\epsilon_0}\right)^{-\alpha_\nu}$, then the factor, A_ν, is computed through the TeV photon flux $\frac{dN_\nu}{dE_\nu}\, E_\nu\, dE_\nu = \frac{1}{4}\frac{dN_\gamma}{dE_\gamma}\, E_\gamma\, dE_\gamma$ as $A_\nu = A_{p\gamma}\,\epsilon_0^{-2}\,2^{-\alpha_p}$ (Halzen 2007, Fraija 2014b). The previous equation was obtained assuming that the spectral indices for neutrino and TeV γ-ray spectra are similar $\alpha_p \simeq \alpha_\nu$ (Becker 2008) and each neutrino carries 5% of the initial proton energy. The neutrino flux is detected when it interacts inside the instrumented volume with effective volume (V_{eff}) and density (ρ_{ice}). Considering the probability of interaction for a neutrino with energy E_ν, the number of expected neutrino events after a period of time T is

$$N_{ev} \approx T\rho_{ice}\, N_A\, \epsilon_0 \int_{E_{\nu,th}} V_{eff}(E_\nu)\sigma_{\nu N}(E_\nu)\, A_\nu \left(\frac{E_\nu}{\epsilon_0}\right)^{-\alpha_p}, \qquad (4)$$

where N_A is the Avogadro number, $\sigma_{\nu N}(E_\nu)$ is the the charged current cross section and $E_{\nu,th}$ is the energy threshold. It is worth noting that the $\nu_\mu + \bar{\nu}_\mu$ effective volume V_{eff} is the effective volume of IceCube (IceCube collaboration 2013).

3. Results and Conclusions

We have showed a theoretical model to interpret the broadband SED of IC310. In the leptonic scenario, we have used the SSC emission to describe the photon spectrum up to a few GeVs. The first peak, at an energy of $\sim 10^{-2}$ eV is described through synchrotron radiation (eq. 3) and the second peak at 1 MeV is explained as Compton scattering emission. To interpret the TeV γ-ray spectrum at low state, we have proposed a hadronic model through pγ interactions. We have assumed that neutral pions are produced in the interaction of accelerated protons in the jet described by a simple power law with the Compton scattering photon population at the emission region.
To find the best fit of our leptonic and hadronic models, we use the method of Chi-square χ^2 minimization as implemented in the ROOT software package. The fit values for the lepto-hadronic model are shown in Table 1. From the fit, we have found the values of Doppler factor $\delta_D = 1.8$, magnetic field $B = 0.12$ G, the radius of emitting region $r_d = 3.98 \times 10^{16}$ cm and electron density 3.61×10^2 cm^{-3}. Additionally, from the pγ interactions we have calculated the number of expected
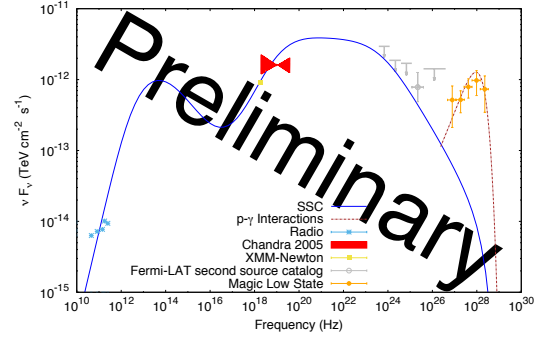
Figure 1.   SED of IC310 adjusted with a lepto-hadronic model.

neutrinos in a hypothetical km^3 telescope. Considering the values $A_{p\gamma}$ and α_p reported in Table 1 and eq. (4), the number of neutrino events expected in the IceCube neutrino telescope is 0.02.

Parameter	IC310
Leptonic model	
$A_{syn,\gamma}$ (MeV cm^{-2} s^{-1})	$(1.37 \pm 0.12) \times 10^{-6}$
α_e	3.03 ± 0.15
$\epsilon_{\gamma,m}^{syn}$ (eV)	0.011 ± 0.005
$\epsilon_{\gamma,c}^{syn}$ (eV)	0.15 ± 0.02
$A_{ssc,\gamma}$ (MeV cm^{-2} s^{-1})	$(4.36 \pm 0.37) \times 10^{-6}$
$\epsilon_{\gamma,m}^{ssc}$ (keV)	0.95 ± 0.05
$\epsilon_{\gamma,c}^{ssc}$ (MeV)	12.01 ± 1.12
Hadronic model	
$A_{p\gamma}$ (MeV cm^{-2} s^{-1})	$(1.11 \pm 0.15) \times 10^{-6}$
α_p	2.2 ± 0.3

Table 1. Values obtained after fitting the spectrum of the IC310.

References

Aleksić, J. & et al. 2014, A&A, 563, 91

Aleksić, J. & et al. 2010, ApJ, 723, L207

Bernardi, M., Alonso, M. V., da Costa, L. N., et al. 2002, AJ, 123, 2990

Brun, R., & Rademakers, F. 1997, Nuclear Instruments and Methods in Physics Research A, 389, 81

Fraija, N., González, M. M., Perez, M. & Marinelli, A. 2012 ApJ, 753, 40

Fraija, N. 2014a, MNRAS, 437, 2187

Fraija, N. 2014b, ApJ, 783, 44

Fraija, N. & Marinelli A. 2016, ApJ, 830, 81

Halzen, F. 2007, Ap&SS, 309, 407

Neronov, A., Semikoz, D., & Vovk, I. 2010, A&A, 519, L6

IceCube collaboration 2013, Science, 342, 0

Optical spectroscopic and photometric observations of unclassified Active Galactic Nuclei in the *Fermi*-2LAC catalogue

L. Klindt[1], B. van Soelen[1], P.J. Meintjes[1], P. Väisänen[2,3], A. Kniazev[2,3]

[1]*Department of Physics, University of the Free State, 9301, South Africa*
[2]*South African Astronomical Observatory, PO Box 9, Observatory 7935, Cape Town, South Africa*
[3] *Southern African Large Telescope, PO Box 9, Observatory 7935, Cape Town, South Africa*

Abstract.
The *Fermi*-LAT 2-year Source catalogue (2LAC) contains approximately 157 sources which are classified as AGN of unknown type (AGU) with no determined redshifts. We have identified a subset of these AGUs for follow-up studies aiming to classify them and determine redshifts, utilizing South African observatories. Optical spectroscopic observations have been performed with the Southern African Large Telescope (SALT) and short term photometric variability of the sources was studied using the SAAO 1.9-m telescope. The results for five candidates are discussed. The spectra are mainly featureless as expected for BL Lacs, however, potential spectral features are present for some sources. Similarly, photometric monitoring shows potential variability, for certain sources.

1. Introduction

Blazars, which are separated into BL Lacartae objects (BL Lacs) and Flat Spectrum Radio Quasars (FSRQs), exhibit strong and rapid multi-frequency variability, as well as radio and optical polarization. The *Fermi*-LAT 2-year Source catalogue (2LAC) consists of a clean sample of 866 gamma-ray sources which are located at high galactic latitudes, of which approximately 157 are classified as AGN of unknown type (AGU) with no determined redshifts (Ackermann et al., 2011). We have identified a subset of these extragalactic AGUs (see Klindt et al. 2015 for full discussion of selection criteria and target list) with the aim of classifying the selected targets from South African observatories. For our optical observing campaign we placed focus on ten of these sources, of which the remaining targets listed in our sample will contribute to future follow-up studies. To achieve our aim we are undertaking a multi-wavelength campaign to establish the distance, type, variability, Spectral Energy Distributions (SEDs), as well as to search for multi-wavelength correlations for these sources.

BL Lacs are optically defined as sources with emission and/or absorption lines with equivalent widths $|W_\lambda| < 5$ Å, and a diluted Ca break value less than 40% (see e.g. Marchã et al. 1996, Landt et al. 2002, Galbiati et al. 2005). Since the optical continuum is dominated by synchrotron emission, redshift measurements of BL Lacs can be troublesome, however, in some cases absorption features,

i.e. Ca II H&K, Mg I and NaD lines, are present. These absorption lines are produced by the host galaxy's stellar population and/or intervening halos.

FSRQs, on the other hand, exhibit lower synchrotron peak frequencies, and have strong narrow and broad emission lines which are produced by the thermal disk and the Broad-Line Region (BLR). The observed lines include for example Hb, Mg II and C IV.

Blazars exhibit flux variability on times scale of less than a day (intra-day variability, IDV), to days to months (short-term variability, STV), and longer (long-term variability, LTV) (see e.g. Wagner & Witzel, 1995, Gupta et al. 2004). The possible sources of the intrinsic variability are the shocks within the jet, hot spots and instabilities in the accretion disk, as well as the binary black hole model which contributes to long term periodic variability (Gupta et al., 2009).

Broad band optical spectroscopy has been undertaken with the Southern African Large Telescope (SALT) and intraday and short term variability has been searched for using the Sutherland High speed Optical Camera (SHOC) on the SAAO 1.9-m telescope. In total we have obtained optical spectra with SALT and the SAAO 1.9-m telescope for twelve sources in our sample, but we determined redshift measurements for eight of these sources from absorption/emission lines featuring in their spectra. The other four sources have featureless spectra. Here we present the optical spectroscopic and photometric observational results for five targets listed in our original sample.

2. Observations

2.1. SALT Spectroscopy

Longslit spectra of four candidate sources were obtained with SALT, utilizing the Robert Stobie Spectrograph (RSS). In order to perform a search for unknown spectral features a low resolution broad wavelength coverage of approximately $3\,800 - 10\,000$ Å was initially obtained. The observations were undertaken during 2014-Semester II and 2015-Semester I, with two configurations. Two sources, namely 2FGL J0044.7-3702 and 2FGL J0201.5-6626, show broad emission lines, suggesting a FSRQs classification, with redshifts of $z = 1.03$ and $z = 1.29$, respectively. The spectra of 2FGL J0730.6-6607 and 2FGL J1218.8-4827 indicate that these sources are of a BL Lac nature with redshifts of $z = 0.11$ and $z = 0.15$, respectively (see Figure 1).

2.2. SHOC Photometry

Observations were undertaken with the SHOC using the SAAO 1.9-m telescope and data reduction was performed utilizing the provided SHOC reduction pipeline.[1] Differential photometry has been performed using comparison stars in the same field of view.

In Figure 2 we present the STV for five sources. We have employed the F-test and the power-enhanced F-test (at the $\alpha = 0.01$ and $\alpha = 0.001$ significance levels), to search for IDV and STV (see e.g. Josh et al. 2011, Gaur et al. 2012,

---

[1]http://www.saao.ac.za/ marissa/SHOCpipeline/
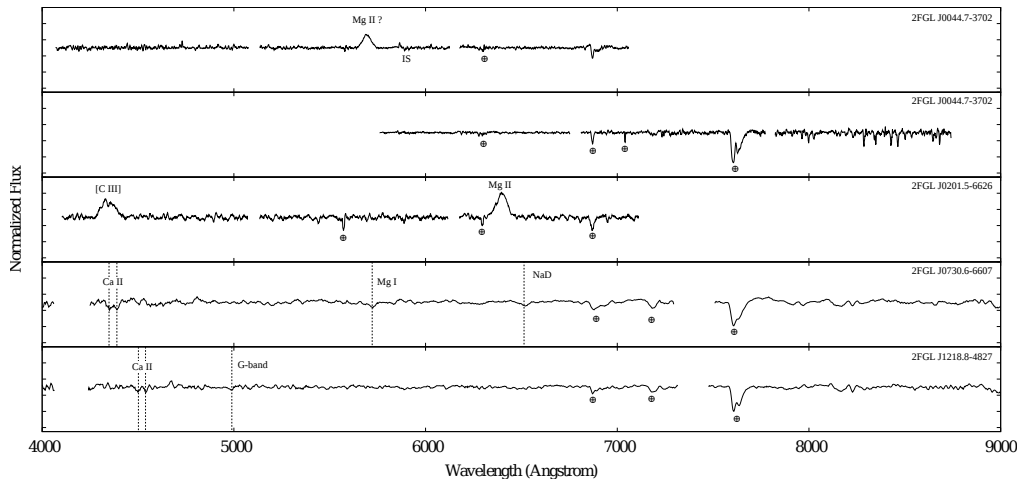
Figure 1. Normalized spectra of four target sources, observed with the Southern African Large Telescope. The top two plots show observations of the same source, 2FGL J0044.7-3702, taken with two different RSS configurations. The gaps in the spectra are due to the spaces between the three CCD in the RSS.

Goyal 2012, Agarwal & Gupta 2015). STV was detected over a time scale of a week for 4 targets, with only 2FGL J0044.7-3702 showing no variability. We found that for most nights the targets listed in our sample do not exhibit IDV with the exception of 2FGL J0201.5-6626, 2FGL J0644.2-6713, 2FGL J0730.6-6607 and 2FGL J1218.8-4827, which showed possible variability in the clear filter on certain nights.

3. Discussion and Conclusion

The RSS spectra obtained with SALT, have yielded promising results for classifying the *Fermi*-2LAC AGU targets in our sample. We have detected broad emission lines, namely Mg II and/or C [III], in the spectra of 2FGL J0044.7-3702 and 2FGL J0201.5-6626, which potentially place these sources in the FSRQ subclass at redshifts of $z = 1.03$ and $z = 1.29$, respectively. 2FGL J0730.6-6607 appears to be BL Lac in nature based on the Ca II H&K, Mg I and NaD absorption lines with a redshift measurement of $z = 0.11$. Potential Ca II H&K and G-band absorption lines from the host galaxy are present in the spectrum of 2FGL J1218.8-4827, which allows for a first approximation of the redshift measurements as $z = 0.15$.

The optical photometry shows STV detected over a time scales of a week for 4 targets in our unclassified *Fermi*-2LAC AGN sample, though the sample does not, in general, exhibit IDV.
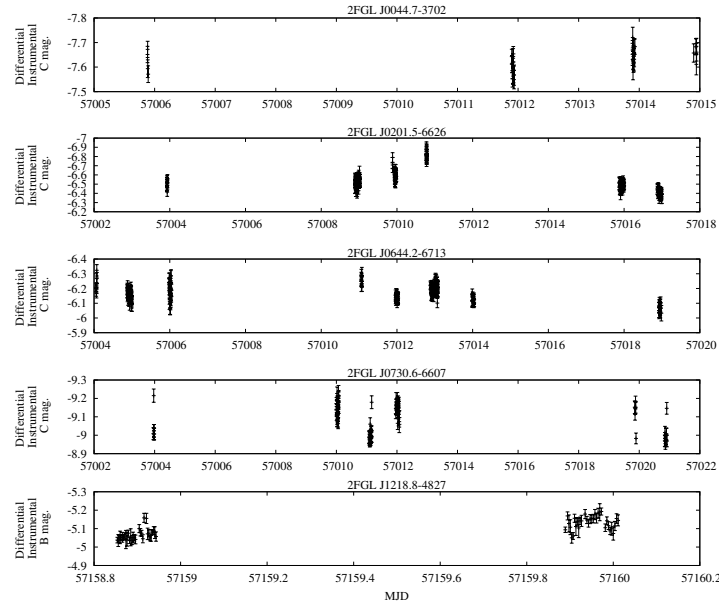
Figure 2. Photometric observations of 5 candidate sources undertaken with the SHOC camera.

References

Ackermann M., et al. 2011, ApJ, 171, 37

Agarwal A., Gupta A.C. 2015, MNRAS, 450, 541

Galbiati E., et al. 2005, A&A, 430, 927

Gaur H., et al. 2012, MNRAS, 425, 3002

Goyal A. 2012, A&A, 544, A37

Gupta A.C., et al. 2004, A&A, 422, 505

Gupta A.C., et al. 2009, ApJ, 690, 216

Joshi R., et al. 2011, MNRAS, 412, 2717

Klindt L., Meintjes P.J., van Soelen B. 2015, in Proceedings of the 59th Annual Conference of the South African Institute of Physics, C. Engelbrecht, S. Karataglidis (eds), p 341

Landt H., Padovani P., Giommi P. 2002, MNRAS, 336, 945

Marchã M.J.M., et al. 1996, MNRAS, 281, 425

Topinka M., et al. 2013, in Proceedings of Gamma-ray Bursts: 15 Years of GRB Afterglows – Progenitors, Environments and Host Galaxies from the Nearby to the Early Universe, A.J. Castro-Tirado, J. Gorosabel and I.H. Park (eds.), EAS Publication Series, 61, 487

Wagner S.J., Witzel A. 1995, ARA&A, 33, 163

Scalar-tensor-vector gravity effects on relativistic jets of AGNs

F.G. Lopez Armengol[1] and G.E. Romero[1,2]

[1]*Instituto Argentino de Radioastronomía CCT La Plata (CONICET), C.C.5 1894 Villa Elisa, Buenos Aires, Argentina*
[2]*Facultad de Ciencias Astronómicas y Geofísicas, Universidad Nacional de La Plata, Paseo del Bosque s/n, 1900 La Plata, Buenos Aires, Argentina*
`flopezar@iar-conicet.gov.ar`

Abstract. We investigate the effects predicted by an alternative model of gravity on the shape and trajectory of relativistic plasma ejections from the central region of Active Galactic Nuclei. Specifically, we calculate the effects of gravitational Lorentz-like forces that arise in the context of Moffat's Scalar-Tensor-Vector Gravity (STVG), produced by a supermassive black hole on a relativistic plasma blob.

1. Introduction

The Scalar-Tensor-Vector Gravity (STVG) theory (Moffat, 2006), also referred as MOdified Gravity (MOG) theory, has successfully explained solar system observations (Moffat, 2006), galaxy rotation curves (Brownstein & Moffat, 2006), and the dynamics of galactic clusters (Moffat & Rahvar, 2014). The theory has also been applied with success to describe the growth of structure, the matter power spectrum, and the cosmic microwave background (CMB) acoustical power spectrum data (Moffat & Toth, 2007). It remains as one of the most attractive alternatives to general relativity as a theory of gravitation, with the advantage that it offers a solution to the dark matter and dark energy problems.

Most of the applications published so far are based on vacuum solutions in the weak field limit. Recently, Moffat (2015) has found black hole solutions in this theory. Here, we use the STVG-Kerr solution to study geodetic motion of relativistic ejections in AGNs and compare them with results obtained in the framework of General Relativity (GR).

2. STVG field equations

In STVG, the gravitational coupling constant G is replaced by a scalar field whose numerical value usually exceeds Newton constant G_N. This enforces a gravitational attraction that adjusts galactic and cosmological observations without requiring the postulation of dark matter. In order to counterpart the enhanced gravitational constant on Solar System scales, Moffat proposed a gravitational repulsive Yukawa-like vector field ϕ^μ, so Newton's gravitational constant can be retrieved and STVG coincides with GR in every Solar System prediction.

The equations of the theory are obtained through the following action for the gravitational field:

$$S = S_{\mathrm{GR}} + S_\phi + S_{\mathrm{G}} + S_\mu + S_{\mathrm{M}}, \tag{1}$$

where

$$S_{\mathrm{GR}} = \frac{1}{16\pi} \int d^4x \frac{1}{G} \sqrt{-g} R, \tag{2}$$

$$S_\phi = \omega \int d^4x \sqrt{-g} \left(\frac{1}{4} B^{\mu\nu} B_{\mu\nu} - \frac{1}{2} \mu^2 \phi^\mu \phi_\mu \right), \tag{3}$$

$$S_{\mathrm{G}} = \int d^4x \sqrt{-g} \frac{1}{G^3} \left(\frac{1}{2} g^{\mu\nu} \nabla_\mu G \nabla_\nu G + V(G) \right), \tag{4}$$

$$S_\mu = \int d^4x \sqrt{-g} \frac{1}{G\mu^2} \left(\frac{1}{2} g^{\mu\nu} \nabla_\mu \mu \nabla_\nu \mu + V(\mu) \right). \tag{5}$$

Here, $g_{\mu\nu}$ denotes the spacetime metric, R is the corresponding Ricci scalar, and ∇_μ is the covariant derivative; ϕ^μ denotes a Proca-type massive vector field, μ is the mass of the field, $B_{\mu\nu} = \partial_\mu \phi_\nu - \partial_\nu \phi_\mu$, and $\omega = 1/\sqrt{12}$; $V(G)$ and $V(\mu)$ denote the potentials of the scalar fields $G(x)$ and $\mu(x)$, respectivly. We adopt the metric signature $\eta_{\mu\nu} = \mathrm{diag}(1,-1,-1,-1)$, and choose units with $c = 1$. The term S_{M} refers to possible matter sources.

In this work, we neglect the mass of the vector field because its effects manifest on kilo-parsec distances from the supermassive source (see Moffat, 2015). Also, since there is still a lot of freedom on the functional form of the scalar field G, in this first work we consider it as a constant, in accordance with Moffat's previous works on vacuum solutions.

Varying the action with respect to $g^{\mu\nu}$ and taking previous simplifications into account, we obtain the metric field equations:

$$G_{\mu\nu} = 8\pi G \left(T^{\mathrm{M}}_{\mu\nu} + T^\phi_{\mu\nu} \right), \tag{6}$$

where $G_{\mu\nu}$ denotes the Einstein tensor, and $T^{\mathrm{M}}_{\mu\nu}$, $T^\phi_{\mu\nu}$ are the matter and vector field energy-momentum tensors, respectively. We adopt for the enhanced gravitational coupling constant the same prescription as Moffat (2006):

$$G = G_{\mathrm{N}}(1 + \alpha), \tag{7}$$

where G_{N} denotes Newton gravitational constant, and α is a free parameter. Within these approximations, STVG coincides with GR for $\alpha = 0$.

Variation of the simplified action with respect to ϕ_μ yields:

$$\nabla_\nu B^{\nu\mu} = \frac{\sqrt{\alpha G_{\mathrm{N}}}}{\omega} J^\mu, \tag{8}$$

where J^μ denotes the four-current matter density, and the constant $\sqrt{\alpha G_{\mathrm{N}}}$ is determined to adjust the known phenomenology.

Finally, variation with respect to particle coordinates δx^μ yields the modified equation of motion:

$$m\left(\frac{d^2 x^\mu}{d\tau^2} + \Gamma^\mu_{\alpha\beta}\frac{dx^\alpha}{d\tau}\frac{dx^\beta}{d\tau}\right) = \kappa m\omega B^\mu{}_\nu \frac{dx^\nu}{d\tau}. \tag{9}$$

With the mentioned approximations, STVG equations 6, 8 and 9, are similar to Einstein-Maxwell equations. In the following, we make use of the equivalence between these formalisms and integrate Eq. 9 for a relativistic jet ejected by STVG-Kerr black hole.

3. STVG-Kerr spacetime

The vacuum axially symmetric solution that represents a rotating black hole in STVG theory is (Moffat 2015):

$$ds^2 = \frac{\Delta}{\rho^2}(dt - a\sin^2\theta d\phi)^2 - \frac{\sin^2\theta}{\rho^2}\left[(r^2 + a^2)d\phi - adt\right]^2 - \frac{\rho^2}{\Delta}dr^2 - \rho^2 d\theta^2, \tag{10}$$

where we have taken units such that $c = 1$, and:

$$\Delta = r^2 - 2GMr + a^2 + \alpha G_{\mathrm{N}}GM^2, \quad \rho^2 = r^2 + a^2\cos^2\theta. \tag{11}$$

Here, a denotes the black hole angular momentum per unit mass and G the effective gravitational constant (see Eq. 7). A Kerr black hole is recovered for $\alpha = 0$. The STVG-Kerr black hole has two event horizons and an ergosphere, just like the classical Kerr geometry. It resembles Kerr-Newman black hole, where the electric charge is replaced by $Q = \sqrt{\alpha G_{\mathrm{N}}}M$, with M the mass of the black hole.

Field equations 6, 8, and geodetic equation 9 for a test particle in the Kerr-Newman black hole geometry have been studied by Carter (1968) and Misner, et al (1973). Replacing the electric charge in Kerr-Newman formalism by $Q = \sqrt{\alpha G_{\mathrm{N}}}M$, leads us to STVG-Kerr geometry results. In this way, the equations of motion for a test particle in the STVG-Kerr geometry are:

$$\rho^2\frac{dr}{d\lambda} = \frac{\sqrt{R(r)}}{c^2}, \tag{12}$$

$$\rho^2\frac{d\theta}{d\lambda} = \sqrt{\Theta(\theta)}, \tag{13}$$

$$\rho^2\frac{d\phi}{d\lambda} = -\left(\frac{aE}{c^2} - \frac{L}{\sin^2\theta}\right) + \frac{aP(r)}{\Delta(r)c^2}, \tag{14}$$

$$\rho^2\frac{dt}{d\lambda} = -\frac{a}{c}\left(\frac{aE\sin^2\theta}{c^4} - \frac{L}{c^2}\right) + \left(r^2 + \frac{a^2}{c^2}\right)\frac{P(r)}{\Delta(r)c^2}, \tag{15}$$

where

$$R(r) = P^2(r) - \Delta(r)\left(m^2 r^2 c^4 + c^2\mathcal{K}\right), \tag{16}$$
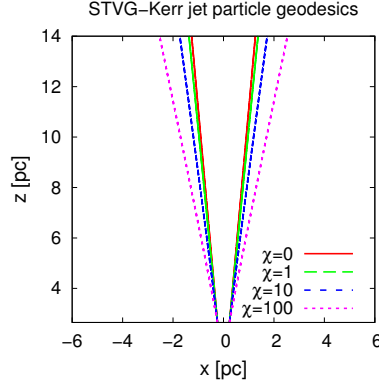
Figure 1. xz-plane trajectories of a test particle ejected by a STVG-Kerr supermassive black hole. The parameter χ quantifies the action of vectorial forces of STVG and corresponding deviations from GR. We model the STVG-Kerr black hole with mass $M = 10^9 \ M_\odot$ and normalized spin $a = 0.99$. We study a test particle with $m = 1$ g, initial radial velocity $v = 0.97c$, and initial position $r_{\text{ini}} = 1 \times 10^{19}$ cm, $\theta_{\text{ini}} = 0.1$, $\phi_{\text{ini}} = 0$, $p_{\theta,\text{ini}} = 0$.

$$\Theta(\theta) = \mathcal{Q} - \cos^2\theta \left[\frac{a^2}{c^2}\left(m^2 - \frac{E^2}{c^2} \right) + \frac{L^2}{\sin^2\theta} \right], \tag{17}$$

$$P(r) = E\left(r^2 + \frac{a^2}{c^2} \right) - La + \frac{mQr}{\sqrt{12}}. \tag{18}$$

Here, we have reinstall the speed of light c, λ denotes a time parameter, (t, r, θ, ϕ) are the particle Boyer-Lindquist coordinates, E stands for the test particle energy, L its angular momentum around the symmetry axis, and m its mass. Further, we have defined the constants of motion:

$$\mathcal{K} = p_\theta^2 + \cos^2\theta \left[a^2\left(m^2 - \frac{E^2}{c^2} \right) + \frac{L^2}{\sin^2\theta} \right], \tag{19}$$

$$\mathcal{Q} = \mathcal{K} - \left(L - \frac{aE}{c^2} \right). \tag{20}$$

In the next section, we integrate equations 12, 13, 14, 15 for a relativistic jet, and show preliminary results of the xz-plane trajectories.

4. Preliminary results

As a first step, we have calculated the geodetic motion of a particle ejected close to the rotational axis of a STVG-Kerr supermassive black hole. We take for the parameter α the same prescription as Brownstein & Moffat (2007):

$$\alpha^2 = \chi \left(60.4 \pm 4.1 \right) \times 10^{14} M_\odot \left(\frac{M}{10^{14} M_\odot} \right)^{0.39 \pm 0.1} M, \tag{21}$$

and we sample different values of the χ parameter.

We use a fourth order Runge-Kutta method to integrate equations 12, 13, 14, 15. The resulting xz-plane trajectory is plotted in Figure 1. As can be seen from the graphic, the effect of the gravitational Lorentz force that appears in STVG results in a lateral deviation of the trajectories from what is expected in GR.

5.   Conclusions

We conclude that STVG theory can be tested in a context not explored before: the environments of a rotating supermassive black hole. Deep, multi-epoch radio interferometric observations are ideal to test the theory, since blobs are expected to produce synchrotron radiation. Best targets are nearby AGNs such as Cen A or systems harbouring more massive black holes as 3C273 or 3C279.

References

Brownstein J. R., Moffat J. W. 2006, ApJ, 636, 721.

Brownstein, J. R., Moffat, J. W. 2007, MNRAS, 382, 29.

Carter, B. 1968, Phys.Rev. 174, 1559.

Misner, C. W., Thorne, K. S., Wheeler, J. A. 1973, "Gravitation", W. H. Freeman and Company.

Moffat J. W. 2006, JCAP, 3, 4.

Moffat, J. W. 2015, Eur. Phys. J. C, 75, 175.

Moffat J. W., Rahvar S. 2014, MNRAS, 441, 3724.

Moffat J. W., Toth V. T. 2007, ArXiv e-prints 0710.0364.

Looking for blazars in a sample of unidentified high-energy emitting Fermi sources: Preliminary results

E. J. Marchesini[1], N. Masetti[2,3], S. A. Cellone[1], I. Andruchow[1],
L. Bassani[2], A. Bazzano[4], R. Landi[2], A. Malizia[2], E. Palazzi[2],
J. B. Stephen[2], P. Ubertini[4]

[1] *Instituto de Astrofísica de La Plata – FCAGLP/CONICET, Argentina*
[2] *Istituto di Astrofisica Spaziale e Fisica Cosmica di Bologna –
INAF, Italy*
[3] *Universidad Andrés Bello – Santiago, Chile*
[4] *Istituto di Astrofisica e Planetologia Spaziali – INAF, Rome, Italy*

Abstract.   It is expected that a large fraction of the unidentified sources detected at γ-rays are blazars. Through cross–correlation between the positions of unidentified objects from the 1FHL Fermi catalogue of γ-ray sources and the ROSAT, XMM Slew and Swift/XRT catalogues of X–ray objects, a sample of 38 associations was found with less than 10 arcsec of positional error. One third of them has recently been classified; the remainder, though believed to belong to the blazar class, has not yet been identified. Therefore, we aim at studying the optical spectra of the counterparts of these unidentified sources in order to find their redshifts and to analyse their nature and main spectral features. We present here our preliminary results from optical spectroscopic observations at the 3.58 m Telescopio Nazionale Galileo (TNG) for 7 of them.

1.   Observations & Data Reduction

Searching for counterparts of high–energy sources is challenging because of the relatively large (several arcminutes) positional error ellipses of γ–ray objects detected with the Fermi satellite. This uncertainty means that a positional correlation with a known object is usually not enough to firmly identify a Fermi source. Cross–correlations were made (Stephen et al. 2010, Landi et al. 2015) between the positions of the 1FHL (Abdo et al. 2010) and Swift/XRT 1SXPS catalogues (Evans et al. 2014), and the ROSAT (Voges et al. 1999) and XMM-Newton surveys (Saxton et al. 2008). A strong level of correlation between unassociated 1FHL objects and soft X–ray sources was found, leading to better positions for all correlated sources; this is evident for the association of a number of gamma–ray objects with a soft X–ray counterpart (Landi et al. 2015). However, 24 of these unassociated 1FHL sources still lack an optical spectroscopic identification. Hence, the need for optical follow–up work is clear.

Seven of these objects were observed with TNG from April to June 2015 (see Table 1) within the framework of our ongoing program dealing with the identification of the nature of γ–ray sources (Masetti et al. 2013), to obtain medium–resolution spectra from $\sim$3700 to 8000 Å. The spectra were reduced,

wavelength and flux calibrated using standard IRAF[1] packages. The wavelength calibration has an estimated error of $3\,\text{Å}$.

2. Results
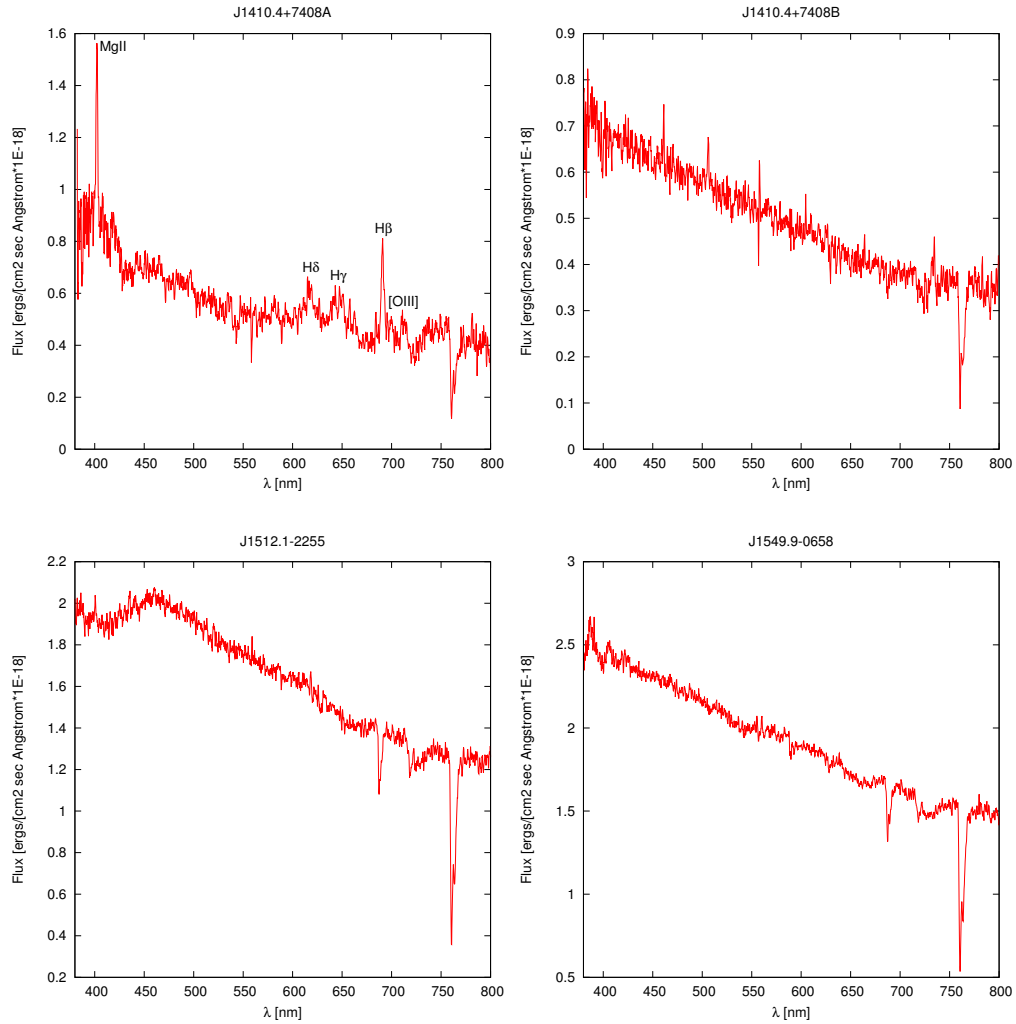
Figure 1.: Optical spectra of six sources presented in this contribution. The name of each object is reported above the corresponding panel.
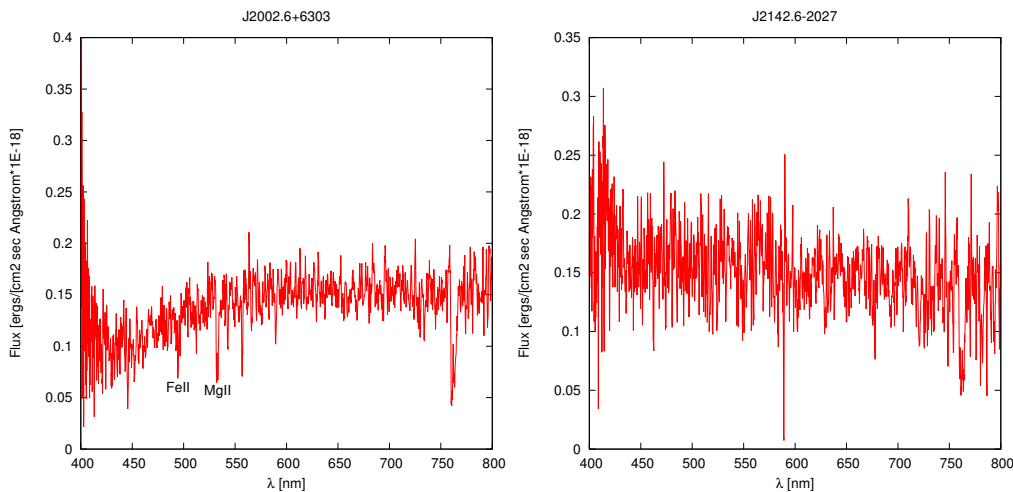

Figure 1.: Continued.

As it can be seen in Figure 1, our sample shows no spectral features other than atmospheric (telluric) ones, with the exception of 1FHL J1410.4+7408A and 1FHL J2002.6+6303. The former has strong, broad emission lines, the most prominent ones at 4021 Å and 6908 Å, which we identify with MgII and Hβ at a redshift of $z = 0.42$, thus allowing us to classify this object as a type 1 quasar. The latter has two absorption lines at 5320 Å and 4940 Å, which we identify as MgII and FeII in an intervening foreground galaxy at $z = 0.9$, meaning that his object is a BL Lac lying at high redshift.

Thus, according to the criteria in Laurent-Muehleisen et al. (1998), every object in our sample presents a BL Lac-type spectrum (i.e. a continuum power–law shape and no strong emission features with equivalent width larger than 5 Å), except 1FHL J1410.4+7408A, which shows a QSO type 1 spectrum.

Object	λ[Å]	EqW [Å]	z	Class
J1410.4+7408A	4021	-12	0.42	QSO 1
J1410.4+7408B	–	–	?	BL Lac
J1512.1-2255	–	–	?	BL Lac
J1549.9-0658	–	–	?	BL Lac
J1841.1+2914	–	–	?	BL Lac
J2002.6+6303	5320	6	≥ 0.9	BL Lac
J2142.6-2027	–	–	?	BL Lac

Table 1.: We report in column 1 the name of the object, in column 2 the wavelength for the most prominent emission/absorption line (if any), in column 3 its equivalent width, in column 4 the estimated redshift (if any), and in column 5 the resulting object type according to our criteria.

3.   Further research

A preliminary spectroscopic analysis of the likely optical counterparts of 7 objects belonging to the 1FHL catalogue and selected through cross–correlation with soft X–ray catalogues and surveys shows that 6 of them are BL Lacs and one is a Type 1 QSO. As a continuation of this work, we aim at further analysing the main characteristics of these objects through their spectral energy distribution, built with the use of multifrequency data from available surveys. Furthermore, in order to complete our sample, we submitted an observing proposal at both Gemini telescopes, which are suitable to obtain the required signal–to–noise ratio for fainter objects. In this way we aim to conclusively pinpoint the nature of the remaining 17 unidentified sources.

References

Abdo A. A. et al. 2010, ApJS, 188, 405
Evans P. A. et al. 2014, ApJS, 210, 8
Landi R. et al. 2015, A&A, 581, A57
Laurent-Muehleisen S. A. et al. 1998, ApJS, 118 , 127
Masetti N. et al. 2013, A&A, 559, A58.
Saxton R. D. et al. 2008, A&A, 480, 611
Stephen J. B. et al. 2010, MNRAS, 408, 422
Voges W. et al. 1999, A&A, 349, 389

Orbital and superorbital variability of LS I +61 303 at low radio frequencies with GMRT and LOFAR

B. Marcote[1,2], M.Ribó[1†], J. M. Paredes[1], C. H. Ishwara-Chandra[3],
J. D. Swinban[4], J. W. Broderick[5,6], S. Markoff[7], R. Fender[5],
R. A. M. J. Wijers[7], G. G. Pooley[8], A. J. Stewart[5], M. E. Bell[9,10],
R. P. Breton[11,6], D. Carbone[7], S. Corbel[12,13], J. Eislöffel[14],
H. Falcke[15,16], J.-M. Grießmeier[17,13], M. Kuniyoshi[18], M. Pietka[19],
A. Rowlinson[9], M. Serylak[20,21,13], A. J. van der Horst[22],
J. van Leeuwen[16,7], M. W. Wise[16,7], P. Zarka[23,13]

[1]*Departament d'Astronomia i Meteorologia, Institut de Ciències del Cosmos, Universitat de Barcelona, IEEC-UB, Barcelona, Spain*
[2−23]*List of affiliations after acknowledgements.*
[†]*Serra Húnter Fellow*

Abstract. LS I +61 303 is a gamma-ray binary that exhibits an outburst at GHz frequencies each orbital cycle of 26.5 d and a superorbital modulation with a period of 4.6 yr. We have performed a detailed study of the low-frequency radio emission of LS I +61 303 by analyzing all the archival GMRT data at 150, 235 and 610 MHz and conducting regular LOFAR observations within the Radio Sky Monitor at 150 MHz. We have detected the source for the first time at 150 MHz, which is also the first detection of a gamma-ray binary at such low frequency. We have obtained the light-curves of the source at 150, 235 and 610 MHz, showing orbital and superorbital modulation. A comparison with contemporaneous RT and OVRO 15-GHz observations shows remarkable differences. At 15 GHz we see clear outbursts, whereas at low frequencies we observe variability with wider maxima. The light-curve at 235 MHz seems to be uncorrelated with the one at 610 MHz. We model the shifts between the maxima at different frequencies as due to changes in the physical parameters of the emitting region assuming either free-free absorption or synchrotron self-absorption, obtaining subrelativistic expansion velocities which are close to the stellar wind velocity for some of the cases.

1. Introduction

LS I +61 303 is composed of a compact object orbiting a young main sequence B0 Ve star every $\approx$26.5 d (Gregory 2002). The radio emission of the source above 1 GHz is clearly orbitally modulated, exhibiting an

outburst per orbital cycle, although these outbursts exhibit changes from cycle to cycle (Ray et al. 1997). The shape of a single outburst is similar in the range of 1.4–23 GHz (Strickman et al. 1998), but the flux density peaks first at the highest frequencies. A long-term modulation of $1\,667 \pm 8$ d, the so-called superorbital modulation, is also observed in the light-curve of LS I +61 303, affecting not only the amplitude of the emission but also the orbital phases at which the outbursts take place (Gregory 2002).

2. Observations and results

We have performed the first detailed study on the low-frequency ($\lesssim 1$ GHz) radio emission of LS I +61 303. We have analyzed the whole archival data from the Giant Metrewave Radio Telescope (GMRT), which include a monitoring at 235 and 610 MHz performed in 2005–2006 and three isolated observations at 235/610 MHz and 150 MHz. We have also conducted observations with the Low Frequency Array (LOFAR) at 150 MHz within the Radio Sky Monitor (RSM). Contemporaneous observations with the Ryle Telescope (RT) and the Owens Valley Radio Observatory (OVRO) at 15 GHz are used as a reference of the behavior of the source.

The data from all the analyzed observations show that the superorbital modulation known at GHz frequencies is still present at the low frequencies (see Marcote et al. 2016, for a detailed review). The left panel in Figure 1 shows the GMRT monitoring and RT data folded with the orbital phase. At 610 MHz we observe a light-curve that is orbitally modulated, with a quasi-sinusoidal shape. The increase of the emission takes place at the same orbital phases than at 15 GHz, but exhibiting a significantly slower decay. Given the differences observed at different orbital cycles, we can only constrain the position of the peak emission to take place between orbital phases $\phi_{\rm orb} \sim 0.8$–1.1, whereas the peak at 15 GHz is clearly located at $\phi_{\rm orb} \approx 0.8$. We observe that the 235 MHz light-curve is not correlated with the 610-MHz or 15-GHz ones. The maximum emission at 235 MHz takes place in the range of $\phi_{\rm orb} \sim 0.3$–0.7.

The source is also detected at 150 MHz with GMRT and LOFAR. Figure 1, right, shows the obtained light-curve at this frequency together with the 15-GHz OVRO data. Despite the poor sampling the light-curve suggests it could be orbitally modulated. Although we cannot clearly constrain the location of the peak emission, there seems to be a delay with respect to the 15-GHz light-curve.

3. Discussion and modeling

We have presented the first detection of a gamma-ray binary at a frequency as low as 150 MHz (searches in other sources have been performed with null results, Marcote et al. 2015), and we have revealed the low-frequency
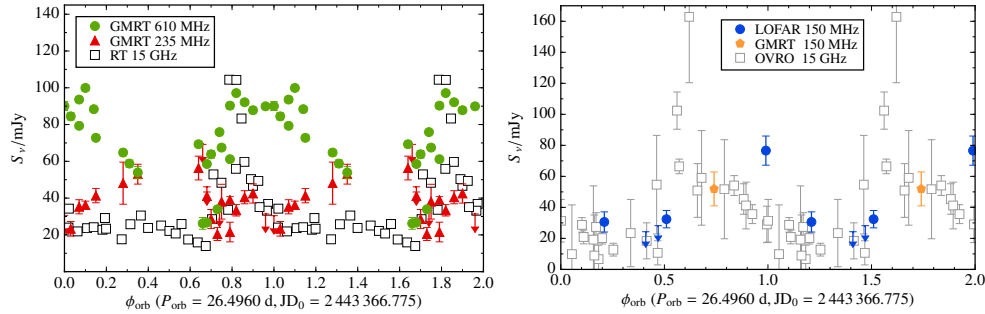
Figure 1. Folded light-curve of LS I +61 303 with the orbital period obtained from the archival GMRT monitoring at 235/610 MHz (*left*) and with GMRT and LOFAR at 150 MHz (*right*). Contemporaneous 15-GHz RT and OVRO data are also shown for comparison. Error bars represent 1-σ uncertainties. Reproduced from Marcote et al. (2016).

variability and provided first evidences of orbital modulation. We report significant differences between the light-curves at 150, 235 and 610 MHz. Whereas the 610-MHz light-curve is roughly coincident with the one observed at 15 GHz and we only observe a slight delay of the peak emission, the 235-MHz light-curve is uncorrelated with respect to that at 610 MHz. More data at low frequencies are essential to determine accurately the variability of the source.

The observed delays between the orbital phases at which the peak emission takes place at different frequencies can be explained by changes in the opacity of the radio emitting region as due to an expansion of this region, producing a shift of the turnover frequency along the orbit. We have considered a one-zone synchrotron emitting region assuming either free-free absorption or synchrotron self-absorption with two different magnetic field dependences. We have obtained in all cases subrelativistic expansion velocities, close to the stellar wind velocity for some of the cases. Although these velocities seem to favor a wind interaction (pulsar) scenario, they could still be explained by the microquasar scenario (see Marcote et al. 2016 for further discussion).

A

Affiliations: [2]Joint Institute for VLBI ERIC, The Netherlands; [3]National Centre for Radio Astrophyisics, TIFR, Pune, India; [4]Department of Astrophysical Sciences, Princeton University, USA; [5]Astrophysics, Department of Physics, University of Oxford, UK; [6]Department of Physics and Astronomy, University of Southampton, UK; [7]Anton Pannekoek Institute for Astronomy, University of Amsterdam, The Netherlands; [8]Mullard Radio Astronomy Observatory, Cavendish Laboratory, The University of Cambridge, UK; [9]CSIRO Astronomy and Space Science, Epping, Australia; [10]ARC Centre of Excellence for All-sky Astrophysics (CAASTRO), The University of Sydney, Australia; [11]Jodrell Bank Centre for Astrophysics, School of Physics and Astronomy, The University of Manchester, UK; [12]Laboratoire AIM (CEA/IRFU - CNRS/INSU - Université Paris Diderot), France; [13]Station de Radioastronomie de Nançay, Observatoire de Paris, PSL Research University, CNRS, Univ. Orléans, Nançay, France; [14]Thüringer Landessternwarte, Tautenburg, Germany; [15]Department of Astrophysics/IMAPP, Radboud University Nijmegen, The Netherlands; [16]ASTRON, the Netherlands Institute for Radio Astronomy, Dwingeloo, The Netherlands; [17]LPC2E - Université d'Orléans / CNRS, Orléans, France; [18]NAOJ Chile Observatory, National Astronomical Observatory of Japan, Tokyo, Japan; [19]Oxford Astrophysics, Denys Wilkinson Building, Oxford, UK; [20]Department of Physics & Astronomy, University of the Western Cape, South Africa; [21]SKA South Africa, Pinelands, South Africa; [22]Dept. of Physics, The George Washington University, USA; [23]LESIA, Observatoire de Paris, CNRS, UPMC, Univ. Paris-Diderot, Meudon, France.

References

Gregory, P. C., 2002, ApJ, 575, 427
Marcote, B., et al. 2015, MNRAS, 451, 4578
Marcote, B., et al. 2016, MNRAS, 456, 1791
Ray, P. S., et al. 1997, ApJ, 491, 381
Strickman, M. S., et al. 1998, ApJ, 497, 419

Low galactic HE gamma-ray blazars in the VVV survey

A. Pichel[1], L.D. Baravalle[2], M.V. Alonso[2,3], A.C. Rovero[1] and
D. Minniti[4]

[1]*Instituto de Astronomía y Física del Espacio (IAFE; CONICET-UBA),
Buenos Aires, Argentina*
[2]*Instituto de Astronomía Teórica y Experimental (IATE;
CONICET-UNC), Córdoba, Argentina*
[3]*Observatorio Astronómico, Universidad Nacional de Córdoba, Argentina*
[4]*Departamento de Ciencias Físicas, Universidad Andrés Bello, Santiago,
Chile*

Abstract. Our motivation is to find blazars among the unidentified
gamma-ray sources detected with *Fermi*-LAT in the crowed galactic plane
region. Searching for photometric characteristics of blazars in the near-
IR using data from the Vista Variables in the Vía Láctea (VVV survey),
we aim to find a method to associate blazars to unidentified gamma-ray
sources. We show preliminary results on the photometric properties of 4
gamma-ray blazars using the color-magnitude and color-color diagrams.
We also compare these results with a different method based on mid-IR
observations acquired with Wide-field Infrared Survey Explorer (WISE).

1. Introduction

The Fermi-LAT Third Source Catalog (Acero et al. 2015) presents 1009 sources
without any known association at other wavelengths over a total of 3033 sources
detected. A statistical study done with non-associated sources of the First Fermi-
LAT catalog (Ackermann et al. 2012) shows that more blazars should be found
within the unidentified sources, especially at low galactic latitudes. The key to
find plausible counterparts to the unidentified *Fermi*-LAT sources is the use of
multiwavelength observations.

Using the WISE preliminary data released in four passbands centered at
3.4, 4.6, 12, and 22 μm, Massaro et al. (2011, 2012) discovered that blazars
are well separated from other extragalactic sources in the mid-IR color space,
identifying the region covered only by blazars. Then, they studied the IR-gamma-
ray properties of a blazar sample detected by WISE and by *Fermi*-LAT, obtaining
a narrower region in the IR color-color diagram called the WISE Gamma-ray
Strip (WGS; D' Abrusco et al. 2012).

We decided then to investigate, both the behavior of the gamma-ray emit-
ting blazars in the near-IR and how to distinguish them from other galactic and
extragalactic sources in the fourth-dimensional color space of the near-IR VVV
magnitudes. In this paper, we describe briefly the technique and results (Sec-
tion 2) to distinguish blazars among the unidentified Fermi-LAT sources using
the VVV survey in the near-IR (Minniti et al. 2010). In Section 3 we present
our conclusions.
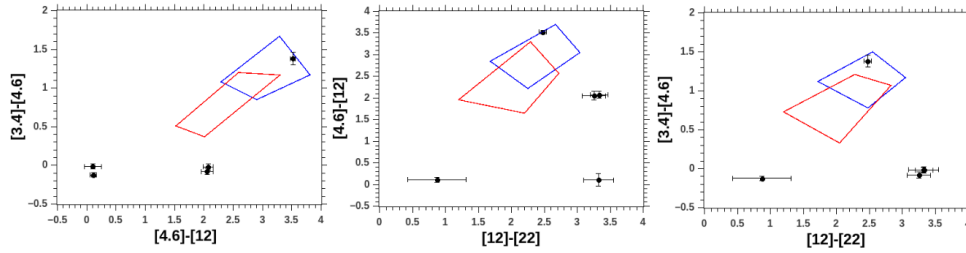
Figure 1.   The color-color diagrams for the FSRQ J1802.6-3940. Only 5 WISE sources were detected (black points) in the error region of the gamma-ray source and one WISE source was found as the counterpart of the FSRQ.
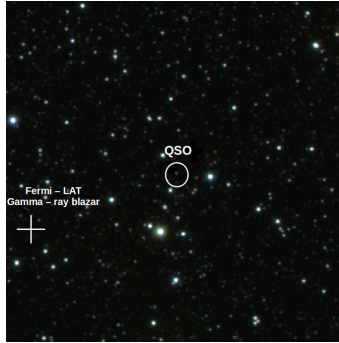

Figure 2.   Combined image (3' x 3') of the FSRQ J1802.6-3940. The QSO (circle) and the gamma-ray source (cross) are shown in white.

2.   Observations and Results

Using the Roma BZCat[1], we found only 4 gamma-ray blazars in the VVV region and all of them are low latitude *Fermi*-LAT sources (1 flat-spectrum radio quasar (FSRQ), 1 BL Lac object, and 2 blazars of unidentified type). We have investigated these sources seeking for common properties among them to find a new IR-gamma-ray connection for blazars. We performed the analysis for all the four high-energy gamma-ray blazars and we are showing only, as an example, the results for FSRQ J1802.6-3940.

Using the WGS method, we applied the criteria that blazars lie in a distinctive region in a 3-dimensional IR color-color plot using observations in the 4 passbands of WISE. We applied the method by making the 2-dimensional projections in the color-color diagrams shown in Fig. 1. The blazar strip is different for BL Lac (red) and FSRQ (blue) objects. We performed this analysis for all the 4 gamma-ray blazars located in the VVV survey and the results from the

—————————————

[1]http://www.asdc.asi.it/bzcat/
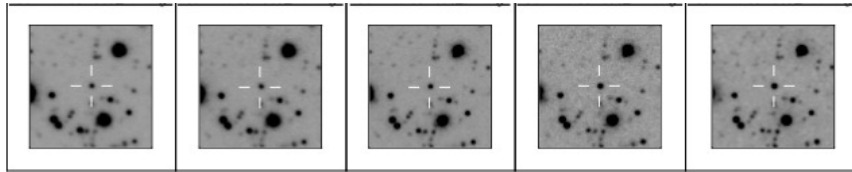
Figure 3.   Image of the FSRQ J1802.6-3940 in the ZYJHKs pass-bands, respectively (from left to right).

FSRQ J1802.6-3940 are shown in Fig. 1. For this blazar only one WISE source fulfilled the WGS method requirements to be a non thermal emission source in coincidence with the position of the FSRQ detected.

For all the 4 blazars we obtained the images from the VVV survey in the five IR passbands (ZYJHKs). First we observed the region centered in the object in detail to make a visual inspection. Figure 2 shows a combined image centered in one of the four studied blazars, the FSRQ J1802.6-3940. It can be noticed that the QSO found (marked in the center of Fig. 2) is identified at a distance to the gamma-ray source of about 1' 30" in right ascension and 8" in declination. We can also see in Fig. 3 that the QSO is detected in the 5 passbands and it presents a red color compared with other objects of the combined image (Fig. 2).

We used the SExtractor+PSFex routines (Bertin 2011) to detect and select all the objects in the field of the FSRQ J1802.6-3940 to perform the photometry. For all detected objects we obtained magnitudes and structural parameters such as ellipticities, half-light radius and a galaxy-star classifier parameter (class_star; Desai et al. 2012). From previous works (Nilo Castellón et al. 2014, Baravalle et al. 2015) we consider the QSO as an stellar object if it presents the Class-Star parameter > 0.9, the Spread-Model < 0.003 and the R1/2 < 2 pix. In Fig. 4, we show the color-magnitude and color-color diagrams including all the detected objects. With a big circle we identify the studied QSO, which shows a feature that distinguishes it from the rest of the objects in the field, as suggested by Cioni et al. (2013).

3.   Conclusions

In this work we studied a new correlation method using the near-IR and the HE gamma-ray bands in order to distinguish blazars among the unidentified gammma-ray sources. Using the Roma BZCat, we found only 4 gamma-ray blazars in the VVV region. For those blazars, we studied first the WISE mid-IR-gamma-ray connection, showing that the method works very well, and found in each case one WISE counterpart associated with the blazar.

We then studied the near-IR using the ZYJHKs passbands from the VVV survey. We performed a photometric study of the 4 blazars and found that one of them, the FSRQ J1802.6-3940, has an associated QSO with observations in the five VVV passbands. Then, we made the color-magnitude and the color-color diagrams finding that the QSO is red compared to other objects in the field.
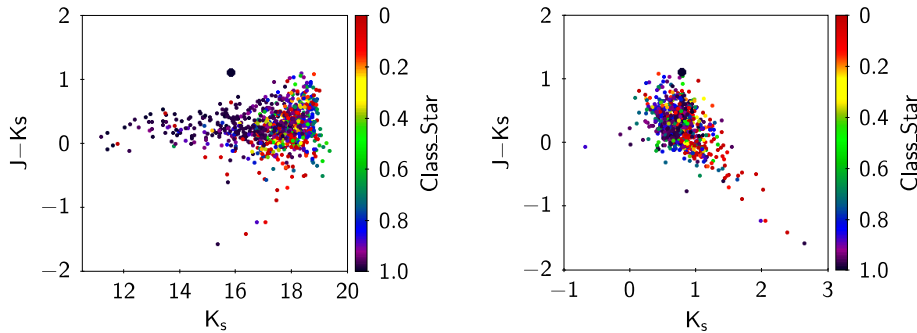
Figure 4.   Color-magnitude (left) and color-color (right) diagrams for all the objects found in the FSRQ J1802.6-3940 region. The colors are related to the Class-Star parameter. The QSO (big black circle) has colors: (J-Ks) > 1 and (Y-J) > 0.5, showing a different behavior from the rest of the objects in agreement with the color-magnitude diagrams presented in Cioni et al. (2013).

For the other 3 blazars further studies are required, considering that the fields around them are more crowded due to their position near the galactic plane.

We plan to continue this work by applying this procedure to all the unidentified Fermi-LAT gamma-ray sources at low latitudes, to search for blazar candidates in the galactic plane. For the identified candidates, we will analyze multiwavelength archival data aiming to determine their physical nature. Eventually, we will propose new observations in radio, optical and/or X-rays.

References

Acero, F. et al., 2015, ApJS ApJS 218, 23
Ackermann, M. et al., 2012, ApJ 753, 83
Baravalle, L.D. et al. 2015, in preparation
Bertin, E. 2011, ASPC 442, 435
Cioni, M.R.L. et al. 2013, A&A 549, 29
Desai, S. et. al., 2012, JPhCS 375, 032011
D'Abrusco, R. et al., 2012 ApJ 748, 68
Massaro, F. et al., 2011, ApJ 740, L48
Massaro, F. et al., 2012, ApJ 752, 61
Minniti, D. et al. 2010, New Astronomy 15, 433
Nilo Castellón, J.L. et al., 2014, MNRAS 437, 2607

The imprint of hot spots on magnetized Kerr accretion disks: probing the cosmic censorship conjecture

Ranea-Sandoval, Ignacio F.[1,2], García, Federico[3,4] and Johannsen, Tim[5,6]

[1] *Grupo de Gravitación, Astrofísica y Cosmología, Facultad de Ciencias Astronómicas y Geofísicas - Universidad Nacional de La Plata. Paseo del Bosque S/N (1900). La Plata, Argentina.*
[2] *CONICET, Godoy Cruz 2290, 1425 Buenos Aires, Argentina.*
[3] *Instituto Argentino de Radioastronomía, CCT La Plata - CONICET, C.C. 5 (1984) Villa Elisa, Buenos Aires, Argentina.*
[4] *Facultad de Ciencias Astronómicas y Geofísicas, Universidad Nacional de La Plata. Paseo del Bosque S/N 1900. La Plata, Argentina.*
[5] *Perimeter Institute for Theoretical Physics, Waterloo, Ontario, N2L 2Y5, Canada.*
[6] *Department of Physics and Astronomy, University of Waterloo, Waterloo, Ontario, N2L 3G1, Canada.*

Abstract.
In general relativity, black holes are uniquely described by the Kerr metric and, according to the cosmic censorship conjecture, curvature singularities are always hidden behind an event horizon. We study the effect of an external magnetic field on the observed light curves of orbiting hot spots in thin accretion disks in Kerr spacetimes with (black holes) and without (super-extreme solutions) horizons. We employ a ray-tracing algorithm to calculate the light curves and power spectra of such hot spots for uniform and dipolar magnetic field configurations and show that the presence of a dipolar magnetic field produces potentially observable signatures which might be useful to probe the nature of compact objects and to test the cosmic censorship conjecture.

1. Introduction

The cosmic censorship conjecture (CCC) remains one of the major open problems in the classical theory of general relativity and many different approaches have tried to shed light on the question of its validity (see, e.g., Penrose 1998; Dotti et al. 2008, 2012). In particular, the development of observational tests capable of distinguishing black holes (BHs) from super-extreme Kerr solutions (SKs) is of great importance in order to confirm the current BH paradigm.

In a recent work, Ranea-Sandoval & García (2015) presented a magnetized generalization of the Page-Thorne accretion disk model (Page & Thorne 1974). Both thermal continuum spectra and fluorescent iron line profiles were analyzed as tools which could potentially determine the nature of fully-collapsed compact objects and the geometry of local magnetic fields present near the disk.

Ranea-Sandoval & García (2015) focussed on uniform (U) and dipolar (D) magnetic field configurations, parametrized by the coupling constant, λ, between the magnetic field strength and the disk matter.

In this paper, we focus on the observational imprints produced by the motion of a hot spot formed in the innermost part of a magnetized accretion disk. Section 2 briefly describes the theoretical framework, while Section 3 shows our results. In Section 4 we summarize our main conclusions.

2.   Hot spot model

Following the model developed by Stella & Vietri (1998), we assume that the hot spot is a small region of isotropic, monochromatic emission that follows a circular trajectory in co-rotation with the accretion disk. In this "blob" model, the emissivity is assumed to be a Gaussian distribution:

$$\epsilon(\mathbf{x}) \propto \exp\left(-\frac{|\mathbf{x} - \mathbf{x}_{\mathrm{hs}}(t)|^2}{2R_{\mathrm{hs}}^2}\right). \tag{1}$$

where the size, R_{hs}, of the hot spot has to be small compared to the radius of its center, located at x_{hs}.

Generalizing a previously developed ray-tracing algorithm (Psaltis & Johansen 2012), we implemented a numerical scheme that tracks the photons emitted at the hot spot to the position of a distant observer, taking into account all the relativistic effects.

3.   Results

Using our algorithm we generated a family of observed light curves produced by corotating hot spots formed in the innermost regions of magnetized accretion disks around both BHs and SKs (García et al. 2016).

In Figure 1 we show several light curves, as a function of the orbital phase, of hot spots formed at $r_{\mathrm{hs}} = 1.1r_{\mathrm{isco}}$ with $R_{\mathrm{hs}} = 0.1r_{\mathrm{hs}}$ around BHs and SKs with masses M and spins a, for different magnetic field configurations, viewed at inclinations of $i = 30°$ (top panels) and $i = 75°$ (bottom panels). For the non-magnetized case, $r_{\mathrm{isco}}(a = 0.95r_g) = 1.937r_g$, $r_{\mathrm{isco}}(a = 1.10r_g) = 0.667r_g$. For the case of uniform magnetic field, these values remain unchanged and for the dipolar case $r_{\mathrm{isco}}(a = 0.95r_g) = 2.467r_g$ and $r_{\mathrm{isco}}(a = 1.10r_g) = 0.565r_g$, where $r_g \equiv GM/c^2$. In the left panels we show the total observed flux. Clear differences in the light curves can be seen between the hot spots formed around $a = 0.95r_g$ BHs (black lines) and $a = 1.10r_g$ SKs (gray lines), the latter of which are fainter in all cases. Moreover, the light curves are narrower (broader) for a high (low) inclination. The presence of a uniform magnetic field has practically no effect on the light curves, while the presence of a dipolar one strongly changes their shapes, as it is larger at the innermost parts of the disk.

When the observed photons are separated into soft ($g \leq 0.9$) and hard ($g > 0.9$) energy bands (central and right panels, respectively), where g is the photon redshift, very different light curves are observed. At high inclinations in the case of either a BH or a SK as well as at low inclinations in the case of a SK
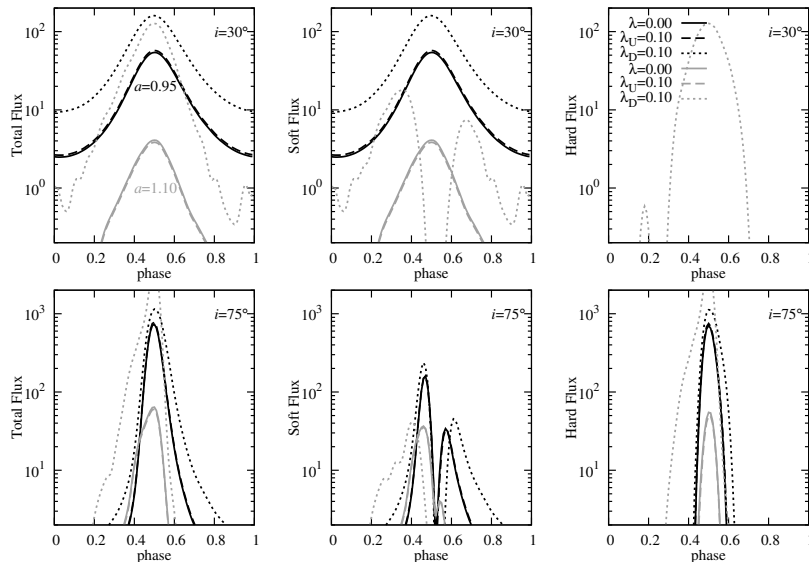
Figure 1. Light curves of corotating hot spots at the innermost part of an accretion disk with different magnetic field configurations around a BH with rotational parameter $a = 0.95 r_g$ (black lines) and a SK with $a = 1.10 r_g$ (gray lines) viewed at inclinations of $i = 30°$ (top panels) and $i = 75°$ (bottom panels). Total flux in arbitrary units. Credit: García et al., A&A, 587, A141, 2016, reproduced with permission ©ESO.

in the presence of a dipolar magnetic field, the light curve has two peaks in the soft energy band, one before and one after the phase corresponding to the peak of the total light curve. In the hard energy band, the contribution of the hard flux to the total observed flux is negligible for low inclinations except for the case of a dipolar magnetic field around SKs (see top right panel of Fig. 1). This causes the location of the ISCO to be closer to the curvature singularity than in the non-magnetized case where the effect of Doppler boosting is sufficiently strong to overcome the effect of the gravitational redshift.

In Figure 2 we present Fast-Fourier Transforms (FFTs) of the light-curves shown in Figure 1. The mode patterns are strongly dependent on the inclination angle, i, both in the number of potentially observable modes and in their relative amplitudes. Differences for large inclinations (bottom panels) between the FFTs of the light curves in the soft and hard energy bands are evident. For small inclinations (top panels), FFTs in the hard energy band are only visible in the SK case in an accretion disk with a dipolar magnetic field, which makes this an interesting tool for a determination of the parameter λ (García et al. 2016).

4. Conclusions

In the framework of the magnetized Page-Thorne accretion disk model developed by Ranea-Sandoval & García (2015) we presented a series of results related to observational imprints produced by the motion of hot spots in the innermost
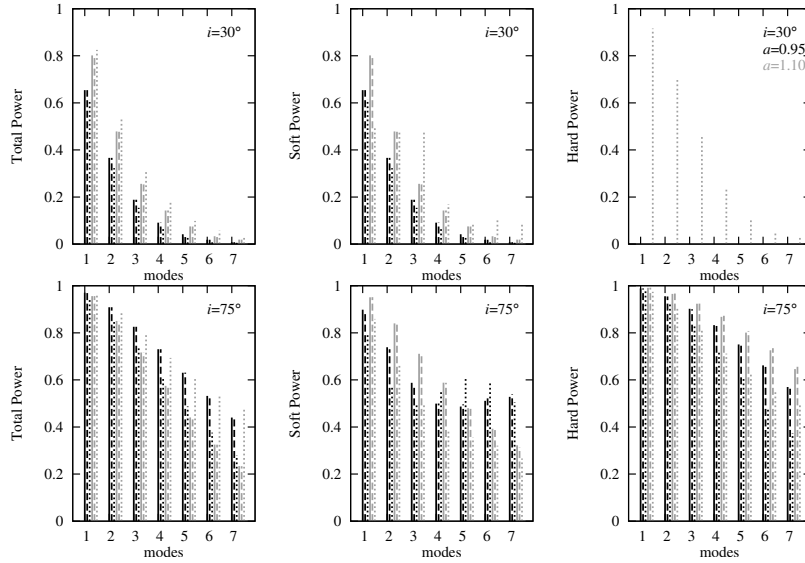
Figure 2. Power spectra of the of the light curves of Fig. 1 (Credit: García et al., A&A, 587, A141, 2016, reproduced with permission ⓒESO).

regions of magnetized accretion disks around Kerr BHs and SKs. For the first time, we simulated light curves and power spectra of hot spots formed around rotating NSs. Systematic fitting of light curves and power spectra to the quasi-periodic variability observed in X-ray binaries might be used to determine the nature of the compact object and to shed some light on the question whether the CCC is valid. Moreover, this tool, combined with thermal continuum spectra and iron line profiles, can be used to estimate the presence of a magnetic field in the neighborhood regions of the compact object and the accretion disk.

References

Dotti, G., et al. 2008, CQG, 25, 245012

Dotti, G., Gleiser, R. G. & Ranea-Sandoval, I.F. 2012, CQG, 29, 095017

García, F., Ranea-Sandoval, I.F. & Johannsen, T. 2016, A&A, 587, A141

Page, D. & Thorne, K. 1974, ApJ, 191, 499

Penrose, R. 1998, in *Black Holes and Relativistic Stars*, ed. R. M. Wald, Chicago, IL: University of Chicago Press, 103

Psaltis, D. & Johannsen, T. 2012, ApJ, 745, 1

Ranea-Sandoval, I. F & García, F. 2015, A&A, 574, A40

Stella, L. & Vietri, M. 1998, ApJ, 492, L59

BATSE data support the multicomponent model for Gamma Ray Bursts prompt emission

J. R. Sacahui[1], S. Guiriec[2,3,4,5], M. M. González[6], C. Kouveliotou[7], N. Gehrels[2] and J. McEnery[2]

[1]*Instituto de Investigación, Escuela de Ciencias Físicas y Matemáticas, Universidad de San Carlos de Guatemala, Guatemala*
[2]*NASA Goddard Space Flight Center, Geenbelt, MD 20771, USA*
[3]*Department of Physics and Department of Astronomy, University of Maryland, College Park, MD 20742, USA*
[4] *Center for Research and Exploration in Space Science and Technology (CRESST)*
[5] *NASA Postdoctoral Program*
[6] *Instituto de Astronomía, UNAM, México 04510, México*
[7] *Department of Physics, The George Washington University, Washington, DC 20052*

Abstract. Observations of the prompt emission of several Gamma Ray Bursts (GRBs) detected with the instruments on-board the Fermi Gamma ray Space Telescope (hereafter *Fermi*) as well with the Burst and Transient Source Experiment (BATSE) on-board the Compton Gamma Ray Observatory (*CGRO*) reveal deviations from the Band function to describe their spectra in the keV-MeV energy range. Analysis of *Fermi* data conclude that GRB prompt emission is adequately fitted with the simultaneous combination of three emission components: a thermal-like component interpreted as the jet photosphere, a non-thermal component interpreted as synchrotron radiation from particles within the jet and an additional non-thermal power-law (PL) function extending from low to high energies in gamma-rays, interpreted as Inverse Compton emission. In this work we present new analysis of three BATSE Bursts, namely GRBs 941017, 970111 and 990123. We show that the BATSE data are fully consistent with the model derived from *Fermi* data and that these three BATSE bursts also exhibit the three different components as reported from *Fermi*, noticing that they present similar spectral behaviour. In addition, the analysis using this three-component model during the prompt emission results in a strong correlation between the time-resolved luminosity and the corresponding rest-frame $\nu F \nu$ spectral peak energy (L_i^{nTh}-$E_{p,i}^{nTh,rest}$ relation). When fitted with a power law the relation have similar indices for all three bursts and these values are also in perfect agreement with the *Fermi* results. This points toward a possible universal emission process intrinsic to the non-thermal component of GRB prompt emission. Using this correlation we estimated the redshift for GRBs 941017 and 970111 using GRB990123 (with known redshift) as reference. The estimated redshifts for these bursts are typical values for long GRBs.

1.   Introduction

The spectra of Gamma Ray Bursts prompt emission in the keV-MeV energy range are usually considered as adequately fitted with the empirical Band function (Band et al 1993) -a smoothly broken power law-. Recently multiple component models seem to be favoured compared to single component ones for GRBs prompt emission. In some cases (González et al. 2003, Ackermann et al. 2011) an additional PL was required to account for spectral deviations at high energies. Recently a thermal like component (C_{Th}) among with a non-thermal (C_{nTh}) one have been discovered in the prompt phase of some bursts observed with *Fermi* (Guiriec et a. 2011, Axelsson et al. 2012). When this thermal component is present the non thermal one is adequately described with a Band function but with different spectral values compared when fitting the Band function alone, making them consistent with the synchrotron emission scenarios. The observed C_{Th} is usually energetically sub dominant compared to the C_{nTh} one which favours highly magnetized jet models.

Guirec et al. (2015) identified simultaneously the three known components in the prompt emission of bright GRBs detected by *Fermi*, namely GRBs 080916C and 090926A. The analysis changed the view of GRB080916C which was considered before as adequately fitted with a single Band function alone (Abdo et al. 2009). While the spectral and temporal behaviour was completely different for the two GRBs, both become similar within the context of the $C_{nTh}+C_{Th}+PL$ model. A strong correlation between the time-resolved luminosity and the corresponding rest-frame $\nu F\nu$ spectral peak energy (L_i^{nTh}-$E_{p,i}^{nTh,rest}$ relation, where "i" counts time intervals) was noted, interestingly these relations for all GRBs are properly described using PLs with very similar index. This relation points towards a possible universal physical mechanism intrinsic to all GRBs, which could be used to measure distances using prompt phase data.

When fitting either $C_{nTh}+C_{Th}$ or $C_{nTh}+C_{Th}+PL$ to the data the indices of these components do not vary much in the same burst or from burst to burst (Guirec et al. 2013, 2015). Indeed α_{nTh} indices present values $\sim$0.7 or $\sim$-1.2 depending on the burst, α_{Th} value is usually $\sim$0.6 and α_{PL} $\sim$-1.5. Therefore the number of free parameters of these models can be reduced by freezing some of them in order to become statistically competitive with the Band function in therms of free parameters.

2.   Data Selection

We focus on a limited sample of three famous bright long GRBs detected with BATSE. These GRBs are of particular interest because they have often been and still are cited to support or discard theoretical interpretations for GRB prompt emission. GRB941017 was the first burst of the pre *Fermi* era for which a strong deviation at high energy from the Band function was reported (González et al. 2003). GRB970111 was considered as adequately fitted to a Band function but with positive values of the lower energy index of the Band function at early times (Gorosabel et al. 1998). The photometric redshift of this burst was estimated to be 0.2<z<1.4 based on its probable association with host galaxies. GRB990123 was an extremely bright GRB considered, so far, as adequately fitted to a Band

function alone (Akerlof et al. 1999). It was the first burst to be simultaneously detected during its prompt phase in γ-ray and optical bands. A 1.61 redshift estimate was reported for this burst (Kelson et al. 1999, Hjorth et al. 1999).

3. Analysis

We first performed a time integrated spectral analysis of the bursts (for GRB941017 see table No.1) to identify the main spectral components of the prompt emission -for details about the procedure of the analysis go to Guiriec et al. (2015)-. It is clear from the Cstat values that a Band function alone is not a good description and that $C_{nTh}+C_{Th}$ and $C_{nTh}+C_{Th}+PL$ significantly improve the Band fits.

Models	Base Component CPL or Band			Additional Component		Cstat/DOF
	Ep (keV)	α	β	BB kT (keV)	PL γ	
GRB941017 from T_0-4.096 s to T_0+118.784						
Band	330±5	-0.78±0.01	-2.35±0.03			205.8/9
$C_{nTh}+PL$	270±4	+0.12±0.07			-1.62±0.01	75.3/8
$C_{nTh}+PL$	272±9	+0.01±0.25			-1.99±0.33	28.2/7
$C_{nTh}+C_{Th}$	784±44	-1.33±0.02		56.0±0.66		25.1/8
$C_{nTh}+C_{Th}$	674±75	-1.30±0.03	-2.41±0.22	56.3±0.73		23.6/7
$C_{nTh}+C_{Th}+PL$	451±52	-0.62±0.27		51.8±2.3	-1.7±0.03	18.3/6

Table 1.   Time integrated analysis of GRB941017 with their 1-σ uncertainties

Then we analysed every burst on fine time scales to follow the evolution of the various components and to verify that the observed spectral features are not merely artefacts due, for instance, to strong spectral evolution. We discuss only the most relevant models for the time-resolved analysis, namely Band, $C_{nTh}+C_{Th}$ and $C_{nTh}+C_{Th}+PL$. We froze α_{nTh} to -0.7 and α_{PL} to -1.5 when fitting the $C_{nTh}+C_{Th}+PL$ model as proposed in Guiriec et al. (2015). Although these parameter estimates may not be completely accurate they are good enough in the context of the present analysis.

The similarities of BATSE and *Fermi* results are notorious when comparing Band and $C_{nTh}+C_{Th}$: α_i^{nTh} is systematically lower than α_i^{Band} and conversely to the Band case the indices α_i^{nTh} are always compatible with the synchrotron scenario. For $E_{peak,i}^{nTh}$ the value is systematically higher than $E_{peak,i}^{Band}$. For the temperature associated to the thermal component a less notorious variation is observed when compared to $E_{peak,i}^{Band}$ and is usually lower. Fitting the $C_{nTh}+C_{Th}+PL$ model give that the values of $E_{peak,i}^{nTh}$ is usually lower that those resulting from the $C_{nTh}+C_{Th}$ fits which is also in total agreement with the *Fermi* analysis.

It was noted from the analysis that in the central engine frame the L_i^{nTh}-$E_{p,i}^{nTh,rest}$ relation present extremely similar indices for all GRBs ($\sim$1.4, $\sim$1.33, $\sim$1.28 for GRBs 941017, 970111 and 990123 respectively), and similar to the ones obtained with *Fermi*, which points out to a possible universal relation. Taking into account the redshift measurement for GRB990123 and using this relation in this BATSE sample we were able to estimate the distances to GRBs 941017 $\sim$1.79 and 970111 $\sim$1.18.

4.   Results and Conclusions

We show that the BATSE data are fully consistent with the model derived from *Fermi* data and that these three BATSE bursts also exhibit the three different components.

The C_{nTh} component overall overpowers the other components in the BATSE energy range from 20 keV to 2 MeV in all three bursts. Its contribution is usually higher than 50% of the total energy released in this range of energy. This component is interpreted as either synchrotron emission from charged particles propagating and accelerated within the GRB jet or a strongly reprocessed photospheric emission.

The C_{Th} contribution is lower, $\leq 20\%$ of the total emission. It is more intense at early times and it is interpreted as emission from the jet photosphere as predicted by the fireball model, but with lower energy contribution than expected.

The PL component energy contribution is roughly few tens of percent although it can be $>70\%$ at early and late times. Because of the limited energy range of BATSE, the additional PL is mostly subdominant compared to C_{nTh} over the whole observed energy range, and it only starts to be dominant at the very high energy of the spectrum. This component is most likely to have inverse Compton origin.

Finally assuming that L_i^{nTh}-$E_{p,i}^{nTh,rest}$ relation is universal as suggested in Guiriec et al (2013, 2015), and using GRB990123 -which has a measured redshift z~1.61- as reference, the redshift for GRBs 941017 and 970111 was estimated (z=1.79±0.07 and z=1.18±0.06 respectively). These values are in consistence with typical ones for long GRBs and for the case of GRB970111 it is in the range of the predicted value considering possible host galaxies ($0.2 \leq z \leq 1.4$) as reported by Gorosabel et al. (1998).

References

Abdo, A. A., Ackermann, M., Arimoto, M., et al. 2009, Science, 323, 1688

Ackermann, M., Ajello, M., Asano, K., et al. 2001, ApJ, 729, 114

Akerlof, C., Balsano, R., Barthelmy, S., et al. 1999, Nature, 398, 400

Axelsson, M., Baldini, L., Barbiellini, G., et al. 2012, ApJ, 757, L31

Band, D., Matterson, J., Ford, L., et al. 1993, ApJ, 413, 281

González, M. M., Dingus, B. L., Kaneko, Y., et al. 2003, Nature, 424, 749

Gorosabel, J., Castro-Tirado, A. J., Wolf, C., et al. 1998, A&A, 339, 719

Guiriec, S., Connaughton, V., Briggs, M. S., et al. 2011, ApJ, 727, L33

Guiriec, S., Daigne, F., Hascoët, R., et. al. 2013, ApJ, 770, 32

Guiriec, S., Kouveliotou, C., Daigne, F., et al. 2015, ApJ, 807, 148

Hjorth, J., Andersen, M. I., Cairos, L. M., et al. 1999, GCN, 219, 1

Kelson, D. D., Illingworth, G. D., Franx, M., Magee, D., van Dokkum, P. G.,
        1999, IAU Circ., 7096, 3

Numerical test of the method for revealing traces of deterministic chaos in the accreting black holes

P. Suková[1] and A. Janiuk[1]

[1] *Center for Theoretical Physics, Polish Academy of Sciences, Al. Lotników 32/46, 02-668 Warszawa, Poland*

Abstract. The high energy radiation emitted by black hole X-ray binaries originates in an accretion disk, hence the variability of the lightcurves mirrors the dynamics of the disc. We study the time evolution of the emitted flux in order to find evidences, that low dimensional non-linear equations govern the accretion flow. Here we test the capabilities of our novel method to find chaotic behaviour on the two numerical time series describing the motion of a test particle around a black hole surrounded by a thin massive disc, one being regular and the other one chaotic.

1. Introduction

In this paper we test our method for revealing the traces of non-linear dynamics in the observed X-ray lightcurves on two numerical trajectories, from which one is regular and the other one is chaotic. We developed and described the method in details in the paper Suková et al. (2016). We also refer the reader to the article by A. Janiuk et al in these proceedings to learn more about astrophysical applications of this method. Here we only briefly summarize its key features.

In our procedure we combine the recurrence analysis[1] with the method of surrogate data. We compute the estimate of Rényi's entropy K_2 (Grassberger, 1983) and compare it with the values obtained for $N^{\mathrm{surr}} = 100$ surrogates made in such a way, that they share the value distribution and power spectra with the original series[2]. Such surrogates represent the hypothesis, that the time series arose from linearly autocorrelated Gaussian process (Theiler et al., 1992). The significance of the non-linearity is given by

$$\mathcal{S}(\epsilon) = \frac{N_{\mathrm{sl}}(\epsilon)}{N^{\mathrm{surr}}}\mathcal{S}_{\mathrm{sl}} - \mathrm{sign}(Q^{\mathrm{obs}}(\epsilon) - \bar{Q}^{\mathrm{surr}}(\epsilon))\frac{N^{\mathrm{surr}} - N_{\mathcal{S}_{\mathrm{sl}}}(\epsilon)}{N^{\mathrm{surr}}}\mathcal{S}_{K_2}(\epsilon), \qquad (1)$$

for chosen recurrence threshold ϵ, where N_{sl} is the number of surrogates, which have only short diagonal lines in their recurrence matrix, Q^{obs} and Q_i^{surr} are the natural logarithms of K_2 for the observed and surrogate data, respectively, $\bar{Q}^{\mathrm{surr}}$ is the averaged value of the set Q_i^{surr}, $\mathcal{S}_{\mathrm{sl}} = 3$ and $\mathcal{S}_{K_2}$ is the significance computed from surrogates with enough long lines according to the relation

$$\mathcal{S}_{K_2}(\epsilon) = \frac{|Q^{\mathrm{obs}}(\epsilon) - \bar{Q}^{\mathrm{surr}}(\epsilon)|}{\sigma_{Q^{\mathrm{surr}}(\epsilon)}}. \qquad (2)$$

---

[1] Using software package provided at `http://tocsy.pik-potsdam.de/commandline-rp.php`.

[2] Produced by the software package TISEAN (Hegger et al., 1999; Schreiber & Schmitz, 2000).
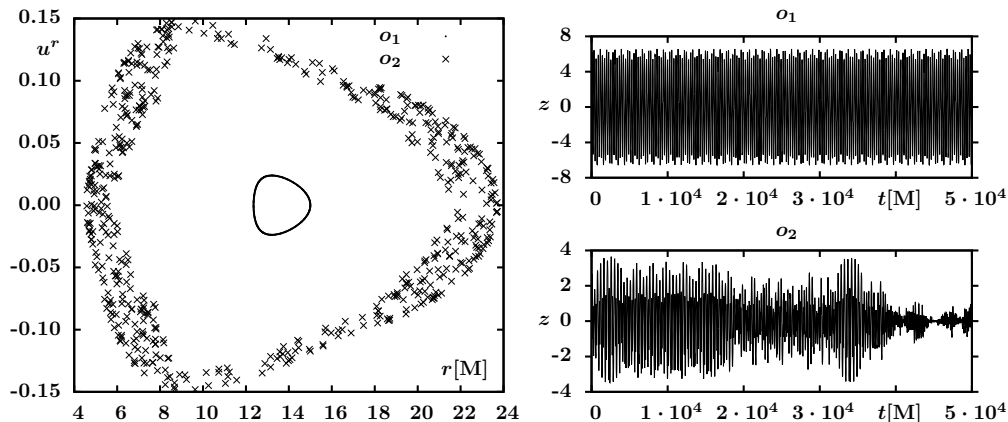
Figure 1.   Poincaré surface of section of regular orbit o_1 and chaotic orbit o_2 (left) and the corresponding time dependence of z coordinate of these orbits (right).

The significance defined in this way expresses how much the value K_2^{obs} differs from the mean value $\bar{K}_2^{\mathrm{surr}}$ measured in the units of the standard deviation of the set $\{K_2^{\mathrm{surr}}\}_{i=1}^{100}$ in the logarithmic scale $\sigma_{Q^{\mathrm{surr}}(\epsilon)}$. The more the observed time series differs from the surrogates obtained assuming the linear process, the stronger is the evidence for non-linearity in the system. We quantize the results with $\bar{\mathcal{S}}_{K_2}$, which is the average of $\mathcal{S}_{K_2}$ over a range of ϵ.

2.   Testing the method with simulated time series

In general our method can be applied to different kinds of time series, which are produced by some dynamical system. Here we test the method applying it on time series, whose nature is known. We choose the numerical time series, which describe the motion of geodesic test particle in the field of a static black hole surrounded by a massive thin disc. The background metric is given by an exact solution of Einstein equations and is described in details in Semerák & Suková (2010). The time series are obtained as the numerical solution to the geodesic equation with this metric using the 6th order Runge-Kutta method As the input data we use the time dependence of the particle's z-coordinate.

We study two numerical trajectories, orbit o_1 being regular and orbit o_2 chaotic, whose Poincaré surface of section and time dependence of z coordinate is depicted in Fig. 1. The two selected trajectories belong to the regular island (o_1) and chaotic sea (o_2) depicted in Fig. 19 of Witzany et al. (2015).

We sample the trajectory with $\mathrm{d}\tau = 10\,\mathrm{M}$ for $\tau_{\max} = 50\,000\,\mathrm{M}$ yielding the data set of $N = 5000$ points. The first minimum of mutual information is at $\Delta t = 90\,\mathrm{M} = k\Delta\tau, k = 9$ for o_1 and $\Delta t = 110\,\mathrm{M}, k = 11$ for o_2, hence we adopt $\Delta t = 100\,\mathrm{M}, k = 10$ for both orbits. We generate the set of surrogates and perform the analysis in the same way as for the observed X-ray lightcurves in Suková et al. (2016).
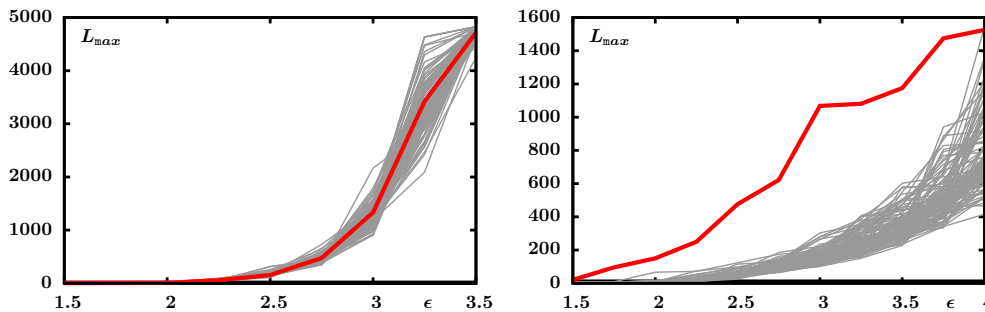
Figure 2. $L_{\max}$ for regular orbit o_1 (left) and chaotic orbit o_2 (right)
with added noise with $\sigma_n = 0.4$ plotted by thick red lines and the same
for the ensemble of surrogates.

At first we investigate the dependence of the length of the longest diagonal line present in the recurrence matrix $L_{\max}$ on ϵ. As expected, the regular trajectory yields very long diagonal lines for small thresholds and $L_{\max}$ goes up almost to the maximal value N. The surrogates behave in a similar way for a little bit higher threshold. This is due to the way how the surrogate data are constructed, as they have exactly the same value distribution but they reproduce the spectrum only approximately depending also on the available length of the data set. In case of regular motion, very narrow peaks are in the spectrum and the error in reproducing such spectrum causes the very long diagonal lines to be broken. This higher value of ϵ for surrogates corresponds to the size of the neighbourhood needed for covering the small discrepancies of the surrogates. The chaotic orbit o_2 provides shorter lines, so that $L_{\max} < 2000$ for the range of thresholds we used. Yet it is significantly larger than the corresponding values for surrogates. Only for very high thresholds, the difference decreases.

Because in reality the data always contain some level of noise, we take the normalized times series for o_1 and o_2 and we add a white noise with zero mean and increasing variance σ_n and rescale the resulting data back to zero mean and unit variance. The surrogates created from the regular orbit with added noise reproduce the spectrum better than for the regular orbit alone (normalised rms discrepancy between the exact spectrum and the exact amplitude stage reported by the `surrogates` procedure decreases from $\sigma_n = 0$ to $\sigma_n = 0.25$).

In Fig. 2 the plots of $L_{\max}$ versus ϵ for the added white noise with $\sigma_n = 0.4$ are shown. The presence of noise shifts up the needed threshold for some lines to occur in RP. For the regular orbit o_1 there is no significant difference from the surrogates. For chaotic orbit o_2 the threshold is also shifted to higher values, but the difference from the surrogates remains.

Our posed null hypothesis is that the data are the product of linearly autocorrelated process and because the regular trajectory can be treated as such (e.g. in the case of a periodic orbit, the points separated by the period T are the same), the significance is small. On the other hand, the chaotic trajectory cannot be treated as linear dynamics and yields high significance.

In Fig. 3 the estimate of K_2 and the significance of its comparison with the surrogates is given for the increasing level of noise ($\sigma_n = 0, 0.05, \ldots, 1.00$). We
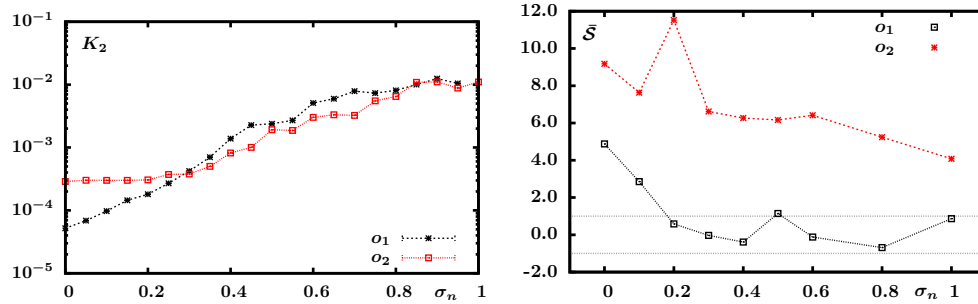
Figure 3. The estimates of the Rényi's entropy K_2 computed for RR$\sim$15% and the significance of its comparison with surrogates with increasing strength of the noise.

note, that for low levels of noise the regular orbit yields much lower value of K_2, which can serve as the differentiation between chaotic and regular motion (see (Semerák & Suková, 2012)). However for increasing strength of the noise, the regular orbit o_1 seems to be more affected than the chaotic one, providing higher K_2 for the noise levels $\sigma_n > 0.25$. Therefore, the significance for the regular orbit drops down bellow one quickly, while the significance for chaotic orbit reaches values around 10 for low noise levels, near 6 for intermediate noise levels and stays around 4 for high noise levels, even up to the case, when the variance of the noise is the same as the variance of the data.

3. Conclusions

The test of the method for finding non-linear dynamics in dynamical systems based on the observed time series shows that for a given length of observational data set (5000 points) we can expect that chaotic dynamics would yield values of significance between 2-10 depending on the strength of the noise. Regular motion would not provide significant result, because even low level of noise present in the measured data destroys the differences with respect to the surrogates.

References

Grassberger, P. 1983, Physics Letters A, 97, 227

Hegger, R., Kantz, H., & Schreiber, T. 1999, Chaos, 9, 413

Schreiber, T. & Schmitz, A. 2000, Physica D: Nonlinear Phenomena, 142, 346

Semerák, O. & Suková, P. 2010, MNRAS, 404, 545

Semerák, O. & Suková, P. 2012, MNRAS, 425, 2455

Suková, P., Grzedzielski, M., & Janiuk, A. 2016, A&A, 586, A143

Theiler, J. at al, 1992, Physica D: Nonlinear Phenomena, 58, 77

Witzany, V., Semerák, O., & Suková, P. 2015, MNRAS, 451, 1770

On going optical photometric monitoring of AGN TeV targets with the Watcher Robotic Telescope

B. van Soelen[1], I.P. van der Westhuizen[1], L. Hanlon[2],
A. Martin-Carrillo[2], P.J. Meintjes[1], D. Murphy[2], H.J. van Heerden[1]

[1] *Department of Physics, University of the Free State, 9301, South Africa*
[2] *School of Physics, University College Dublin, Belfield, Dublin 4, Ireland*

Abstract. Active Galactic Nuclei (AGN) show variability on various time scales and present complex correlations between these variations at different wavelengths. Simultaneous multi-wavelength observations can therefore be used to place constraints on the different emission models. In May 2015 we began optical photometric monitoring of a subset of the known TeV emitting AGN using the Watcher Robotic Telescopes (Boyden Observatory, South Africa) to obtain long term photometric monitoring of these sources. Currently 17 targets are included in this monitoring campaign. The sources are observed once per night in the V, R & i' bands, depending on observability and weather. The V, R and V-R light curves of four blazars are presented, all of which show variability which is consistent with previous studies. This demonstrates the feasibility of using the Watcher telescope to provide long term optical photometric monitoring of TeV blazars.

1. Introduction

The Watcher Robotic Telescope is a fully automated system located at the Boyden Observatory, South Africa. The system was initiated by the University College Dublin (UCD) Space Science Group, and is run in partnership with the Czech Technical University in Prague (ČVUT), the Institute for Astrophysics of Andalucia (IAA) and the University of the Free State (UFS). The primary science aim of the telescope is the rapid optical follow-up of gamma-ray burst triggers initiated by the Gamma-ray Coordination Network (see e.g. Murphy et al. 2015 & Martin-Carrillo et al. 2015a). Time that is not dedicated to GRB observations is used for observations of both galactic and extra-galactic sources. For example, Watcher has recently been used to follow the cataclysmic variable ASASSN-15ni (Martin-Carrillo et al. 2015b, 2015c).

To complement other multiwavelength observations we have begun, in May 2015, a long term monitoring programme of known TeV blazars, which have previously been detected with Imaging Atmospheric Cherenkov Telescopes, with the aim of providing long term multi-filter observations that can be used to place constraints in correlation studies.

The Spectral Energy Distributions (SEDs) of blazars are, in general, dominated by the non-thermal emission produced in relativistic jets, which is highly Doppler boosted since the direction of propagation lies close to our line of sight. The SEDs of the blazars show two distinct components at lower (radio to UV/X-

ray) and higher (X-ray to gamma-ray) energies. In the leptonic scenario, the lower energy component is produced through synchrotron radiation, while the higher energy component is produced through inverse Compton scattering of either the synchrotron produced photons, or external photons originating from, for example, the accretion disc, broad line region or dust torus. However, alternative hadronic models have been proposed (e.g. Böttcher et al. 2013).

If both the low and high energy components are produced through the same population of particles, there should be a correlation between the different components. However, observations have shown complicated behaviour with observed correlations, lags, anti-correlations and orphan flare events (e.g. Krawczynski et al. 2004, Blazejowski et al. 2005, Abdo et al. 2010, Fossati et al. 2008). In one recent example a search for correlation from PKS 2155-304 between TeV observations undertaken with H.E.S.S. (High Energy Stereoscopic System) and optical observations with the ATOM (Automatic Telescope for Optical Monitoring) telescope, found a complex relation which depends on the colour and gamma-ray state of the source (Abramowski et al. 2014).

Below we discuss the Watcher Robotic Telescope, the strategy of the monitoring campaign, preliminary results and the proposed future improvements.

2.   The Watcher Robotic Telescope

The Watcher telescope is a 16 inch Cassegrain design (f/14.25) telescope, equipped with a Meade (f/6.3) focal reducer and is used with a Paramount ME equatorial mount. When a trigger is received from the Gamma-ray Coordination Network (GCN) the telescope automatically repoints and begins observations within, on average, 45 seconds after receiving the alert. An Andor iXon+ 888 CCD (1024x1024 pixels) is currently mounted, which records a 10'×10' field of view (with the focal reducer). V, R, g', r', i', Clear, and OIII filters are available. The telescope dome is fully automated with continuous monitoring of the atmospheric conditions with an on-site weather station, cloud meter and precipitation sensor.[1]

3.   TeV blazar monitoring campaign

Currently 17 known TeV AGN targets, spread over a broad range in right ascension, are being observed as part of the long term monitoring campaign. Given the smaller size of the telescope, observations have been limited to sources brighter than 18th mag. All observations are controlled by the telescope's scheduler (with the highest priority given to observations of GRBs). Observations of the TeV AGN targets are scheduled to occur once per night, with each observation divided into 6 exposures of 60 seconds each, in the B, V and i' filters. The actual observation cadence depends on the observability of the source (airmass, weather, etc.) as well as if higher priority sources are being observed.

[1]More information is available on the Watcher Telescope at http://watchertelescope.ie/
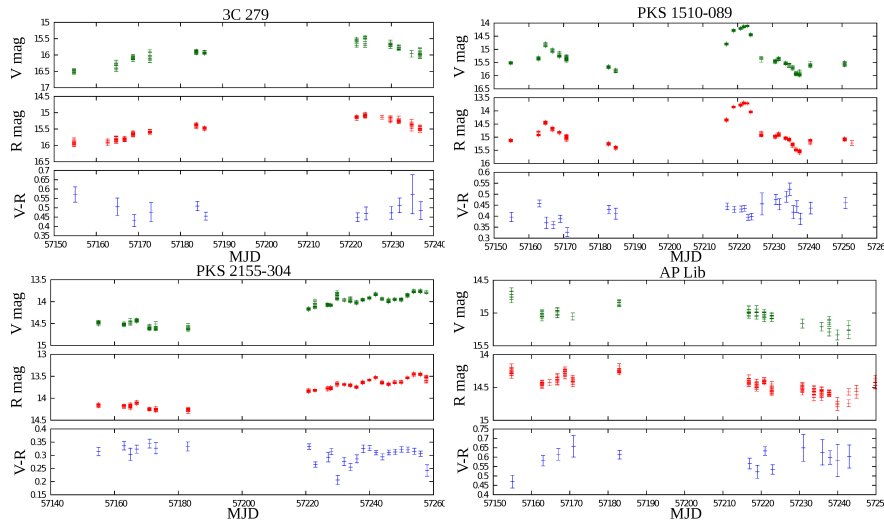
Figure 1.   V, R and V-R light curves for 3C 279 (*top left*), PKS1510-089 (*top right*), PKS 2155-304 (*bottom left*) and AP Lib (*bottom right*).

4.   Data reduction and analysis

All data frames are corrected for the bias offset and flat field using the standard IRAF/NOAO/CCDRED packages. The exposure times are short enough, and the camera cooling efficient enough, that dark current effects are assumed to be negligible. Photometry is performed using the NOAO/DAOPHOT packages, for multiple apertures, and aperture optimizations is performed using the NOAO/PHOTCAL packages.

Differential photometry is performed using a weighted average of a selection of comparison stars on the same field of view, following a method similar to that outlined in Everett & Howell (2001). Each star is weighted according to $\omega = \sigma_{\mathrm{err}}^{-2}$ where σ_{err} is the error given by the PHOT function. Where known apparent magnitudes are available for the comparison stars, the differential light curves are corrected for the offset between the average instrumental magnitudes of the companion stars and their known apparent magnitudes. The variability in the V-R colour is calculated from the daily binned magnitude in each filter.

5.   Results

Figure 1 shows the results from the initial optical photometric monitoring of four prominent blazars (3C 279, PKS 1510-089, PKS 2155-304 & AP Lib). For each source, the V, R and V-R light curves are shown. As expected all four sources shown here exhibit the long term optical variability expected for AGN. Similar variability has been reported for these sources by, e.g. Abramowski et al. (2014), Sandrinelli et al. (2014), Wierzcholska et al. (2015).

In particular, PKS 1510-089 shows a large flaring event during the monitoring period. The first peak, around MJD 57165, occurs around the same period of

a reported increase at TeV energies by the MAGIC (Major Atmospheric Gamma Imaging Cherenkov Telescopes) telescope (Mirzoyan et al. 2015). All sources also show variations in the V-R colour as shown by the change in V-R with time and brightness.

6.   Future Development

The preliminary results for the four sources demonstrate that long term monitoring is feasible using the Watcher Telescope. The planned future developments for this project are: the expansion of the number of monitored sources, the implementation of a fully automatic data reduction and analysis pipeline, providing public access to the data generated by the analysis pipeline, and, ideally, using the data to trigger alerts for other multi-wavelength observations.

7.   Conclusions

The automated Watcher telescope, while designed for GRB follow-up observations, is well suited to long term monitoring of known and candidate TeV AGN sources. The optical observations obtained thus far demonstrate the feasibility of using the system to perform long term monitoring of blazar targets and the multi-filter observations can be used to place constraints on the multi-wavelength observations of known TeV AGN.

References

Abdo A.A. et al. 2010, Nature, 463, 919
Abramowski A. et al. 2014, A&A, 571 A39
Blazejowski M. et al. 2005, ApJ, 630, 130
Böttcher M., Reimer A., Sweeney K., Prakash A. 2013, ApJ, 768, 54
Everett M.E. & Howell S.B. 2001, PASP, 113, 1428
Fossati G. et al. 2008, ApJ, 677, 906
Krawczynski H. et al. 2004, ApJ, 601, 151
Martin-Carrillo A. et al. 2015a, GCN Circular 18085
Martin-Carrillo A. et al. 2015b, ATel 7855
Martin-Carrillo A. et al. 2015c, ATel 7875
Mirzoyan R. et al. 2015, ATel 7542
Murphy D. et al. 2015, GCN Circular 17947
Sandrinelli A., Covino S., Treves A. 2014, A&A, 562, A79
Wierzcholska A. et al. 2015, A&A, 573, A69

Optical spectroscopic monitoring of the variation in the circumstellar disc in PSR B1259-63/LS 2883 during the 2014 periastron passage

B. van Soelen[1], P. Väisänen[2,3], A. Odendaal[1], I. Sushch[4,5], L. Klindt[1], P.J. Meintjes[1]

[1] *Department of Physics, University of the Free State, Bloemfontein, 9301, South Africa*
[2] *South African Astronomical Observatory, PO Box 9 Observatory, 7935, South Africa*
[3] *Southern African Large Telescope, PO Box 9 Observatory, 7935, South Africa*
[4] *Centre for Space Research, North-West University, Potchefstroom, 2520, South Africa*
[5] *Astronomical Observatory of Ivan Franko National University of LâĂŽviv, vul. Kyryla i Methodia, 8, 79005, LâĂŽviv, Ukraine*

Abstract. The γ-ray binary system PSR B1259-63/LS 2883 passed through periastron in May of 2014 and was the focus of intensive multi-wavelength campaigns. During the previous periastron, a large flare was detected at GeV energies 30 days after the 2010 periastron passage by *Fermi*-LAT. This event was re-detected during 2014 at a similar orbital phase. In order to place better constraints on the behaviour of the circumstellar disc around periastron, we performed optical spectroscopy of the Hα and He I (λ6678) lines with the Southern African Large Telescope (SALT) from 33 days before until 78 days after the 2014 periastron. The Hα line remains single peaked through all observations, but with a noted asymmetry and variation in shape. The He I line remains double peaked and shows a variation in the relative peak heights. Both lines show an increase in the equivalent width which peaks after periastron. The line strengths before periastron are, however, weaker than were detected around the 2010 periastron, though are comparable after periastron.

1. Introduction

The γ-ray binary system PSR B1259-63/LS 2883 consists of a 48 ms pulsar in an approximately 3.4 year orbit around the Be star LS 2883 (Johnston et al. 1992). The interaction between the pulsar and stellar winds leads to the formation of a shock, resulting in non-thermal radio, X-ray and γ-ray emission, which is strongest around periastron. The presence of a circumstellar disc around LS 2883 alters the interaction region when the pulsar passes close to the disc, (inferred by the eclipse of the pulsed radio signal). Over the last two periastron passages observations with *Fermi*-LAT have detected a flare-like event starting approximately 30 days after periastron (e.g. Abdo et al. 2011, Caliandro et al 2015, Tam et al. 2015) at a phase when the other non-thermal emission is de-

creasing. However, there is an indication of a multi-wavelength component, as a hardening in the X-ray emission has been noted around the period of the *Fermi* flare (e.g. Chernyakova et al. 2015). Since the interaction between the pulsar and disc near the second disc crossing could have an important effect on the non-thermal emission, it is important to follow the variation in the circumstellar disc around periastron. For an approximately three month period around the 2014 periastron, which occurred on the 4th of May 2014 (MJD 56781.42), we observed the binary system with the Southern African Large Telescope (SALT) as well as with the SAAO 1.9-m telescope. Below we briefly discuss SALT as well as summarize the results of the optical observations reported in van Soelen et al. (2016) and Chernyakova et al. (2015).

2.   The Southern African Large Telescope

The South African Astronomical Observatory (SAAO) operates and manages the optical and infrared telescopes located at the Sutherland station, located in the Northern Cape, South Africa (32.38°S, 20.81°E). This includes the Southern African Large Telescope (SALT) as well as a number of smaller telescopes.

SALT, a 10 metre class telescope, was built between 2000-2005, following a similar design as the Hobby-Eberly Telescope (HET). The primary mirror, which consists of 91 hexagonal segments, has a fixed elevation angle of 37° relative to the zenith, which greatly reduced the cost of construction. Due to this design observations are limited to declinations between $+10°$ to $-72°$. The tracking of astronomical sources is achieved by moving the science instruments located at the prime focus and the track time is between 1 to 3 hours, depending on the declination of the target (O'Donoghue et al. 2006, 2008).

SALT is currently equipped with four instruments: SALTICAM, the Robert Stobie Spectrograph (RSS), the High Resolution Spectrograph (HRS) and a visitor instrument, the Berkeley Visible Image Tube camera (BVIT).

SALTICAM   This is the primary imager instrument on SALT. The detector consists of two mosaicked 2048×4012 pixel E2V Technologies CCDs (see e.g. O'Donoghue et al. 2006). The system is specifically chosen to be sensitive in the ultra-violet and optical range. The plate scale at the detector is 0.14 arcsec/pixel, with an 8 arcmin diameter science usable field of view.

RSS   The three main modes of operation of the RSS are long-slit spectroscopy, multi-object spectroscopy and Fabry-Perot imaging spectroscopy (e.g. Kobulnicky et al. 2003). The fourth mode, spectro-polarimetry is currently being commissioned. The spectrograph is equipped with six diffraction gratings, which are operated in first order. Standard long-slit spectroscopy can be performed with a selection of 7 slits which range in width from 0.6 to 4 arcseconds. Multi-object spectroscopy is performed by using slits that are laser cut into a carbon fibre mask, allowing for the spectra of multiple objects to be extracted in a single observation. The Fabry-Perot (e.g. Rangwala et al. 2008) is available in low-resolution, medium-resolution, high-resolution and tunable filter modes.

HRS   The High Resolution fibre-feed échelle spectrograph (e.g. Crause et al. 2014), has a wavelength coverage of 3700–5550 Å and 5550–8900 Å on two sepa-
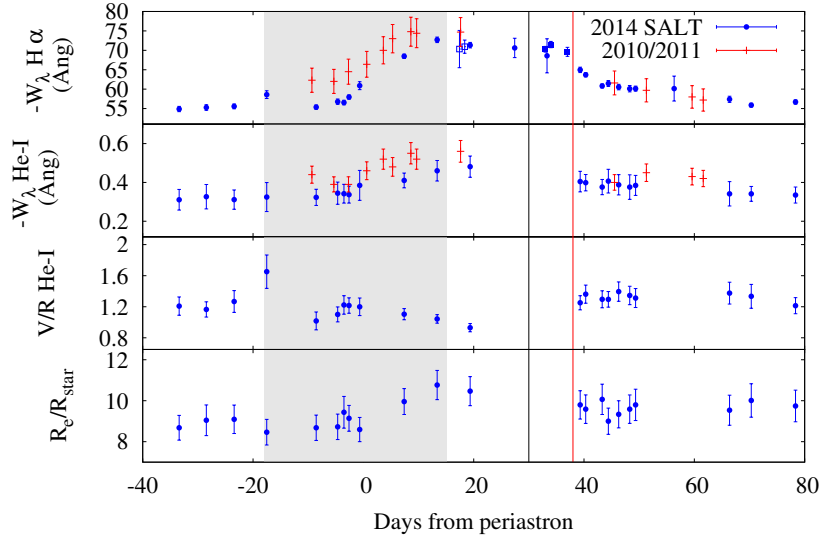
Figure 1. Equivalent width of the Hα (top), and equivalent width, V/R variation and emission location of He I as observed with SALT in 2014 (blue circles, van Soelen et al. 2016). The 2010/2011 observations are shown for comparison (Chernyakova et al 2014). Also shown are observations undertaken with the SAAO 1.9-m (blue open squares, van Soelen et al. 2016, filled squares Chernyakova et al. 2015). The black and red vertical lines show the time of the onset and peak of the 2014 *Fermi* flare, respectively (Caliandro et al. 2015). The shade region indicates the period of the pulsar eclipse (Chernyakova et al 2014).

rate channels. The spectrograph can operate in four modes, namely, low resolution ($R \sim 15000$), medium resolution ($R \sim 40000$), high resolution ($R \sim 65000$) and high stability ($R \sim 65000$, optimized for radial velocity measurements).

BVIT This visitor instrument is a very high time resolution (< 1 microsecond) photon counting camera (e.g. Siegmund et al. 2008).

3. Observations of the PSR B1259-63/LS 2883

The γ-ray binary system PSR B1259-63/LS 2883 was observed with SALT using the RSS from 33 days before (30 April 2014) until 78 days after (21 July 2014) the 2014 periastron passage. The RSS was configured to observe 6176.6 – 6983.0 Å to focus on the Hα and He I lines. Each observation consisted of 3 to 4 exposures for a total integration time of ~ 500 seconds, achieving a signal to noise ratio of ~ 200. The Hα emission line was also observed with the SAAO 1.9-m telescope between 17–18 days (van Soelen et al. 2016) and 33–38 days (Chernyakova et al. 2015) after the 2014 periastron.

Both the Hα and He I lines remain in emission through all observations, with $W_{\lambda,\text{H}\alpha} \approx -61$ Å and $W_{\lambda,\text{He}} \approx -0.57$ Å over the observation period. The

Hα line is an asymmetric, single peaked emission line, while the He I line shows a double peaked emission line, superimposed on the underlying stellar absorption line. The orbital variations of the lines around the 2014 periastron are shown in Fig. 1 (blue points) in comparison to the 2010 periastron (red points). There is a marked change in the asymmetry and an increase in the equivalent width at 17 days before periastron, with an increase in the violet component. This occurs around the time of the first disc crossing.

The V/R variation of the He I shows an increase in the asymmetry around the first disc crossing, a general decrease in V/R after periastron, with the red component becoming slightly stronger (V/R $= 0.93 \pm 0.05$) around the second disc crossing. From the change in the separation of the V&R peaks we have calculated the location of the He I emission in the circumstellar disc (Huang 1972). This shows the emission location varies between $8.3 < R/R_\star < 10.8$ around periastron (Fig. 1), moving further out in the disc around periastion, to a maximum around the same period as the maximum equivalent width.

4.   Discussion & Conclusion

The observations confirm the general trend previously observed for PSR B1259-63/LS 2883, with an improvement in the orbital phase coverage. The Hα EW is lower than the 2010 observations which we suggest is due to the intrinsic variability associated with the Be star. This may indicate a lower mass for the disc around the 2014 periastron passage. A more detailed description is given in van Soelen et al. (2016). From a comparison to multi-wavelength results around this period it has been suggested that there is a change in the mass of the disc during the period following the *Fermi* flare (e.g. Chernyakova et al. 2015).

References

Abdo A.A., et al. 2011 ApJ, 736, L11
Caliandro G.A., et al. 2015, ApJ, 811, 68
Chernyakova M., et al. 2014, MNRAS, 439, 432
Chernyakova M., et al. 2015, MNRAS, 454, 1358
Crause, L.A. et al. 2014, SPIE, 9147, 6
Huang S. 1972, ApJ, 171, 549
Johnston S., et al. 1992, ApJ, 387, L37
Kobulnicky H.A., et al. 2003 SPIE, 4841, 1634
O'Donoghue D. et al., 2006, MNRAS, 372, 151
O'Donoghue D. et al., 2008, SPIE, 7018, 13
Rangwala N., Williams T.B., Pietraszewski C., Joseph C.L., 2008, AJ, 135, 1825
Siegmund O.H.W.S., et al. 2008, AIP Conf. Proc., 984, 103
Tam P.H.T., et al. 2015, ApJ, 798, L26
van Soelen B. et al., 2016, MNRAS, 455, 3674